Microstructural characterization and mechanical properties of 9%Ni steel welds by submerged arcwelding process using nickel-base alloys

Pablo Ozaeta Laverde

Facultad de Química

Ciència I Tecnologia dels materials

Microstructural Characterization and Mechanical Properties of 9%Ni steel welds by Submerged Arc Welding process using Nickel-base alloys.

Pablo Ozaeta Laverde

Director: Josep María Guilemany I Casadamon

Catedratic Universitat de Barcelona.

Tutor: Josep María Guilemany I Casadamon

Catedratic Universitat de Barcelona

Para Jimena

Agradecimientos

Catorce años han transcurrido desde aquel primer proyecto, el TK-3000 construido en el Puerto de Barcelona. Catorce años en los que muchísimas personas me han apoyado, guiado y enseñado. Los primeros en mi lista de agradecimientos son Jorge Ros y Justo Narrillos, quienes me brindaron la oportunidad de incorporarme al equipo LNG. De Japón, El Dr. Norihiko Katayama, Kikuchi, Tanaka e Isashi, compañeros de IHI con los que compartimos momentos difíciles y agradables. De Alemania, Josef Heineman y Stephan Eich y todo el equipo de UTP que tanto me ayudaron. De Lincoln Juan Ortiz, Jordi Donate, Silvia, Carmen, Joaquín, Craig Dallam, Ángel Vidal y Ángela Lázaro, por el apoyo recibido. De Holanda: Vincent Van Der Mee, Jan Hilkes, Peter Van Erk y Fred Nissen, por los sabios consejos. De USA, Tim O'Donnel, Teresa Melfi, Jon Procario, Mike Lattesa, Patrick Whalen, Tom Angelino, por el apoyo y ayuda. De Bose a Lauro Mula y Jesús Domenech. Y Miguel Ángel Pascual compañero y amigo de la UCV. A todos ellos y muchos otros de los que me acuerdo, y de los que no me acuerdo.

…Muchas Gracias.

En La Universidad, un equipo fabuloso de compañeros y amigos, María, Judith, Verónica, Marck, Jessica, Alejandra, Sergi, Irene y Nuria Cinca con quien he compartido muchas horas, muchos días. Además quiero reconocer y dar especial agradecimiento a mi tutor y maestro el Dr. Josep María Guilemany quien ha creído en mi proyecto, me ha apoyado y animado a no abandonar… A todos vosotos CPTeros…

…Muchas Gracias.

Para terminar me queda Malena, quien me ha acompañado, apoyado y empujado por veinte años, y no sólo en este proyecto de doctorado…

Cierro este corto pero sentido agradecimiento con un mensaje de gratitud para *"Mis Chicas"* Rosa María y Jimena, que son el centro de mi vida y mi fuente de energía y amor…

Para todos los que estáis, y los que habéis estado…

…Mil Gracias

Contents

Antecedentes, Motivación y Objetivos:

En 2003 me incorporé al equipo de diseño y construcción de Felguera-IHI de un tanque para el almacenamiento de Gas Natural Licuado. Este proyecto representaba un reto importante para todos los integrantes del equipo ya que estábamos iniciando desde cero la ingeniería de detalle de este tipo de tanques, aunque contábamos con el apoyo de IHI, el socio japonés, con amplia experiencia en este tipo de proyectos. Durante este período desarrollamos todos los planos, procedimientos y especificaciones que permitirían ejecutar el proyecto.

En julio del mismo año, en el departamento de Calidad y Soldadura iniciamos un estudio comparativo de los consumibles de soldadura, con el fin de seleccionar los productos que cumplirían con los requisitos de diseño. En este estudio se determinaron los parámetros de

Fig A- 1: Soldeo de cupones en verano 2003

soldadura y se evaluaron la resistencia mecánica transversal y longitudinal, la ductilidad, la tenacidad a la fractura a -196ºC y la resistencia a la fisuración, de cuatro marcas de electrodos revestidos para el soldeo con SMAW y tres pares alambre-

fundente para el soldeo con SAW, usando en estos últimos, hilo de 2,4mm de diámetro.

Se soldaron veintiséis probetas, para determinar los parámetros de soldadura y propiedades mecánicas y cuarenta y una probetas para evaluar la sensibilidad a la fisuración. El material base en todas ellas fue acero 9%Ni de 21mm de espesor.

Fig A- 2: Ensayos de fisuración durante pruebas de verano 2003

Este estudio comparativo fue liderado por Justo Narrillos, quien fuera Jefe de Soldadura de Felguera IHI, y guiado por el Dr. Norihiko Katayama, Chief Welding Manager de IHI, quien estuvo durante dos meses al frente de los ensayos.

De los resultados obtenidos se seleccionaron y compraron los consumibles que se usaron para la construcción del primer tanque; aunque los valores de resistencia mecánica de las tracciones cilíndricas del metal de soldadura estuvieron un poco por debajo de los valores esperados, las tracciones trasversales presentaron valores de resistencia mecánica altos, rompiendo, la mayoría de las muestras por el metal base, lo cual es destacable por la diferencia de propiedades mecánicas entre el metal base y el metal de soldadura.
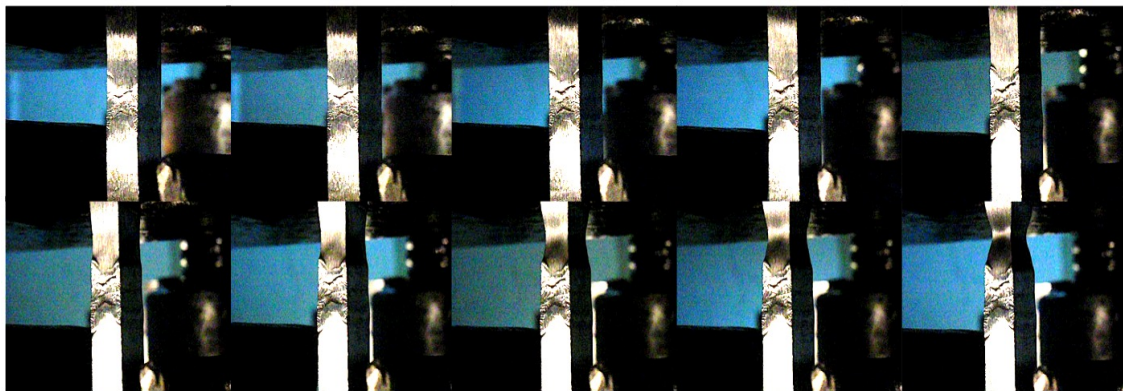
Fig A- 3: Tracción prismática. Deformación por metal base

El acero 9%Ni tiene un límite elástico nominal de 520MPa y una resistencia a la rotura por encima de los 700 MPa; en cambio, el metal de soldadura usado tiene su límite de elasticidad a los 400MPa y la rotura a 690MPa. Durante el ensayo de tracción transversal la deformación plástica siempre inició en el metal de soldadura, pero a medida que se aumentaba la carga, la deformación plástica pasaba al metal base, donde después de una marcada deformación plástica se producía la ruptura siempre por encima de 700MPa.

En vista de los bajos valores obtenidos en las tracciones cilíndricas del metal de soldadura, en enero del 2004 se inició un segundo estudio, en el que se evaluó el efecto de la rigidez mecánica y la

Fig A- 4: Probetas para evaluar el efecto de la rigidización.

dilución sobre la resistencia mecánica de las probetas cilíndricas del metal de soldadura.

Es importante aclarar, que según API 620, Norma que define los criterios de diseño y construcción del tanque, los espesores de las chapas se calculan después de seguir una serie de condicionantes, a partir de los valores obtenidos de las tracciones cilíndricas del metal de soldadura. La diferencia en costes entre usar la resistencia mecánica de las tracciones cilíndricas o la resistencia de las tracciones transversales, era de varios cientos de miles de euros, y en vista de la negativa de usar el resultado de las tracciones transversales, se realizó un estudio intensivo para mejorar los valores de resistencia mecánica de las probetas cilíndricas, lo cual implicaba determinar las variables metalúrgicas y las del proceso de soldeo que afectaban estos resultados, y cómo afectaban.

Para el estudio realizado en enero de 2004, se soldaron otras doce probetas en chapa de 12mm y 21mm. Se estudió principalmente el efecto de la rigidización mecánica por ser una de las recomendaciones de Welland [4-3-1] y también la recomendación de los fabricantes de consumibles. Los resultados obtenidos de este set de probetas no fueron concluyentes debido a la alta variabilidad de los valores de resistencia medidos de las probetas cilíndricas.

En agosto del mismo año se soldó otro set de trece probetas, en esta oportunidad en Alemania, en las instalaciones del fabricante de los consumibles de soldadura comprados. Allí se evaluó el efecto del diseño de junta y velocidad de enfriamiento.

Con los resultados de este estudio se determinaron las condiciones de soldeo para obtener los resultados esperados en la homologación del procedimiento de soldadura, cumpliendo de esta forma con los requisitos de diseño.

Fig A- 5: Soldeo de juntas horizontals.

Como se mostrará más adelante, la mayoría de los resultados presentaron variaciones tan amplias de resistencia mecánica que dificultaron la interpretación correcta del efecto de la variación de la variable.

Durante el soldeo de las probetas de homologación del procedimiento se observó un problema de porosidad no observado en todas las probetas soldadas hasta la fecha. Durante el soldeo del primer tanque, trabajos iniciados en noviembre-diciembre de 2004, se presentaron problemas importantes de desescoriado y porosidad durante la ejecución de la soldadura. Alrededor del 80% de las reparaciones efectuadas fueron debidas a inclusiones esféricas de escorias. Se determinó que la causa principal de estos problemas era la baja fluidez del metal de soldadura, lo cual dificultaba la desgasificación y la separación de las fases metálica y escoria.

Para mejorar la fluidez del baño se decidió aumentar la densidad de corriente, a través de la reducción del diámetro del hilo. En marzo de 2005 se inició un nuevo estudio, donde se compararon dos fluxes, el usado en producción y uno nuevo, con hilos de 2,4mm y de 1,6mm. Para este estudio se soldaron probetas para determinar los parámetros óptimos así como una

Fig A- 6: Ensayos para determiner el efecto del diámetro del hilo.

serie de probetas para determinar la sensibilidad al Re-Heat Cracking. Para la determinación de propiedades mecánicas se soldaron ocho probetas en espesores de chapa de 12mm y 26,5mm. El primer conjunto de probetas ensayado presentó unos resultados mecánicos moderados, mientras que, con el segundo conjunto de probetas, soldadas con hilo de 1,6mm y el quinto flux, se consiguieron los resultados mecánicos más altos del histórico ensayado, incluso a la fecha de hoy.

La reducción del diámetro del hilo eliminó prácticamente al 100% las inclusiones esféricas de escoria, la porosidad durante el soldeo, mejorando el desescoriado de forma radical. Además, aumentó la velocidad de soldadura al incrementare el "Deposition Rate", observándose además una ligera mejora en la resistencia mecánica tanto de las tracciones transversales como de las cilíndricas,

Fig A- 7: Tanques LNG. Puerto de Barcelona

tanto en las probetas de este ensayo como en la homologación de los procedimientos de soldadura.

En noviembre de 2005 se inició el soldeo de producción del segundo tanque, confirmándose la mejora de la limpieza del metal depositado, el desescoriado y la porosidad, pero surgió un problema inesperado en la inestabilidad de arco y alimentación del hilo (feedability) que continuó durante toda la soldadura de las juntas horizontales de este segundo tanque.

Una vez finalizada la soldadura del segundo tanque, en abril del 2006 comencé a trabajar en Lincoln Electric, con el fin de evaluar equipos y consumibles y desarrollar una cartera de productos para el soldeo de tanques para el almacenamiento de 9%Ni.

Se iniciaron 3 proyectos:

1. Feedability test for SAW, en el cual se probaron diferentes configuraciones de

Fig A- 8: Banco de pruebas. Lincoln-KD. Barcelona.

máquinas, lanzas y puntas de contacto, con el fin de determinar el conjunto correcto para garantizar un proceso de soldeo estable y continuo.

2. Selección de un par alambre-fundente que maximice propiedades mecánicas y con una buena soldabilidad. Este trabajo se realizó en varias etapas, haciendo pruebas preliminares de soldabilidad con diferentes fluxes en España en 2007 y evaluación de propiedades mecánicas en julio-agosto de 2008.

3. Creación de un alambre tubular, Flux Core Wire, con una aleación base níquel específicamente diseñada para esta aplicación.

En este contexto de trabajos, inicié mi doctorado en la Universidad de Barcelona, bajo la tutoría y dirección del Profesor Josep María Guilemany, en el curso académico 2006-2007, con el objetivo de estudiar la microestructura del metal depositado y comprender su efecto sobre las propiedades mecánicas.

El proyecto de selección del par alambre-fundente se inició en octubre de 2006, cuando se evaluaron criterios de soldabilidad, tales como estabilidad de arco, acabado superficial, desescoriado, etc. Como metal de aporte se seleccionó la aleación Hastalloy C-274 con cuatro fluxes de la casa. Como elementos de control o comparativo de esta prueba se usaron dos fluxes de la competencia frecuentemente usados en esta aplicación.

La segunda etapa de este proyecto se desarrolló en verano de 2008, en la casa matriz de Lincoln Electric en Cleveland, Ohio. En esta etapa se ensayaron cuatro fluxes, dos aglomerados y dos fundidos, con el fin de determinar propiedades mecánicas y condiciones óptimas de soldeo.

El par alambre-fundente seleccionado en estas pruebas ha sido usado para el soldeo de ocho tanques: tres en España: dos en Gijón 2011-2013 y uno en Bilbao 2014-2015; un tanque en Chile, 2011-2013 y otros cuatro tanques en China, 2011-2013.

Con este par se han conseguido buenos resultados en las homologaciones de procedimientos de soldadura de estos proyectos, tanto en las tracciones

Fig A- 9: Weld-tech Lincoln-Cleveland

transversales como en las tracciones cilíndricas, cumpliendo con los requisitos de resistencia necesarios en cada proyecto. Durante la producción se ha depositado un metal de soldadura con muy pocas inclusiones de escoria, presentando buen desescoriado y desgasificado.

En 2009 y a raíz de la crisis económica mundial se pararon varios proyectos de construcción de plantas de LNG, por lo que se canceló el proyecto de creación de hilo tubular. A mí me desplazaron a Francia, por lo que suspendí, en su momento mis estudios de Doctorado.

Entre el 2009 y el 2015 estuve desarrollando proyectos en Francia, España, Chile y Arabia. Finalmente, en noviembre de 2015, inicié un periodo sabático para terminar el Doctorado. Para finalizar el programa de investigación, se seleccionó el set experimental realizado en verano de 2008. Del cual se obtuvo un buen producto, aunque se presentaron, una vez más, variaciones importantes en los resultados. En esta ocasión, el objetivo ha estado orientado a determinar las causas que producen la alta dispersión en los resultados y que ha dificultado la interpretación de los resultados y la toma de decisiones.

1. Introduction.

1.1 LNG tank.

Natural gas is transported by pipelines at high pressure, LPG, where the maximum rentable length are around dozens of thousands of kilometers or at low temperature and ambient pressure by LNG sea carriers, where natural gas could be transported **for longer distances** than LPG technology.

At both side of LNG production chain, the product should be temporally storage; after liquefaction while is waiting to be charged on LNG carriers, and at receiver side, while it is waiting to be processed in regasification plant. This temporal **storage of** Natural Gas is made in liquid state a temperature below -165**ºC** in LNG tanks, which are designed like huge multi-layer thermo, with few insulator **layers** place**d** between different structural parts of the tank.

1.1.1 Base metal.

Carbon steels and most ferritic materials change from ductile to brittle below certain temperature, which depends on the chemical composition, heat treatment and material thickness, this temperature is called "Transition Temperature". This natural characteristic makes ferritic materials not been used in applications at temperatures below -80ºC.

The heat-treated 9% nickel steels have good toughness at temperatures below -196°C along with a high mechanical strength. There are two 9%Ni steels, the ASTM A353 which is double normalized and tempered and the ASTM A553 which is quenched and tempered. The A553 T1 steel has a microstructure consisting of tempered martensite, bainite, and about 4% of stable austenite obtained during tempering of the steel just above the austenite transformation temperature**.**

These steels have good weldability, so any of common welding processes, SMAW, GTAW, FMAW and SAW, could be used to weld them. Although SMAW and SAW are the most frequently used welding processes, FCAW has shown good performance in recent years.

9%Ni steel tends to be easily magnetized, keeping it for a while. Residual magnetism per se doesn't represent any issue for the steel, but it yes during welding by any electric arc procedure, producing "Arc Blow" troubles what create rejectable discontinuities in the

deposited weld metal.

Fig 1- 1: LNG tank, shell erection process.

Residual magnetism issue is controlled avoiding that plate will be exposed to any magnetic field, avoiding the plate handled by magnetic manipulators and even avoiding that trucks will be parked below high-tension electric conduction lines.

1.1.2 Weld Metals.

These steels could be welded using similar chemical composition filler metals if appropriated heat-treatment is applied to match base metal mechanical properties. Filler metals having 12% nickel have also been developed, showing good toughness but low ductility. Welds made with this consumable have shown good results in the laboratory test, but have not been accepted for the construction of large vessels.

For LNG Tank construction, these solutions are not viable. Therefore, high nickel austenitic consumables are used. Nickel base alloys are chosen due their good strength, good toughness at -196°C and because its thermal expansion coefficient is very close to 9% Ni steel

thereby reducing the thermal stress during tank operation.

Fig 1- 2: SAW process on horizontal joint

9

1.1.3 Welding Consumables.

For the SAW welding process there are different types of wires based on NiMo and NiCrMo alloys. In Europe and USA AWS A5.14 ER-NiCrMo-3 or AWS A5.14 ER- NiCrMo - 4 are the commonly used.

The AWS A5.14 ER NiCrMo-3 is an Inconel 625 type alloy, which increases its mechanical strength by the formation of precipitates. Due to its chemical composition Gamma prime, Delta and Mu precipitates, and carbides MC, M6C and M23C6 are stable in the solid phase, but the thermo-mechanical treatment will define final phases distribution.

Undiluted weld metal tensile tested has an UTS around 760 MPa, yield strength around 510 MPa and elongation around 46%, making it the ideal consumable to be used for this application. But its high hot cracking sensitivity makes that many tanks constructors reject to use it. However, should note that using the proper flux and right welding parameters, is possible and reliable to get sound welds with highest mechanical properties.

The AWS A5.14 ER NiCrMo-4 is a Hastalloy C-276 alloy type, which increases its strength by solid solution. Only M_6C rich molybdenum carbides and μ precipitates are stable in the solid phase. Undiluted weld metal tensile tested has an UTS around 690 MPa, yield strength over 400 MPa and elongation around 35%, making it an acceptable consumable to be used for this application, specially due it lower hot crack sensitivity.

Due that mechanical strength of this alloy system is controlled by solid solution mechanism, dilution with base metal should has an important role on tested strength by cylindrical all weld metal tension test, where the place where the sample was obtained could has an important effect.

This is one of hypothesis in this dissertation, attempting to compare its effect against other typical welding variables. Using X-ray fluorescence technique, main alloy elements will be determined on each tensile tested sample and will be statistically correlated with other parameter.

1.2   Welding Metallurgy of Deposited Weld metal.

1.2.1   Nickel Alloys system

Nickel belongs to group VIII of the Transition elements together with Iron and Cobalt. It has the atomic number 28 and its atomic mass 58,6934 representing a composite of 5 stable isotopes. In solid state it has FCC crystallographic structure with a lattice constant of 0,35167nm at 20ºC. Nickel doesn't show allotropic transformations in the entire ranges of temperatures up to the melting point. It electronic configuration is Ar 3d8 4s2.

Pure nickel has 0,2% offset yield strength of 59MPa and Ultimate Tension test of 317MPa with an elongation of 30%.

Due the high solubility of many other elements, there are an important amount of commercial alloys, which improves its mechanical properties by solid solution or secondary phase's precipitation.
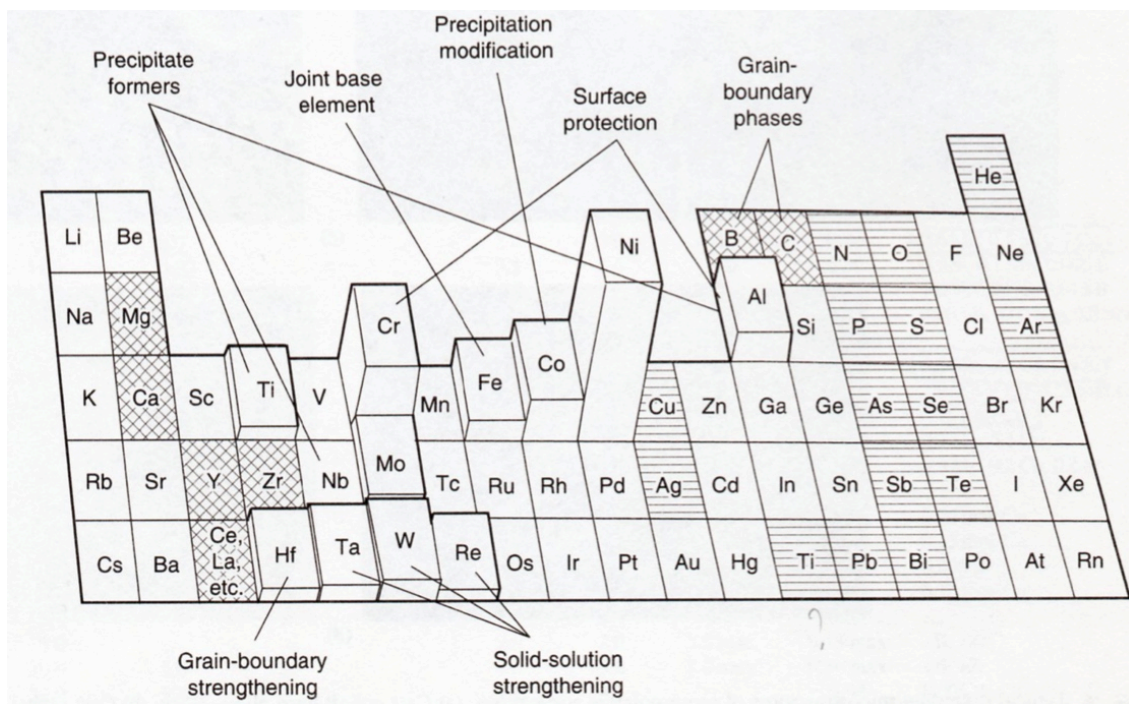
Fig 1- 3:Effect of alloying elements

Elements like Cu, Mo, Cr, Fe, W and Co has wide solubility range in nickel and mainly are added like solution strengthener or carbides formers. Other elements like Al, Ti, Nb, are mainly adds due it tendency to form GCP phases with huge impact on mechanical properties. Also B, Zr, C and Hf are adds due its beneficial effect on grain boundary.

The following figure shows a schematic of some of the commercial nickel base alloys, which have been grouped by aggregate main alloys and the hardening mechanism used to obtain the desired characteristics.

The most important uses of nickel base alloys are: Chemical resistance in degrading environments, corrosive or radiant and High temperature resistance. The use for cryogenic applications is marginal, although its performance is adequate.

1.2.2   Solidification

a) Weld Metal microstructure

Deposited weld metal has an austenitic, FCC, crystallographic structure that is

Fig 1- 4: Nickel alloys family

stable since solidus temperature to room temperature. For this reason, weld metal microstructure is constituted by large grains formed by dendrites or cells. In both interdendritic and intergranular zones is where segregated alloys elements' and other concentrated impurities can lead the formation of secondary phases as last solidification constituent. [1-11].

b) Solute segregation.

Hastelloy C-276 weld metal tends to form TCP phases that precipitate as last solid in both interdendritic and intergranular zones, during solidification. The most common secondary phases on this NiCrMo alloy are the called Mu phase and P phase.

Several researchers coincide that either Mu and P phases play a detrimental role on weld metal ductility, rupture strength, impact toughness and corrosion resistance by several mechanisms.

c) Sub grain boundary

Subgrain boundary defines the boundary that between the primary solidification structures, dendrites or cells. This zone is compositionally defined by the concentration of segregated solute during solidification. This subgrain boundary is characterized by the high coherence between the coincident crystallographic orientations, produced by the subgrains growth along preferential crystallographic directions, which correspond to <100> directions in both the BCC and the FCC systems. This subgrain boundary is crystallographically defined as "Low Angle" boundary and is characterized by a low density of dislocations along it because they can be easily crossed [1-11].

d) Grain Boundary

The grain boundaries are those areas where the grains that grow by solidification of the liquid coincide, being the result of the competitive growth of the grains. As coincident grains have different directions and growth orientations, these grain boundaries are characterized by a high angular misorientation, also known as "High Angle" boundaries, which generates a network of dislocations.

The grain boundaries also have a compositional component, in which most of the impurities and the segregated elements are concentrated during solidification. These compositions lead the formation of low-melting point compounds

1.2.3   Precipitates

Hastalloy C-276 deposited weld metal show two different type of precipitates, intermetallic topological close package and carbides. The first one, also known as TCP, adversely affect mechanical properties due austenitic phase depletion of key alloy elements like Mo, W, etc, and due incoherent interphase between precipitates and matrix. Carbides in general tend to increase mechanical properties if they precipitate in grain bulk, but weaken it strength if they precipitate in grain boundary. Carbides tend to precipitate at grain boundary due to strong positive segregation of carbon [3-4]. Of course Carbide type, shape and quantity have an important role on actual effect on weld strength.

The chemical composition of Mu, P and M_6C phases are very close; This is the reason why it is not possible to identify these phases by EDX in SEM. The closeness of P and Mu phase composition is not surprising since these are adjacent phases in Fe-Ni-Mo and Ni-Cr-Mo ternaries alloy system [3-5]. Even some researchers thought that P phase is a transient phase decomposing to de the stable Mu phase [3-5].

The Mu phase kinetic of formation depends on two steps, nucleation and growth. By K. Zao [3-4] Mu phase seems to be nucleated from M6C carbides, what is supposed because both phases have an almost same crystal structure and composition.

C-276 alloy usually show only Mu and P phases as TPC precipitates. But in our study, and due weld metal high iron pick up, presence of other intermetallic phases should not be discarded.

1.2.4   Intermetallic phases

a) µ phase

(Ref 2.4-1) µ phase belongs hexagonal system, its space group correspond to D^8_{5d}-hR3m (Fig 1-), with rhombohedral lattice a=0,476nm and c=2,56nm (Zhao, et al. 2005) (Handbook 2000) (Raghavan;, Berkowitz and Scanlon 1982). [3-4][3-5][1-13]

μ Phase has a compositional formula like B_7A_6, where B is any element of Group VIII-B (Fe, Co & Ni), and A could be any element of group V-B (V, Nb & Ta) and VI-B (Cr, Mo & W). It has a wide composition range, where B varies between 42 to 56 mol%. In our alloy system μ phase usually has this composition $(Fe,Co)_7(Mo,W)_6$, where Ni and Cr could replace any of A or B elements.
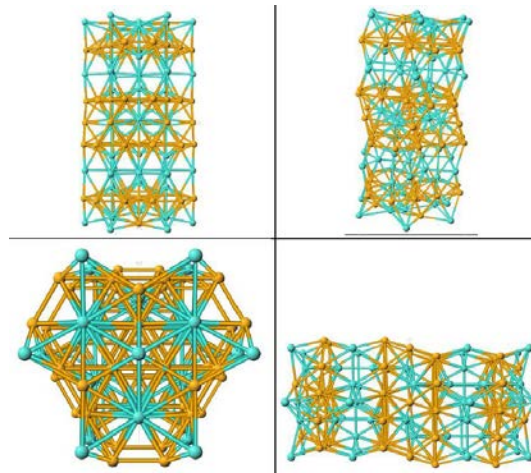
Fig 1-5. μPhase Cristal Structure D^8_5, Space Group hR3m

Presence of Mu phase is harmful for rupture strength, toughness, ductility and corrosion resistance, (Zhao, et al. 2005) (Handbook 2000). But precipitation of moderate amount of needle-like of μ Phase do not affect neither tensile strength nor room temperature toughness (Zhao, et al. 2005) in accordance with Simonetti and Caron, research done on single crystal. [3-1]

There are a couple of mechanisms that explain why mechanical properties are affected by μ Phase precipitation. First one, is due brittleness of μ Phase, which produce interfacial decohesion and crack initiation, because it acts as a barrier to moving dislocations at interface. And second one, because the loss of some of the key solid solution strengthening elements, which are concentrated in μ phase (Zhao, et al. 2005)

Once μ phase precipitates, it is difficult to be dissolved by heat treatment (Zhao, et al. 2005) (Raghavan;, Berkowitz and Scanlon 1982)

μ phase distribution is heterogeneous and it is mainly concentrated at interdendritic area. Elements microsegregation during alloy solidification explain μ phase preference location at interdedritic area, where Mo is concentrated.

1.3 Submerged Arc Welding Process.

1.3.1 Introduction.

Submerged arc welding process main feature is that the arc is produced inside (submerged in) a powder. The electric arc discharge is produced between a metallic wire, which is the filler metal, and metallic pieces to be joined, base metal. the electric power is supplied by welding machine which one could be operated at constant voltage or constant current mode, each welding mode has its own characterizes, CC mode is better with thick wires and high currents, and CV mode is better with thin wires, filled at high speed (high deposition rate) or in specials conditions where its self-regulated arc improve arc stability.

1.3.2 Fluxes

The powder is known as flux, and is made by big amount of compounds like oxides, carbides, salts, etc, which give them its features. Because the electric arc welding is made inside the flux, operator protection is one of the fluxes functions. The energy of the arc produce first decomposition of some of flux compounds producing some gases like CO_2 or fumes removing the air in arc area protecting the melted metal, Some of sodium or potassium salts between other compounds, are ionized by the arc energy, supplying ions to the column of plasma affecting on arc stability and the total energy given by the arc.

Melted flux produce the slag, who play an important weld metal cleaning role removing oxides, sulfides, and other chemicals compounds and dissolved gases which affect in negative way deposited weld metal properties.

Fluxes are manufactured by melting together all its compounds, milling it at proper size after its solidification, or by agglomeration of its compounds in small particles, by peletization and synterization process. In both cases particles sizes distribution and average size are important variable for degassing and bead shape.

1.4   Previous works and results:

In spring 2003, our team began an LNG Tank design and construction project. This Tank will be erected on Barcelona Port. From Design point of view one of the critical issued was to know the actual weld metal strength, because this value was required to define the Allowable Stress, which is used to calculate plates thickness of each course of the tank, following the design criteria of API 620 standard.

The First trial done was guided by IHI, The Japanese partner, who had huge experience on design and construction on LNG tanks, between others. 4 brands of high nickel stick electrodes, 4 wire-flux pair and 3 brand of austenitic stick electrodes were tested to choose the consumables to by used in the first project. The tested features were: Mechanical strength, Toughness ant -196ºC, ductility, and cracking resistance.

The filler metal used in that trial was ER NiCrMo-4 of 2,4mm of diameter, All welds were performed on 9%Ni steel plates, 12 and 21mm thick, beveled with asymmetric and un balance "K" and "X", respectively, using DC+ current and using 4 fluxes.

Note: The numerical notation system used in this thesis: decimal separation with comma and separation of thousands with point (example: 1,500,25)

1.4.1   1st trial: Selection of Welding Consumables to weld and LNG Tank, Summer Fall 2003

Only two, of the four tested wire-flux pairs', exceeded the cracking test. In second step they were mechanically tested. Weld metal toughness, ductility and prismatic tension

Test ID	Wire Diameter	welding position	Buttered	Flux	Plate Thickness	CT	Amperage [A]	Voltage [V]	Welding speed [cm/min]	Head position [°]	Rp0,2 [Mpa]	UTS [Mpa]	A4 [%]	LONGI TUDIN AL OR TRANS VERSE	AWMT Sample Diam
S4E-14	2,4 mm	2G	No	F3	21,0 mm	DC+	320 330	28		-5º	388	688	48,8	L	6mm
US4D-22	2,4 mm	2G	No	F4	21,0 mm	DC+	320 330	28		-5º	443	698	45,6 %	L	6mm
US4E-21	2,4 mm	2G	No	F4	12,0 mm	DC+	320 330	28		-5º	416	676	37,5 %	L	6mm
US4E-21	2,4 mm	2G	No	F4	12,0 mm	DC+	320 330	28		-5º	403	668	40,0 %	L	6mm

Table 1-1: 1st trial results

test were easily passes. In contrast, the results of the cylindrical, longitudinal tensile test along the weld bead were just below the expected values.

In the case of the prismatic tensile tests, often fractures are produced in the base metal side, even when plastic deformation had been started in weld metal zone. In this trial and the rest of tests carried out later, same behavior has always been observed with UTS values have always been around 700 MPa, regardless plate thickness. Since having performed tests in plates from 9.6mm to 37mm.

1.4.2 2nd Trial Restraint and Buttering effect on mechanical properties, Winter 2004

In view of the low results of mechanical strength obtained in first trial, a second trial is performed following recommendation found in reference [5-2][5-3][5-4][5-8][5-9][5-11][5-18][5-20] and [5-23]. In particular, recommendations done by WG Welland in 1978, [4-3-1] and welding consumables fabricators were followed to determine which variables would be evaluated. Finally second trial was designed to determine the effect of stiffening and Dilution in the mechanical strength of the deposited metal.

Test ID	Wire Diameter	welding position	Buttered	Flux	Plate Thickness	CT	Amperage [A]	Voltage [V]	Welding speed [cm/min]	Head position [°]	Rp0,2 [Mpa]	Rm [Mpa]	A4 [%]	LONGITUDINAL OR TRANSVERSE	AWMT Sample Diam
US4E-27 a1	2,4 mm	2G	No	F4	12,0 mm	DC	320 330	28		-5°	440 441	659 680	33,1 38,1	L	4mm
US4E-27 a2	2,4 mm	2G	No	F4	12,0 mm	DC	320 330	28		-5°	419 442	656 619	35,6 24,5	L	4mm
US4E-27 b	2,4 mm	2G	No	F4	12,0 mm	DC	320 330	28		-5°	450 452	672 657	40 35,6	L	4mm
US4E-28 a1	2,4 mm	2G	No	F4	21,0 mm	DC	320 330	28		-5°	428 426	649 617	35 27,5	L	4mm
US4E-28 a2	2,4 mm	2G	No	F4	21,0 mm	DC	320 330	28		-5°	441 437	663 655	33,7 29,4	L	4mm
US4E-28 b	2,4 mm	2G	No	F4	21,0 mm	DC	320 330	28		-5°	438 454	662 698	41,2 38,7	L	4mm
US4E-29 a1	2,4 mm	2G	No	F4	12,0 mm	DC	320 330	28		-5°	376 392	609 611	42,5 41,2	L	4mm
US4E-29 b	2,4 mm	2G	No	F4	12,0 mm	DC	320 330	28		-5°	421 382	630 607	40,6 41,9	L	4mm
US4E-30 d1 T	2,4 mm	2G	No	F4	21,0 mm	DC	320 330	28		-5°	464 MPa	688 MPa	47,5 %	T	4 mm
US4E-30 d1	2,4 mm	2G	No	F4	21,0 mm	DC	320 330	28		-5°	452 445 472 496 466	609 668 736 750 713	21,9 42,5 48,2 38,4 42,4	L	4mm 5mm
US4E-30 d2	2,4 mm	2G	No	F4	12,0 mm	DC	320 330	28		-5°	499 491 420 458	740 601 714 714 706	36,3 17,5 40,8 40,8 48,2	L	4mm
US4E-30 d2 T	2,4 mm	2G	No	F4	12,0 mm	DC	320 330	28		-5°	467 MPa	636 MPa	39,4 %	T	4mm
US4E-31 a1	2,4 mm	2G	Yes	F4	12,0 mm	DC	320 330	28		-5°	463 445	707 717	34,4 47,5	L	4mm
US4E-31 b	2,4 mm	2G	Yes	F4	12,0 mm	DC	320 330	28		-5°	413 414	667 664	47,5 41,5	L	4mm

Table 1-2: 2st trial results

In this test, 12 samples were welded from which 32 cylindrical specimens were tensile tested. If results are analyzed by sample is seen that some samples show around 30MPa of variation between the UTS's results of its tested specimens. Even when some samples were retested, higher variation was reached.

The worst is that the results variation within a test is bigger than variation between two tested conditions, reason why is not possible to determine the actual effect produced by the variation done.

1.4.3 3rd trial: Joint design and cooling rete effect on mechanical strength, Summer 2004

This third trial was performed in Germany in Welding Manufacture facilities with the scope to determine the proper welding conditions to be used during qualification of the welding procedures.

18 samples were welded at that time, where Two types of joints, voltage, current, DC+, DC- and AC and even cylindrical tensile sample diameter were evaluated. From this

Test ID	Wire Diameter	welding position	Buttered	Flux	Amperage [A]	Voltage [V]	Welding speed [cm/min]	Head position [°]	Rp0,2 [Mpa]	Rm [Mpa]	A4 [%]	AWMT Sample Diam
6185,2	2,4	2G	no	F4	280-300	27-28	40-60		438 446	681 674	37% 34,6%	12,7
6229	2,4	1G	no	F4	280-300	25-26	40	90	478 466	678 632	30,5% 22,6%	12,7
6230	2,4	2G	no	F4	280-300	25-26	40-60		464 468	659 669	28,5% 31,4%	12,7
6233	2,4	1G	no	F4	280-300	26-27	50	90	461 447	693 643	38,7% 26,3%	12,7
6235	2,4	2G	no	F4	280-300	25-26	40-60		441 447	678 667	34,6% 31,4%	12,7
6236	2,4	1G	no	F4	280-300	27	50	90	464 458	694 692	37% 37,5%	12,7
6250	2,4	2G	no	F4	280-300	27-28	40-60	0°(90°)	470 469 D 474	708 689 D 630	39,9 28,6 A5 21,8	12,7 / 10 / 6,4
6253	2,4	1G	no	F4	280-300	26	50	90	470 475 x 454	708 702 XXX 689	41,7 5,6 x 35,4	12,7
6254	2,4	2G	no	F4	280-300	26	40-60	5	471 465	694 713	36,6 35,5	6,4
6255	2,4	2G	no	F4	280-300	26	40-60	5	495 489	702 661	43,3 24,2	6,4
6256	2,4	2G	no	F4	320-340 / 340-360	26	40-60	7	471 459 453 446	666 691 675 684	26,7 32,2 34,2 38,1	6,4
6258	2,4	2G	no	F4	320-340	26	40-60	7	418 433	645 679	32,2 40,1	6,4
6259	2,4	2G	no	F4	320-340	34	40-60	7	443 431	598 615	21 25,4	6,4

Table 1- 3: 3st trial results

welded samples 32 cylindrical tensile specimens were tested, getting the optimal conditions for to perform the Qualification of Welding Procedures.

Finally, welding procedures for the 1st two tanks were welded and approved at on time and fulfilling design requirements.

Even when target was reached, it is seen that some test showed high variation on tested results.

1.4.4 4th Trial: Changing Wire Diameter, spring, summer 2005

During tank production some troubles happened on horizontal weld by Sub Arc process as: deslaging, porosity, lack of fusion and slag inclusion. After review several papers, and few interviews with consumables manufactures, being decided to try with thinner wire, increasing the

Fig 1- 6: Four trial test

19

current density and so the fluidity of the molten weld metal

Trials were performed in three steps: first to determine the new set of welding parameters and cracking sensitivity. Second: a first mechanical test trial. And third: a

Test ID	Wire Diameter	welding position	Buttered	Flux	Plate Thickness	CT	Amperage [A]	Voltage [V]	Welding speed [cm/min]	Head position [°]	Rp0,2 [Mpa]	UTS [Mpa]	A4 [%]	LONGITUNINAL OR TRANSVERSE	AWMT Sample Diam
U 12-1	1,6mm	2G	No	F4	12,0 mm	DC+				-5°	433 436	679 680	33 32	L	6mm
U 21-1	1,6mm	2G	No	F4	21,0 mm	DC+				-5°	447 453	670 681	30 34	L	6mm
SM-12-1	1,6mm	2G	No	F2	12,0 mm	DC+				-5°	405 470 429	673 709 665	43 34 40	L	6mm
SM 21-1	1,6mm	2G	No	F2	21,0 mm	DC+				-5°	419 403 406 431	657 667 680 690	40 43 46 42	L	6mm
SM-12-2	1,6mm	2G	No	F2	12,0 mm	DC+				-5°	453 439	716 721	44 22	L	6mm
SM 21-2	1,6mm	2G	No	F2	21,0 mm	DC+				-5°	500 503	751 755	38 40	L	6mm

Table 1- 4: 4st trial results

second mechanical test trial after adjustment done on welding parameters.

The results were not free of scattering, but in this trial have been gotten the best mechanical strength values ever gotten even till now.

Production welding confirmed the expected improvement from point of view of weld metal soundness, but some issues regarding arc stability and wire feedability happened.

1.4.5   U-27 Sample, Spring 2007

This was the first welded sample to be used in Ph.D. research. This sample was welded using flux F2, 1,6mm wire, DC+ on 27mm thick 9%Ni steel plate. To try to understand the effect of strain, thermal cycles and residual stress on mechanical strength, both welded side were tested, A and B. Results shown that welded side, where the samples are machined, has a substantial effect on measured strength.

Test ID	Wire Diameter	welding position	Buttered	Flux	Plate Thickness	CT	Amperage [A]	Voltage [V]	Welding speed [cm/min]	Head position [°]	Rp0,2 [Mpa]	UTS [Mpa]	A4 [%]	LONGITUNINAL OR TRANSVERSE	AWMT Sample Diam
U 27 A	1,6mm	2G	No	F4	27,0 mm	DC+				-5°	481 474	707 718	36 38	L	6mm
U 27B	1,6mm	2G	No	F4	27,0 mm	DC+				-5°	450 451	642 678	21 29	L	6mm

Table 1- 5: U-27 test results

1.4.6   Linc01 sample, Summer 2007

First sample welded using a modified Lincoln flux. This sample showed more than 24 different types of cracks on weld metal and was intensively
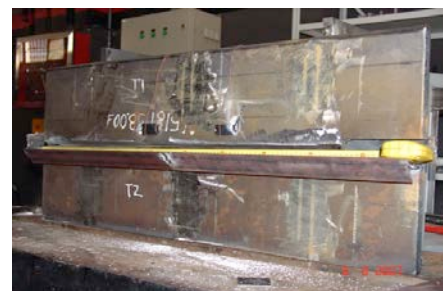
Fig 1- 7: Lin 01 test sample

studied to identified the different types of cracks occurred on high nickel alloys weld metal. These results were presented on October 2008 to get DEA diploma.

Test ID	Wire Diameter	welding position	Buttered	Flux	Plate Thickness	CT	Amperage [A]	Voltage [V]	Welding speed [cm/min]	Head position ["]	Rp0,2 [Mpa]	UTS [Mpa]	A4 [%]	LONGI TUNIH ALOR TRANS VERSE	AWMT Sample Diam
Linc I	1,6mm	2G	No	F4	12,0 mm	DC+				-5º	468 431	660 690	24,1 41,7	L	6mm
Linc III BS	1,6mm	2G	No	F4	21,0 mm	DC+				-5º	486 491	683 620		L	6mm
Linc IV BS	1,6mm	2G	No	F2	21,0 mm	DC+				-5º	462 442	650 688	23,4 %	L	6mm
Linc IV C	1,6mm	2G	No	F2	12,0 mm	DC+				-5º	508 500	679 721	23,4 %	L	6mm
Linc IV FS	1,6mm	2G	No	F2	21,0 mm	DC+				-5º	445 465	656 682	26,2 %	L	6mm

Table 1- 6: Lin 01 test results1

2. Experimental Procedure.

2.1 Base Metal and Welding Consumables.

This study were done as a benchmarking between three of the most popular submerged arc welding fluxes used to weld LNG Tanks and the best Lincoln flux to be introduced in the LNG market by Lincoln Electric CO.

The benchmarking trials were started earliest 2007 when 4 Lincoln fluxes were tested and compared with other 2 competitors' fluxes. In that trial, arc stability, slag detachability and weld metal finishing were the evaluated characteristic. These parameters are often used to define wire/flux pair weldability.

In this dissertation used fluxes are going to be identified as F1, F2, F3 and F4. Two of them were agglomerated type: F1 is basic fluoride aluminate type, with Al2O3 and CaF2 like main compounds, and neutral pick up of Mn and Si; and F4 which is basic aluminate type, with Al2O3, MgO, CaO and MnO like main compounds, this flux produce around of 1% of Mn pick up, in accordace wirh EN-760 standard.

The other two fluxes were fused; both were calcium silicate type, with CaO, MgO and SiO2 like main compounds, producing an important Si pick up.

F1	EN 760	SA AF 2 64 AC H5
F2	EN 760	SF CS 2 DC H5
F3	EN 760	SF CS 2 AC/DC H5
F4	EN 760	SA AB 2

	Chemical composition of flux (%)												Basisity
	MnO	SiO$_2$	Al$_2$O$_3$	TiO$_2$	ZrO$_2$	CaO	MgO	CaF$_2$	FeO	Na$_2$O	K$_2$O	BaO	(IIW)
F1		10-15	36-42					43-48		1-5	1-5		1,65
F2	0,02	31,1	2,68	0,11		6,73	4,84	6,55	0,08	0,83	1,02	1,99	1,55
F3	0,26	36,48	3,07	0,09	<0,05	27,58	5,69	17,48	0,29	1,14	1,59	2,59	1,48
F4	7,39	6,72	47,6	<0,05	<0,05	21,23	0,094	18,53	0,076	1,37	1,05	<0,05	1,52

Basisity(IIW)=〔CaF$_2$+CaO+MgO+BaO+SrO+Na$_2$O+K$_2$O+Li$_2$O+0.5(MnO+FeO)〕/〔SiO$_2$+0.5(Al$_2$O$_3$+TiO$_2$+ZrO$_2$)〕 (%)

Note: The numerical notation system used in this thesis: decimal separation with comma and separation of thousands with point (example: 1,500,25)

Chosen filler metal was AWS A5.14 ER-NiCrMo-4, in two different diameters, the standard 1,6mm and the nonstandard 2mm. This variable was chosen to know the effect of wire diameter/current density on deposited weld metal mechanical properties. As was explained in Chapter 1, on production welds, reduction of wire diameter produced sound and clean deposited weld metal.

Used base metal was the ASTM A-553 T1, quenched and tempered type of the 9% Nickel steel of 20mm thick. The 12m length and 2,37m wide plate was Manufactured by Industeel at Belgium factory, and identified as plate number 580431/1 heat 17823, certified number 458937.

The plate was cut in wing samples for few different test performed on LECO. The wind plates for this trial were 170mm wide and 500mm length. Wind samples edges were beveled with asymmetrical "X" joint design and $^1/_3$ - $^2/_3$ offsets as shown below, following actual bevel preparation of production welds.

Length	500
W	170
T	20
K	10,2
L	7,8
H	10,3
I	5,7
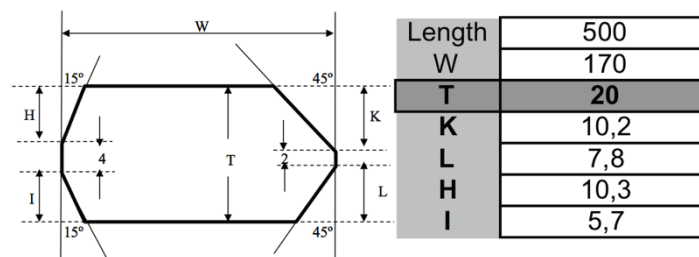
Fig 2- 1 Bevel design

All samples were both side welded in horizontal position (2G), like actual samples plates for welding procedure qualification are welded, and also as actual production welding.

2.2   Design Of Experiment:

For each flux was chosen a testing program with 2 levels of 3 variables, getting a factorial 2^3 testing design, therefore 8 plate-samples were welded with each flux, getting a total of 32 plate-samples welded for this trial.

Due residual magnetism issue of 9%Ni steel, is recommended that production welds been done by AC current to avoid arc blow tendency produced by magnetic fields. But in earliest 2000, most of the submerged arc welding machines only works in DC polarity, so most of the tank builders used DC power suppliers to weld the horizontal joints, without alternative to use AC current in this process.

Around 2005 some Manufactures of welding machine introduced a new, high tech, welding machines capable to weld in AC or DC current and others setups that would improve productivity and mechanical properties too.

Current polarity has important effect on deposition rate, on arc energy distribution and also on dilution. So, current type is within evaluated variables to determine its impact on weld metal strength.

The voltage was the last studied variable. The voltage together with the welding current determines the energy of the electric arc, in other words, the heat supplied by the electric arc, or Heat input. Voltage has also direct influence on the ratio between amount of melted flux and the amount of weld metal and on welding bead width.

When voltage is increased the arc length is increased too. So, more flux is melted by longer arc. Then, voltage variations are important to get the proper relationship between weld meat and slag. But this variation becomes critical when active or semi active fluxes are used, because weld metal chemistry is changed.

The Weld bead surface finishing, as well as its roundness are determined by slag's surface tension. In horizontal welds, weld metal weight and its fluidity must be supported by the slag and by unmelted flux weight. The proper surface finishing is obtained with the correct balance between these factors, in which the voltage plays a very important role, determining the amount of slag formed, in other words, the amount of melted flux.

By experience on production welds, root welding passes always are performed at lower voltage, between 25v and 27v, depending on the gap between plates. All filling passes, between second layer and penultimate layer, are welded around 2 voltage

more than voltage used in root pass. Finally, passes in last layer or capping passes are made at higher voltage and higher travel speed to produce flat and wider welding beads.

For this trial two different voltage level were defined, low voltage level using 25v for root pass, 27v for filling passes and 29v for capping passes, and higher voltage with 27v-29v-31v for welding beads in respective layers.

Wire feed speed was choose to get same deposition rate welding with 1,6mm and 2,0mm wire, trying to get same number of passes per side with both wires. Then 1,6mm wire was feed at an average 543 $^{cm}/_{min}$, and 2,0mm wire at 343$^{cm}/_{min}$, with an average deposition rate of 30 $^{gr}/_{min}$ with both wires.

Next table show welding condition used to weld each sample.

ID TEST	WIRE		FLUX				CURRENT TYPE		WELDING PARAMETER	
	1,6mm	2,0mm	F1	F4	F2	F3	CV AC sq	CV DC+	HIGH VOLT	LOW VOLT
P01	X		X				X			X
P02	X		X				X		X	
P03	X		X					X		X
P04	X		X					X	X	
P05	X				X			X	X	
P06	X				X			X		X
P07	X				X		X			X
P08	X				X		X		X	
P09	X			X			X		X	
P10	X			X			X			X
P11	X			X				X	X	
P12	X			X				X		X
P13	X					X	X		X	
P14	X					X	X			X
P15	X					X		X	X	
P16	X					X		X		X
P17		X	X				X		X	
P18		X	X				X			X
P19		X	X					X	X	
P20		X			X		X		X	
P21		X	X					X		X
P22		X		X			X		X	
P23		X		X			X			X
P24		X		X				X	X	
P25		X		X				X		X
P26		X			X		X			X
P27		X			X			X	X	
P28		X			X			X		X
P29		X				X	X		X	
P30		X				X	X			X
P31		X				X		X	X	
P32		X				X		X		X

Table 2- 1: Design of experiment

2.3   Welding Equipment:

Sample were welded in Lincoln Electric Weld-Center, Cleveland, Ohio, using a Power Wave AC-DC 1000 welding machine and a KeyPlant column&beam, as follow configuration

Fig 2- 2: Welding equiment

PW AC-DC 1000 was the newest high tech welding machine, which one incorporated digital control of welding current wave shape, controlling welding current frequency, balance and offset, and able to weld with direct and alternating current.

This welding machine also has a data acquisition module capable to get hundreds of values of welding current, voltage, wire feed speed per second and arc time. This feature was used to collect the welding parameters of each deposited welding bead. Welding travel speed was computed by wing plate length divided by arc time.

Actual heat input, heat on wire, deposition rate and welding impedance of each welding bead were computed using this data.

2.3.1 Weld Beads distribution

The sample plates have been fabricated from 9%Ni steel, 21mm thick and joined by Submerged Arc welding process in the horizontal position (2G), see Fig 3- 3, using an asymmetrical and unbalanced "X" joint as are the production welds joints. The joints were multi-passes filled, by six weld beads per side, although some sides of the samples have been filled only 3 passes.

Once the first side has been full filled, the second side root's is gouge by a hand grinder removing the first layers of first welded pass. Once sound weld metal is
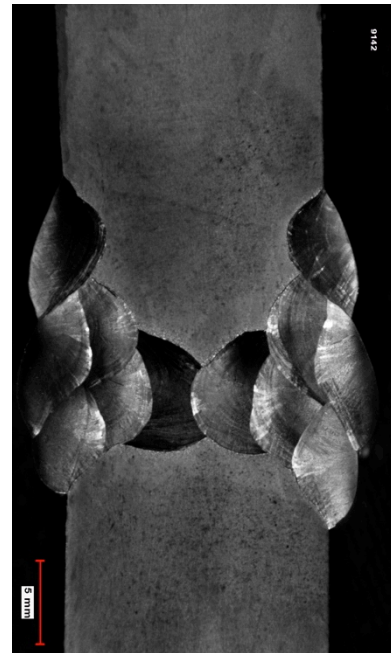
Fig 2- 3: Macro sample

found, second side filling process is started.

The finished joint is expected to be symmetrical regarding deposited weld metal without evident angular deformation.

2.4 Mechanical Properties:

Testing program were performed in accordance with API 620 welding Procedure Qualification requirement, trying to get maximum mechanical strength, with good cracking resistance at cryogenic temperature.

Cylindrical All Weld Metal Tension Test, Charpy V Notch @ -196ºC and deposited weld metal chemical analysis, were the test used to compare deposited weld metal toughness and strength by each flux, and the effect of the evaluated variables.

First set of test, two cylindrical all weld metal sample and three 10X10mm Charpy V notch and chemical analysis, were performed in Lincoln Electric Facilities, in Cleveland Ohio, autumn 2008.

Due high dispersion on mechanical strength results, in winter of 2016 was decided to test two additional cylindrical samples of deposited weld metal to get more data for statistical analysis. These tests were performed at Bose Laboratory, in Tiana Barcelona.
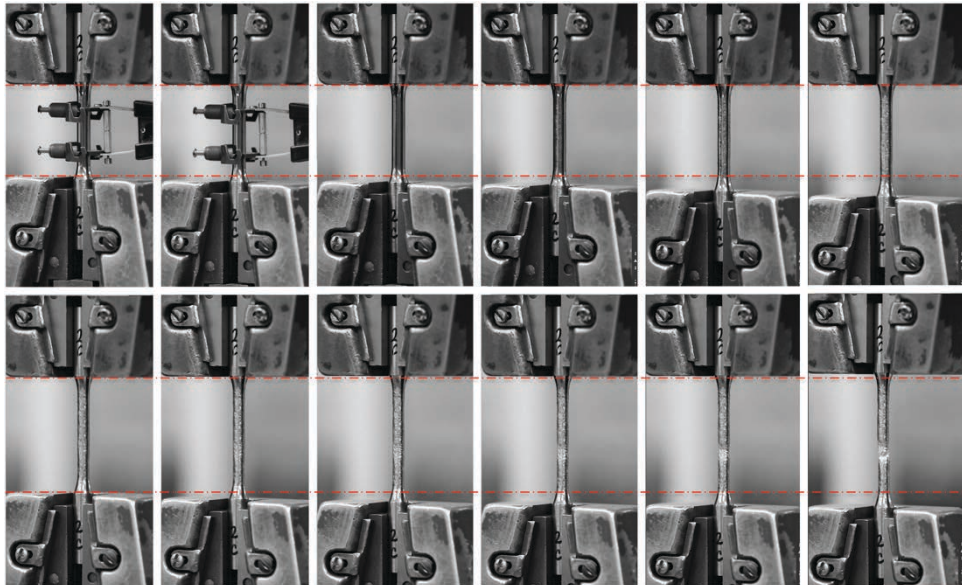
Fig 2- 4: Tensile test sequence

2.4.1 Mechanical Strength.

API 620 standard states that if the selected weld metal has a lower mechanical strength than base metal, and its minimum yield point is not defined in the standards, then deposited weld metal mechanical strength shall be determined by 2 "All Weld Metal Tensile Test" (AWMTT) using cylindrical tensile specimens as defined in ASME-SFA 5.11. The values is obtained in this test are used to determine the allowable stresses that determine the thickness of the shell tank plates, in other words to define the weight of the material needed for the construction of the tank.

2.4.2 Impact Test.

The Charpy impact test performed according to ASTM E23 with standard 3 10x10x50mm specimens tested at -196ºC, using liquid nitrogen as the cooling medium, determined material toughness, at low temperature. In accordance with API 620 average absolved energy at -196ºC should be higher than 50 Joules.

2.5   Structural Characterization

Structural characterization has been done by mean of macro, micro and X-ray diffraction (XRD). Macro pictures of the welded joint were first characterization done, showing welding bead shape, size and locations. These macros were prepared in Lincoln Electric Facilities, in Cleveland Ohio, in fall 2008.

AWM polished and etched samples were compared with these macro images to determine where the cylindrical tensile specimens were extracted.

2.5.1   X-ray spectrography (XRD)

X-ray difraction has been used mainly to know or discard secondary phases presence. Also been used to compare two AWMT samples toke from the same welded sample and big difference of mechanical strength. For X ray diffraction was used a Siemens D500 θ-2θ Bragg-Bretano type, using Cu Kα_{1+2} (α_1= 1,5405980 and α_2= 1.5444260) radiation at 45 kV and a current of 40mA.

2.5.2   AWM samples preparations for Structural Characterization.

AWMT samples after tensile test were cut in area were plastic deformation doesn't happen. Each AWMT section were mounted in Bakelite, then grinded by sand paper till 1200P, and finally polished by 6 microns and 1 micron of diamond powder.

This as polished surface, before etching, was analyzed by optical microscope to determine inclusions and sizes and distribution pattern.

Both chemical and electrolytic etching techniques were used to reveal deposited weld metal microstructure, but due the different composition of base metal and weld metal, is not possible to reveal at same time base metal, heat affected

Fig 2- 5: Micro sample

zone and deposited weld metal microstructure.

29

Several etching solutions were used to show deposited weld metal solidification structure, precipitated phases and inclusions.

AWM samples preparation have been performed in University of Barcelona, Thermal Spray Center (CPT) Laboratory

2.5.3   Chemical Etching.

Chemical etching were done using Marble and Kalling but neither one of them made an homogeneous etching on all welded beads, then were not possible to have a general overview of microstructure and precipitates on each welding bead. Also Glyceregia agent was tried but with out any indication of etching even after few of minutes.

For example as showing on figure xx, using Marble agent on Linc 01 sample after 35 seconds, welding beads 1, 2, 3, 7 and 11 are properly etched while welding beads 4, 5, 6, 8, 9, and 10 are not etched. When last referenced welding beads are etched the first ones are over etched making difficult the microstructural analysis. Even after 15 minutes beads 8, 9 and 10 were not etched. The etching behavior is schematically shown also on figure.

Chemical Etching

Using Marble agent after 35 seconds, welding beads 1, 2, 3, 7 and 11 are properly etched while welding beads 4, 5, 6, 8, 9, and 10 are not etched

Note: Arrow's thick, and indication of reactivity, or etching speed.

X: No etched welding beads even after 15 minutes
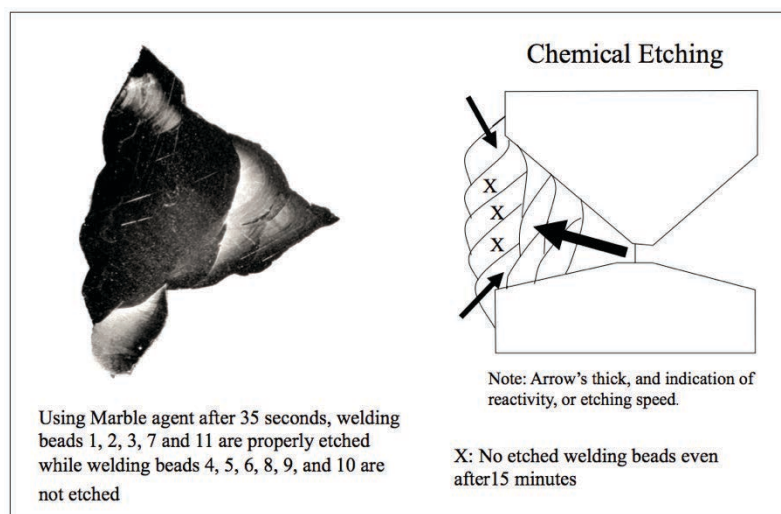
Fig 2- 6: Response of the chemical etching

2.5.4 Electro Etching.

Electro etching were done using Lucas, 10% Chromic Acid and Per chloric acid + ethanol + glyceregia. HP 6224B DC power supplier supplied electric current with a stainless steel cathode.
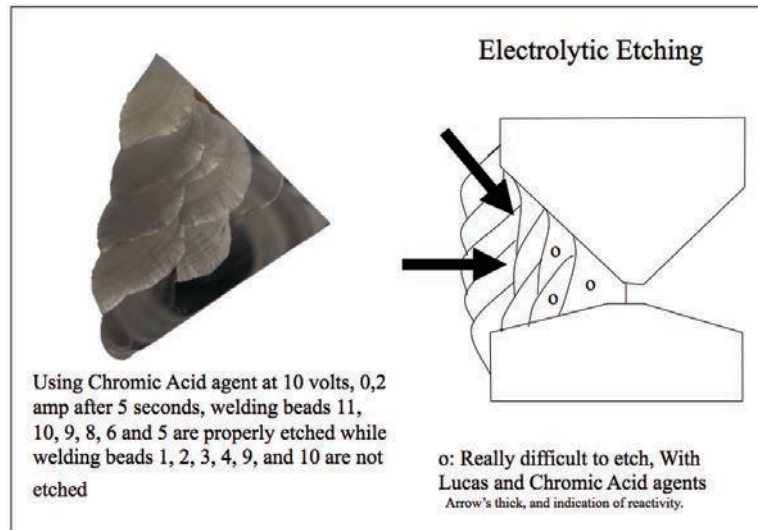
Fig 2- 7: Response of electrochemical etching

At the beginning, electro etching were performed with voltage ranges indicated by ASM Handbook, but again non homogeneous etching were obtained, but in contrary sense than chemical etching, that is outer beads were etched first than inner ones. For example using Lucas agent at 2 volts first 3 passes were not properly etched when the outer beads were yet over etched.

Most homogeneous etching was obtained at voltages between 20 to 25 v, current density around 0,004 A/mm2 and etching times of 5 to 10 seconds per immersion. The worst of this etching condition was the non-repeatability and lack of stability, but with most homogeneous etching.

2.5.5 Structural and Microstructural Analysis of polished samples and fracture surfaces.

a. Macro analysis.

Macro images, up to 10X were done using a 8MG pixels digital camera which was fitted with a 10X magnification lens. This camera was used to get macro picture of AWM polished
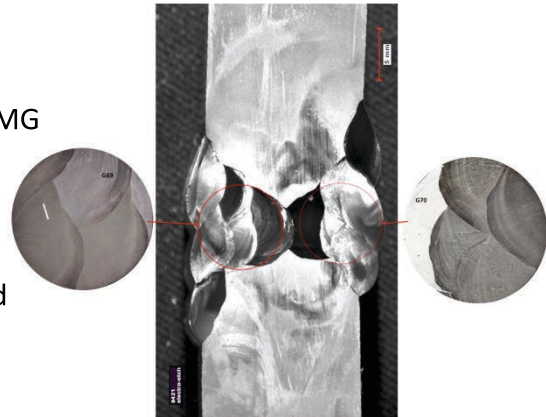
samples and macro pictures of fracture surfaces.

Fig 2- 8: Macro Sample

a) Microanalysis.

Micro analysis of polished and etched surfaces up to 1000X magnification was done by Leica DMI 5000 M Optical microscope with digital camera Leica DFC 290, to see grains

sizes and morphology, solidification pattern and to get a general view of particles shapes and distribution.

Sometimes an image comprehension (for example: particles distribution or location regarding a fusion line or grain boundary) is improved by expanding its field of view; this expansion is made joining several optical microscopes' photos. Automatic digital photo`s joining was made with Panorama Stitcher, Version 1.8 (21) software.

Also solidification pattern, particles shapes and its distribution were analyzed at magnification ranges of 500X to 15.000X using a JEOL JSM-5310 Scanning

Fig 2- 9: Optical and electronic microscopes

Electron Microscope for polished and etched AWM samples. This electron-scanning microscope was used for micro fractography analysis.

When higher magnifications were needed, for example: for grain boundary images and for better shape definition of terminal solidification particles the JEOL JSM-7100F Field Emission Scanning Electron Microscope was used with magnification up to 50.000X.

2.6 Fracture surface analysis

2.6.1 Macro fractography.

Macro fractography were done using the 8MG pixels digital camera, which was fitted with a 10X magnification lens.

2.6.2 Micro fractography.

Micro fractography since 15X up to 20.000X were done by JEOL JSM 5310 Scanning electron microscopy due to its wide depth of field.

2.7 Hardness test.

Microhardness test, have been performed in accordance with ASTM E-92 with a Matsuzawa MTX Alpha Microhardness tester, using a Vickers identator, loaded with 50gf to 200gf for 15 seconds.

To get more details about the hardness profile near to the fusion line, Knoob identator were used loaded with 50gf for 15 seconds.

Fig 2-10: Hardness Equipment

2.8 Chemical Composition:

2.8.1 LECO

Deposited weld metal chemical composition were performed at Lincoln Electric Cleveland facilities. Due to the sample plate joint design in "X", both welding sides were chemically analyzed and reported as ID side and OD side.

Heavy elements analysis was performed by Optical Emission Spectrometer OBLF Model QSG 750, Carbon and Sulfur content were analyzed by an LECO CS 600 and Oxygen and Nitrogen were analyzed by LECO TC-436

2.8.2 Distribution Profile of Heavy Elements.

Distribution profile of the heavy elements was determined using the X-ray fluorescence (XRFA) technique using a Fisherscope XRAY XDAL.
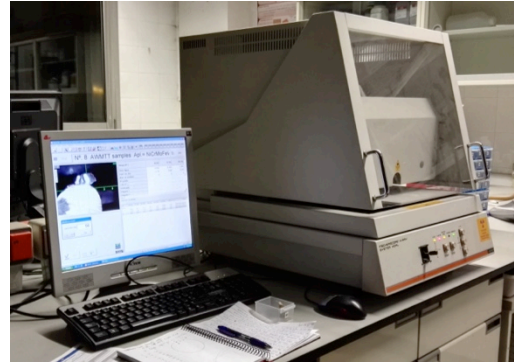
This technique were used to determine weld metal dilution profile, up to nine hundred measurements were done per sample,

Fig 2- 11: XRF equipment

observing the effect of the convective forces on elements distribution on a welding bead, or the detailed dilution percentage of each weld bead.

Equipment calibration was done using a piece of AWS A5.14 ER NiCrMo-4 wire with following chemical composition:

Classification   **AWS A5.14/A5.14M : ERNiCrMo-4**
ISO 18274 : S Ni 6276
(NiCr15Mo16Fe6W4)

Chemical analysis (%)												According to EN10204:2004 3.1
C	Si	Mn	P	S	Cr	Ni	Mo	Cu	V	Co	W	Fe
0,01	0,06	0,5	0,01	0,00	15,4	58	16,2	0,06	0,04	0,0	3,9	5,7

Table 2- 2: Chemical composition of the sample used for calibration

2.8.3 Qualitative and Quantitative micro chemical analysis

Chemical micro-analysis of observed particles, interdendritic regions or in dendrite core were done by Energy-dispersive X-ray spectroscopy (EDX) technique using a BRUKER NANO X-FLASH DETECTOR 5010, installed on JMS 5310 SEM.

2.9 Statistical Analysis:

Statistical analysis was performed by MiniTab Express Versión 1,5 2014-2016 For MAC.

2.10 Image Analysis:

Image J: Version 2.0.0-rc-43-/1.51d

3. Results And Discussion

As mentioned above, the set of samples analyzed in this research were welded in Lincoln Electric main facilities, Cleveland, Ohio, in the summer of 2008. The target was to get the best wire-flux pair to weld, by submerged arc welding, the LNG tank horizontal joints.

This trial was started early 2007 when 4 new fluxes were benchmarked with two fluxes from competitors. In that trial, the arc stability, the slag detachability and the weld metal finishing were evaluated features.

In the second step, four fluxes were compared. Now, the mechanical strength and toughness of deposited weld metal were the comparison parameters.

This testing program was mainly focused on the qualification of the welding

Fig 3- 1: Welding samples setup.

procedure following API 620 requirements. This standard states that maximum allowable design stress is determined by the weakest structural component strength, either the base metal or the weld metal.

For this application, the weakest structural component is the deposited weld metal. Therefore improving PQR results have big influence on tank cost reduction, and have

been one of the main targets of all tested performed by in previous and future trials in this application.

 Like is done during WPS' qualification, the sample plates were welded in horizontal position (2G), using an asymmetrical and unbalanced "X" joint as are the production welds joints.

Wire diameter has important effect on deposition rate and arc density. Wire diameter reduction was the key for improving weld metal deslagging and degassing on second welded tank. Also welding time was reduced by increased deposition rates.

In March to May, 2005, were done a trial to determine the wire diameter effect on deposited weld metal mechanical strength using two fluxes and two wires, one of 2,4mm and other of 1,6mm of diameter. Those results suggested that mechanical strength was also improved by reducing wire diameter.

For this trial two wires were used, one of 1,6mm and other of 2,0mm of diameter. To get similar passes distribution in all welded samples, using both wires; the different deposition rate of each wire was compensated by adjusting the wire feed speed (WFS). So, the WFS used with 2,0mm wire was 345 cm/min, meanwhile WFS used with 1,6mm wire 545 cm/min.

Voltage is one of the key parameters to be controlled. The length of the welding arc is the main parameter affected by electrical voltage. The arc length is reduced with at lower voltage, shorts arc reduce pick up of air elements like nitrogen and oxygen, which are harmful for weld metal toughness and strength. The right voltage level produces the proper weld bead width-deep ratio, which is important to reduce hot cracking risk.

In this trial voltage tested at two levels, low voltage and high voltage. Low voltage set up were: Root pass 25v, filling passes 27v and capping passes 29v. High voltage set up was: Root pass 27v, filling passes 29v and capping passes 31v.

Last tested welding variable was the current type, using in this trials direct and

alternating currents.

This testing program with three variables, Current Type, Wire Diameter and Voltage level, tested at two levels, AC-DC, 1,6-2,0mm and High and Low voltage, produce an experimental design factorial 2^3 type, with 8 samples welded by flux, with a total of 32 samples welded, Table 3- 1 show the Test ID with variable condition of each one.

ID TEST	WIRE		FLUX				CURRENT TYPE		WELDING PARAMETER	
	1,6mm	2,0mm	F1	F4	F2	F3	CV AC sq	CV DC+	HIGH VOLT	LOW VOLT
P01	X		X				X			X
P02	X		X				X		X	
P03	X		X					X		X
P04	X		X					X	X	
P05	X				X			X	X	
P06	X				X			X		X
P07	X				X		X			X
P08	X				X		X		X	
P09	X			X			X		X	
P10	X			X			X			X
P11	X			X				X	X	
P12	X			X				X		X
P13	X				X		X		X	
P14	X				X		X			X
P15	X				X			X	X	
P16	X				X			X		X
P17		X	X				X		X	
P18		X	X				X			X
P19		X	X					X	X	
P20		X			X		X		X	
P21		X	X					X		X
P22		X		X			X		X	
P23		X		X			X			X
P24		X		X				X	X	
P25		X		X				X		X
P26		X			X		X			X
P27		X			X			X	X	
P28		X			X			X		X
P29		X				X	X		X	
P30		X				X	X			X
P31		X				X		X	X	
P32		X				X		X		X

Table 3- 1: Design of Experiment Variables and Test ID.

3.1 Testing Results:

3.1.1 Mechanically tested Samples:

Cylindrical tensile samples, Diameter 6mm:

- 63 samples tested in 2008.
- 62 samples tested in 2016.

Charpy V notch standard 10X10mm samples

- 32 sets of 3 specimens were impact tested at -196ºC.

3.1.2 Chemical Composition:

- Chemical composition was analyzed on each side of the sample welded in Lincoln Electric facilities.

Additionally, By X-ray Fluorescence technique following array of measurements were performed:

1. 3X3 array of measurements on cylindrical section of tensile specimen, close to the fracture surface. Target: to get average chemical composition of each tensile tested sample. Measurement performed on 180 AWMT specimens.
2. 10X10 array of measurements on cylindrical section of tensile specimen, close to the fracture surface. Target: Identification of weld beads on fracture surface
3. 30X30 array of measurements on the base of the tensile specimen. Target: detailed chemical composition, and other characteristics.

The tables with result of each test are shown finishing this chapter.

3.1.3 Welding Parameters:

Using data acquisition module incorporated on welding machine, 4 values per second of instantaneous welding current, voltage and wire feed speed were recorded of each weld bead of each welded samples. Additionally, Arc Start (date and time), and Arc Stop (date and time) information is recorded. This data is filed in a txt document,

which could be used by any datasheet software.

With these data following items are computed by its formulas:

Direct Welding Parameters:

Average Amperage

$$A = \frac{\sum A_{Inst}}{\sum Values}$$ [Ampere] Eq. 1

Average voltage

$$V = \frac{\sum V_{Inst}}{\sum Values}$$ [Volts] Eq. 2

Arc Time

$$Arc_{time} = Arc_{stop}^{time} - Arc_{start}^{time}$$ [Seconds] Eq. 3

Travel Speed

$$T_{Speed} = \frac{PlateSample_{Lenght}}{Arc_{time}}$$ [cm/min] Eq. 4

Indirect Welding Parameters:

Energy:

Heat Input

$$HI = \frac{A \cdot V \cdot 60}{T_{speed}}$$ [kJ/cm] Eq. 5

Heat on Wire

$$H_{wire} = \frac{A \cdot V \cdot 60}{WFS}$$ [J/mm] Eq. 6

Related to the density of electrons crossing an area:

Arc Density

$$Arc_{Density} = \frac{A}{\pi \cdot r_{wire}^2}$$ [A/mm^2] Eq. 7

Related to the Amount of Deposited Metal:

Deposition Ratio

$$DR = \frac{\rho_{wire\,alloy} \cdot \pi \cdot r_{wire}^2}{T_{speed}}$$ [gr/cm(length of weld)] Eq. 8

Related to the Electrical resistance:

Electrical impedance

$$Z = \frac{V}{A}$$ [Ω] Eq. 9

Note: The numerical notation system used in this thesis: decimal separation with comma and separation of thousands with point (example: 1,500,25)

3.2   DOE Variables effect.

The obtained results from performed tests have been statistically analyzed by MiniTab Express. In most of the graphic or tables DOE variables had been identified as follow:

	F1	F2	F3	F4
Flux	1	2	3	4

	AC	DC
Current type	1	2

Voltage Level	LV	HV
	1	2

Wire Diameter	1,6	2,0

3.2.1   Flux type effect on Mechanical Strength.

Eight plate samples were welded per flux in accordance with experimental design shown above. From each welded sample 4 cylindrical tensile specimens were machined from deposited weld metal, so there are 32 tensile results per flux.

FLUX BRAND NAME	N	Minimum	Q1	Median	Q3	Maximum	95% Median CI
1	31	397,000	439,000	448,000	474,000	525,000	(441,675; 466,325)
2	30	425,000	433,750	452,000	465,000	486,000	(435,457; 460,856)
3	30	398,000	428,000	446,000	470,500	493,000	(439,688; 461,771)
4	30	412,000	424,250	432,500	454,250	473,000	(425,000; 444,543)

FLUX BRAND NAME	N	Minimum	Q1	Median	Q3	Maximum	95% Median CI
1	31	628,000	662,000	676,000	686,000	731,000	(670,350; 681,299)
2	30	643,000	660,750	675,000	689,750	724,000	(665,601; 683,771)
3	30	626,000	656,250	680,000	697,250	721,000	(661,686; 689,543)
4	30	628,000	642,000	648,500	658,250	697,000	(643,000; 653,771)

Fig 3- 2 Weld Metal Strength by Fluxes.

Boxplot results analysis show that both yield strength and UTS of the samples welded by fluxes F1 to F3 have quite similar results, see Fig 3- 2, all of them with high probability to meet API 620 standard requirement.

By other way, rupture strength of tensile samples welded using flux F4 are below

41

minimum acceptable values in accordance with API 620 standard, even when elastic limits of all tested samples were above standard requirements.

Variance statistical analysis confirms that from the statistical point of view, mechanical strength medians are not different. Fig 3- 3 shows the graphics of Tukey, Fisher, HsU and Dunnett variance analysis used to compare the obtained results.

Fig 3- 3 Variance Analysis of welds metal Strength, by Fluxes.
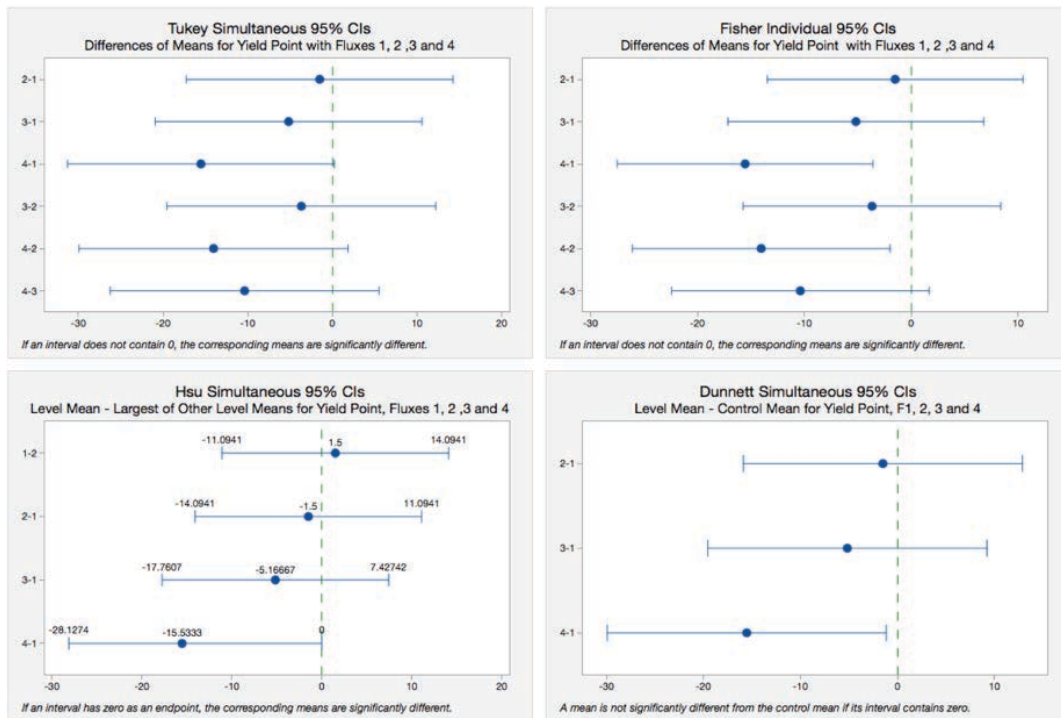
As seen, flux type play a small role on deposited weld metal strength. But has big influence on weldability and welding performance, which are key factors to get a sound weld metal.

3.2.2   DOE Variables effect on Mechanical Strength

Even when results dispersion is so high, analyses of averages give a brief idea how DOE variables affect yield point and ultimate tensile strengths.

Fig 3- 4 and Fig 3- 5 shown the averages strength values for each test condition together with the range of 95% of confidence, for yield point and UTS, respectively.

Yield Point
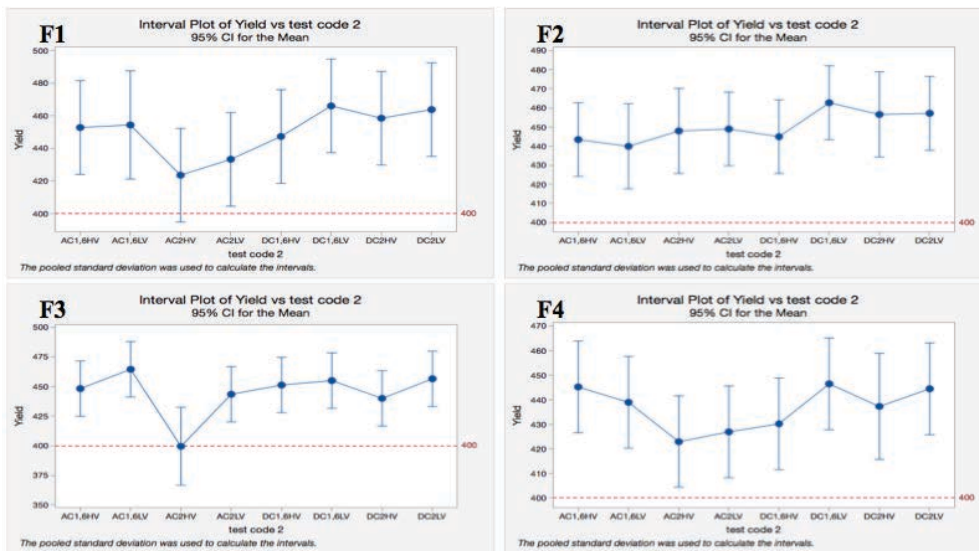
Fig 3- 4: Interval Plot of Yield Strength versus DOE variables by flux

An overview of the variation effect tendency is shown in **Fig 3- 6**, where is easy to see that DC produce stronger welds than AC. This result is clearer with 2,0mm wire, which provides an average yield point 4,7% higher and an average UTS 3,7% higher. Using 1,6mm wire this improvement effect is no clear (yield 0,4%; UTS -0,2%), at least in analyzed ranges

UTS
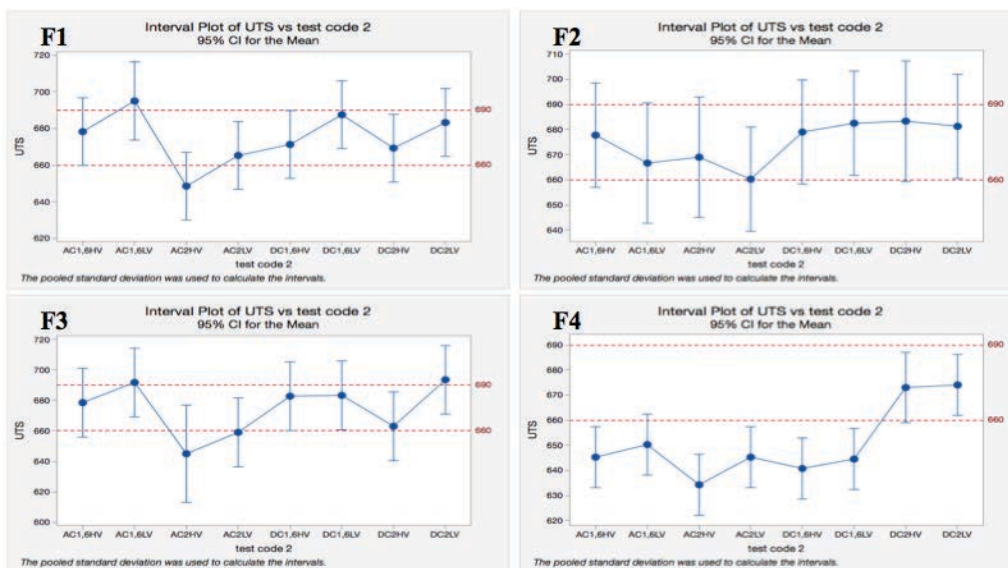
Fig 3- 5: Interval Plot of UTS versus DOE variables by flux

43
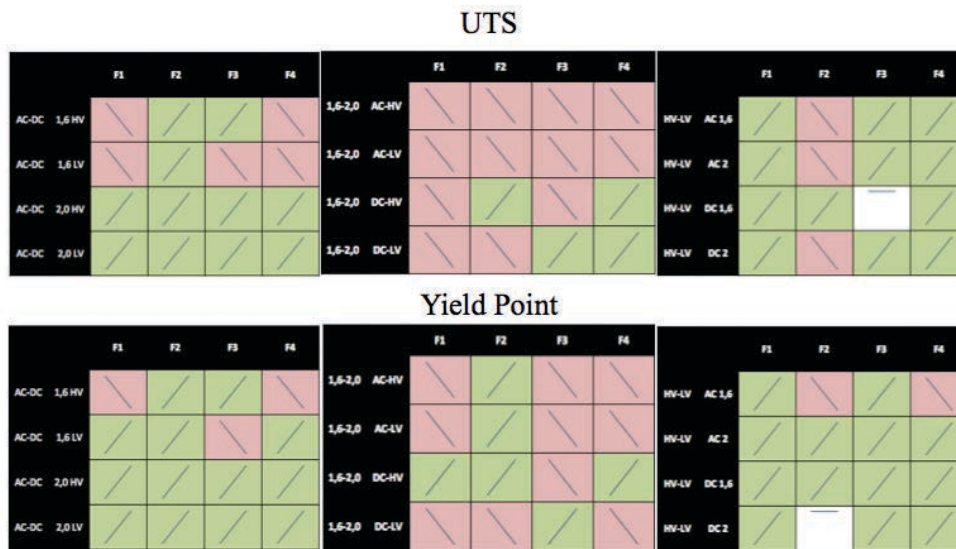
Fig 3- 6: Overview of Variations effect of DOE Variables on Mechanical Strength.

Change of the wire diameter produces a substantial effect on electrical current density and in deposition rate due to its strong effect on melting rate. Its effect on mechanical strength, and within DOE variables ranges, is a little bit more apparent when welds are done by AC, in which cases averages improvement of 4% and 3% of the yield and UTS are reached when wire diameter is reduced to 1,6 from 2,0mm. Using DC, differences between means are below 1%.

The voltage has an indirect effect on weld metal strength. The samples welded high voltage set up are weaker than those welded with the low voltage set up, with a maximum difference between its means close to 10% for yield and close to 5% of UTS.

Of course, this tendency only could be understood within the ranges where DOE variables were studied. The actual effect of DOE variables on weld metal strength should be determined by increasing variables ranges or with better control of hidden variables.

ANOVA analysis was performed with these results and had been found that the observed variance of the results are not statistically significant to guarantee that this differences had been produced by applied variations on tested variables. But taking account, the results of the previous works could be considered acceptable the stated behavior.

3.2.3 DOE Variables effect on Welding Parameters

a) Welding Current.

DOE variables have their stronger effect on welding current, which is and indirect variable of this trial. When submerged arc welding are made using a Constant Voltage mode (CV), the setup of welding machine is Voltage and WFS, while welding current being determined by the physic of the process and by the response of the welding machine. WFS was then the fifth DOE's variable because this value was chosen to produce the same deposition rate while using either 1,6 or 2,0mm wires.

Using a wire of 1,6mm the average currents range were between 264 amp to 303 amp, that represent a 14% of the variation, while average currents range were between 280 amp to 346 amp when using 2,0mm wire, representing a 21% of the current variation. The difference between both means are only 10%, but welding currents range is 82 amp wide, which represent 30% regarding minimum current. Like is known, one of the electrical current features is penetration, in others words, dilution percentage. See Table 3-2.

Correlation: Flux code; D code; CT code; VL code; Amp; Volt; WFS; Heat Input; Heat on wire; Arc Density; Dep Rate; [mohm/mm2]

Correlations

	Flux code	D code	CT code	VL code	Amp	Volt	WFS	Heat Input	Heat on wire	Arc Density	Dep Rate
Amp	0,148255	0,591546	-0,643628	-0,051734							
	0,1046	<0,0001	<0,0001	0,5731							
Volt	0,004861	0,082015	-0,100790	0,944502	0,103841						
	0,9578	0,3712	0,2713	<0,0001	0,2570						
WFS	0,028613	-0,999931	0,006274	0,055148	-0,591132	-0,084909					
	0,7554	<0,0001	0,9456	0,5480	<0,0001	0,3545					
Heat Input	0,283405	0,514661	-0,283436	0,504919	0,602209	0,622682	-0,515714				
	0,0016	<0,0001	0,0016	<0,0001	<0,0001	<0,0001	<0,0001				
Heat on wire	0,016874	0,955553	-0,216315	0,054663	0,778622	0,212960	-0,955771	0,653621			
	0,8542	<0,0001	0,0172	0,5515	<0,0001	0,0190	<0,0001	<0,0001			
Arc Density	0,075994	-0,923955	-0,205664	0,017392	-0,315151	-0,082216	0,924332	-0,372067	-0,809600		
	0,4074	<0,0001	0,0236	0,8498	0,0004	0,3700	<0,0001	<0,0001	<0,0001		
Dep Rate	-0,080025	-0,377838	0,122595	-0,110772	-0,326776	-0,224295	0,380868	-0,369533	-0,409561	0,371775	
	0,3829	<0,0001	0,1804	0,2264	0,0003	0,0134	<0,0001	<0,0001	<0,0001	<0,0001	
[mohm/mm2]	-0,088531	0,919139	0,254422	0,128409	0,265735	0,233817	-0,919644	0,457489	0,808006	-0,951934	-0,336614
	0,3342	<0,0001	0,0049	0,1604	0,0032	0,0098	<0,0001	<0,0001	<0,0001	<0,0001	0,0002

Cell Contents: Pearson correlation
P-Value

Table 3- 2 Correlation Coefficients between DOE Variables, ARC Values, and Weld Metal Strength.

If welding current is analyzed by current type, on Table 3- 3, it is seen that AC produces wider currents ranges (D=80 amp) than ranges of welding currents produced by DC (D=32 amp). What means that the difference between average welding current of the samples welded using AC is high, meanwhile the average current of the samples

welded by DC were closer. The voltage has an indirect effect on welding current. The use low voltages produce high currents
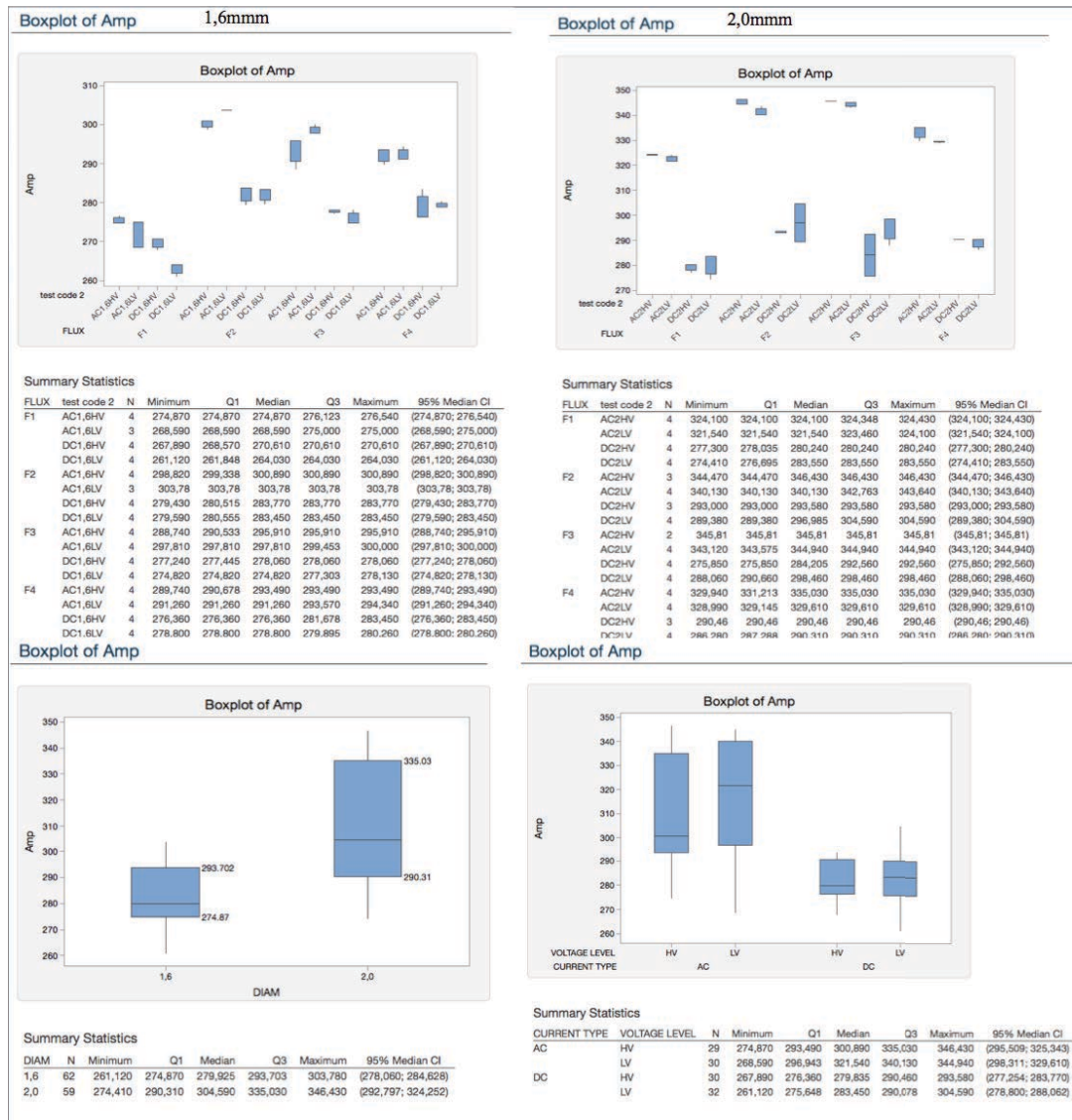
Table 3- 3: Welding Current

Next chapter deposited weld metal chemical composition will be studied, and both, chemical composition and welding features will be correlated to understand its effect on mechanical strength.

b) Welding Voltages, Travel Speed (TS) and Wire Feed Speed (WFS).

Like been commented above, instantaneous welding current, voltage and WFS are recorded by the welding machine data acquisition device as a rate of 4 times per

second, and saved in an txt file, also starting and finishing time are recorded in txt file and used together with plate length to compute the welding travel speed.

c) *Energy of the weld, Deposition ratio, Electrical Impedance.*

On tables App 3-9 to App 3-13 values of Heat Input, Heat on wire, Deposition Rate, Electrical impedance and Electrical Stick-out times electrical resistivity are given with Boxplots. All these parameters show interesting patterns that will be correlated with weld metal strength trying to understand results dispersion causes.

3.3   Direct and Indirect Welding parameters effect on Weld Metal Strength

When weld metal strength is correlated with welding parameters, the higher coefficient is 0,35 and 0,43 for heat input regarding yield and UTS respectively, reaching to 0,69 for CVN, table 3-4. When yield and UTS values are plotted versus heat input, Fig 3- 7: Yield Point and UTS vs. Heat Input, an inverse relationship is observed but with high scattering what produce the low correlation coefficients, Table 3- 4.

All Fluxes
Correlation: Amp; Volt; WFS; Heat Input; Heat on wire; Arc Density; Dep Rate; [mohm/mm2]; Z [ohm]; Yield; UTS; CVN

Correlations

	Amp	Volt	WFS	Heat Input	Heat on wire	Arc Density	Dep Rate	[mohm/mm2]	Z [ohm]
Yield	-0,337444	-0,226580	0,156026	-0,359397	-0,254523	0,051141	-0,117549	-0,066491	0,190669
	0,0002	0,0125	0,0875	<0,0001	0,0048	0,5775	0,1991	0,4687	0,0362
UTS	-0,372217	-0,255527	0,137236	-0,434225	-0,254535	0,022572	-0,018851	-0,037894	0,256036
	<0,0001	0,0047	0,1333	<0,0001	0,0048	0,8059	0,8374	0,6799	0,0046
CVN	0,073939	0,249586	0,622479	-0,022941	-0,436887	0,764083	0,371308	-0,693032	0,208674
	0,6926	0,1757	0,0002	0,9025	0,0140	<0,0001	0,0397	<0,0001	0,2599

Cell Contents: Pearson correlation
                P-Value

Table 3- 4: Correlation Coefficients between Welding Parameters, ARC Values, and Weld Metal Strength.

When plot`s data are grouped (Fig 3- 8) by electrical current type, is observed that there are more AC points (blue) in the bottom right of the graph, while the upper left corner is dominated by the DC points (red). This behavior is consistent with the previous analysis, where it was shown that the welds made using AC produces higher amperage currents, higher heat inputs, and therefore welds with lower mechanical strength.
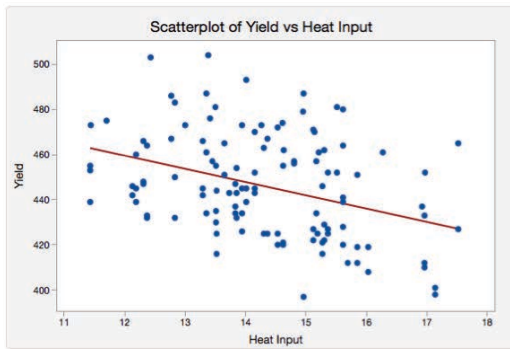
47
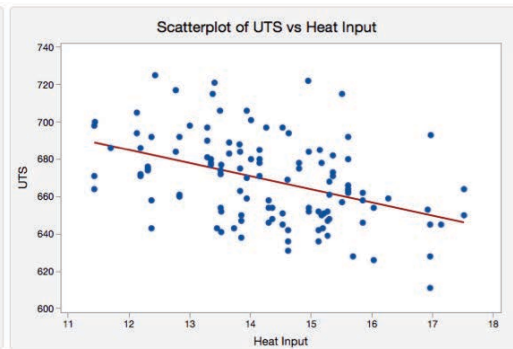
If the analysis is done by wire diameter, it is observed that welds made with 2mm wire, under the experimental conditions, produce weaker welds. Same results are gotten when welds are done using high voltage level, which although they produce lower amperage currents but still, more energetic welds due to its higher potential difference.

But any of explained behaviors could be used alone to describe the scattering observed on weld metal strength because its regression fit lines are very close or even seems to be the same.

Another way to show the weakness of welding parameters and the rest of the indirect computed values, is using the Best Subset Regression tool, see Table app 3-15, where is shown that best possible model using only this values only give a maximum R_{adj}^2 of 28,2%, and maximum R_{pred}^2 lower than 23%.

Continuing with the analysis; While electrical current is increased, higher is the heat inputs, and then, lower cooling rates, which in agreement with several authors, produce weaker welds [5-1] to [5-4],[5-8],[5-9],[3-1].

But also, when electrical current is increased the weld penetration is deeper, doing that more amount of base metal will be mixed with the filler metal, reducing the level of the main strengtheners elements on deposited weld metal. This loss of alloying

elements is especially critical for solid-solution strengthened alloys.[4-1][5-9][5-1][5-2][5-4][5-16][5-18][5-20][1-16]

As a simple way to show the effect of chemical composition on 2D Yield vs. heat input plot, the main alloying elements were ranked by percentiles, and grouping the data by the level of them, Fig 3- 9: UTS vs. HI by 2 level ranked Alloying Elements. These plots show that chemical composition has and important role on data scattering because strength results are clearly ranked, producing differentiated regression fit lines.
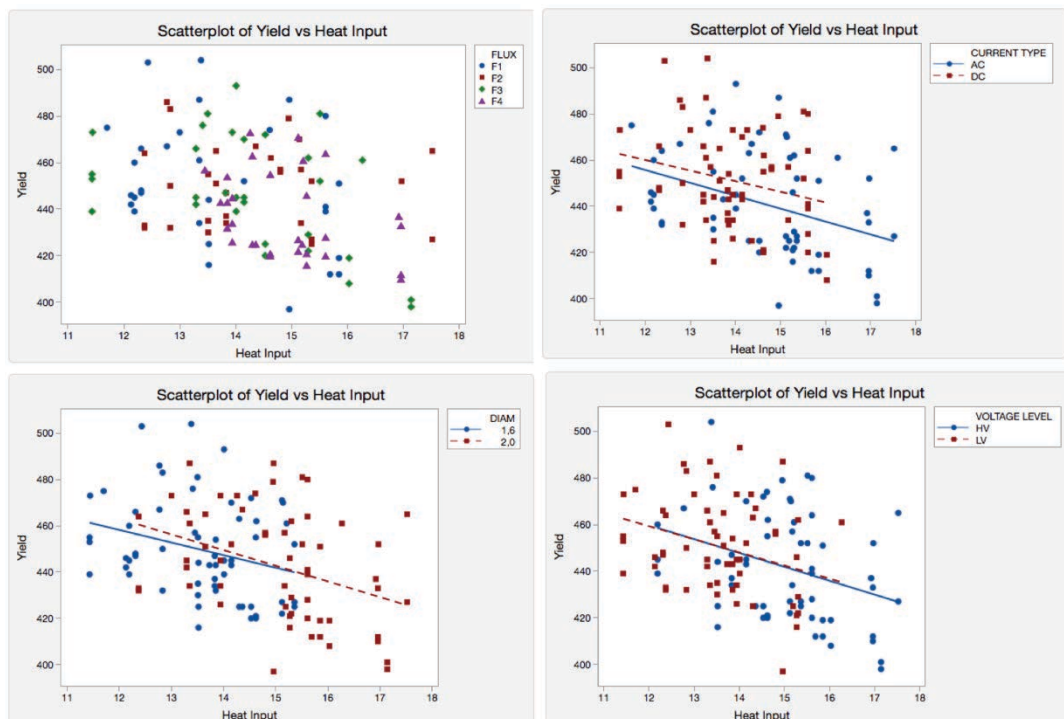
Fig 3- 8: Yield Point and UTS vs. Heat Input by DOE variables.
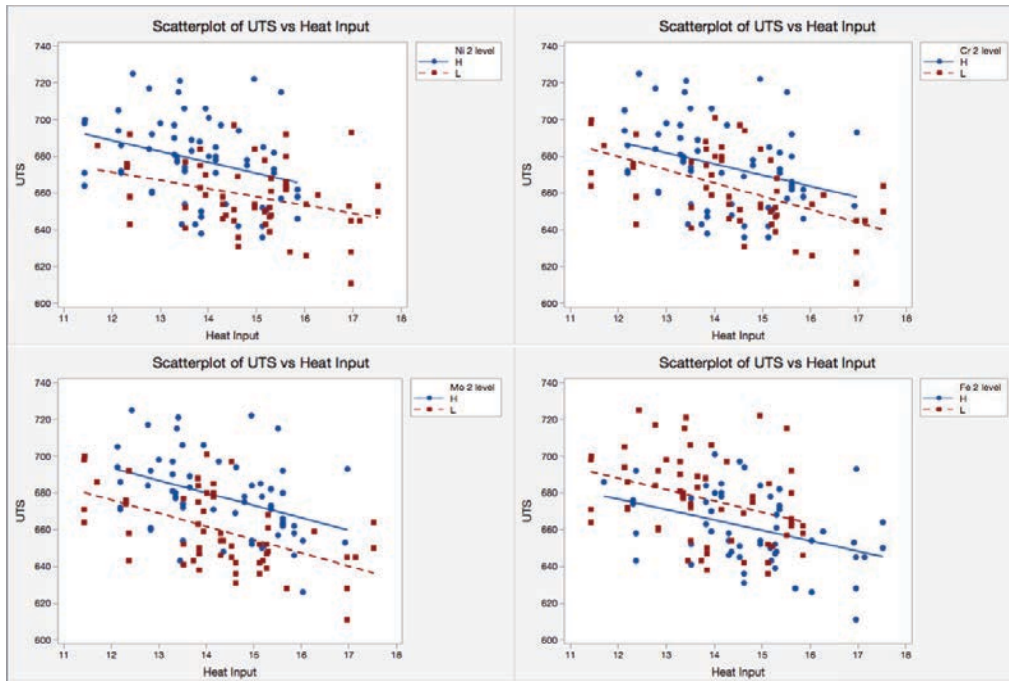
Fig 3- 9: UTS vs. HI by 2 level ranked Alloying Elements.

3.4   Chemical Composition Effect on Weld Metal Strength

Above, chemical composition was presented as key factor of cylindrical tensile test results scattering, by plotting UTS against Heat Input, using grouped values by their level of alloying elements. These plots gave a good overview of the alloying elements pattern effect. Pearson Correlation Coefficients, Table 3- 5, give more details about how strong is the effect of each alloying element on each strength value. Following Cieslak publications, Ni_{eq}, Cr_{eq} and Mo_{eq} values are going to be introduced in this analysis.

Correlation: %Nieq G; %Creq G; %Moeq G; %Ni G; %Cr G; %Mo G; %Fe G; %W G; Yield; UTS

Correlations

	%Nieq G	%Creq G	%Moeq G	%Ni G	%Cr G	%Mo G	%Fe G	%W G
Yield	-0,373565	0,455560	0,307416	0,463692	0,455560	0,278707	-0,456999	0,362222
	0,0003	<0,0001	0,0036	<0,0001	<0,0001	0,0086	<0,0001	0,0005
UTS	-0,388405	0,497065	0,308290	0,590734	0,497065	0,277584	-0,537643	0,370172
	0,0002	<0,0001	0,0035	<0,0001	<0,0001	0,0088	<0,0001	0,0004

Cell Contents: Pearson correlation
                P-Value

Table 3- 5: Correlation Coefficients between General Chemical Composition and Weld Metal Strength, Fluxes F1 , F2 and F3.

Note: To improve data adjustment, all outliers values were reviewed, corrected or

deleted. Also results from flux F4 were not used for following analysis.

General chemical composition of each welded test was taken from each side of each welded plate and after removing weld metal over thickness, see Fig 3- 10. But since several weld beads have been required to fill each side of welded test, and since each tension specimen has been obtained from different areas of the weld joint, is expected that each tested tensile sample doesn't have, necessarily, same chemical composition of the analyzed area for General Chemical Composition. Reason why, improvement of correlation coefficients is expected by using the actual tensile samples chemical composition.
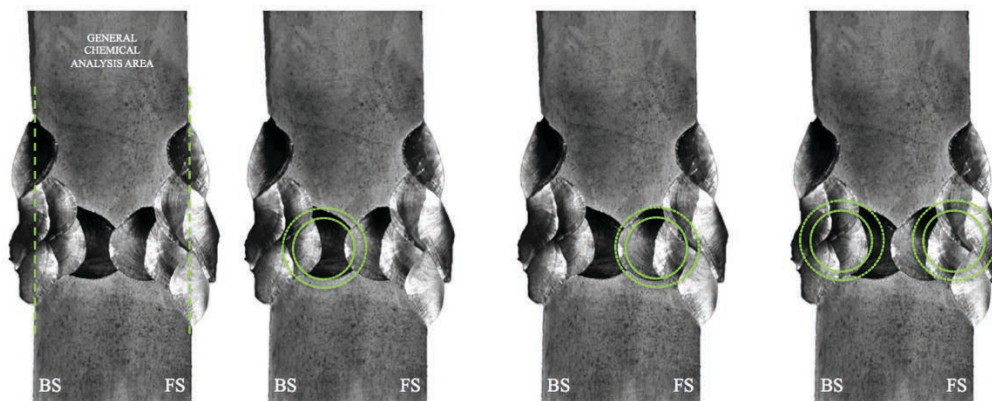
Fig 3- 10: Location of General chemical analysis and tensile samples extraction

3.4.1   Actual Chemical composition of each tested cylindrical tensile sample

Chemical composition of each tensile sample was analysed by X-ray Fluorescence (XRF) technique. As shown on Fig 3- 11 each cylindrical sample were cut close to the fracture surface, and on this surface an 3X3 XRF measurements array was performed, getting a total of 9 compositional measurement per sample.

At this step only the percentage of Ni, Cr, Mo, Fe, W and Co, were checked, without equipment calibration. Small trial was performed to determine XRF measurement error, by both collimators All measurements were done using Nickel filter, 0,3mm Collimator, See Table 3- 6. Each measurement was done in 60 seconds.

Fig 3- 12 shows histograms of %Ni, %Cr, %Mo, %Fe and %W measurements done by

XRF technique. Total have been performed 1105 measurements on 123 tensile samples. Compositional ranges gotten by XRF are little bit wider than ranges gotten from general chemical composition measurements, where maximum measured value of $\%Ni_{Max}=51$ or $\%Fe_{Max}=41$ and minimums of $\%Ni_{min}=37$ or $\%Fe_{min}=18$, meanwhile these max and minimums measured on tensile samples were $\%Ni_{Max}=55$, $\%Fe_{Max}=60$ and $\%Ni_{min}=30$, $\%Fe_{min}=13$.
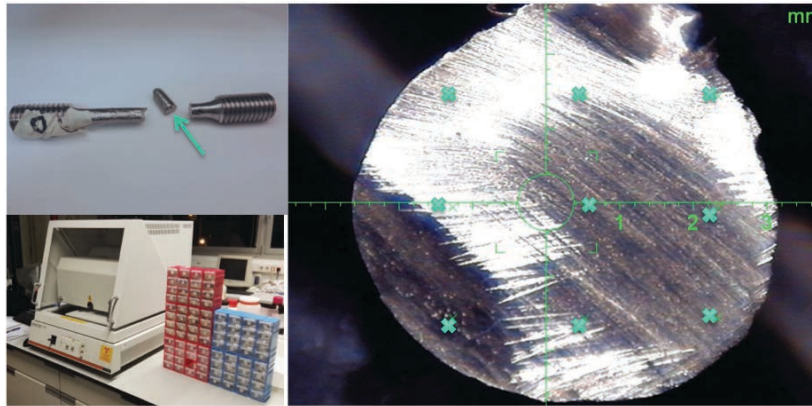
Fig 3- 11: 3X3 array of alloying elements measurements performed by XRF technique on cylindrical tensile specimens

0,3 mm Colimator						0,1mm Colimator					
ID	%Ni	%Cr	%Mo	%Fe	%W	ID	%Ni	%Cr	%Mo	%Fe	%W
1	42,20	11,70	11,00	32,80	2,24	1	41,50	11,3	10,6	34,5	2,1
2	42,20	11,60	10,90	32,90	2,36	2	40,90	11,7	10,7	34,9	1,8
3	42,10	11,70	11,00	33,00	2,27	3	41,80	11,2	10,4	34,4	2,2
4	42,30	11,70	10,90	32,70	2,34	4	41,40	11,5	11,0	34,0	2,1
5	42,00	11,80	11,20	32,90	2,12	5	41,20	11,1	11,2	34,6	1,9
6	42,10	11,80	11,10	32,90	2,20	6	41,40	11,5	10,1	35,5	1,4
7	42,10	11,80	10,90	33,10	2,20	7	41,20	11,4	11,0	34,6	1,7
8	42,40	11,90	11,00	32,50	2,23	8	41,90	9,9	10,8	35,2	2,3
9	41,90	12,00	11,00	32,90	2,17	9	42,40	11,0	11,2	33,3	2,1
10	41,90	11,90	11,00	33,00	2,24	10	41,00	11,0	11,1	34,9	2,0
	%Ni	%Cr	%Mo	%Fe	%W		%Ni	%Cr	%Mo	%Fe	%W
Average	42,12	11,79	11,00	32,87	2,24	Average	41,47	11,2	10,8	34,6	2,0
Des Stand	0,16	0,12	0,09	0,17	0,07	Des Stand	0,45	0,5	0,4	0,6	0,3
% of Error	0,4%	1,0%	0,9%	0,5%	3,3%	% of Error	1,1%	4,6%	3,4%	1,8%	13,1%

Table 3- 6 Determination of the repeatability or measurement error of XRF technique by different collimator
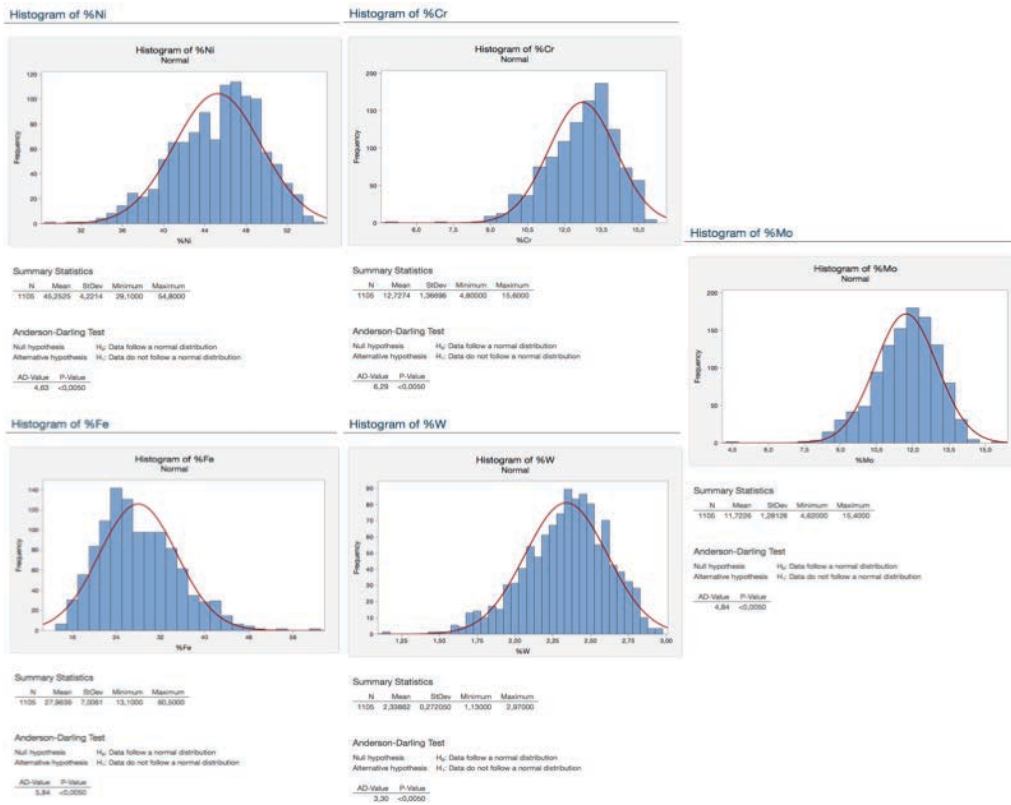
Fig 3- 12: Histogram of alloying elements measurements on cylindrical tensile samples.

3.4.2 General vs. Actual Chemical composition effect on Correlation Coefficients

Now, when tensile samples' strength is correlated with its own chemical composition, see Table 3- 7, Pearson coefficients rise 0,8 for UTS regarding almost all alloying elements and their equivalents values. This correlation is graphically shown with the test sheets made for each tested sample,

Fig 3- 13 and Fig 3- 14, where are shown some of representative samples test sheet

Fig 3- 13), sorted by its UTS level, where is easy to see that tensile samples with Ni 53/Cr15/Mo13,4/W2,7 has a Rp0,2% 446/UTS 705, with the Fe around 15%. When chemical composition fall to Ni 41/Cr11/Mo10/W2,0 has a Rp0,2% 425/UTS 645 with %Fe around 40. While higher is it dilution level, higher iron pick up, lower is it UTS. Now using only chemical composition Best subsets regression tool, see App 3- 16, maximum R2 reach 70% of adjustment, with a maximum prediction capacity around 67%, with expected standard deviations lower than 12 MPa.

53

Correlation: %Nieq G; %Creq G; %Moeq G; %Ni G; %Cr G; %Mo G; %Fe G; %W G; Yield; UTS

Correlations

	%Nieq G	%Creq G	%Moeq G	%Ni G	%Cr G	%Mo G	%Fe G	%W G
Yield	-0,373565	0,455560	0,307416	0,463692	0,455560	0,278707	-0,456999	0,362222
	0,0003	<0,0001	0,0036	<0,0001	<0,0001	0,0086	<0,0001	0,0005
UTS	-0,388405	0,497065	0,308290	0,590734	0,497065	0,277584	-0,537643	0,370172
	0,0002	<0,0001	0,0035	<0,0001	<0,0001	0,0088	<0,0001	0,0004

Cell Contents: Pearson correlation
P-Value

Correlation: %Nieq XRF; %Creq XRF; %Moeq XRF; %Ni XRF; %Cr XRF; %Mo XRF; %Fe XRF; %W XRF; Yield; UTS

Correlations

	%Nieq XRF	%Creq XRF	%Moeq XRF	%Ni XRF	%Cr XRF	%Mo XRF	%Fe XRF	%W XRF
Yield	-0,559457	0,549684	0,558973	0,552984	0,549684	0,559345	-0,560841	0,515846
	<0,0001	<0,0001	<0,0001	<0,0001	<0,0001	<0,0001	<0,0001	<0,0001
UTS	-0,811711	0,793526	0,813254	0,812805	0,793526	0,816942	-0,820355	0,732861
	<0,0001	<0,0001	<0,0001	<0,0001	<0,0001	<0,0001	<0,0001	<0,0001

Cell Contents: Pearson correlation
P-Value

Table 3- 7: Correlation Coefficients between General and Actual Chemical Composition with Weld Metal Strength.

This strong dependence between chemical composition and mechanical strength is nothing new, especially for this type of nickel alloy, which its strength is controlled by solid solution. But, What is actual new from gotten information by XRF is how big could be the chemical composition different between weld beads which are forming the cylindrical segment of the tensile sample.

Fig 3- 13: Information given on Sample Test Sheet.

54

P01

Test	P01	Yield	UTS	Elong
Sample	09136-01A	446 MPa	705 MPa	36%
BM	9%Ni 21 mm			
w/f	F1			
AWMTT Sample	LECO / 6,35 mm / L /	Joint X 45º 15º	Ovality	Hook Crks
Diam / Current	w=1,6 / C=AC 60 Hz	Testing Delay 35 d	IntPass Temp 80ºC	DepWM 853 gr
Num Passes	10 p / <-->			
C Density	139 Amp/mm2			
AVG HI	8,4 KJ/cm			

%Fe	x1	x2	x3
y1	15,1	16,2	15,3
y2	15,3	15,2	19,6
y3	15	15,4	16,2

%Ni 53,0±0,85
%Cr 15,0±0,28
%Mo 13,4±0,34
%W 2,7±0,12

P32

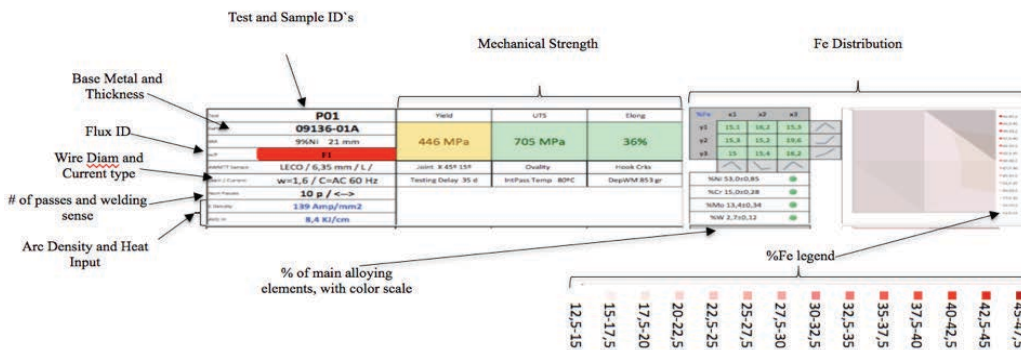| Test	P32	Yield	UTS	Elong
Sample	10438-01A	445 MPa	697 MPa	39%
BM	9%Ni 21 mm			
w/f	F3			
AWMTT Sample	LECO / 6,38 mm / L /	Joint X 45º 15º	Ovality	Hook Crks
Diam / Current	w=2 / C=DC + Hz	Testing Delay 6 d	IntPass Temp 80ºC	DepWM 883 gr
Num Passes	12 p / <-->			
C Density	97 Amp/mm2			
AVG HI	8,0 KJ/cm			

%Fe	x1	x2	x3
y1	22,1	22,2	22
y2	22	22,8	30,6
y3	21,8	22,2	25,1

%Ni 47,6±1,66
%Cr 13,4±0,62
%Mo 12,9±0,56
%W 2,6±0,16

P13

Test	P13	Yield	UTS	Elong
Sample	09722-02A	427 MPa	671 MPa	45%
BM	9%Ni 21 mm			
w/f	F2			
AWMTT Sample	LECO / 6,43 mm / L /	Joint X 45º 15º	Ovality	Hook Crks
Diam / Current	w=1,6 / C=AC 60 Hz	Testing Delay 8 d	IntPass Temp 80ºC	DepWM 1393 gr
Num Passes	12 p / <-->			
C Density	100 Amp/mm2			
AVG HI	9,0 KJ/cm			

%Fe	x1	x2	x3
y1	25,3	25,7	26
y2	26	26,8	27,4
y3	38,5	27,6	27,2

%Ni 45,2±2,77
%Cr 12,3±1,00
%Mo 11,3±0,83
%W 2,3±0,22

P17

Test	P17	Yield	UTS	Elong
Sample	10125-01A	412 MPa	662 MPa	46%
BM	9%Ni 21 mm			
w/f	F1			
AWMTT Sample	LECO / 6,35 mm / L /	Joint X 45º 15º	Ovality	Hook Crks
Diam / Current	w=2 / C=AC 60 Hz	Testing Delay 28 d	IntPass Temp 80ºC	DepWM 722 gr
Num Passes	9 p / <-->			
C Density	110 Amp/mm2			
AVG HI	10,3 KJ/cm			

%Fe	x1	x2	x3
y1	36,2	34,4	35,9
y2	35,9	31,1	26,9
y3	32,4	28,4	27,2

%Ni 43,3±2,51
%Cr 12,3±0,83
%Mo 11,4±0,89
%W 2,3±0,17

P14

Test	P14	Yield	UTS	Elong
Sample	09725-01A	430 MPa	654 MPa	40%
BM	9%Ni 21 mm			
w/f	F2			
AWMTT Sample	LECO / 6,43 mm / L /	Joint X 45º 15º	Ovality	Hook Crks
Diam / Current	w=1,6 / C=AC 60 Hz	Testing Delay 7 d	IntPass Temp 80ºC	DepWM 1422 gr
Num Passes	12 p / <-->			
C Density	98 Amp/mm2			
AVG HI	8,6 KJ/cm			

%Fe	x1	x2	x3
y1	42,9	34,1	41,1
y2	41,1	30,9	32,2
y3	33,6	30,3	31,6

%Ni 41,5±2,65
%Cr 11,2±0,86
%Mo 10,7±0,86
%W 2,0±0,17

P08

Test	P08	Yield	UTS	Elong
Sample	09143-02A	425 MPa	645 MPa	40%
BM	9%Ni 21 mm			
w/f	F3			
AWMTT Sample	LECO / 6,38 mm / L /	Joint X 45º 15º	Ovality	Hook Crks
Diam / Current	w=1,6 / C=AC 60 Hz	Testing Delay 22 d	IntPass Temp 80ºC	DepWM 808 gr
Num Passes	10 p / <-->			
C Density	149 Amp/mm2			
AVG HI	10,5 KJ/cm			

%Fe	x1	x2	x3
y1	45,8	35,1	45,9
y2	45,9	31,3	31
y3	44,1	32,4	30,9

%Ni 41,2±4,69
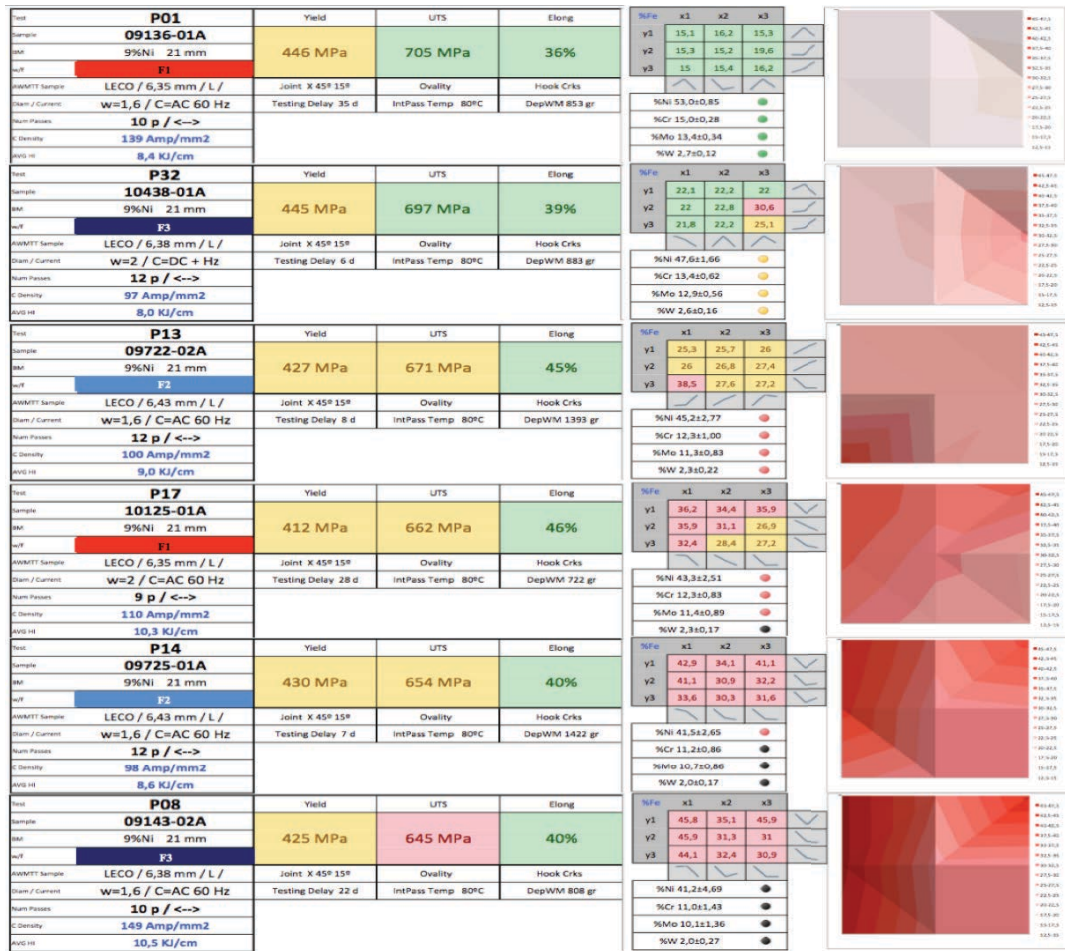%Cr 11,0±1,43
%Mo 10,1±1,36
%W 2,0±0,27

Fig 3- 14: Test sheet of each test tensile sample, Showing Samples ID, DOE variables, Mechanical strength, Chemical composition and plot with %Fe profile on tensile sample cross section (white %Fe=12,5 / Red %Fe= 47,5)

3.5 Difference between chemical compositions measured per sample

To give an idea of measured chemical composition differences found in one cylindrical tensile sample, from each sample are taken the minimum and maximum value of each alloy elements. Relative Difference are computed using these values with the following formula:

$$Relative\ Difference = \frac{\%Xmax - \%Xmin}{Averge(\%X)} \qquad \text{Eq. 10}$$

Table 3:8 shown the histograms of relative difference of the measured alloying elements in each sample. For Ni, Cr Mo and W minimal differences are around 6% and maximum are around 53%. Histograms shown higher frequency differences between 19% to 26%. Measurements of iron are showing same pattern with minimum of 15%, maximum of 105% and mayor frequency measurements in 50% of differences.
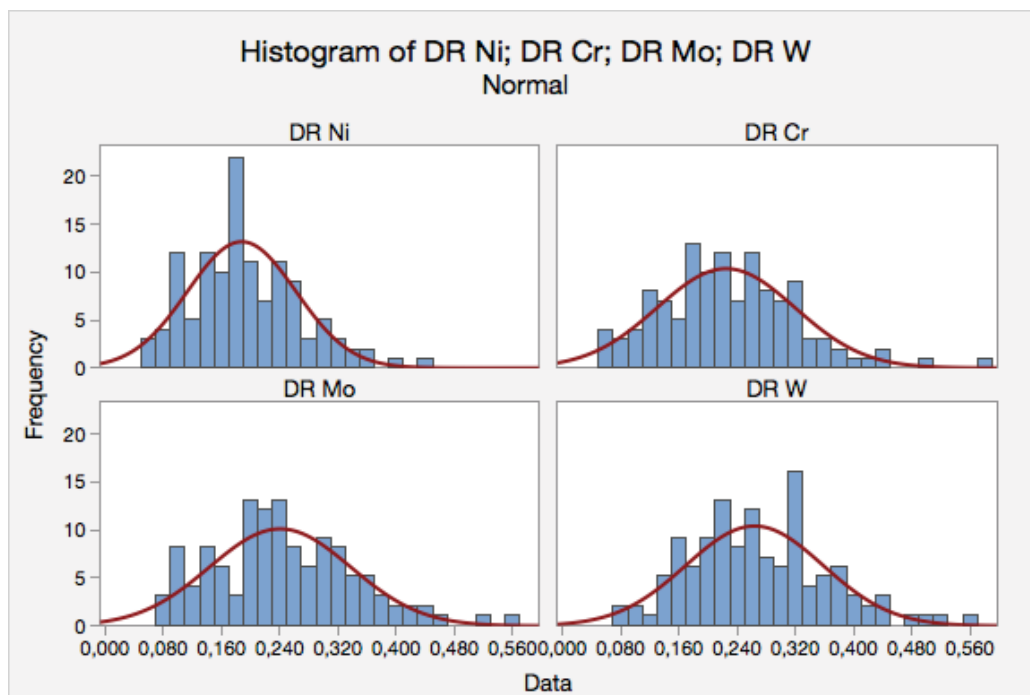

Fig 3- 15: Histograms of Relative Different on measurements of alloying elements on tensile samples.

Other way to show how big is chemical composition effect on cylindrical tensile sample strength is plotting, in the same graph yield point, UTS and %Mo of each tested tensile sample, grouped by DOE variables and Test ID. All these data are shown on App 3- 8 together UTS acceptable range, Maximum and minimum Mo_{eq} values and minimum

56

required yield strength.

To get more resolution on alloying elements distribution, 30X30 measurements array were performed getting a total of 900 XRF measurements per sample. Fig 3- 16 shown %Ni distribution over cross section of samples G19 and G156 from test ID P31. These samples shown 90MPa UTS difference and 70MPa yield point difference and are placed on UTS$_{ranking}$ in position 8 the sample G156 and in position 122 the sample G19, *. On the specimen G156 the Ni content is over 50% on close to the 90% of its, with only a couples of zones, welding beads FS4 and FS1, where in %Ni is around 45%.
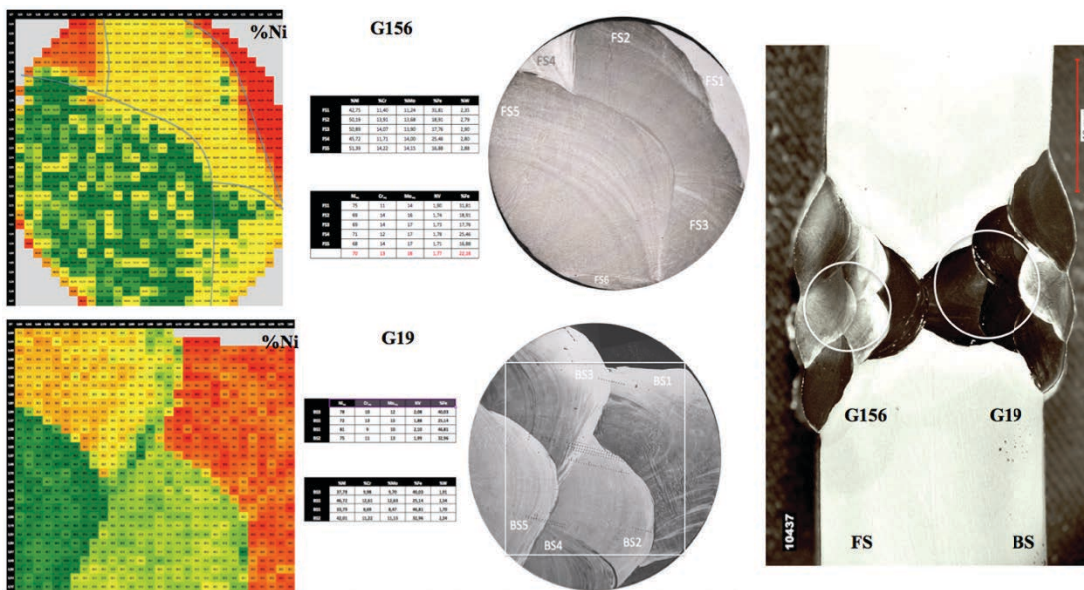

Fig 3- 16: %Ni distribution on cylindrical tensile sample cross-section, for samples G19 and G156, Test ID P31.

G156 specimen was machined from the outer side of the Finishing Side (FS) or last welded side, as is indicated on macro section. G156 has a tensile strength of 481/715 MPa (Rp0,2%/UTS). In the other hand, on the sample G19 the Ni content over cross section is clearly ranked in 4 zones, where the average measured %Ni is BS1=34%, BS2=42, BS3=38% and BS5=46%. G19 tensile sample was machined from the inner zone of the first side welded, Backing Side (BS), with a tensile strength of 408/625MPa.

3.6   Welding Parameters effect on weld metal toughness

Absorbed energy by impact test at -196ºC is one of the materials and joints requirements in design standards. For this application is requested that average absorbed energy shall be bigger than 50 joules for deposited weld metal and HAZ.

For this study have been prepared and tested a set 3 of specimens per each experiment, in accordance with ASTM E94. Like is shown in Fig 3- 17, the lower average value per flux is 75 joules, which reach 50% over the standard requirements (50 joules).

Average CVN results show strongest correlation with wire diameter and current type, grouping and ranking the data in accordance with them. For same amperage welds performed with 1,6mm of diameter wire and or with AC current produce more tough welds than those performed usign2,0 mm wire and DC currents. CVN and wire diameter show a direct relationship, while CVN and current type show a reverse relationship between them.

Form fluxes point of view, both fused fluxes are showing same behavior, with $(^{CVN}/_{HI})_{(1,6mm)}$ around 14,5 and $(^{CVN}/_{HI})_{(2,0mm)}$ around 4,5. In case of agglomerated flux F4 both $(^{CVN}/_{HI})_{(1,6mm)}$ and $(^{CVN}/_{HI})_{(2,0mm)}$ are almost parallel and around 7, while F1 flux shown the lowest factors $(^{CVN}/_{HI})_{(1,6mm)} =1,2$ and $(^{CVN}/_{HI})_{(2,0mm)} =3,3$, Fig 3- 18.

Even when heat inputs values are around 10 KJ/cm, what is in the recommended range for nickel alloys welds; direct relationship between energy and absorbed energy is contrary than expected results, which implies that some uncontrolled factor is been improved when current is increased.

Boxplot of CNV
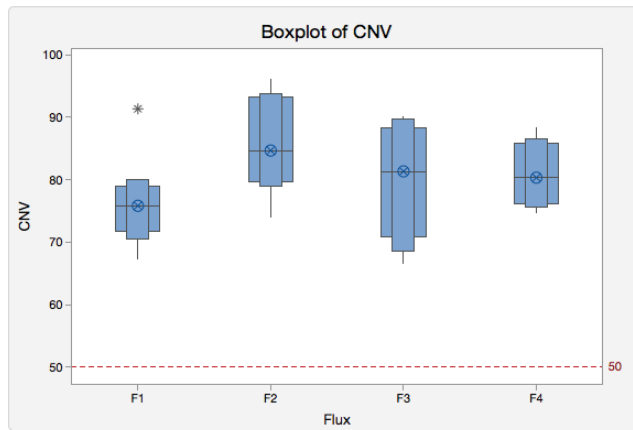
Summary Statistics

Flux	N	Minimum	Q1	Median	Q3	Maximum	95% Median CI
F1	8	67,333	71,833	75,833	78,917	91,333	(70,452; 80,106)
F2	8	74,000	79,667	84,667	93,250	96,000	(78,990; 93,817)
F3	8	66,667	70,917	81,333	88,333	90,000	(68,538; 89,688)
F4	8	74,667	76,083	80,333	85,917	88,333	(75,602; 86,462)

Fig 3- 17: Average absorbed energy by Charpy V notch test by Fluxes
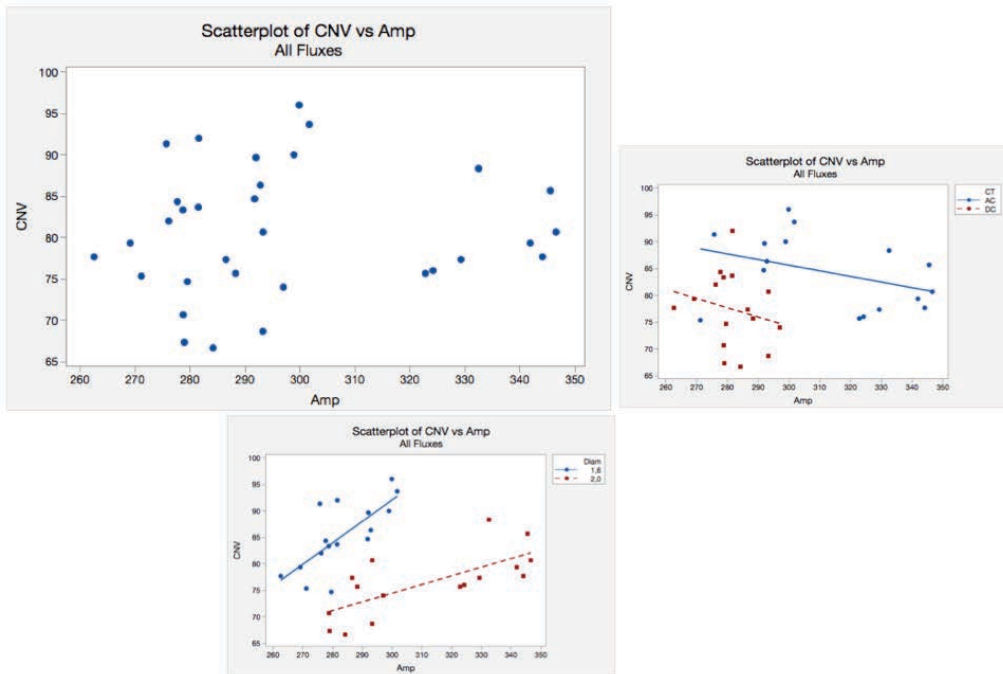

Fig 3- 18: Effect of welding current on CVN values grouped by current type and wire diameter.
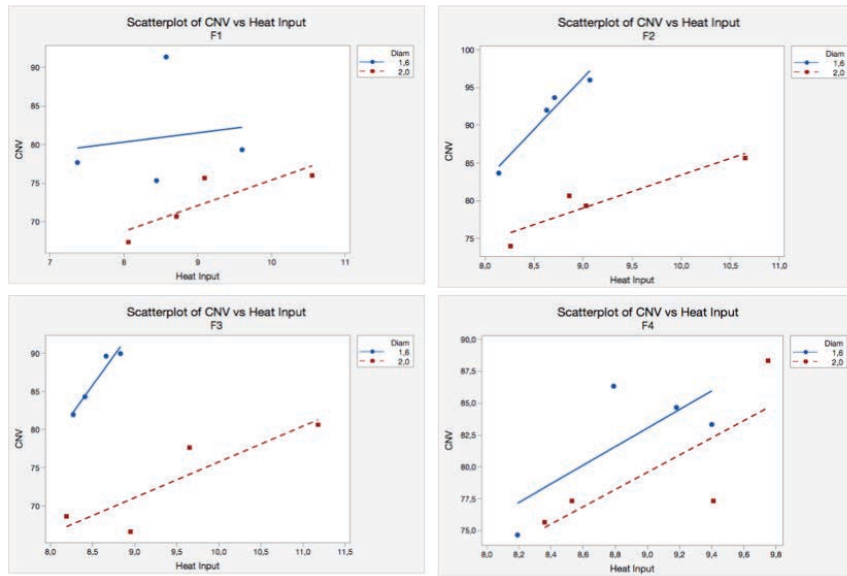
Fig 3- 19: Effect of Heat input on CVN values by fluxes and DOE variables.

3.7   X-ray diffraction analysis

XRD technique was used to compare from structural point of view both tested samples, G19 and G156, to try to understand causes of their strength difference, and also to know if any secondary phase is present. In accordance with [3-4] $M_{23}C_6$ carbides shows their peaks around 18º, 33º and 46º, M_6C show its peaks around 56º, 70º and 80º and µ phase peaks are around 37º, 44º and 46º. But in both diffraction spectrum, from sample G19 and G156, there are only 5 peaks corresponding to the main diffractive planes of the crystalline FCC systems, and there are no indication of any peak around previously cited angles, what indicate that at least there are no enough amount of and/or particles size is to small of secondary phases to be detected by this technique.

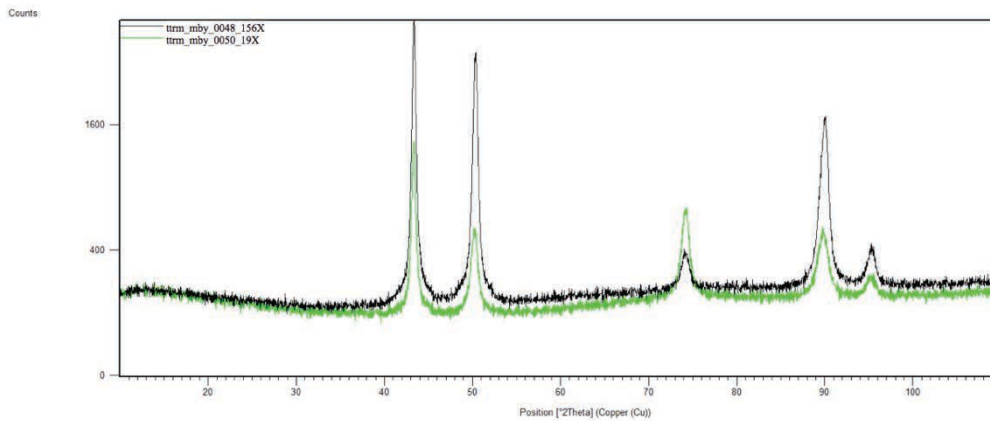Fig 3- 20 shown both overlapped spectrums of G19 and G156 samples, making easy its comparison. First features is that peaks P1, P2, P4 and P5 are ahead around 0,2º regarding G156's peaks, Fig 3- 21. P1 has smallest offset, 0,036º and P5 the greater 0,272º. P3 is the only peak of G156 that is 0.170 ° ahead of G19, Table 3- 8: Results of Spectrum Peaks' analysis(A). Another feature is width difference at half height; G156's peaks P1, P3 and P4 wider than those of G19, see Table 3- 8(b). Both data are consistent with each other indicating that G19's crystallographic lattice is slightly bigger than G156's lattice.

Table 3- 8 C and D show G19 and G156 lattice parameters calculation following Bragg's formulation, for each one of the 5 peaks. Again, G19's lattice is slightly bigger than G156's lattice.

To know if dilution effect is the responsible of lattice grow, weighted radius computed from XRF data will be compared with Average radius computed from formula xx using XRD data.

Weighted radiuses have been computed using atomic fraction times atomic radius of each of the elements [1] getting hypothetical radius produced by alloying elements contribution. Results, r_{XRF} data from Table 3- 8 (C) and (D), shown that even when Iron

---

[1] http://www.knowledgedoor.com/2/elements_handbook/atomic_radius.html

61

atoms are bigger than nickel atoms, global effect of dilution reduce weighted radius because also the bigger atoms proportion is reduced.

From both analyzed samples, G19 has higher dilution, and smaller weighted radius, but from XRD data shown higher lattice parameter. So this results show that crystals grow seems to be not produced only by chemical composition effect.
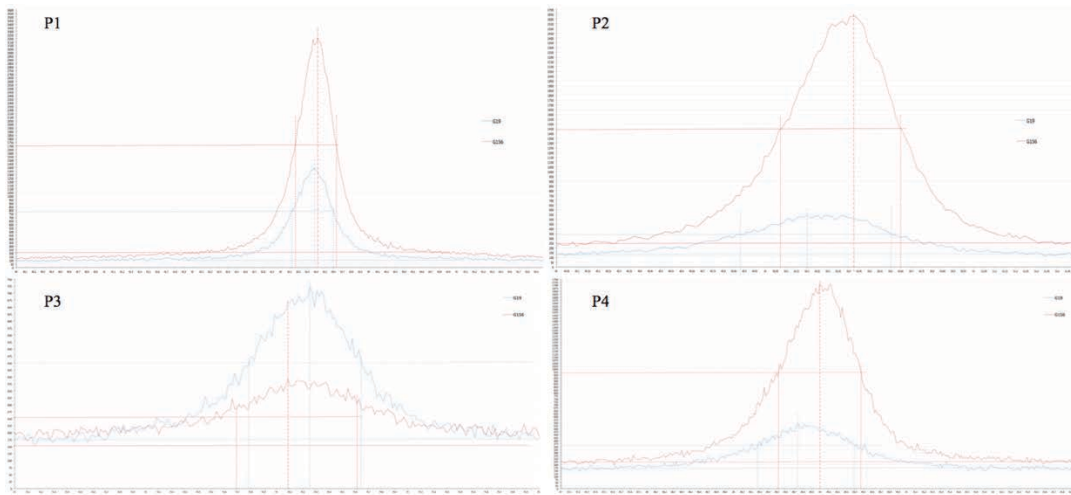

Fig 3- 21: Peaks' analysis of Diffractions spectrums

(A)

	Peaks' Location (2θ)			
	G19	G156		Loc Diff
P1	43,384 º	43,418 º		0,034 º
P2	50,201 º	50,422 º		0,221 º
P3	74,256 º	74,086 º		-0,170 º
P4	89,743 º	89,998 º		0,255 º
P5	95,013 º	95,285 º		0,272 º

(B)

	Peak Width			
	G19	G156		WidthDiff
P1	0,460 º	0,470 º		0,010 º
P2	0,720 º	0,580 º		-0,140 º
P3	0,860 º	0,920 º		0,060 º
P4	0,570 º	0,960 º		0,390 º
P5				

(C)

	2θ	$d_{(h,k,l)}$	Plane	$h^2+k^2+l^2$	a_0	r_{XRD}	r_{XRF}
	43,384 º	2,084 Å	(1 1 1)	3	3,610 Å	1,276 Å	1,271 Å
	50,201 º	1,816 Å	(2 0 0)	4	3,632 Å	1,284 Å	
G19	74,256 º	1,276 Å	(2 2 0)	8	3,610 Å	1,276 Å	
	89,743 º	1,092 Å	(3 1 1)	11	3,621 Å	1,280 Å	
	95,013 º	1,045 Å	(2 2 2)	12	3,619 Å	1,279 Å	
				Average	3,618 Å ⬆	1,279 Å ⬆	1,271 Å ⬇

(D)

	2θ	$d_{(h,k,l)}$	Plane	$h^2+k^2+l^2$	a_0	r_{XRD}	r_{XRF}
	43,418 º	2,082 Å	(1 1 1)	3	3,607 Å	1,275 Å	1,275 Å
	50,422 º	1,808 Å	(2 0 0)	4	3,617 Å	1,279 Å	
G156	74,086 º	1,279 Å	(2 2 0)	8	3,617 Å	1,279 Å	
	89,998 º	1,089 Å	(3 1 1)	11	3,613 Å	1,277 Å	
	95,285 º	1,042 Å	(2 2 2)	12	3,611 Å	1,277 Å	
				Average	3,613 Å ⬇	1,277 Å ⬇	1,275 Å ⬆

(E)

	h	k	l
G19	0,99972	1,00089	0,99933
G156	1	0,99969	1,00004

(F)

		a_0		r_{XRD}		r_{XRF}
G19	⬆	3,618 Å	⬆	1,279 Å	⬇	1,271 Å
G156	⬇	3,613 Å	⬇	1,277 Å	⬆	1,275 Å

Table 3- 8: Results of Spectrum Peaks' analysis

Another possible cause of reticular growth is deformation. In order to determine if

there is any evidence of anisotropy in the diffraction spectra, the equations obtained from the Bragg Law are solved and applied to the first three peaks. The results obtained, Table 3- 8 (E) show that there is a small difference between the sizes of these unit vectors, which could show the existence of any component of reticular deformation produced by internal stresses, or simply be caused by intrinsic measurement errors.

The hypothesis of crystal deformation due strain produced by internal stress can also be supported with the peaks' location and width data. From peaks' location point of view, an increase in the distance $d_{(h, k, l)}$,according to the Law of Bragg, produce peak`s displacement towards smaller 2θ angles, whereas peaks' widening implies a reduction of $d_{(h, k, l)}$, due atomic interference of waves who produce the wave cancellation effect[2]. If peaks' displacement / widening effects are not uniform, these effects could be produced by anisotropic deformation's due to internal stress.

3.8   Hardness Analysis

The micro hardness technique was systematically used to try to identify the heat affected zone extension, and relationship between chemical composition, hardness and the mechanical strength of the weld bead.

3.8.1   Test P26

a) G10

Sample G10 is the tensile tested specimen with lower mechanical strength (Rp0,2%=433MPa/UTS=643MPa) from Test P26, and placed on position 111 on $UTS_{ranking}$. P26 Test was welded using fused flux F2, filler metal of 2mm of diameter, AC current and with voltage set to Low Level. Average hardness of the BS1 weld bead is around 218 HV.

When cross-sectional hardness profile through fusion lines between BF1 and its

---

[2] Http://www.upct.es/~dimgc/webjoseperez/DOCENCIA_filivos/Aplicaciones_DRX_Apuntes_y_ejercicios.pdf

neighbors was analysed, a hardening effect over 10% was observed in deepness between 0,1 to 0,3mm back of fusion lines. Stronger and deeper effect is shown with weld bead FS1, which have higher heat input, 14,36 KJ/cm, compared with BS3 (HI=8,4KJ/cm) and BS2 (HI=7,8KJ/cm).
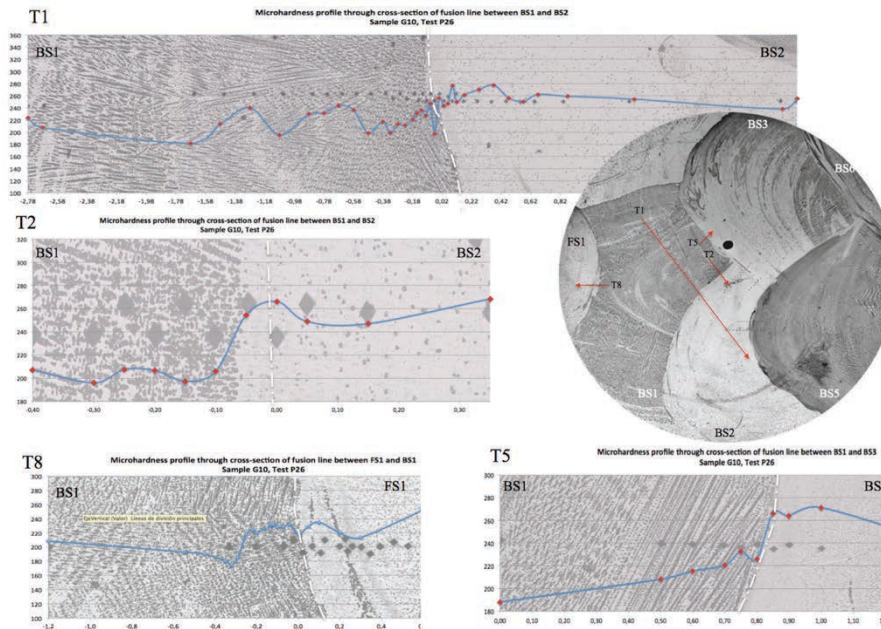
Fig 3- 22: Hardness profiles through fusion lines, Sample G10, Welding bead BS1

ANOVA statistical technique confirms that BS1's deposited weld metal show a hardened layer placed on HAZ. This layer is an averaged of 20HV harder than average hardness from the center of the bead. This hardener may be produced by the thermal cycle of the welding process. From residual plot is observed that all residual values from 28 position to 43 are negative, which could be explained because the average hardness on the bottom of the BS1 weld bead is the lowest mean of this set of data, see boxplot of hardness. Maybe, the hardness in the bottom area of BS1 being lower by local chemical composition.

One-Way ANOVA: Hardness versus Zone

Method

Null hypothesis	H₀: All means are equal
Alternative hypothesis	H₁: At least one mean is different

Equal variances were assumed for the analysis.

Factor Information

Factor	Levels	Values
Zone	2	Center ; HAZ

Analysis of Variance

Source	DF	Adj SS	Adj MS	F-Value	P-Value
Zone	1	6077,0	6076,97	22,32	<0,0001
Error	48	13069,1	272,27		
Total	49	19146,1			

Model Summary

S	R-sq	R-sq(adj)	R-sq(pred)
16,5007	31,74%	30,32%	26,49%

Means

Zone	N	Mean	StDev	95% CI
Center	33	208,657	18,009	(202,882; 214,433)
HAZ	17	231,930	12,968	(223,883; 239,977)

Pooled StDev = 16,5007

Grouping Information Using the Tukey Method and 95% Confidence

Zone	N	Mean	Grouping
HAZ	17	231,930	A
Center	33	208,657	B

Means that do not share a letter are significantly different.

Tukey Simultaneous Tests for Differences of Means

Difference of Levels	Difference of Means	SE of Difference	95% CI	T-Value	Adjusted P-Value
HAZ - Center	23,273	4,926	(13,368; 33,177)	4,72	<0,0001

Individual confidence level = 95,00%
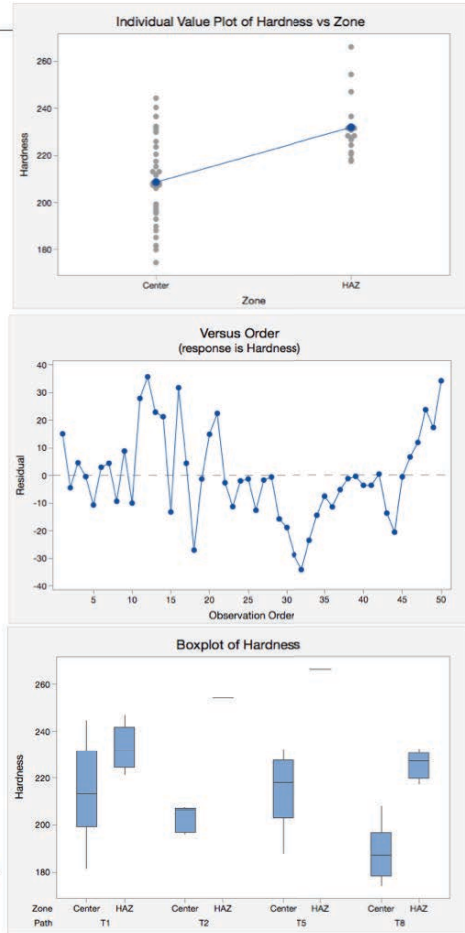
Fig 3- 23: ANOVA analysis of HAZ's hardness data, sample G10, weld bead BS1

While the hardness profiles in Heat affected zone of bead BS2 do not show any significant variation of the average 260 HV of this weld bead. This behavior had been verified through 4 different paths, T3 and T4 in HAZ with BS3 and T7 and T9 in HAZ with BS5.
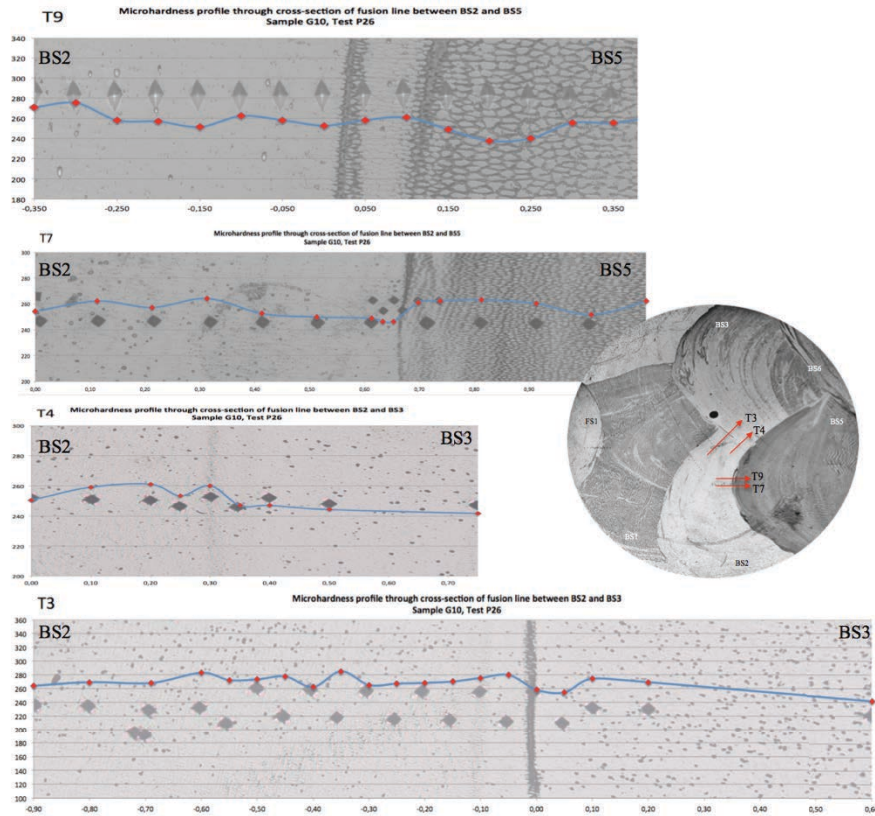
Fig 3- 24: Hardness profiles through fusion lines, Sample G10, Welding bead BS2

b) G148

Sample G148 is the stronger specimen (Rp$_{0,2\%}$=464MPa/UTS=692MPa) from Test P26. It is placed on position 24 on UTS$_{ranking}$. Its cross-sectional hardness profile through fusion line between FS2-FS3 and FS5, fig3-24, show softened area 0,3mm thick, back of fusion line. In this section, the average hardness of 295HV is reduced to 285HV, which is around of 4% of softening, verified through 5 different measurement paths through fusion line between FS2-FS3 and their neighbor FS5. In this case, both weld beads, FS3 and FS2, have been analyzed together because their chemical equivalents are close (Ni$_{eq}$=75/Cr$_{eq}$=11; Mo$_{eq}$=13). In front of fusion line, average hardness on FS5 is over 305 HV.

66
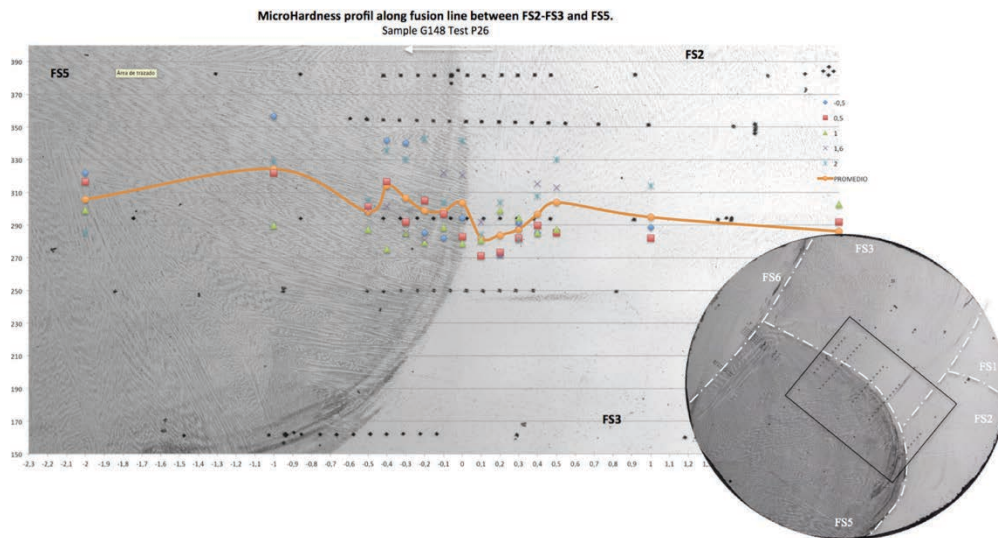
Fig 3- 25: Hardness profiles through fusion lines, Sample G148, Welding bead FS2 and FS3

When hardness profile was analyzed through cross-section of fusion line between FS5 and FS6 there are no evidence of any effect back of fusion line, on heat-affected zone.
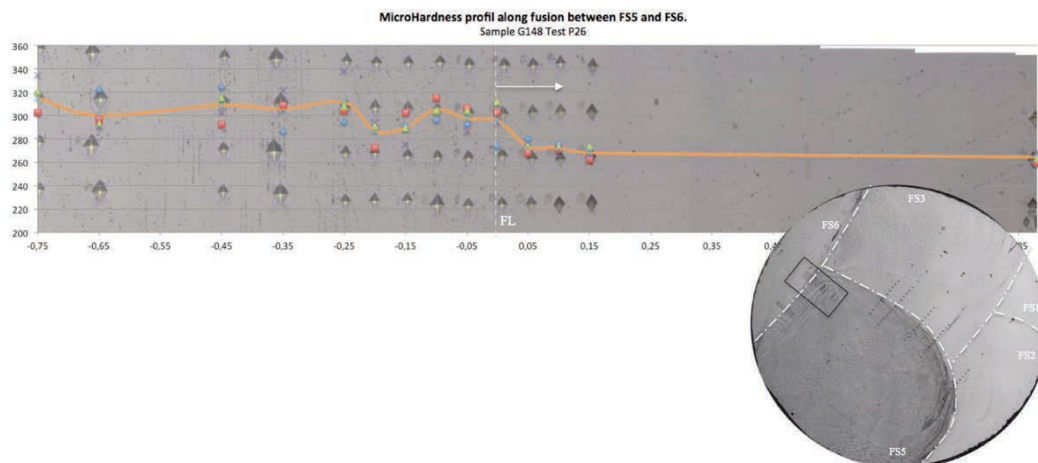
Fig 3- 26: Hardness profiles through fusion lines, Sample G148, Welding bead FS5

3.8.2 Test P09

a) Sample G81

Test P09 was the first wing plate welded using agglomerated flux F4, with the 1,6 mm wire, AC and low voltage setup. G81 is almost the stronger sample ($Rp_{0,2\%}$=461MPa/UTS=651MPa) from Test P09, being in place 94 o $UTS_{ranking}$. Its average hardness profiles have been study by 4 paths through each fusion line, as shown in Fig 3- 27.

The gotten values show that weld metal`s hardness of sample G81 seen to be not affected by thermal cycles produced by the welded passes applied on them, at least in range of welding parameters used in this trial..
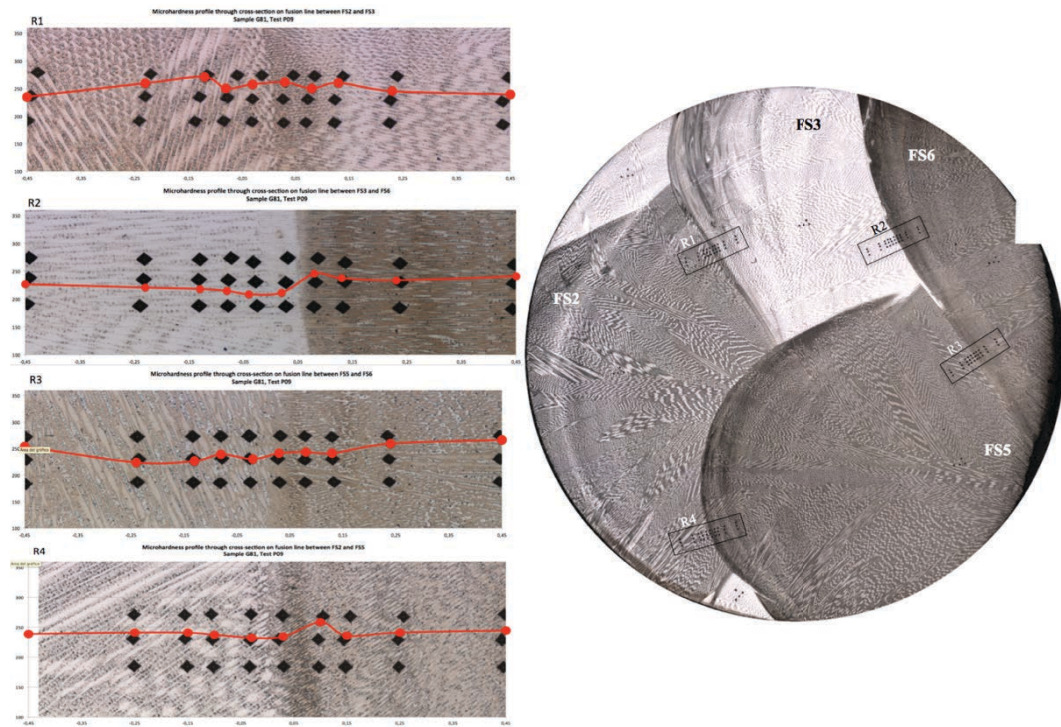
Fig 3- 27: Hardness profiles through fusion lines, Sample G81.

3.8.3   Test P31

P31 test is one of the tests with bigger mechanical strength difference between its tested tensile samples, Its samples are placed on position 8, 82, 87 and 122 on $UTS_{ranking}$, reason why this sample have been deeply study. This test has been welded using fused flux F3, filler metal of 2mm of diameter, direct current and high voltage setup.

a) Sample G19

In bottom area of some of its weld beads were observed in both, macro and micro specimens, a differentiated etched area, Fig 3- 28 A and B. This area could promote the initiation of the fracture mechanism on sample G19 or others. An area similar than this has been also observed at least on fracture surface of tensile samples G18 and G155.
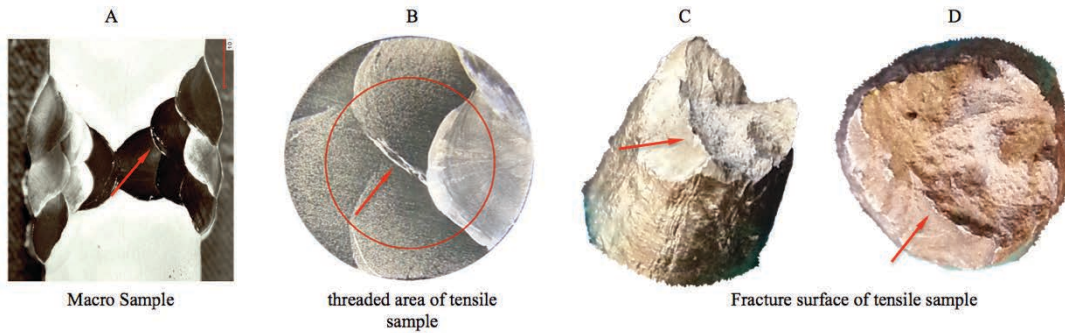
Fig 3- 28: Bottom area of weld bead observed on macro and micro etching on sample G19.

This zone is the bottom of the weld bead BS3, and corresponds to the first solidification layer from BS2. The average hardness in this zone is 255 HV, which is 13% harder than the average hardness of the weld bead BS3 and 6% harder than weld bead BS2, from which it starts its solidification. The chemical analysis showed that this area has higher nickel than its adjacent areas, which is 15% more regarding average nickel content of same BS3 weld bead and 5% more regarding BS2. As will shown later, this element distribution is produced by effect of convective circulation, known as the Marangoni effect.
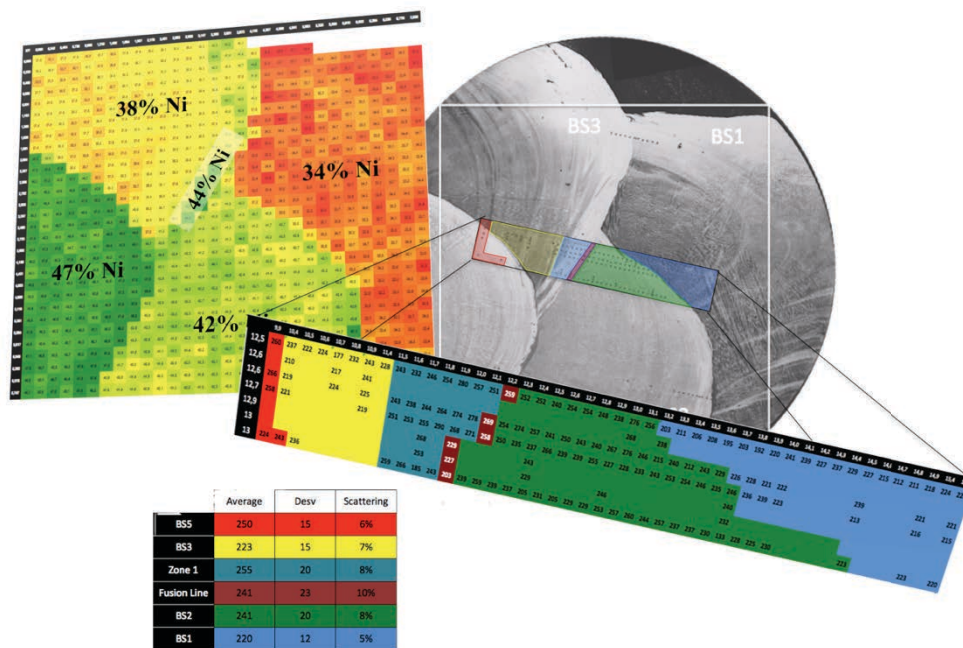
Fig 3- 29: Chemical analysis and micro hardness measurement done on bottom area of weld bead BS3.

Sample G19 was the weaker of the 4 tested samples of test P31, with $Rp_{0,2\%}$ of 408 MPa and UTS of 626 MPa. Its average Chemicals Equivalents is Ni_{eq}=76,5, Cr_{eq}=10,75

69

and Mo_{eq}=12,5, and average hardness of its 4 weld beads is 236HV. It is placed in position 122 of 124 in $UTS_{ranking}$, Then it is one of the weakest samples tested in this trial
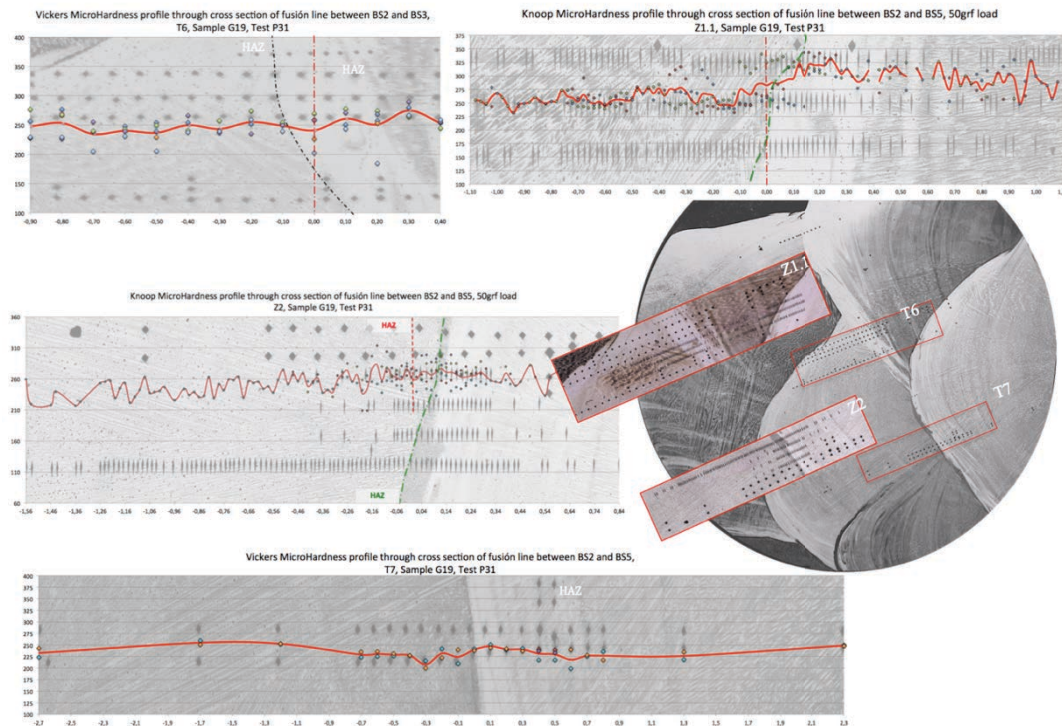
Fig 3- 30: Hardness profiles through fusion lines, Sample G19, Welding bead BS2

The heat affected area of BS2 welding bead, both in the melting zone with BS3 and BS5, doesn't show any softening or hardening caused by thermal cycle of the weld beads. In order to increase the resolution of hardness results, Knoob indentator with a load of 50 grf was used, getting up to 5 knoob hardness measurements by each Vickers measurement. Average results by lines shows greater variability, which seems to be associated with the main orientation of grain growth. But even with this scattering, a variation of the mean hardness of the analyzed area is not appreciated.

When hardness analysis is performed in BS1 weld bead through fusion lines with weld beads BS2 and BS3 a lost of hardness of around 7% is observed. In T9 sample softening was measured 0,1mm deep back from fusion line, meanwhile softening effect on T8 sample is evident up to 0,3mm deep from BS3 borderline.

Taking in account hardness values of path T8, T9 and T6, with a total of 41 values statistical analysis of variance is used to determine if observed softening effect is statistically significant. Through ANOVA technique was determined that observed softening effect of 7% is significant (p-value <0,0001 and f-value 30,27). This weld bead has a Ni_{eq} of 81%, a Cr_{eq} of 9 and 10% of Mo_{eq}.
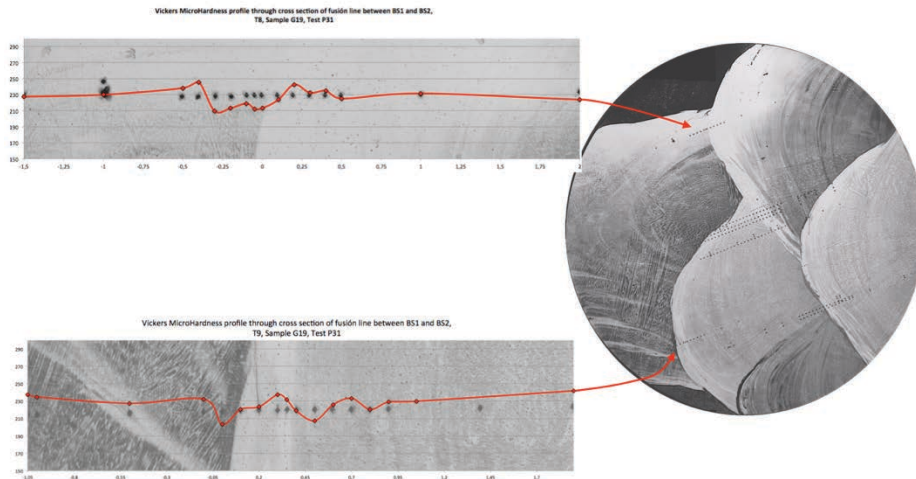
Fig 3- 31: Hardness profiles through fusion lines, Sample G19, Welding bead BS1
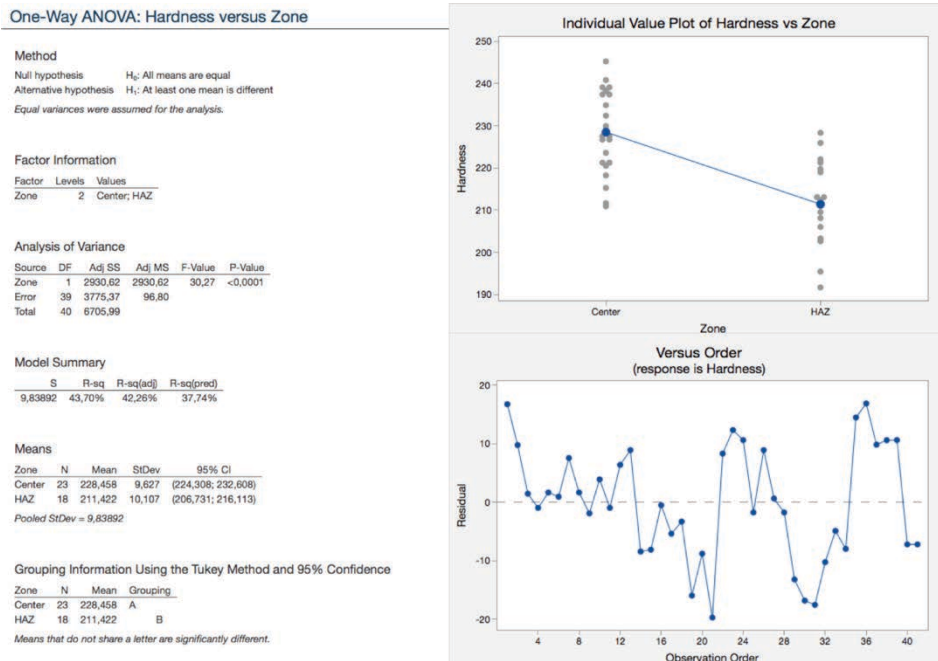
Fig 3- 32: ANOVA analysis of HAZ's hardness data, sample G19, weld bead BS1

3.8.4 Test P14

a) Sample G91

Test P14 was welded using fused type flux F2, with a wire of 1,6 mm of diameter, AC current and low voltage setup. P91 had higher tensile strength of its group, with Rp0,2%=481 MPa and UTS=724MPa, which is 9% over the average of other 3 samples of this group. It's average equivalents composition is Ni_{eq}=69, Cr_{eq}=12 and Mo_{eq}=16. This sample has been where obtained from external zone of the finishing side.

From hardness point of view P91 has an average hardness of 257 HV. FS3 and FS4 are the weld beads with lower hardness, 245HV and 244HV respectively; meanwhile the harder ones were FS2 and FS5, an average hardness of 270HV for FS2 and 275HV for FS5.
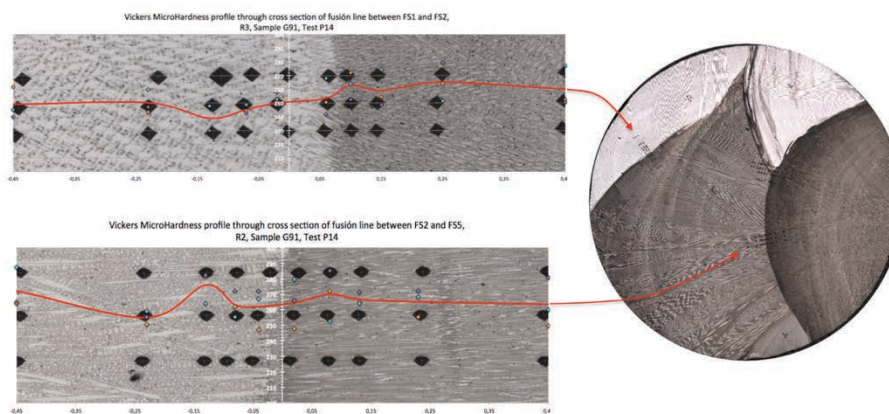
Fig 3- 33: Hardness profiles through fusion lines, Sample G91.

HAZ of FS1weld bead show a hardness reduction of 4,4% within 0,3mm deepness range, which one is not statistically significant (p-value 0,8328 and f-value 0,21). Similar case is observed on FS2's HAZ, where there are not clear effect, because mean value of 12 hardness measurements done within 0,3mm deep from fusion line is only 2% below average hardness value of the 7 measurement performed deeper. Now, taking all hardness measurements done on FS2 from path R1, R2, R3 and form C2 are gotten a total of 47 values. All these values are statistical analysis by ANOVA technique, which support that FS2's hardness is not affected by thermal effect of the weld bead FS5(p-value 0,7514 and f-value 0,01). FS2 weld bead has a Ni_{eq} of 70%, a

Cr_{eq} of 14 and 17% of Mo_{eq}.

3.8.5 Test P01

a) Sample G65

Test P01 was the first sample welded for this trial, it was welded using agglomerated flux F1, with a wire of 1,6 mm of diameter, AC current and low voltage setup.

By mistake during welding operation, FS side was welded before than BS, so actual joint sides are not equilibrated, as expected from original joint design. This mistake made that first welded side have been filled with only 4 passes, when the standard was 6 passes per side. This deviation didn't seem to be so critical; especially when in total 9 samples were welded with less than 6 passes in some of their side.

P65 had highest tensile strength of all 124 tested samples, It is placed in Position1 form $UTS_{ranking}$, with $Rp_{0,2\%}$=525 MPa and UTS=731MPa, which is 11% over the average $Rp_{0,2\%}$ and 4% over the average UTS of group. It's average equivalents composition is Ni_{eq}=69, Cr_{eq}=14 and Mo_{eq}=16. This sample has been obtained from external zone of the last welded side.
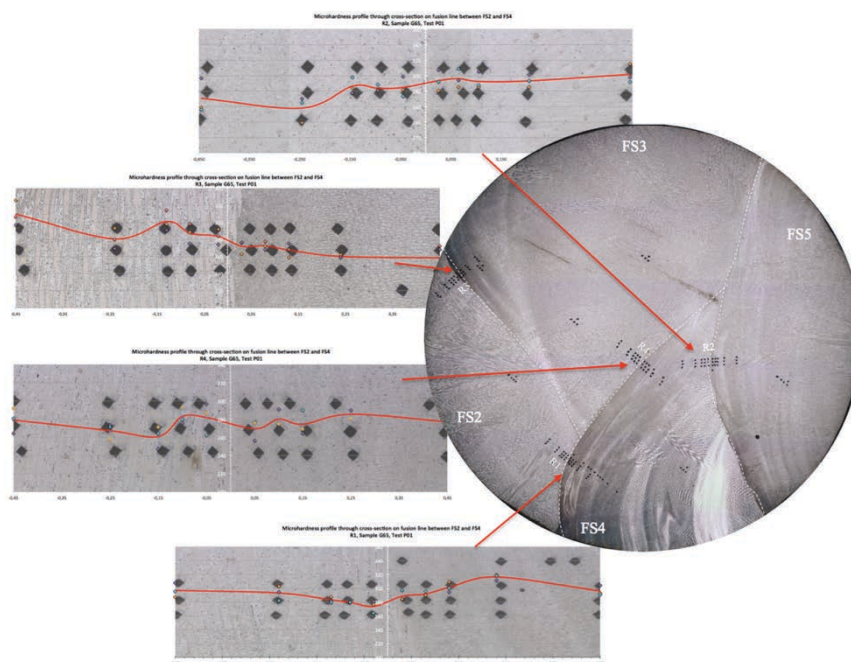
Fig 3- 34: Hardness profiles through fusion lines, Sample G65.

From hardness point of view P65 has an average hardness of 278 HV. Where FS2, FS4 and FS5 are the harder weld beads, with average values around 290HV. Lower average hardness values were around 260HV for FS3.

HAZ of weld bead FS3 show an 8% of hardening regarding the rest of measurements in bead center. This area en 0,15mm deep back from fusion line. Variance analysis applied to measured values supports that observed hardness variation is due location effect (p-value <0.0001 f-value 18,67).

In case the HAZ of weld bead FS2, two measurements path were performed, with weld beads FS4 and FS3, showing both HAZ's a softening effect of 5%, with an average deepness of 0,10mm. ANOVA analysis once again support that observed variance is due location effect with a probable error lower than 0,01%.

In case of FS4's HAZ through the statistical analysis of variance it was determined that observed hardening effect is not significant (p-value 0.9034 f-value 0.01). This weld bead has a Ni_{eq} of 71%, of which 22,25 corresponds to iron, a Cr_{eq} of 13 and 15% of Mo_{eq}. Meanwhile weld beads FS3 and FS2 have pretty similar composition with 69% of Ni_{eq}, of which 16,16 and 16,63 are from iron respectively, 15% of Cr_{eq} and 16% of Mo_{eq}.
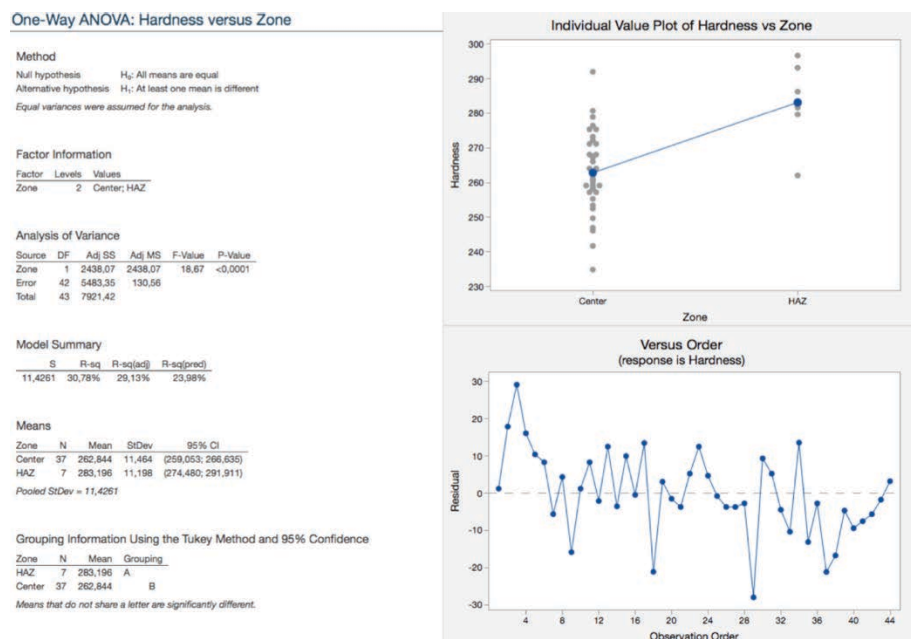
Fig 3- 35: ANOVA analysis of HAZ's hardness data, sample G65, weld bead FS3

One-Way ANOVA: Hardness versus Zone

Method

Null hypothesis	H_0: All means are equal
Alternative hypothesis	H_1: At least one mean is different

Equal variances were assumed for the analysis.

Factor Information

Factor	Levels	Values
Zone	2	center; HAZ

Analysis of Variance

Source	DF	Adj SS	Adj MS	F-Value	P-Value
Zone	1	2163,24	2163,24	19,48	<0,0001
Error	42	4664,44	111,06		
Total	43	6827,69			

Model Summary

S	R-sq	R-sq(adj)	R-sq(pred)
10,5384	31,68%	30,06%	25,33%

Means

Zone	N	Mean	StDev	95% CI
center	24	295,514	12,611	(291,173; 299,855)
HAZ	20	281,432	7,278	(276,677; 286,188)

Pooled StDev = 10,5384

Grouping Information Using the Tukey Method and 95% Confidence

Zone	N	Mean	Grouping
center	24	295,514	A
HAZ	20	281,432	B

Means that do not share a letter are significantly different.
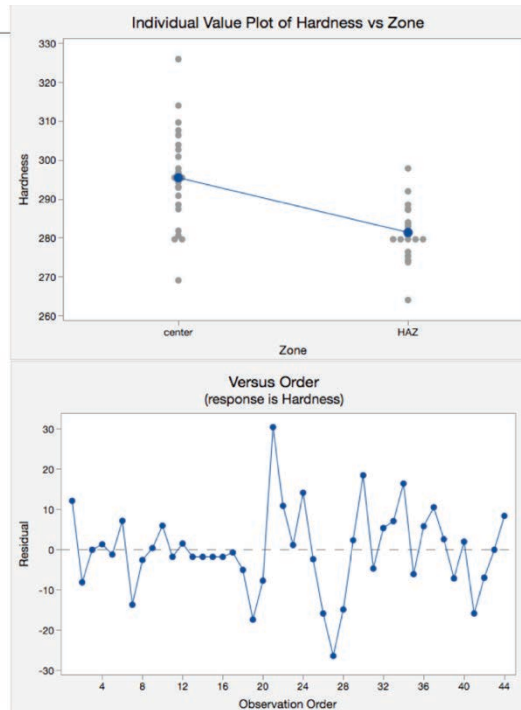
Fig 3- 36: ANOVA analysis of HAZ's hardness data, sample G65, weld bead FS2

3.9   Fractographic Analysis.

To remember, one of the motivations to do this doctoral research is to understand why cylindrical tensile test results scattering is produced.

Since the first tests carried out in 2003, welding consumables selection trials for the first LNG tank construction project, up to the last welding procedures approvals of the Norte Grande project in Chile, 2012, have been developed several test programs and welding procedures qualifications, among which more than 200 cylindrical tensions specimens of deposited weld metal have been machined and tested. Always result interpretation has been difficult due to scattering of results, so always decision-making had not been easy.

From above comments, the location where the cylindrical specimen is obtained plays a very important role in the test results, because this location defines the overall chemical composition of the cylindrical section tested and the interaction between weld beads.
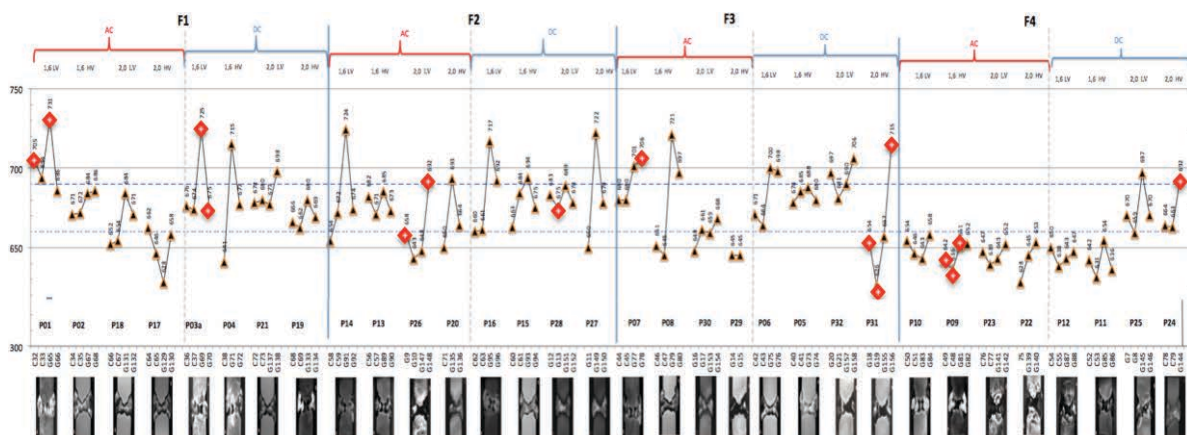
Fig 3- 37:UTS results per tensile sample, grouped by DOE variables, with reference to Test ID and Sample ID

Tensile specimens have been ranked by their UTS value and assigned its positional value, so UTSranking has been created for easy reference where the samples are located regarding its mechanical strength.

Fig 3- 36 give an idea how large is the difference between the rupture strength of the tensile samples of any of the test performed. For example test P31, where its tensile

specimens' are located in position 8, 82, 87 and 122 in UTS ranking. Or test P03a, with its UTS results placed in positions 2, 49, 50 and 53. or Test P08, with its samples set on 5, 16, 93 and 104. This level of dispersion explains why any statistical technique fails to try to found the effect of any variable regarding test strength.

Within this subchapter, the Fractographic technique is going to be used to try to identify any other feature promoting early fracture. The fracture surfaces of the strongest and weakest tensile samples will be analyzed looking for fracture patterns to explain difference strengths.

a) Sample G81
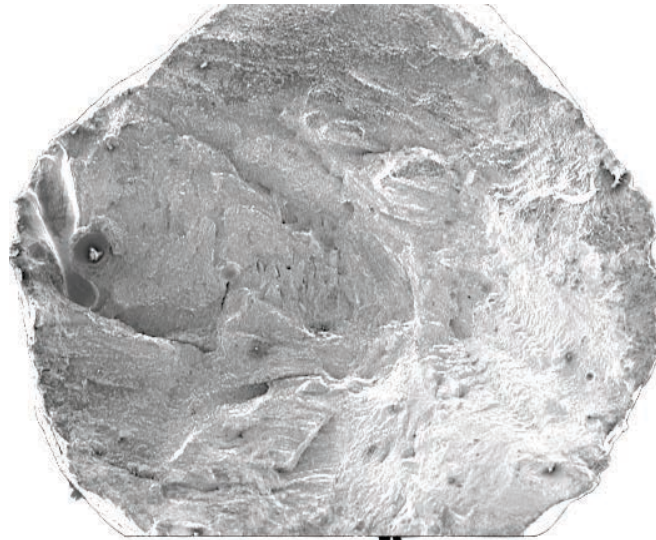
Tensile specimen G81 is located in position 94 of 124 regarding its mechanical strength, but even when it has one of the lower UTS values, it is one of the stronger of its group, where the worst ones fall down to position 112 and 117.

For this trial agglomerated flux F4 was used, welding were done by AC current, with a wire of 1,6mm of diameter and high voltage set up. Tensile specimen was mechanized from outer area of finishing side. Weld beads FS2, FS3 and FS5 form cylindrical area of tensile specimen.

%Ni	%Cr	%Mo	%Fe	%W	%Co	%V	%Ta	%Nb	%Hf	%Zr	%Ti	%Mn
46,58	12,87	11,67	24,57	2,47	0,027	0,032	0,001	0,002	0,092	0,001	0,108	1,866

	%Ni	%Cr	%Mo	%Fe	%W
FS2	46,03	12,73	11,58	25,67	2,44
FS3	42,32	11,50	10,47	32,06	2,18
FS4	43,88	11,93	10,81	29,17	2,38
FS5	48,43	13,44	12,32	21,27	2,56
FS6	48,77	13,56	12,45	20,53	2,58

Test: **P09**
DOE(variables): F4–AV-1,6mm-HV
Sample: **G81**
Tensile: RP02 461/UTS 651 MPa
UTS_Ranking: **94/124**
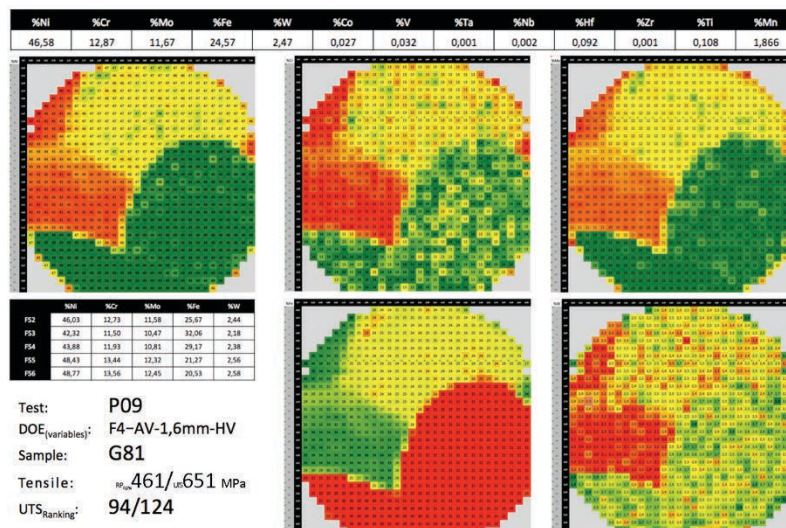
Fig 3- 38: G81 sample summary table.

Result of tensile test was 461 MPa for yield strength and 651 MPa for UTS, and as had been high-lighted above, this is one of the worst results of this trial and this is why is the first specimen to be analyzed by Fractographic technique.

To be able to relate the fracture initiation area with weld beads, an 10X10 array of XRF measurements were carried out, in a parallel plane an close to fracture surface. The XRF 10X10 results of this exploration were compared with the XRF 30X30 analysis performed on non-plastically deformed sample, thus identifying, by chemical composition, the location of weld beads at the fracture surface.

Direct identification of weld beads on fracture surface can not be done by shape-factor alone, since due to the differential mechanical resistance of each weld bead (produced by the different chemical composition), plastic deformation of each one is also different, so shape-factor between them before and after the test is different. Macroscopically this effect is evidenced by differential texturization that occurs on specimen's cylindrical section during the tensile test.
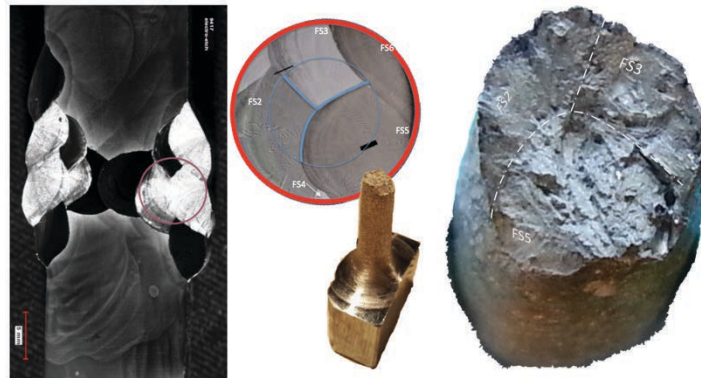
Fig 3- 39: Sample G81, Macro with weld beads distribution.

Macroscopically, 2 main areas are observed, one almost horizontal, very faceted and texturized, horseshoe shape. It is full formed from FS5 weld bead, which is the area where sample rupture was started. This area is less than a half of the cross-section sample's area. Rest of the fracture surface corresponded with shear lip, which is formed from weld beads FS2 and FS3, Fig 3- 39.
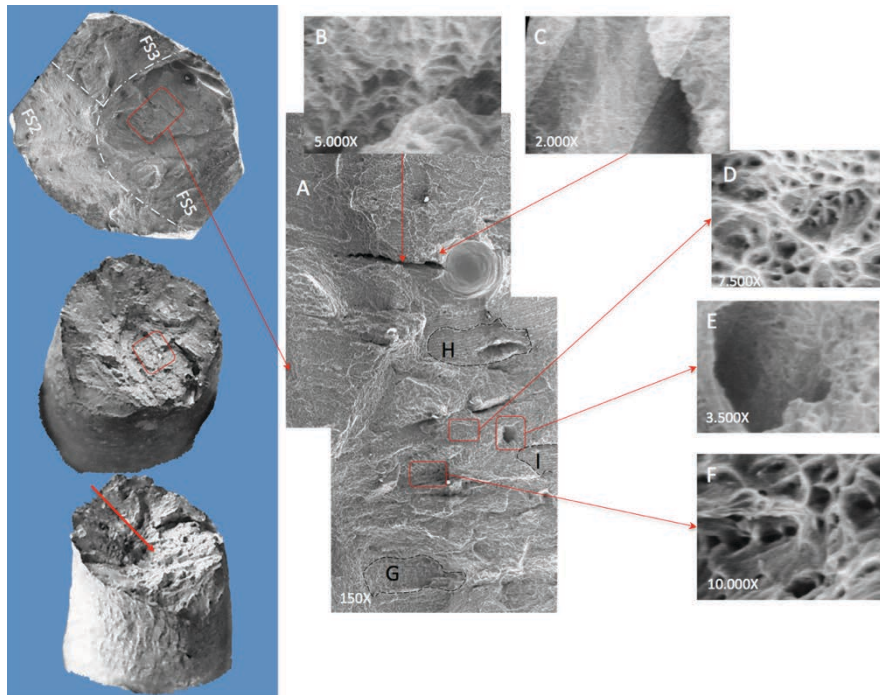
Fig 3- 40: Sample G81, Features on fracture surface 1

Using Scanning electron microscope is observed that central fracture area has a faceted texture of intergranular Quasi-clevage rupture (ASM Vol 12, p 55), see Fig 3-40A, together with open cracks and blowhole surfaces.

This decohesive rupture along grain boundary should not be a priori classified as brittle fracture because observations done at higher magnifications shown, Fig 3- 40D and F, micro-voids coalescence fracture mechanism which is a clear indication of ductile fracture pattern and also due high yield strength showed by the specimen during tensile test. Also, areas like G, H and I, shown a ductile fracture mechanism.

But of course, its poor ultimate tensile strength together with the intergranular decohesion, entrapped gases, and open cracks are clear indicators that lost mechanical strength are made by some kind of damaged produced on grain boundary (ASM Vol 12, p 51) [4-4-2].

Open cracks surfaces shown flat and smooth areas surrounded by small shear lips, which, Fig 3- 40B, C, in accordance with ASM Vol 12, page 59[4-4-2], could be produced by micro plastic tearing process that operate at micro scale. This feature is characteristic of a tentative fracture mode called tearing topography surface (TTS),

ASM 12, p 57. [4-4-2]
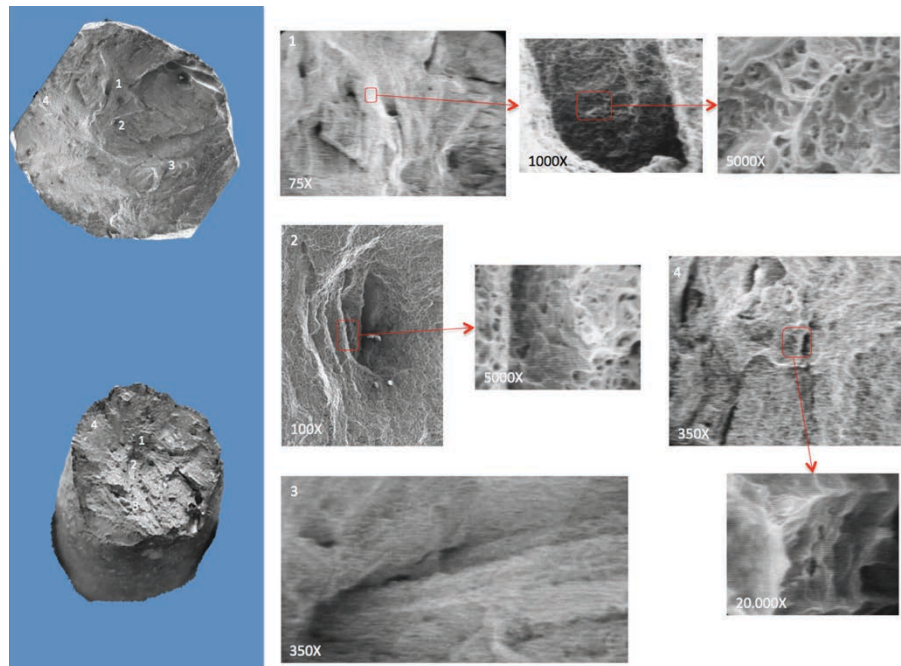
Fig 3- 41: Sample G81, Features on fracture surface 2

Not only starting fracture area is showing intergranular fracture mode. On shear lips areas where faster cracking propagation happen due overload mechanism, grain decohesion seems to be the dominant fracture mode, see Fig 3- 41, 1, 2 and 3, with a topological tears surfaces (TTS) in cracking areas.

b) Sample: C48
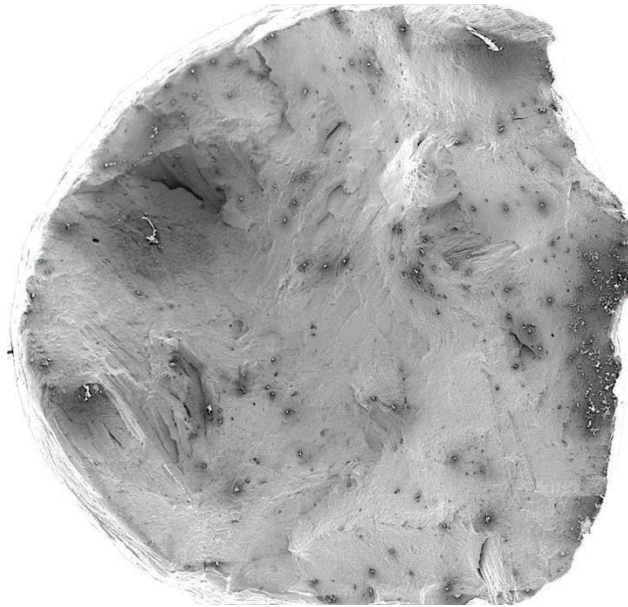
Sample C48 is the weakest specimen from test P09. It is in position 117. This cylindrical tensile sample where obtained from central area of 1st welded side, backing side, and then have more dilution with base metal, rising up its average iron content to 31%. Both yield strength and UTS down to 422/636 Fig 3- 42

Ni	Cr	Mo	Fe	W
43,8	12,5	10,9	31,2	2,2

Test: P09
DOE(variables): F4-AV-1,6mm-HV
Sample: C48
Tensile: $R_{p0,2\%}$ 422 /UTS 636 MPa
UTS Ranking: 117/124
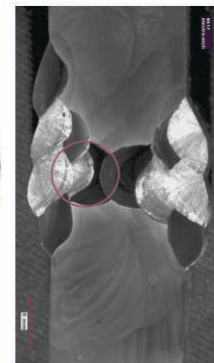
Fig 3- 42: C48 sample summary table.

Low magnification scanning electron microscopy images show more texturization than G81, produced, again, by decohesion of grains. At high magnification quasi-cleavage with MVC(Micro Voids Coalescence) mode is shown, and an important amount of open cracks are on fracture surface. Fig 3- 43.
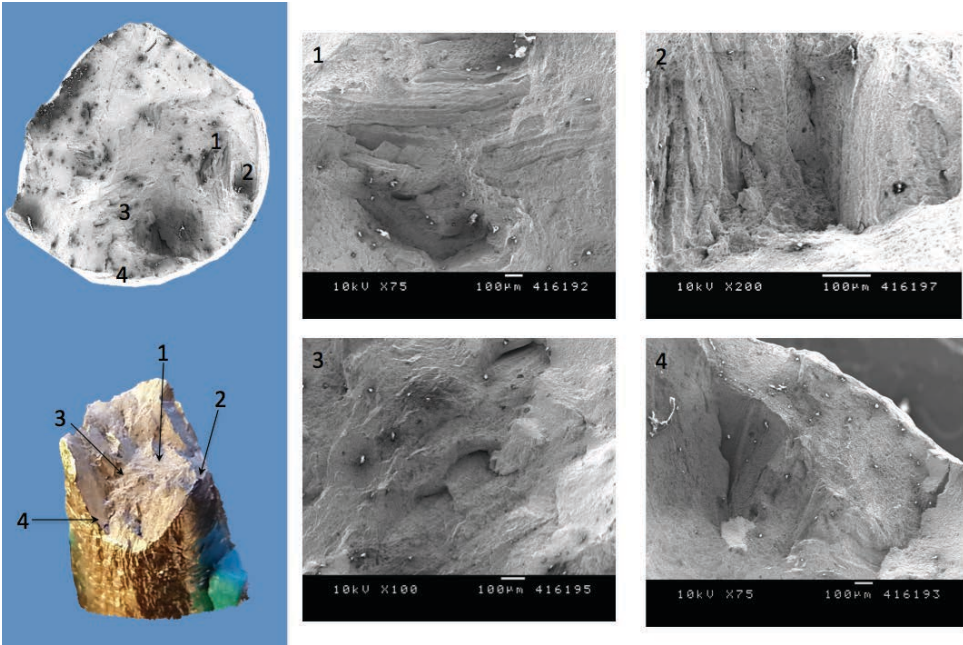
Fig 3- 43: Sample C48, Features on fracture surface

3.9.1.b.1 Sample C49
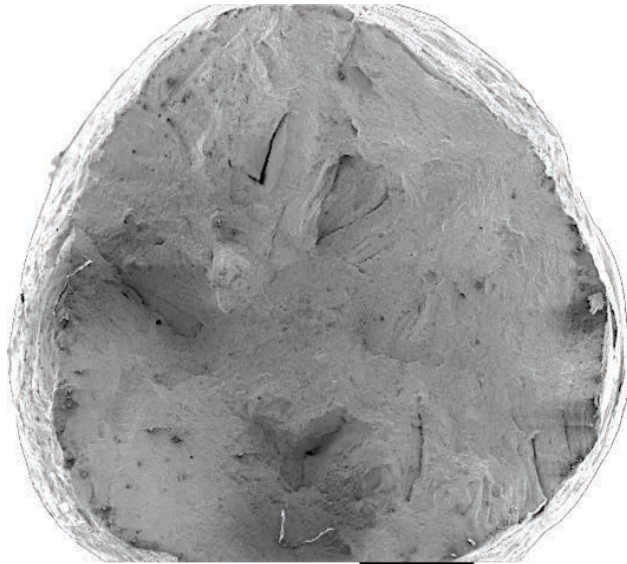
Sample C49 is in position 112 with the elastic limit at 642 MPa and fracture resistance of 642 MPa

This cylindrical tensile sample where obtained from same place than C48, with almost same dilution, 28% of iron.

Ni	Cr	Mo	Fe	W
45,3	13,2	11,3	28,0	2,3

Test: P09
DOE$_{(variables)}$: F4-AV-1,6mm-HV
Sample: C49
Tensile: $Rp_{0,2\%}$ 427 / $_{UTS}$ 642 MPa
UTS$_{Ranking}$: 112/124
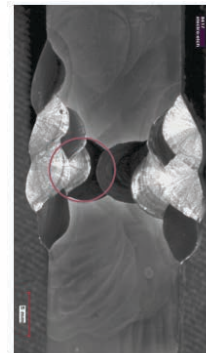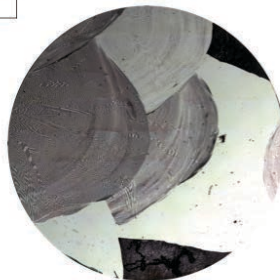
Fig 3- 44: C49 sample summary table.

Low magnification scanning electron microscopy images show similar texturization than 48, maybe with bigger perpendicular cracks. Fig 3- 45.

At higher magnification it see that these perpendicular cracks have flatter tears marks than G81. Rest of the surface are show quasi-cleavage with MVC(Micro Voids Coalescence) mode is shown like the other samples.
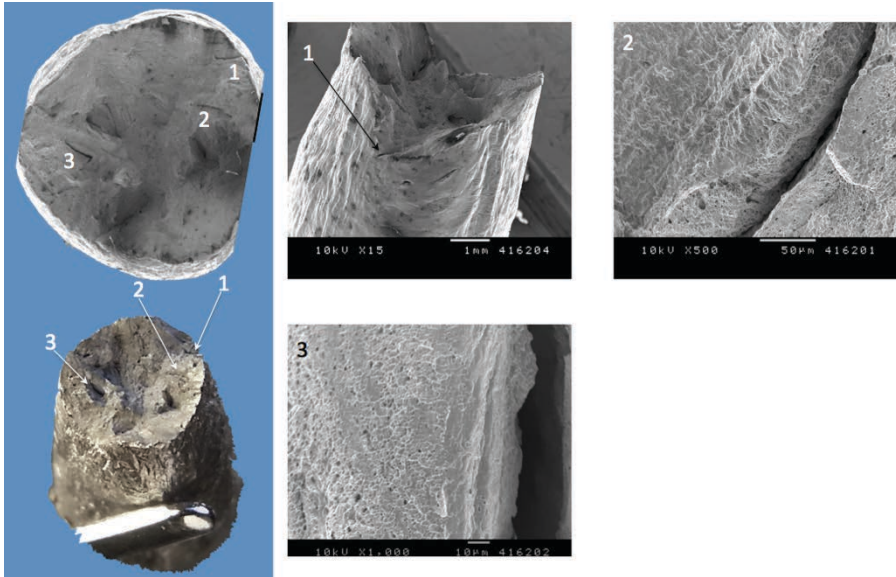
Fig 3- 45: Sample C49, Features on fracture surface

3.9.2 Test P26

Test P26 sample plate were welded using fused flux F2, AC current, 2,0mm wire and with low voltage setup. Its 4 tensile sample are placed in positions 111, 98, 81 and 24 on UTS ranking, giving a clear indication that there are some hidden variable which are producing better or worst results in sample tested weld metal. Fig 3- 46

a) Sample G09
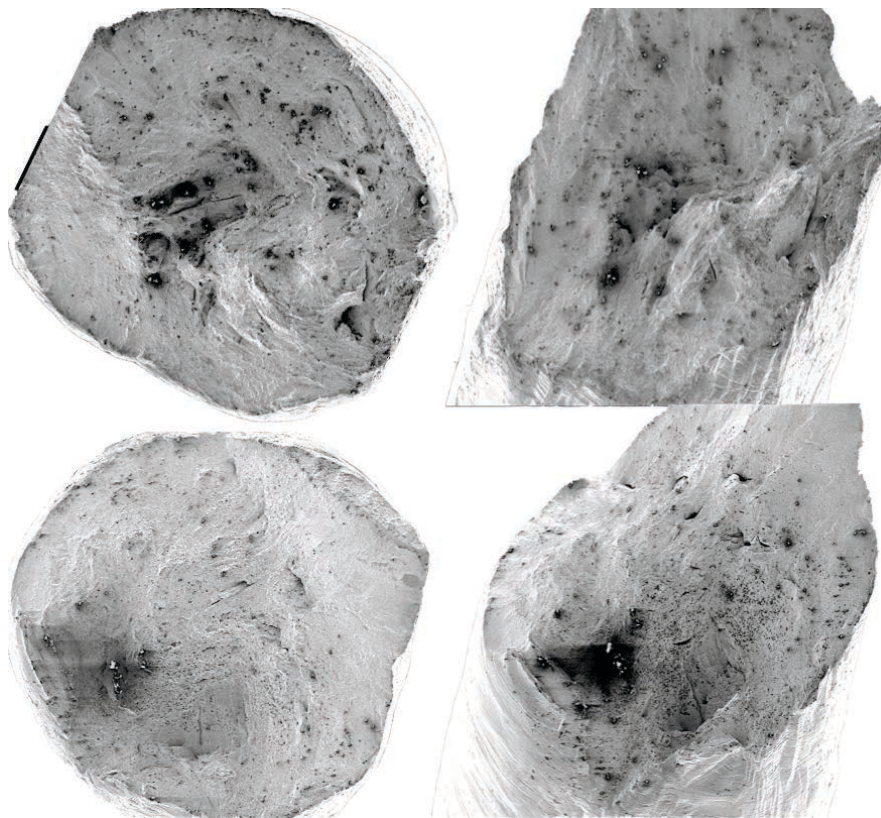
Ni	Cr	Mo	Fe	W
40,4	11,2	10,4	36,0	2,1

Test: P26
DOE$_{(variables)}$: F2-AV-2,0mm-LV
Sample: G09
Tensile: Rp$_{0,2\%}$432 /$_{UTS}$ 658 MPa
UTS$_{Ranking}$: 81/124
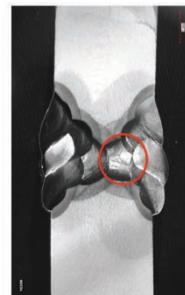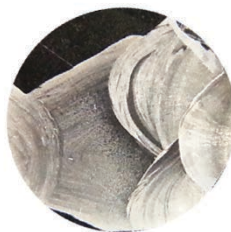
Fig 3- 46: G09 sample summary table.

It is the second sample in accordance with its mechanical strength, but is placed in weak samples side. This tensile specimen had been obtained from central area of first

86

side welded. Weld beads BS1, BS2 and BS3 form it mainly, with an average iron content of 36%.

Low magnification images show an intergranular fracture mode, with an important amount of open cracks on fracture surface, as shown on figures Fig 3- 47 to Fig 3- 48. At higher magnification is observed that main of the cracks located in shear lips area, see Fig 3- 49 1 and 2, seems to be produced during specimen rupture.

Meanwhile, equiaxed dimples produced by uniaxial load form almost all shear lip surface and parabolic dimples produced by shear when grain are separated between them by decohesion, see Fig 3- 50.
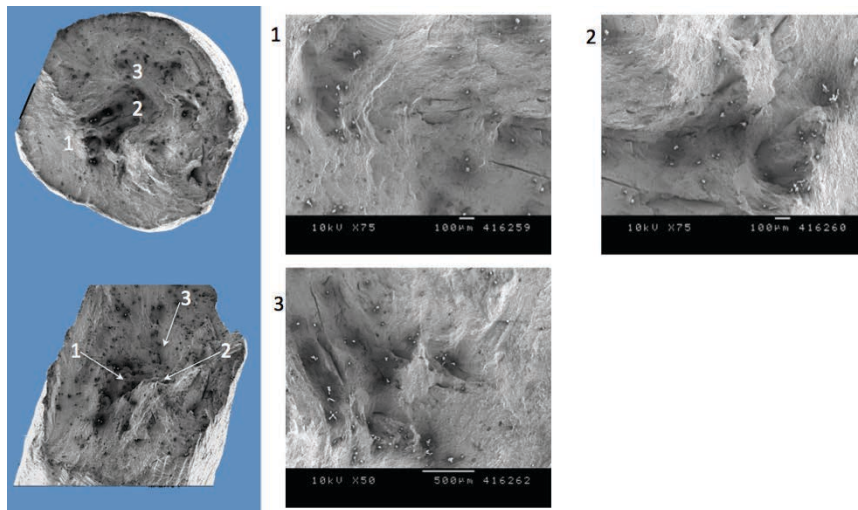
Fig 3- 47: Sample G09, Features on fracture surface 1
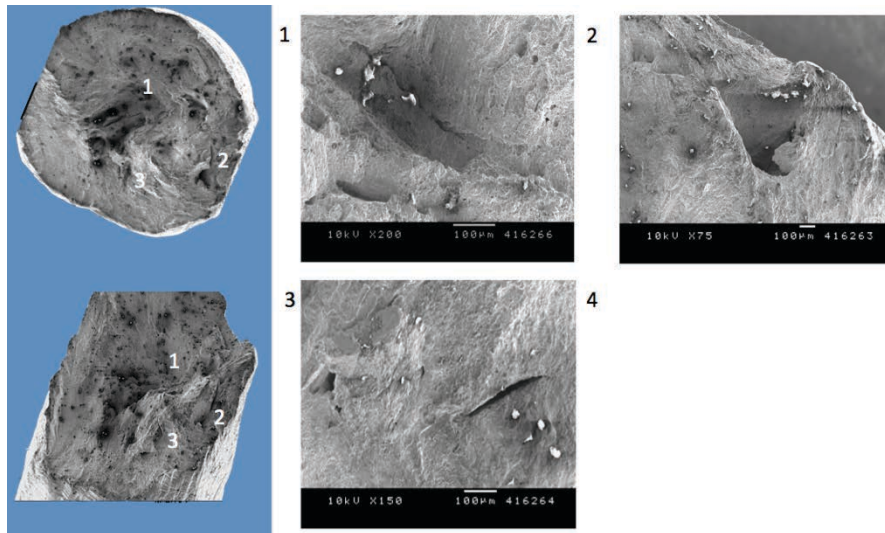
Fig 3- 48: Sample G09, Features on fracture surface 2

Fig 3- 49: Sample G09, Features on fracture surface 3
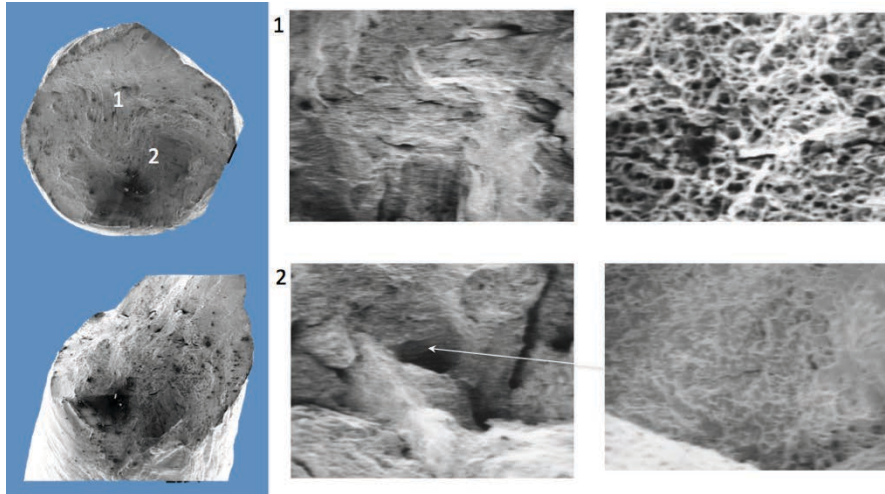
Fig 3- 50: Sample G09, Features on fracture surface 4

b) Sample G10

Sample G10 is the weakest specimen of the group and it is located in position 111 of the UTS ranking, with and yield strength of 433 MPa, and 643 MPa of ultimate tensile strength, Fig 3- 51. It has almost same content of iron than G09 and was obtained from same location than G09 too.

Ni	Cr	Mo	Fe	W
39,7	10,9	10,1	37,3	2,1

Test: P26
DOE$_{(variables)}$: F2-AV-2,0mm-LV
Sample: G10
Tensile: Rp$_{0,2\%}$433 /UTS 643 MPa
UTS$_{Ranking}$: 111/124
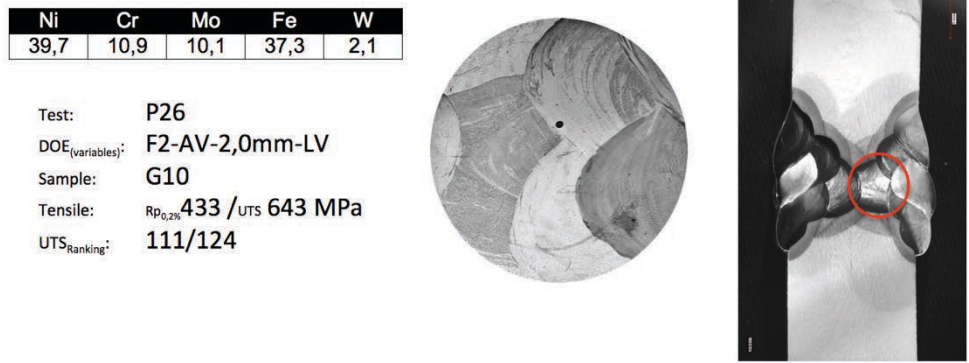
Fig 3- 51: G10 sample summary table.

From macroscopic point of view, fracture has two main areas, first one is almost perpendicular to sample axis, with less than 20% of perpendicular circular area. Second fracture surface is developed mainly at 45º.

On this fracture surface at 45º, grains decohesion is not so evident than in other samples, but still happen as shown Fig 3- 52, 1.
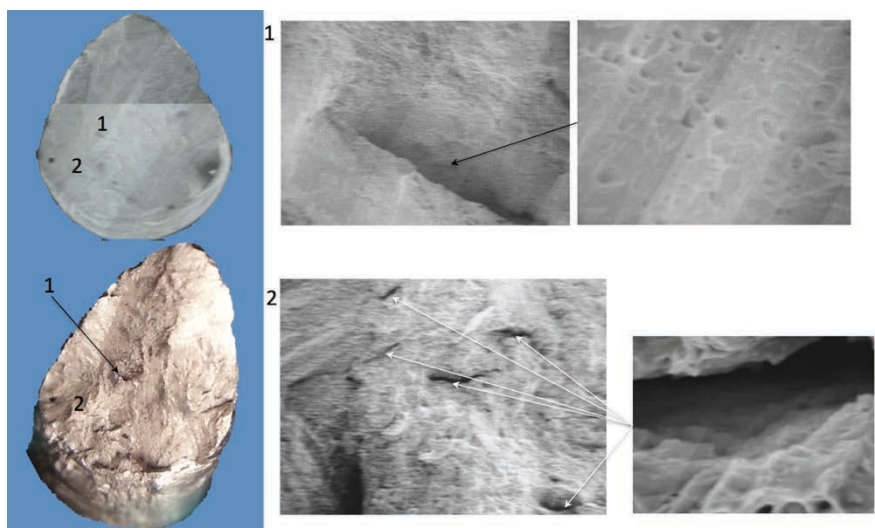
Fig 3- 52: Sample G10, Features on fracture surface 1

90

Open cracks on this surface are showing a flatter profile, Fig 3- 52, 2, Indicating that these cracks already existed in the weld metal, and being produced by mechanisms other than the MVC.

On first area, intergranular fracture mode is again evident, Fig 3- 52 and Fig 3- 53, with grain decohesion by MVC ductile mode. Showing equiaxed (1) and parabolic dimples (2). In (2) the development of a grain boundary is also observed.
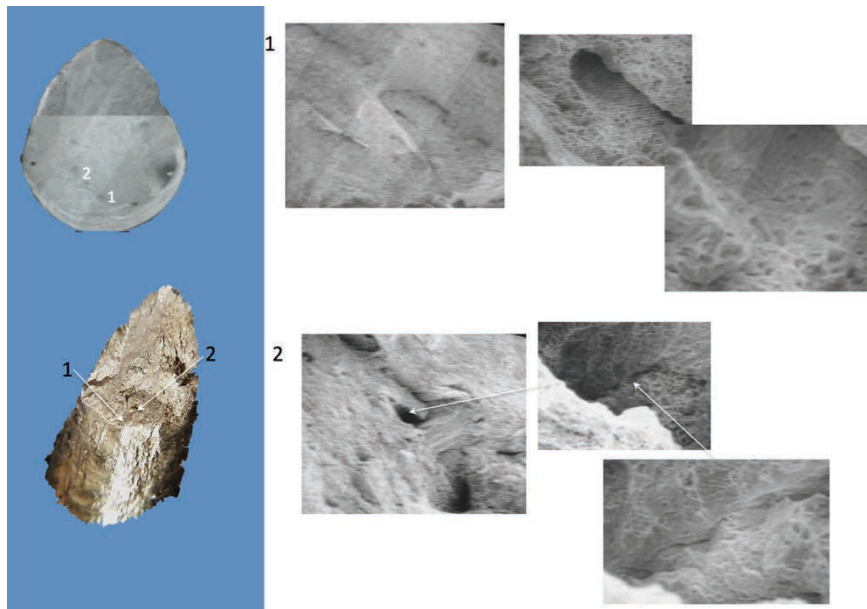
Fig 3- 53: Sample G10, Features on fracture surface 2

Same grain boundary is also in Fig 3- 54, where is showing, A and B, evidence of debonding [4-4-3] along precipitates particles during solidification or along cavities produced by Ductility Dip Cracking phenomena, which have been observed on polished samples for micro analysis, in Fig 3- 55 is shown an example of 1st steps of DDC cavities observed on polished and un etched G148 sample, where the cavities are up to 10microns length and have been nucleated on precipitates who are pinning GB displacement.
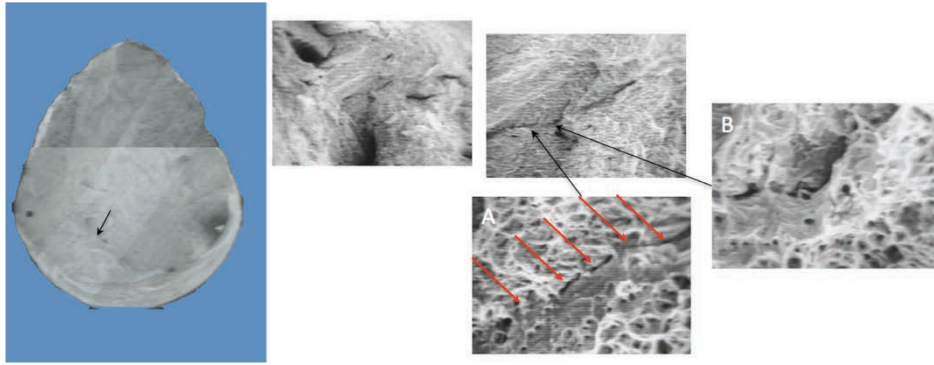
Fig 3- 54: Sample G10, Features on fracture surface 3
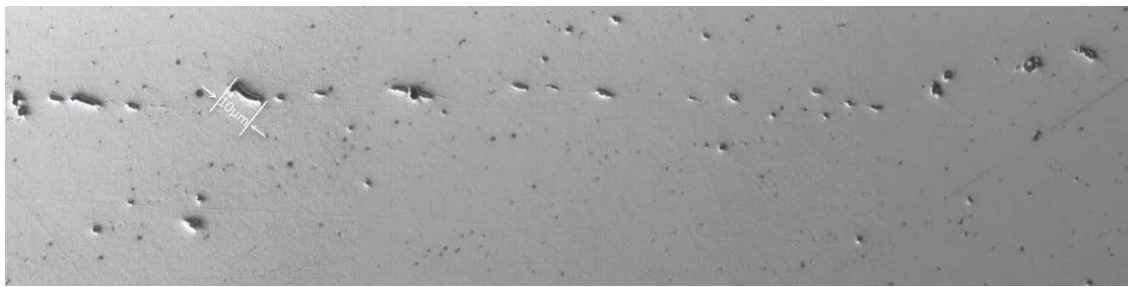
Fig 3- 55: Alignment of cavities observed on G148 sample, which is the 1st step of Ductility Dip Cracking
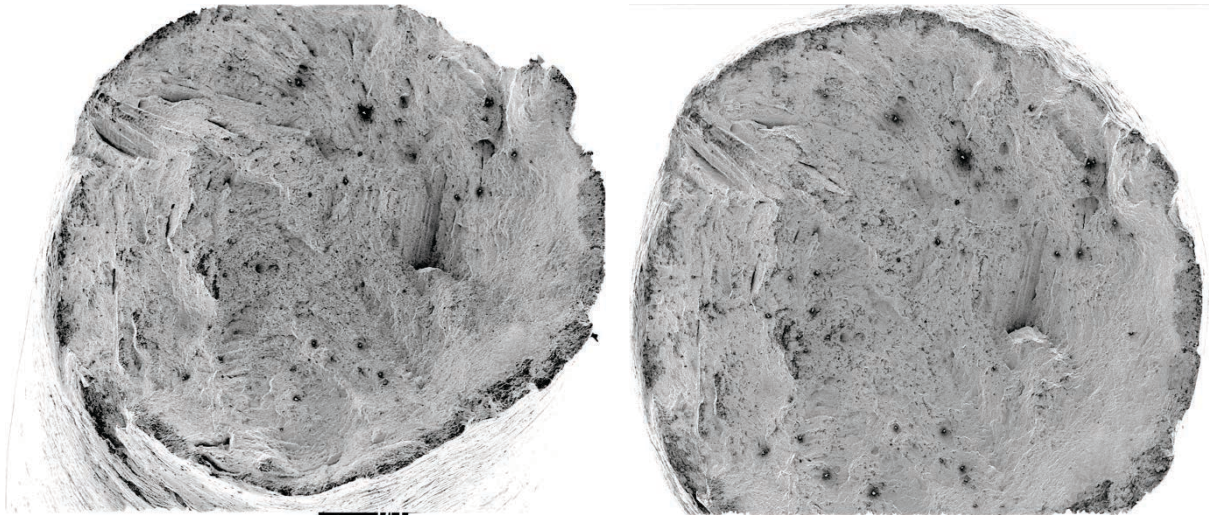
Sample G147 is the couple specimen of G148; both specimens tested In Barcelona on January 2016. Due limited remaining material, both tensile samples were machined in parallel from the piece of plate. Then G147 was obtained from external zone of backing side and G148 was machined from external zone of finishing side.

Even when both samples were machined from the same piece of plate, and welded with same conditions its UTS are 48MPa difference, which represent a 6,6% of deviation between their average value. That's mean that sample G147 is in position 98 meanwhile G148 is in position 24 in UTS ranking. But now, from point of view of the Yield strength the strength of these samples are very close 467 versus 464, which represents a deviation of only 0,6%.

Ni	Cr	Mo	Fe	W
46,7	13,2	12,5	25,2	2,5

Test: P26
DOE(variables): F2-AV-2,0mm-LV
Sample: G147
Tensile: Rp0,2% 467 /UTS 648 MPa
UTS Ranking: 98/124
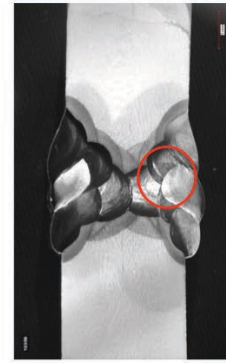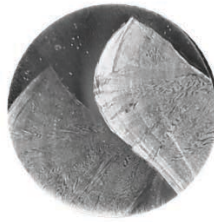
Fig 3- 56: G147 sample summary table.

Other couples of samples only have a difference of 0,2% between their elastic limit and 2,3% of their UTS. Actually, the tensile strength of sample G147 is in the same range of strength shown by samples G09 and G10, but its yield strength is paired with the strength shown by G148.
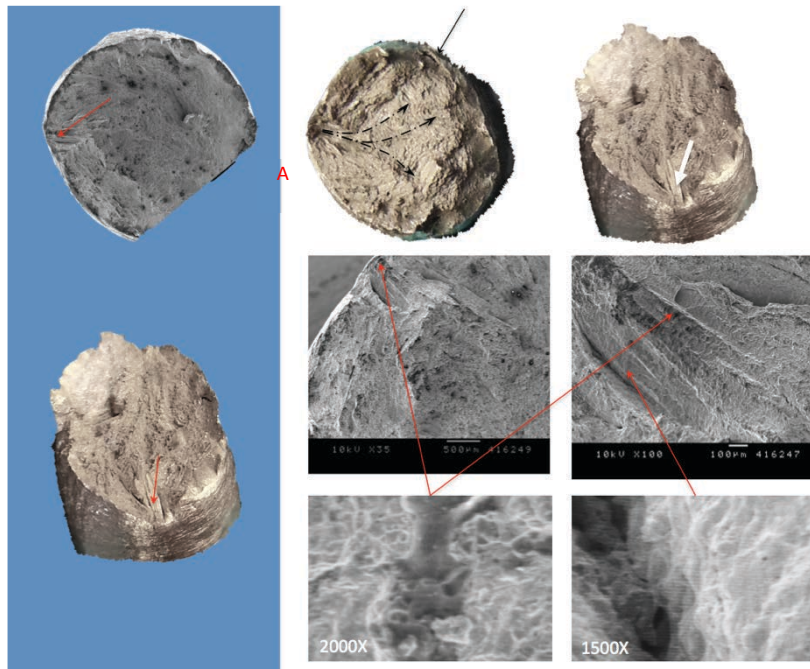
Fig 3- 57: Sample G147, Features on fracture surface 1

From macroscopic point of view sample G147 show textured surface, with open crack naked eyes visible. Chevron marks indicate that fracture started at "A", where is see a straight lines surrounded by open and also strait cracks. SEM images show a quasi-cleavage fracture surface with evidence of brittle pattern.

Other feature of this sample was the presence of "Hook Cracks" [2-6][2-12][2-13] on

94

cylindrical surface. Which ones are associated with internal defects as micro cracks or brittle areas, which ones are opening during tensile test.
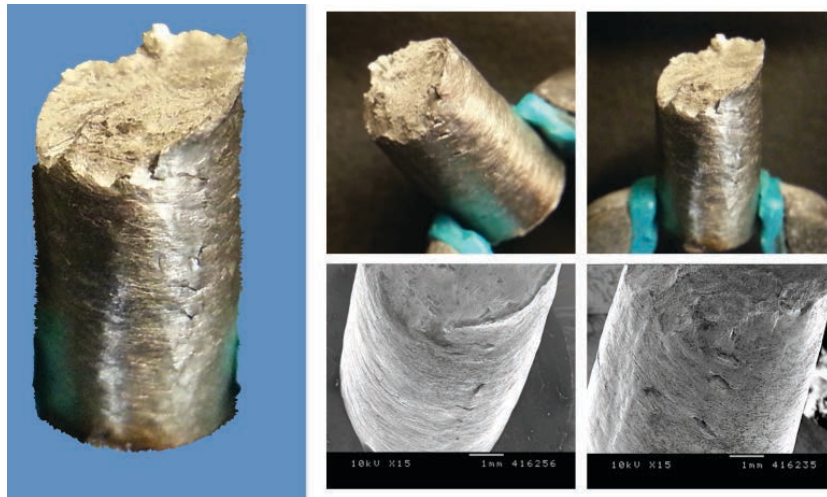
Fig 3- 58: Sample G147, Features on cylindrical specimen surface
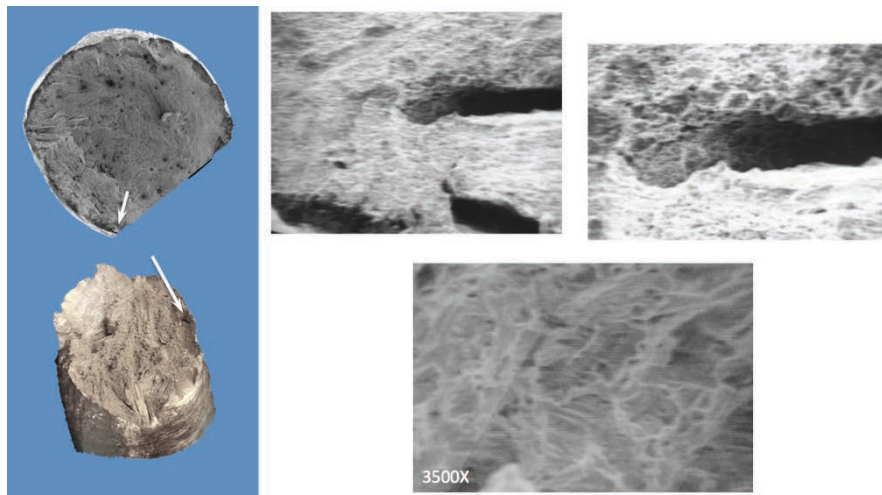
Fig 3- 59: Sample G147, Features on fracture surface 2

Rest of fracture surface are showing same features than other samples; intergranular fracture by grain decohesion showing ductile fracture mode by micro voids coalescence, as shown in Fig 3- 60 and Fig 3- 61.
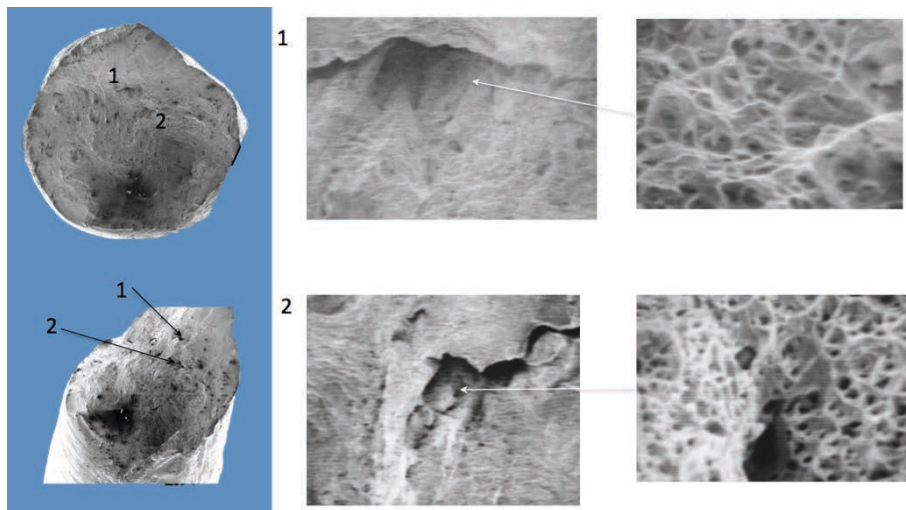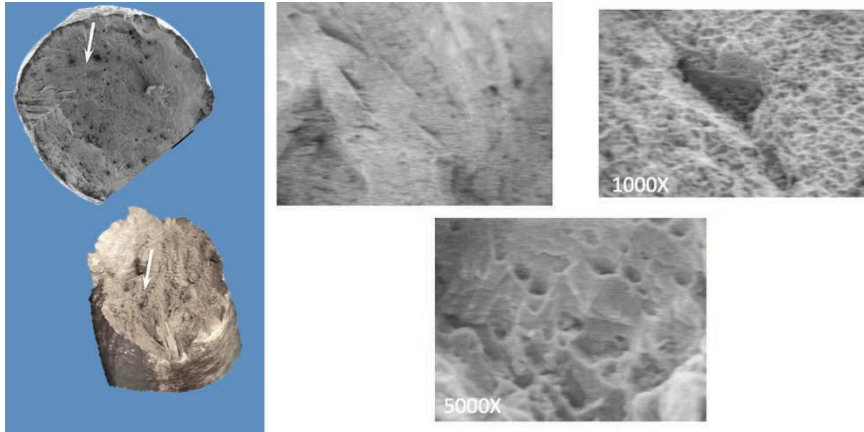
Fig 3- 60: Sample G147, Features on fracture surface 3
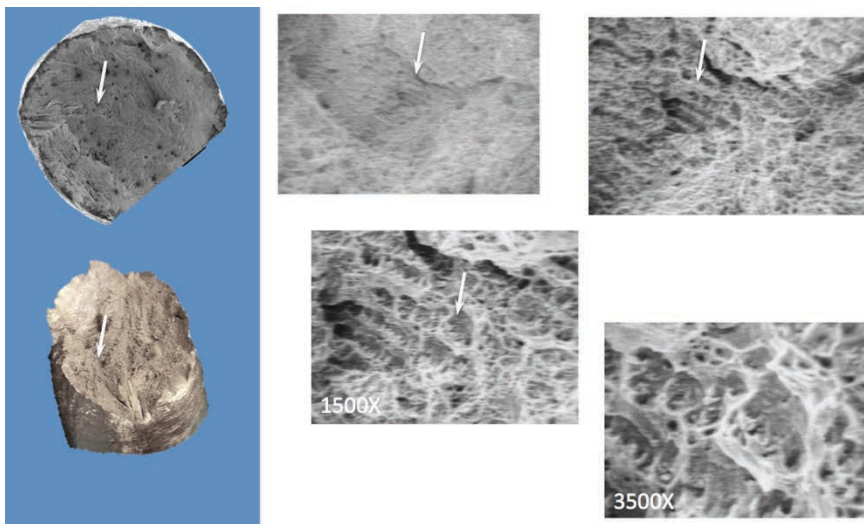
Fig 3- 61: Sample G10, Features on fracture surface 4
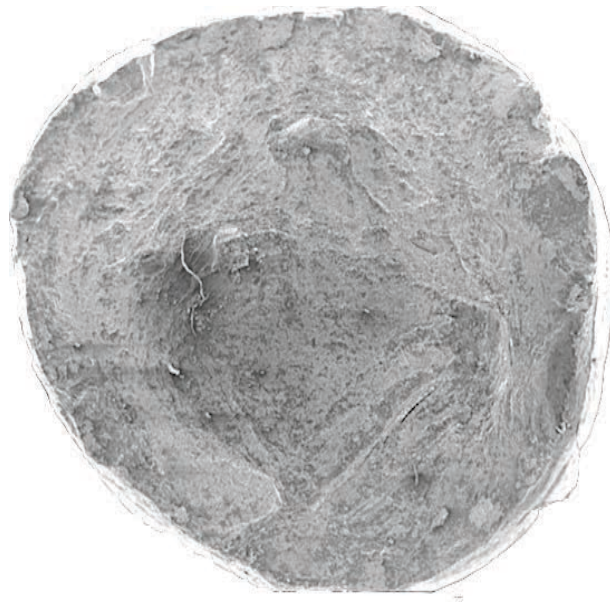
Sample G148 is the stronger sample of its group, and also is placed within of 25% of the best results of this trial, it been located on position 24 of UTS ranking, Fig 3- 62.

This sample was machined from external area of first welded side, having an average iron content of 30%.

%Ni	%Cr	%Mo	%Fe	%W	%Co	%V	%Ta	%Nb	%Hf	%Zr	%Ti	%Mn
42,94	11,56	11,90	30,51	2,43	0,078	0,124	0,003	0,021	0,101	0,003	0,094	0,423

	%Ni	%Cr	%Mo	%Fe	%W
BS1	34,20	8,89	8,42	46,36	1,67
BS2	40,39	10,90	10,51	35,58	2,14
BS3	42,19	11,55	11,10	32,37	2,27
BS5	46,18	12,72	12,40	25,64	2,54
BS6	42,31	11,52	11,18	32,10	2,29

Test: P26
DOE(variables): F2-AV-2,0mm-LV
Sample: G148
Tensile: $R_{p0,2\%}$ 464 / UTS 692 MPa
UTS(Ranking): 24/124
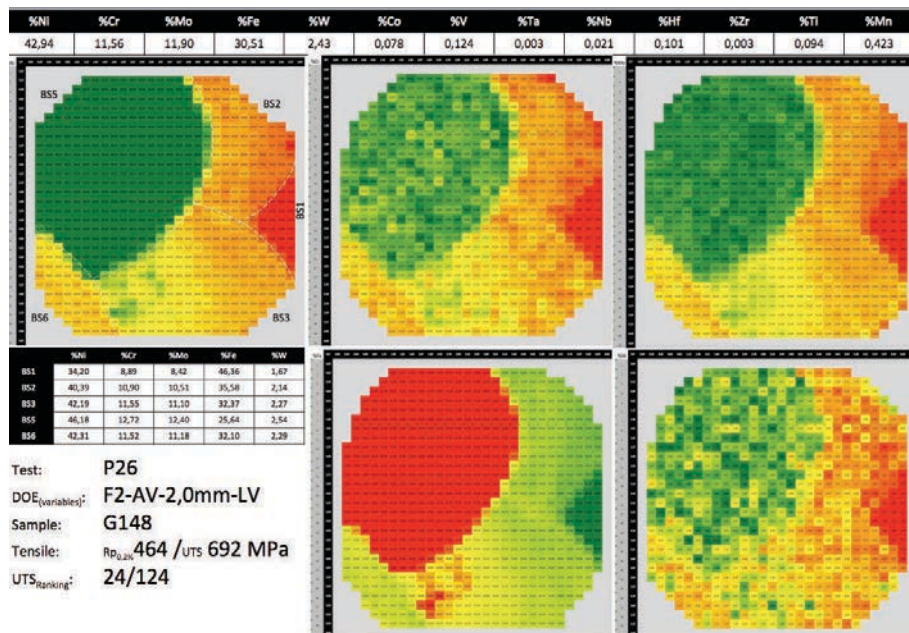
Fig 3- 62: G148 sample summary table.
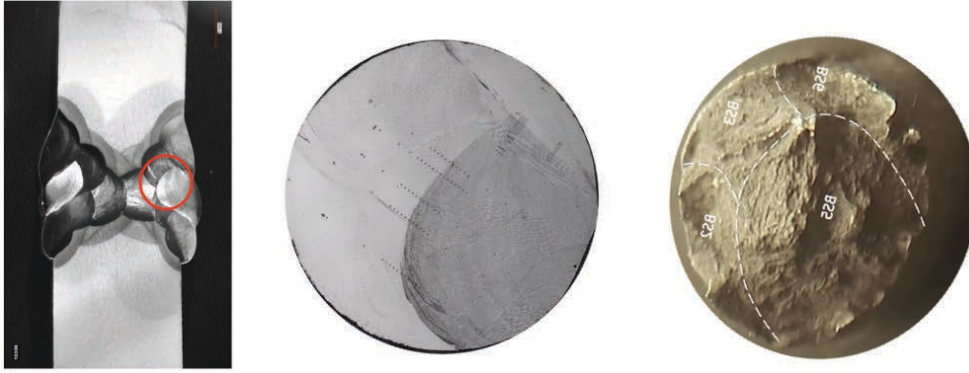
Weld beads BS1, BS2, BS3, BS5 and BS6 are forming the cylindrical area of the tensile sample, but only the first 4 beads had been identified close to the broken surface, see Fig 3- 63.

From a macroscopic point of view, the fracture is initiated within BS5, but just in borderline with weld beads BS3 and BS6, point identifies as "A". see Fig 3- 64. In the upper area of fractography, two long and straight beam are seen which are surrounded by open cracks (1). This structure could be associated with a long grain (1) observed within BS5, which develop parallel to the BS6 borderline.

Fracture initiation point also could associate with the small enriched (with higher nickel, Chromium, molybdenum) area of BS3, see Fig 3- 62, which could act like a stress concentrator.

From a Microscopic point of view, fracture surface keeps it intergranular fracture mode, with ductile grain decohesion.
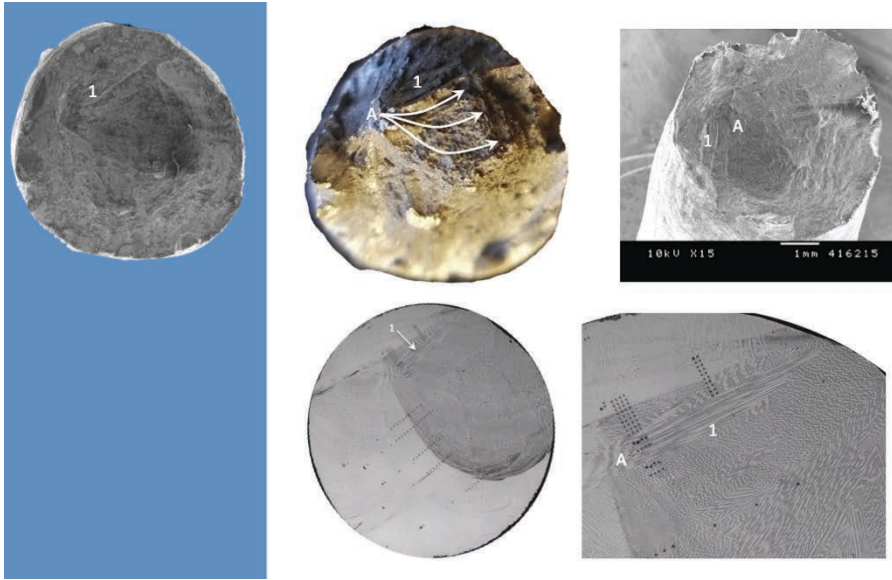
Fig 3- 64: Sample G148, Features on fracture surface.

3.9.3 Test P07

a) Sample G78
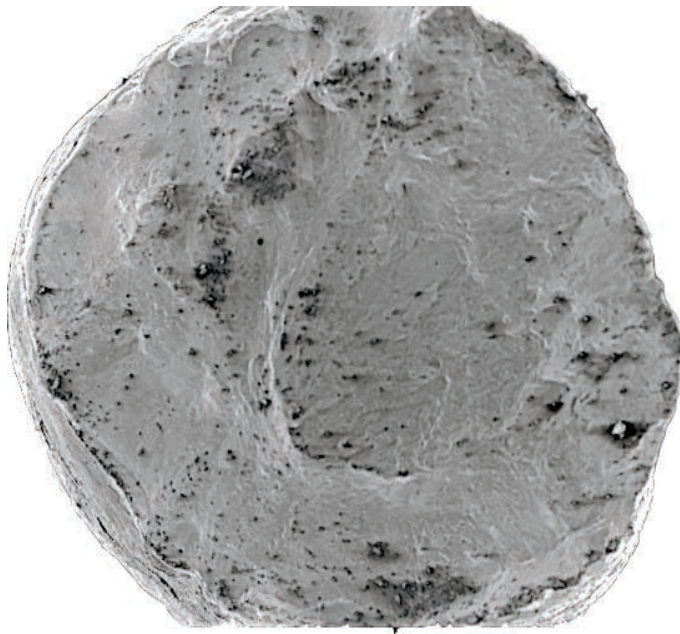
Test plate P09 were welded with thinner wire, low voltage set up, alternating current and the other fused flux, F3. Its 4 tensile specimens show high UTS, both broken in LECO had UTS of 680MPa and those broken in Barcelona had 701 and 706 MPa. Last ones placed on position 12 and 9 in UTS ranking, Fig 3- 65.

Test:	P07					Test:	P07					Test:	P07				
DOE(variables):	F3-AV-1,6mm-LV					DOE(variables):	F3-AV-1,6mm-LV					DOE(variables):	F3-AV-1,6mm-LV				
Sample:	C44					Sample:	C45					Sample:	G77				
Tensile:	$Rp_{0.2\%}$445 /$_{UTS}$ 680 MPa					Tensile:	$Rp_{0.2\%}$439 /$_{UTS}$ 680 MPa					Tensile:	$Rp_{0.2\%}$493 /$_{UTS}$ 701 MPa				
UTS(Ranking):	39/124					UTS(Ranking):	40/124					UTS(Ranking):	12/124				
Ni	Cr	Mo	Fe	W		Ni	Cr	Mo	Fe	W		Ni	Cr	Mo	Fe	W	
46,3	12,6	11,6	27,2	2,4		44,8	12,2	11,3	29,4	2,3		46,6	12,9	11,7	26,3	2,4	

Fig 3- 65: P07 Test summary table.

Even when those specimens tested in LECO where machined from the center on the plate and those test in Barcelona were taken form the external areas, their iron pick up is between 25 and 30%.

%Ni	%Cr	%Mo	%Fe	%W	%Co	%V	%Ta	%Nb	%Hf	%Zr	%Ti	%Mn
47,31	12,73	11,75	25,27	2,53	0,025	0,039	0,003	0,001	0,105	0,002	0,130	0,401

Test: P07
DOE(variables): F3-AV-1,6mm-LV
Sample: G78
Tensile: Rp0,2% 481 /UTS 706 MPa
UTSRanking: 9/124
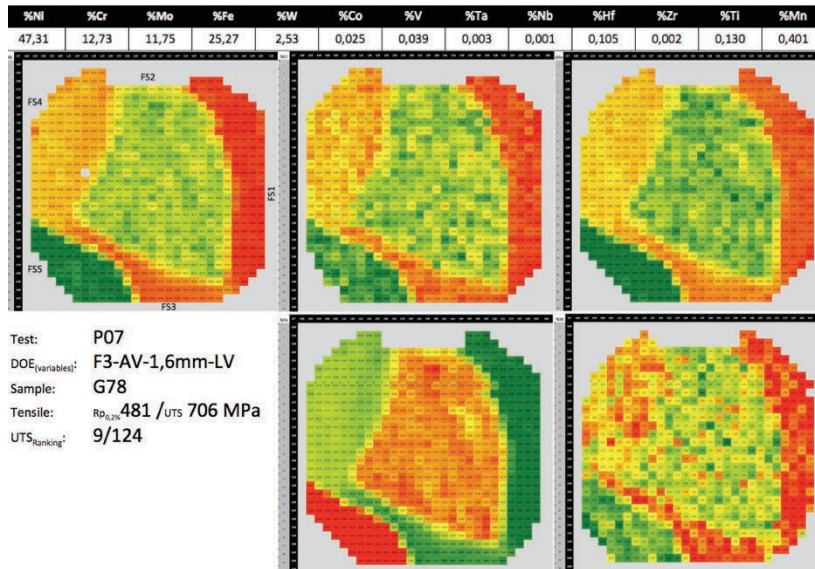
Fig 3- 66: G78 sample summary table.

From compositional surface plotting is observed that G78 is formed by weld beads FS1, FS2, FS3, FS4 and FS5, with FS2 being in the center of tensile specimen, and with less than 50% of the cross-section, Fig 3- 66.

Macro specimen   Micro Specimen   Broken Tensile Specimen   Broken Tensile Specimen, SEM image
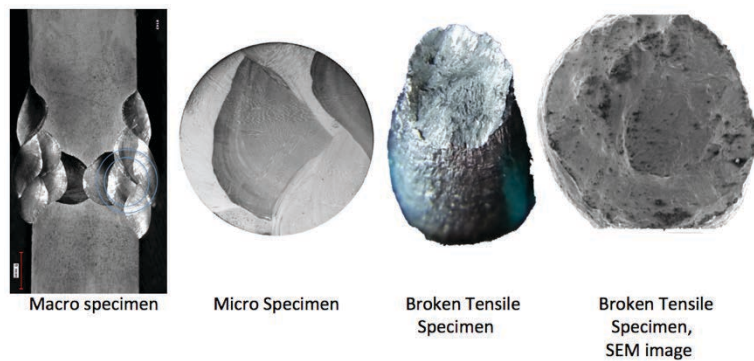
Fig 3- 67: Sample G78, Macro, Micro and Fracture surface

From a macroscopic point of view, fracture was initiated on FS2, may be in it center area, where sample shows rough surface. More than 60% of cross section is formed by shear lip. Fig 3- 67
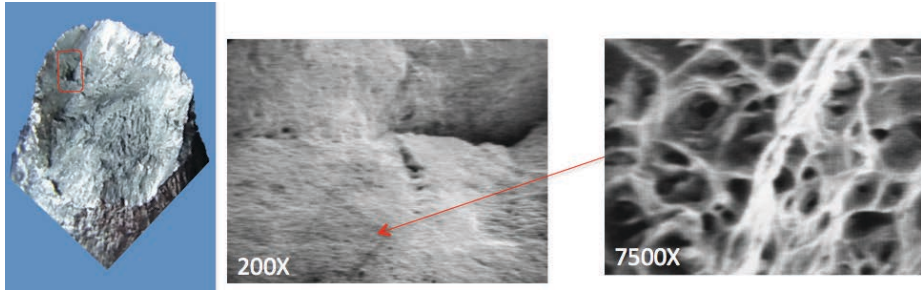
Fig 3- 68: Sample G78, Features on fracture surface 1

From a microscopic point of view, main fracture mode is intergranular with grains decohesion by formation and coalescence of micro voids, Fig 3- 69, Fig 3- 70, and Fig 3- 71.
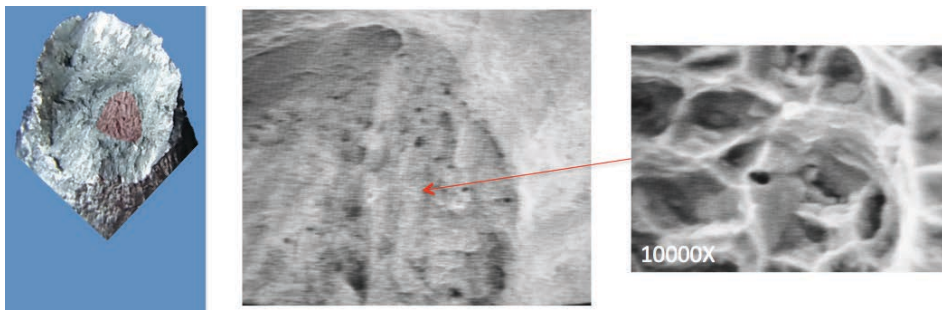
Fig 3- 69: Sample G78, Features on fracture surface 2

Also open cracks are observed on fracture surface, some of them produced during grains debonding, but other produced on during welding operation, either by solidification or re heating.
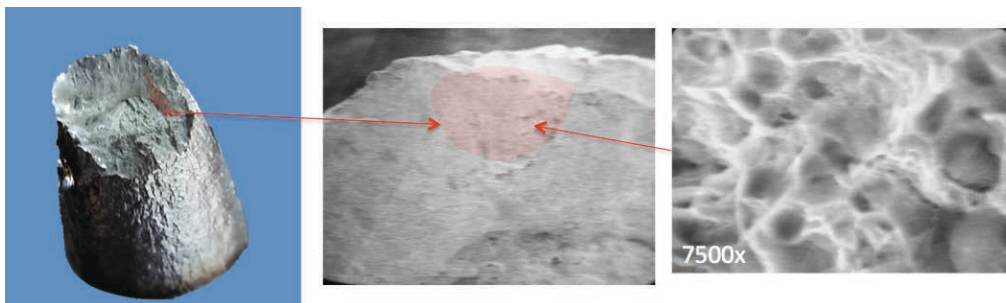
Fig 3- 70: Sample G78, Features on fracture surface 3
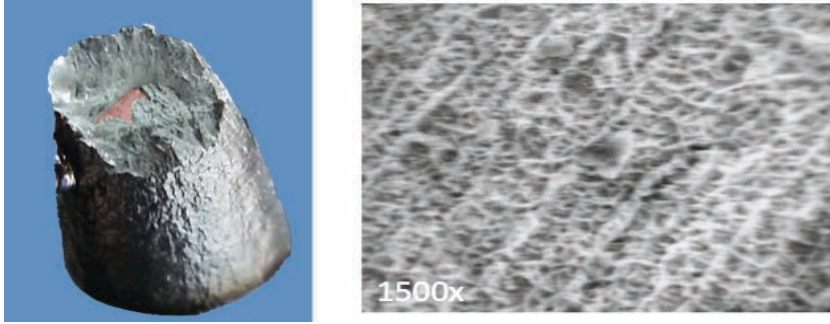
Fig 3- 71: Sample G78, Features on fracture surface 4

3.9.4   Test P31

Test plate welded with flux F3 by direct current, high voltage and the thicker wire was identified as P31. This is one of the tests who have more difference between their tensile specimens' strength, been them in positions 122, 87, 82 and 8 in UTS ranking.

a) Sample G18
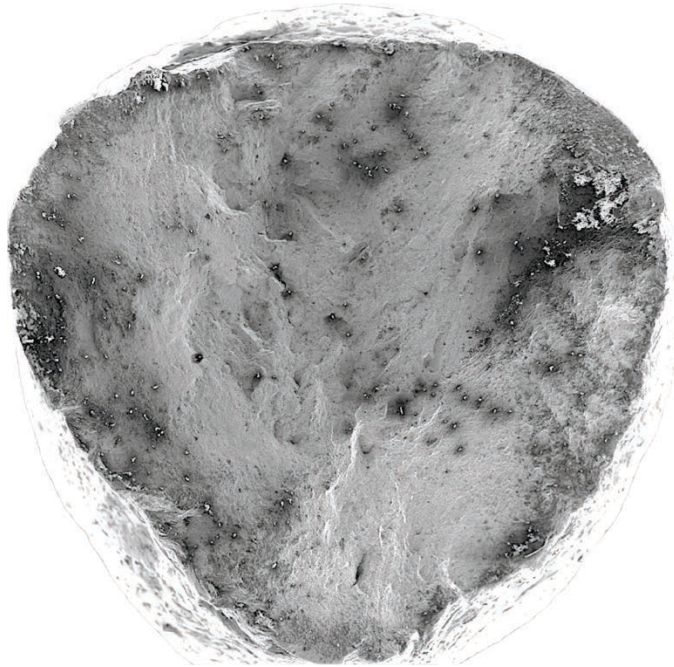
Samples G18 and G19 were tested in LECO laboratory, and were machined from central area of the joint, been formed mainly by weld beads BS1, BS2, BS3 and BS5, Fig 3- 72. G18 is placed on position 82, having ultimate tension strength of 654 MPa with an iron content of 33,5%, Fig 3- 72

Test:	P31
DOE(variables):	F3-DC-2,0mm-HV
Sample:	G18
Tensile:	$R_{p0,2\%}$419 /$_{UTS}$ 654 MPa
UTS(Ranking):	82/124

Ni	Cr	Mo	Fe	W
41,8	11,5	11,0	33,5	2,2
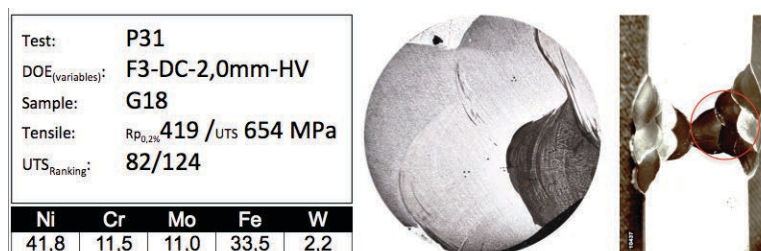
Fig 3- 72: G18 sample summary table.

Its fracture surface is showing an important amount of opened cracks, distributed all

along fractured surface, but more concentrated in central (1) area. At lower magnification it see the texturized surface produced by intergranular fracture mode, Fig 3- 73
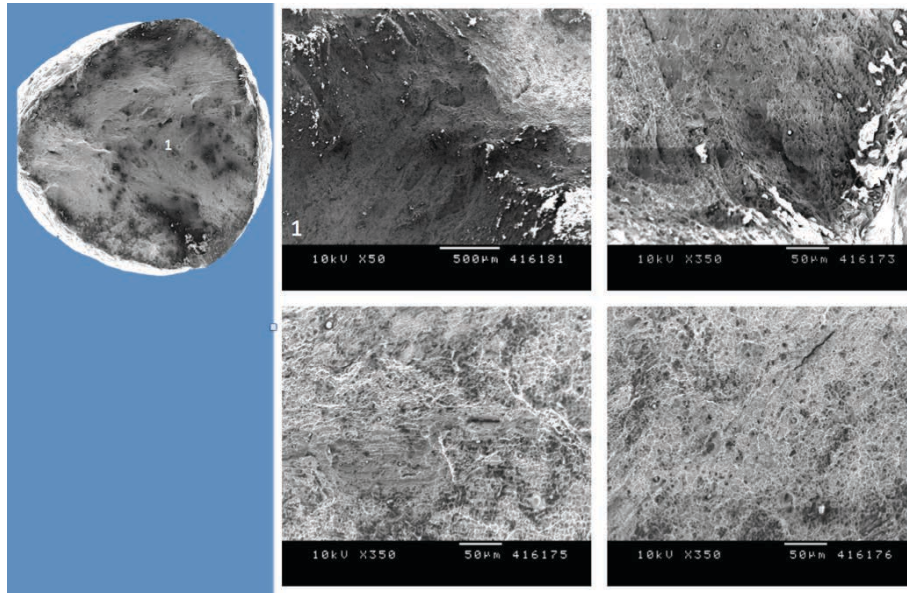
Fig 3- 73: Sample G18, Features on fracture surface

b) Sample G19:
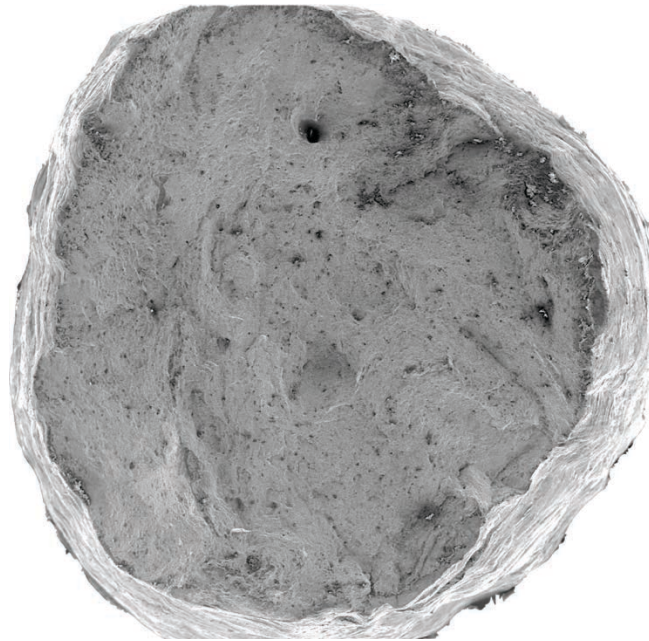
G19 the weakest specimen of its group and maybe of the entire trial, been placed in position 122 of 124 of the UTS ranking, but also is showing one of the lower elastic limits.

Test: P31
DOE(variables): F3-DC-2,0mm-HV
Sample: G19
Tensile: $R_{p0,2\%}$ 408 / UTS 626 MPa
UTS Ranking: 122/124

	%Ni	%Cr	%Mo	%Fe	%W
BS3	37,78	9,98	9,70	40,03	1,91
BS5	46,72	12,61	12,63	25,14	2,54
BS1	33,79	8,69	8,47	46,81	1,70
BS2	42,01	11,22	11,15	32,96	2,24
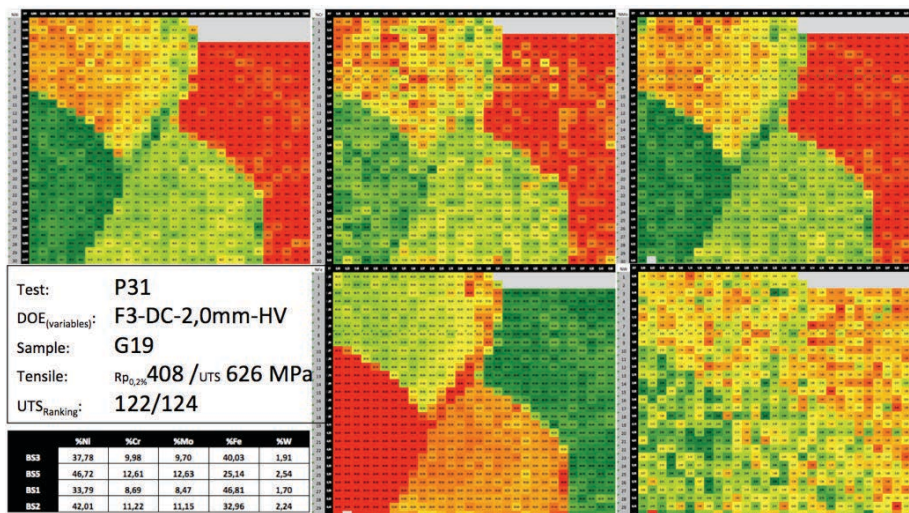
Fig 3- 74: G19 sample summary table.

From the chemical composition there are two items to be commented, first is the high compositional variation between weld beads. Regarding nickel, BS5 have 47% of nickel what is 13 units of percentage higher than average nickel content of BS1 and 9% higher than BS3. Regarding Chromium and Molybdenum its variation are around 4

106

units of relative composition, meanwhile iron content variation up to 22%. This unbalanced alloying elements distribution produces a differential mechanical strength between the weld beads.

The second features of this sample has been analyzed by hardness test and presented above, which is the presence of an enriched area of key alloying elements, nickel, chromium and molybdenum, see 3.9.3.1. This enriched zone is producing a harder plane, between 6% and 13% harder than its surrounded hardness.

To know where this enriched area is placed on fracture surface, it been performed XRF analysis on a 10X10 array of measurements. With this technique enriched area was identified, placing it just on a hill produced by BS5's tearing, but without clear continuity through BS3-BS2 borderline.

What been observed is that observed crest on fractured surface, red dotted line, has occurred in an area of slightly lower nickel content inner of welding bead BS2.
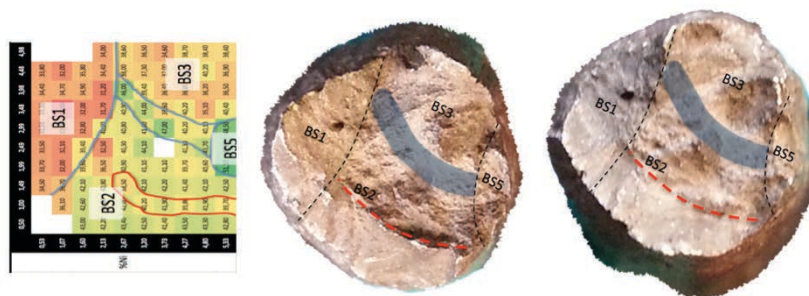
Fig 3- 75: Compositional Profile on Fracture surface, and correlation with macro fracture features.

Fractographic analysis at lower magnification shows the intergranular fracture mode, with some opened cracks, but maybe less than observed in other samples, and cavities of gases. Its rough surface is an indication that grains decohesion happen by ductile mechanisms. At higher magnification the dimples of ductile fracture mode are observed,
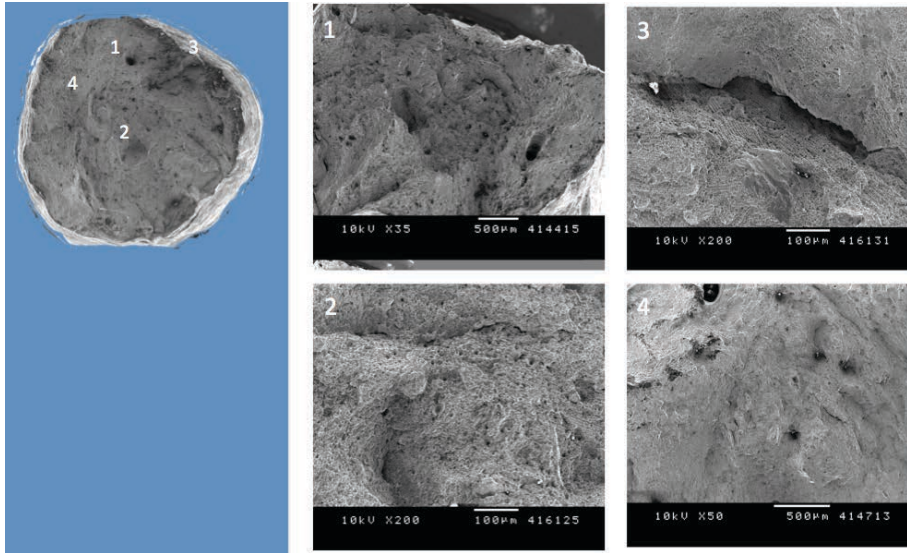
Fig 3- 76: Sample G19, Features on fracture surface 1
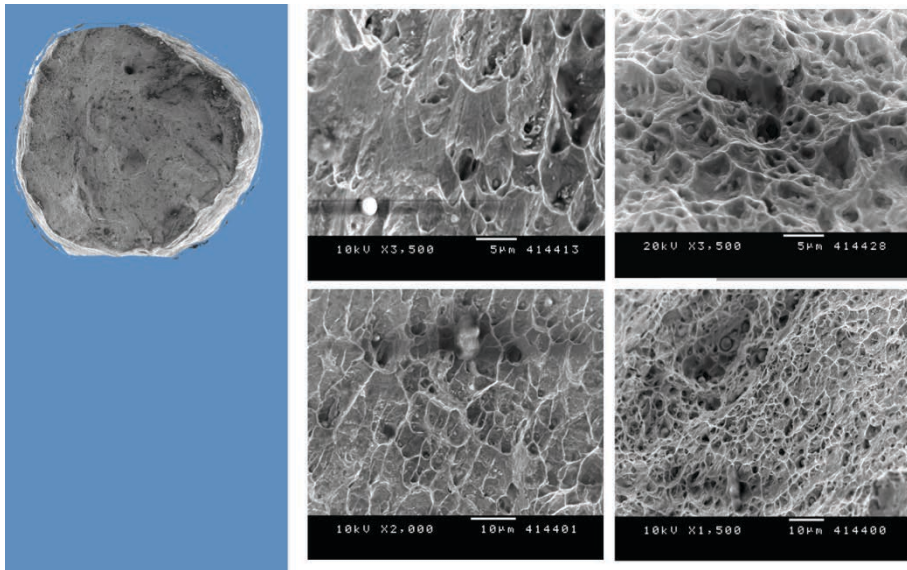
Fig 3- 77: Sample G19, Features on fracture surface 2
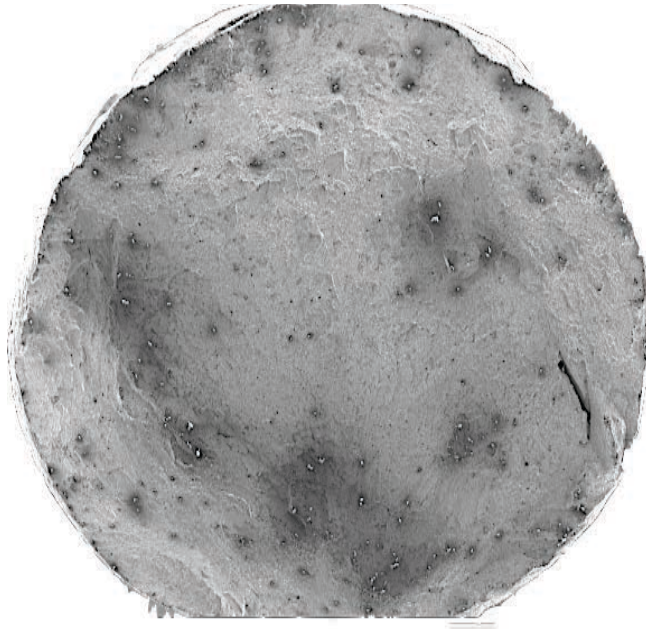
This tensile specimen is within the 10th strongest tested samples of the entire trial, and it placed on position 8. From the chemical point of view this is the sample with lower dilution, or in other words, with lower iron content from its group.

The average iron content of the other 3 samples was 32,5% and this sample has 19,1%, which is 40% less amount of averaged iron.   But also Molybdenum and Chromium content of this sample is around 22% higher then the average of the other 3.

Additionally, and not least, the variation of the content of the key alloying elements between weld beads are lower in this sample than compositional variation found in G19 sample. In this sample Nickel variation is 5 units while G19 were 13 compositional units. The variations of Molybdenum and Chromium rise to 1,7 units and for iron rise to 9% units of compositional percentage.

%Ni	%Cr	%Mo	%Fe	%W	%Co	%V	%Ta	%Nb	%Hf	%Zr	%Ti	%Mn
49,87	13,65	14,24	18,77	2,88	0,081	0,124	0,002	0,028	0,103	0,003	0,073	0,392

	%Ni	%Cr	%Mo	%Fe	%W
FS1	42,6	11,5	11,3	31,6	2,3
FS2	50,2	13,9	13,7	18,9	2,8
FS3	51,1	14,2	14,0	17,5	2,9
FS4	46,3	12,5	12,4	25,7	2,6
FS5	51,4	14,2	14,1	16,9	2,9

Test: P31
DOE(variables): F3-DC-2,0mm-HV
Sample: G156
Tensile: Rp$_{0,2\%}$481 /$_{UTS}$ 715 MPa
UTS(Ranking): 8/124
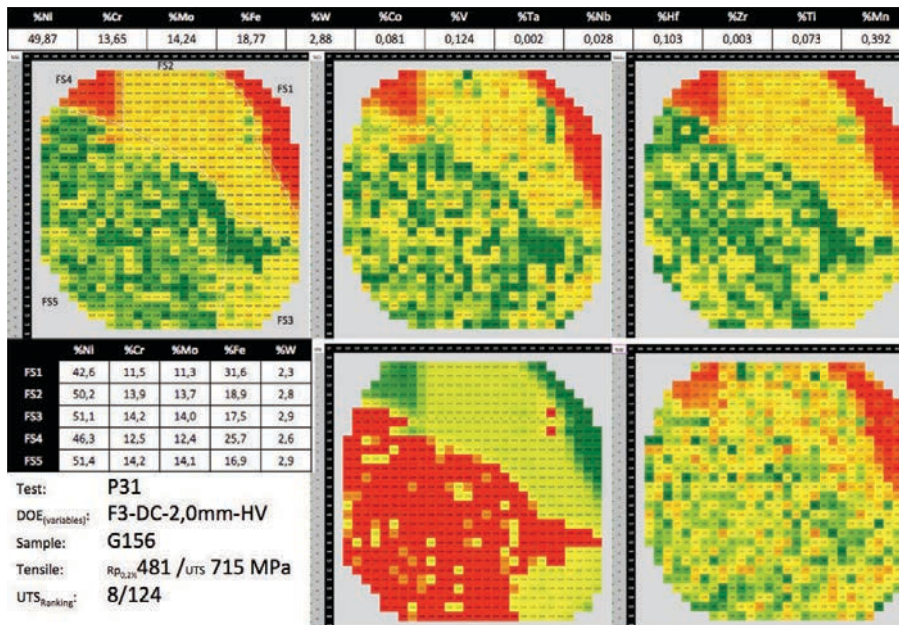
Fig 3- 78: G156 sample summary table.

This cylindrical tensile sample was machined from outer zone of second welded side. Weld beads FS2, FS3 and FS5 are forming near to 90% of the 6mm diameter cylindrical section. Fracture seems to have initiated at the tip of the FS1, and propagated through weld bead FS2 and FS5 producing a radial pattern shown in Fig 3- 79.
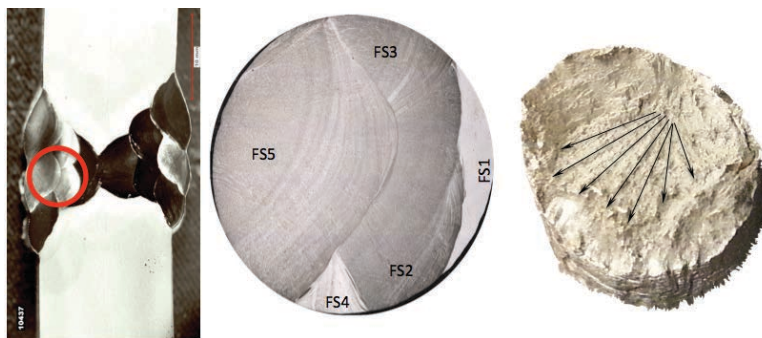
Fig 3- 79: Macro and Micro sample with identification of weld beads, identification of Fracture initiation areas.

The fractography show intergranular rupture pattern with grains decohesion by ductile mechanism. Even when the rupture was produced by intergranular fracture, its surface is flatter, less texturized, than fracture surface of other samples which show lower strength. There are only two open cracks on its surface, both seem to be produced by thermal effect. Fig 3- 80

110
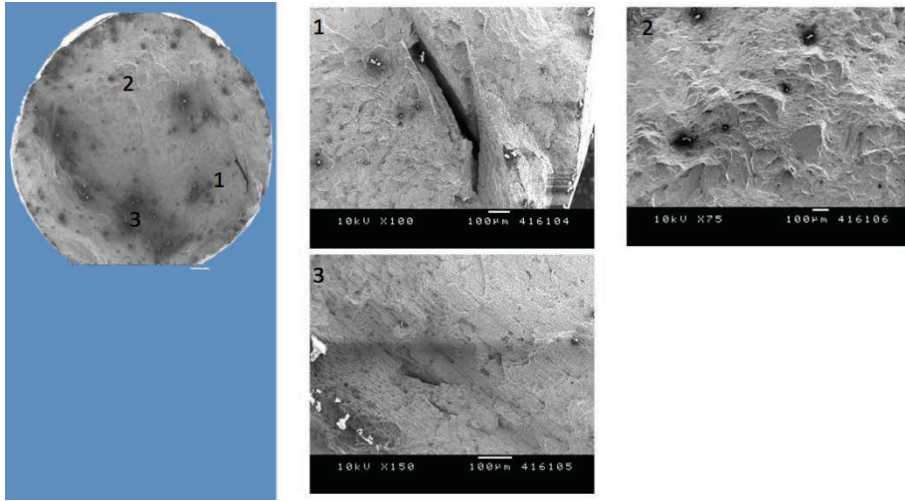
Fig 3- 80: Sample G156, Features on fracture surface

3.9.5 Test P03a

This test plate has been welded using agglomerated flux F1 with direct current, the thinner wire and high voltage set up. Its tensile specimens test in LECO are placed on position 49 and 53, while those specimens tested in BOSE are located in positions 50 and 2.

a) Sample G70
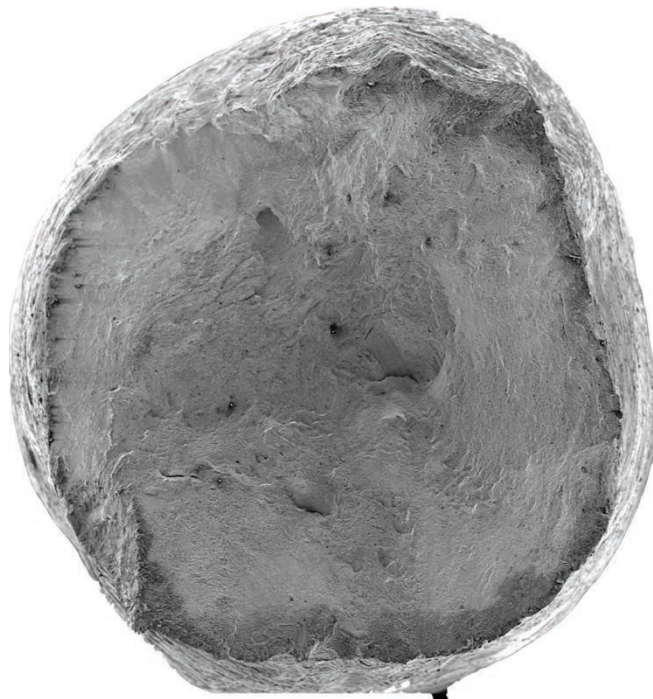
Like been introduced above, sample G70 is the weakest of the samples test in BOSE from its group having similar UTS than those specimens were been taken more centered than it, but from same side. Actually their chemical compositions are almost same.

The compositional variations between their weld beads are important. The difference of the nickel content between BS1 and BS5 is 15 compositional units, 5 unit of difference for Chromium and Molybdenum and iron reaching a difference of 25 units of compositional percentage. This variation range is pretty close than compositional variation observed on sample G70, commented above.
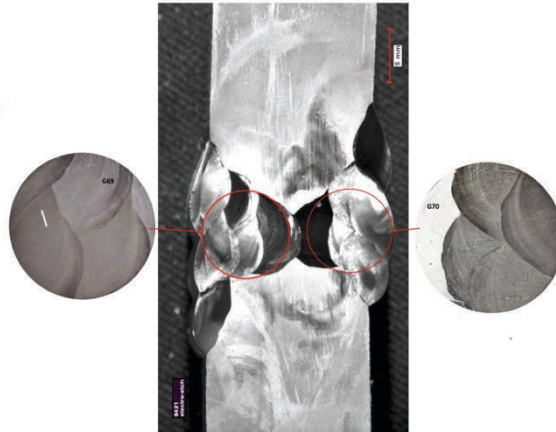
Fig 3- 81: Macro sample showing the location of sample G70 and G69

On compositional plotting again is clearly observed the effect of convective agitation, produced by called Marangoni effect, which produce a wide enriched area on bottom of weld beads BS2 and BS3. Also in middle of BS2 is observed an area that is enriched of iron.

%Ni	%Cr	%Mo	%Fe	%W	%Co	%V	%Ta	%Nb	%Hf	%Zr	%Ti	%Mn
47,84	13,07	11,96	24,45	2,51	0,012	0,031	0,001	0,001	0,094	0,000	0,122	0,347

Test: P03a
DOE(variables): F1-DC-1,6mm-HV
Sample: G70
Tensile: Rp0,2% 466 /UTS 675 MPa
UTS Ranking: 50/124

	%Ni	%Cr	%Mo	%Fe	%W
BS1	38,19	10,10	9,04	40,52	1,89
BS2	48,60	11,30	12,31	23,15	2,54
BS3	49,21	13,58	12,55	21,99	2,60
BS4	48,20	13,18	12,19	23,82	2,52
BS5	52,88	14,63	13,64	16,01	2,82
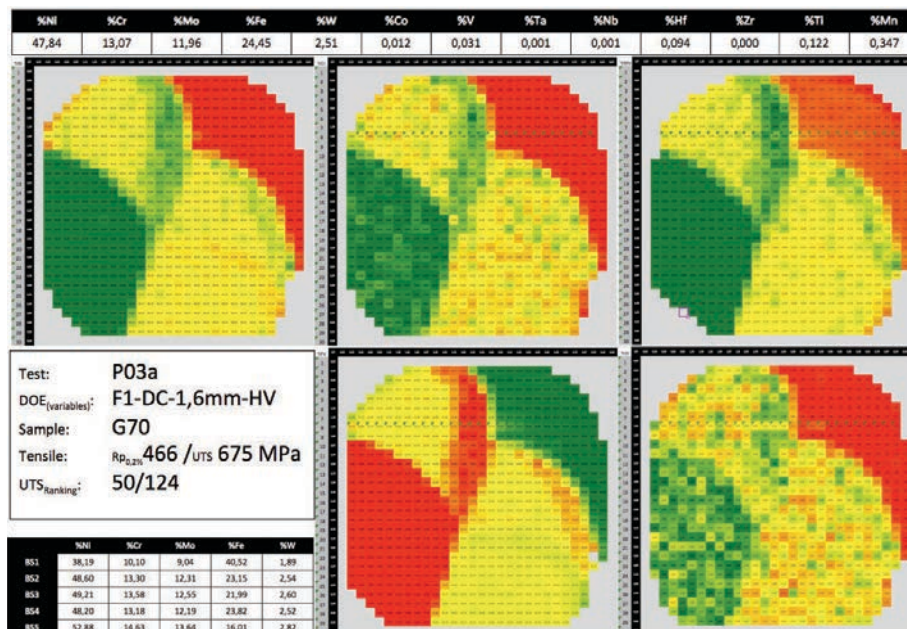
Fig 3- 82: G70 sample summary table.

By electron microscopy is observed that main area of the fracture surface is developed by shear. The fracture show in its bottom a straight line which is more or less in the zone where is expected to be located the enriched area. Also in this bottom area is observed an open crack, which it seems to be produced by thermal effect due to characteristic fracture mode shown in Fig 3- 83.

113
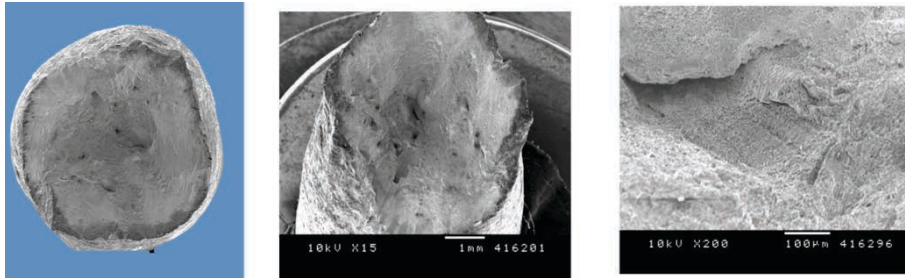
Fig 3- 83: Sample G70, Features on fracture surface

At higher magnification is observed that fracture happens by ductile mechanisms on its entire surface. The Internal surface of opened cracks shows a shallow profile characteristic of both hot and solidification cracking. Fig 3- 84
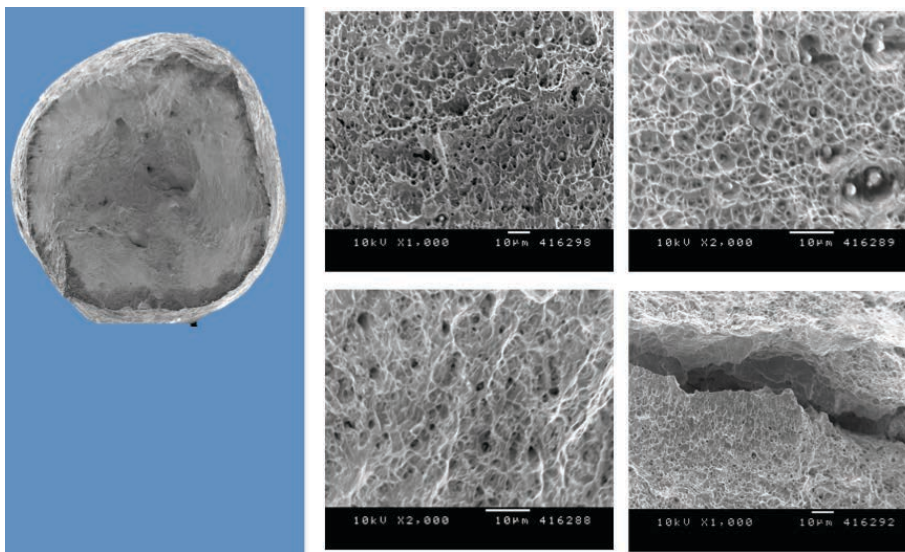
Fig 3- 84: Sample G70, Features on fracture surface

On Fig 3- 85 is show a hot cracking on sample G91. Internal cracking surface show a shallow profile observed on several open cracks on some of the studies fracture surfaces. This is a confirmation that several cracks observables on fracture surface were on matrix before cracking, and even some of them could promote early fracture.
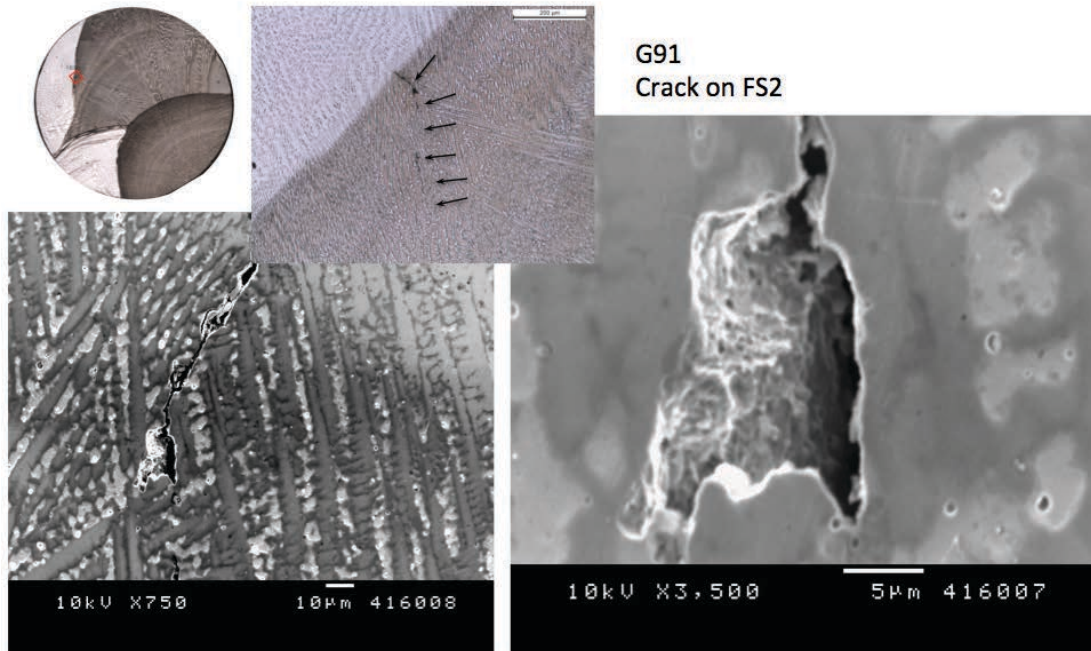
Fig 3- 85: Solidification cracking surface produced on sample G91
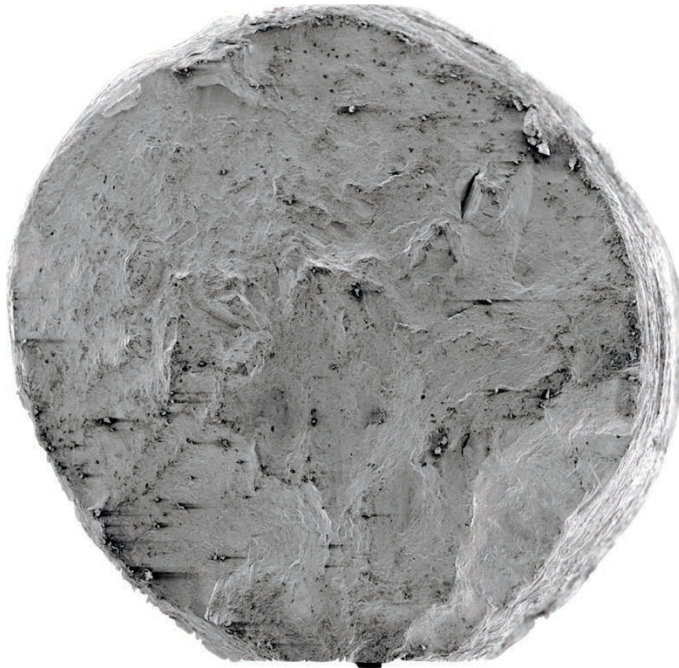
Sample G69 is the stronger specimen of its group, and the second stronger of the entire trial. This cylindrical tensile specimen where machined from external area of the last welded side. Weld beads FS2, 3 and 5 cover more than 90% of its cross-section. Then, mainly 3 weld bead are forming the cylindrical section, but again the key factor is that the difference between their weld beads compositional chemistry is very small; with a maximum variation of nickel content of 4 units, 1,2 and 1,3 of Chromium and Molybdenum and only 6 units of maximum difference on iron content. Fig 3- 86

From chemical compositional plots and from macro and micro samples it seems there not alloying enriched zones, or at least they are no so evident as seen on G70 or G19 samples.

There are no surprises regarding its fracture surface. It is intergranular, with grains decohesion by ductile mode. There are few tiny crack on its surface, which are more or less parallel oriented with applied load and, then having low impact on mechanical strength. Fig 3- 87 and Fig 3- 88.

%Ni	%Cr	%Mo	%Fe	%W	%Co	%V	%Ta	%Nb	%Hf	%Zr	%Ti	%Mn
50,54	13,89	12,82	19,78	2,76	0,013	0,032	0,001	0,001	0,132	0,001	0,143	0,338

Test: P03a
DOE(variables): F1-DC-1,6mm-HV
Sample: G69
Tensile: Rp0,2% 503 /UTS 725 MPa
UTSRanking: 02/124

	%Ni	%Cr	%Mo	%Fe	%W
FS1	47,31	12,87	11,86	25,39	2,44
FS2	52,33	14,46	13,54	16,83	2,82
FS3	48,34	13,25	12,27	23,06	2,56
FS5	51,07	14,07	13,14	18,87	2,74
FS6	51,48	14,21	13,28	18,25	2,77
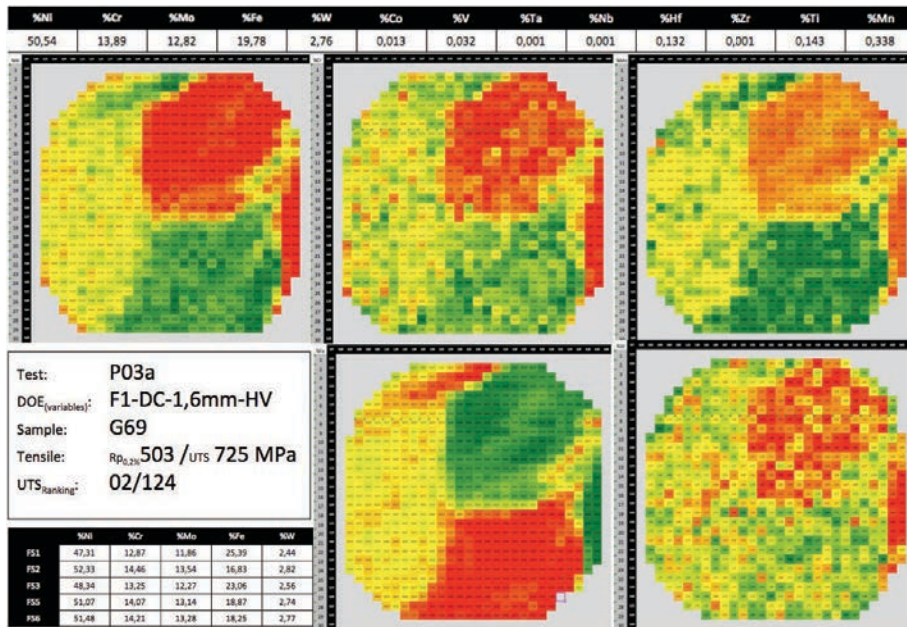
Fig 3- 86: G69 sample summary table.
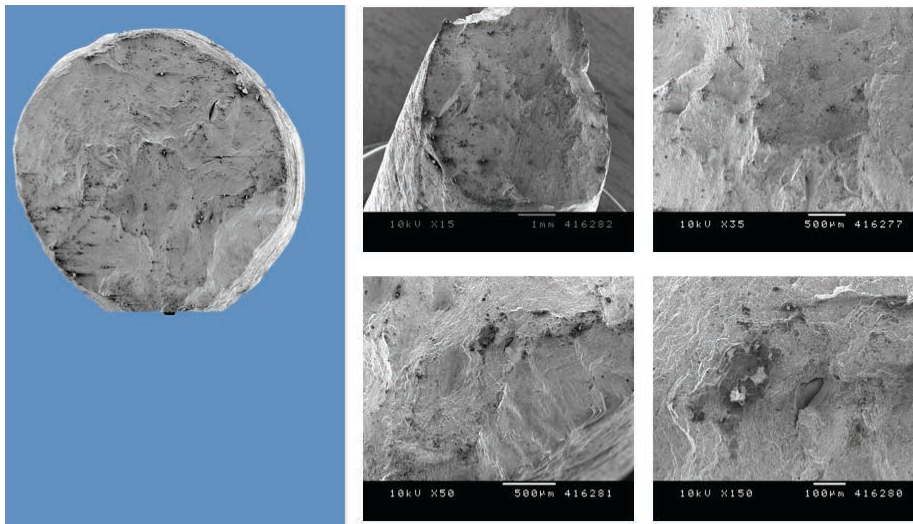
Fig 3- 87: Sample G69, Features on fracture surface 1

117
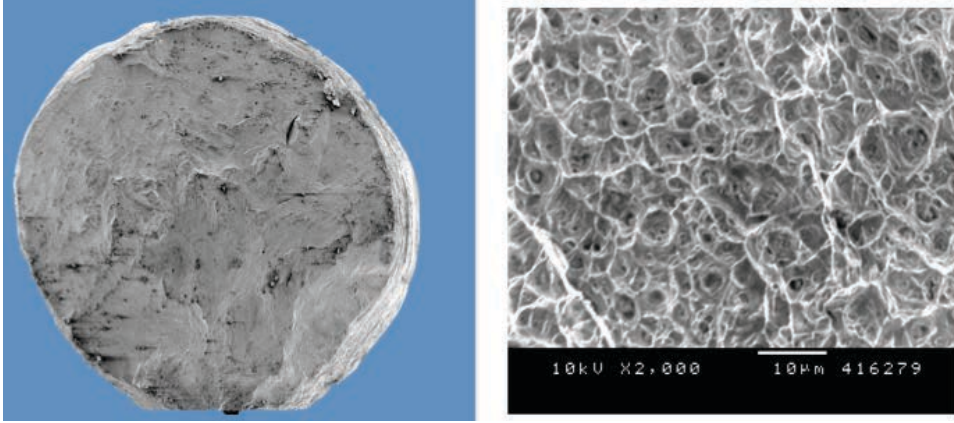
Fig 3- 88: Sample G69, Features on fracture surface 2

3.10 Structural Analysis

3.10.1 Slag Inclusion on polished surface

As polished surface show big amount slag inclusion, which mean sizes between 0,33 and 0,53 micron.

This sizes distribution has been obtained as follow. 1st, each Macro sample was polishing, up to 3 Micron diamond powder; 2nd, the centre of each weld bead was identified by a dot; 3rd, From

these centres were taken 16 micrographics at 500X, 4 pictures at each side of the dot, left, right, up and down. These pictures were analyzed using the "Particles analyzer" module of ImageJ software; the lists given by ImageJ were statically analyzed by MiniTab Express.
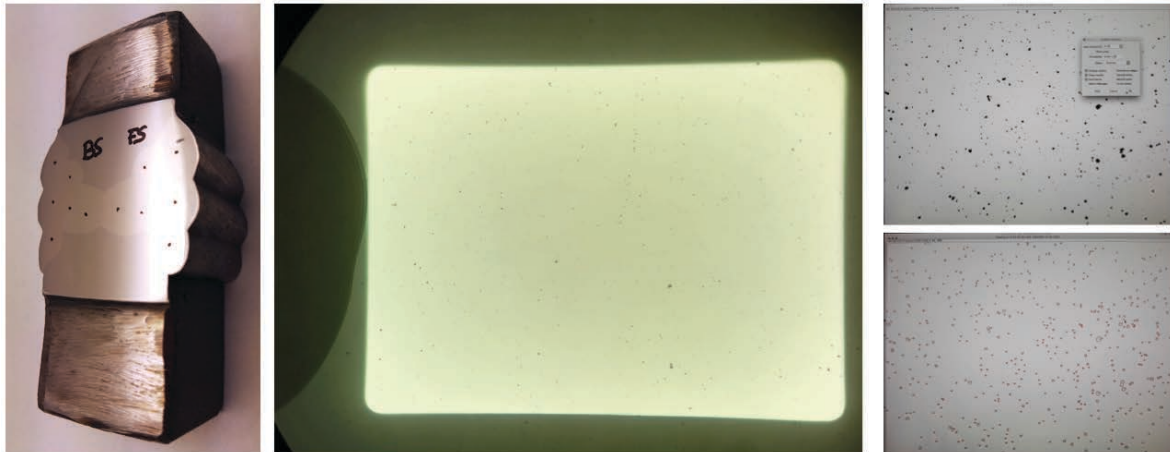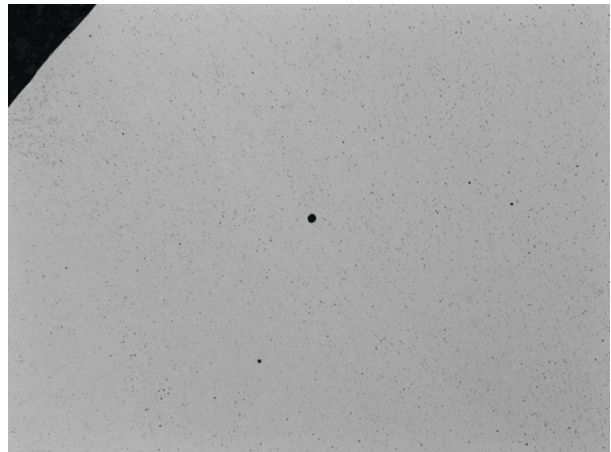
Fig 3- 89: Slag Inclusion analysis process. Location of, photos, image processing and sizing and counting process.

As seen from statistical analysis results, there are no clear effects of DOE variables on inclusions size neither by Current type nor by voltage level.

Also, even when there is some difference between particles mean size by weld bead, a pattern is not observed when the data of different experiments are compared, So that, at least from analyzed data, it is not observed that inclusion size and distribution been

directly affected by the weld beads.
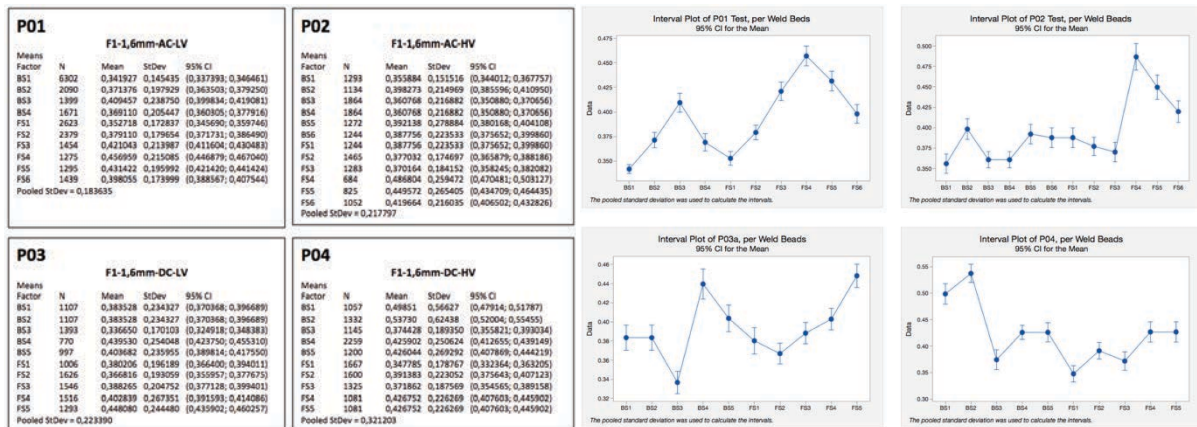
Fig 3- 90: Average size of inclusions and number per weld bead by welded sample

3.10.2 Solidification's structures, columns and dendrites.

a) Dendritic Size Evolution

From the fusion line begins the solidification of the new weld bead. Due the thermal gradient between non preheated plate and the melted drops of filler metal, this area has the faster cooling rates, which produce thin dendritic solidification structure. In the first 300 microns from fusion line, dendrites are around 5 micron wide. From 600 to 800 microns from fusion line, the average dendrites width is around 8 micron. Fig 3- 91

Fig 3- 91: Dendrite width evolution from Fusion line, sample G91

3.10.3 Grain boundary, sub grains boundary and migrated grain boundaries.

a) Test 31

1) Sample G156

Grain boundary at FS2 weld bead it seen like thick and tortous film located along grains borderline, and often decorated by last solidification intermetallic particles, see Fig 3-92.
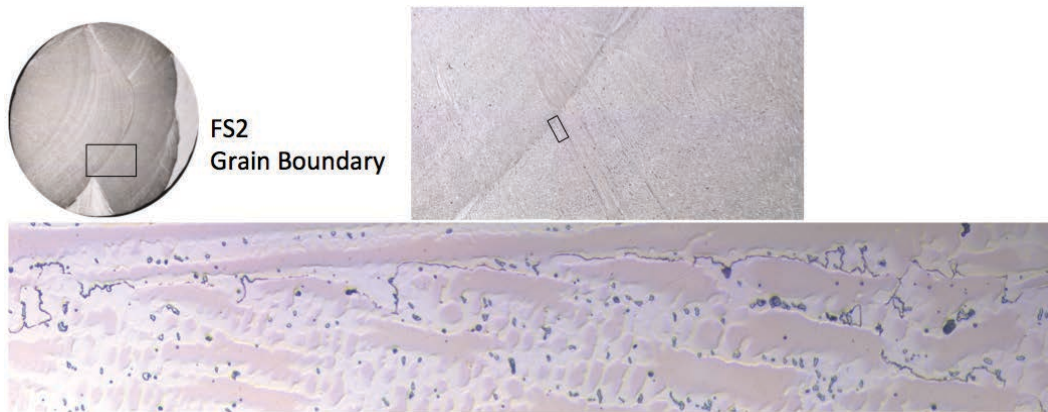
Fig 3- 92: Grain boundary close to fusion line between weld beads FS2 and FS5, Sample G156.

In some areas, grain boundary seems to have been displaced toward the dendritic core, as shown by black arrow in Fig 3- 93. This area is placed close to fusion line between FS2 and FS5, which is within the heat-affected zone. The energy given by reheating could help grain boundary displacement toward a lower energy place, reducing in that way residual stress of deposited weld metal.

Also, in the same figure is observed that the grain boundary displacement has not been continuous. It movement has been fixed in several positions by precipitates, as shown by black arrow on Fig 3- 93.

b) *Test P26*

1) Sample G147

Sample G147 is located in position 98, so it been one of the weakest sample of the trial. Most of its grain boundaries look like very thin line made by straight segments, and was seen in G156, fixed in several points by precipitates. This type of grain boundary seems to move easily toward the dendritic core, as seen in several path in Fig 3- 94A .

This grain boundary is difficult to see, but its observation is enhanced using Differential interference contrast microscopy technique as show in image B of Fig 3- 94.
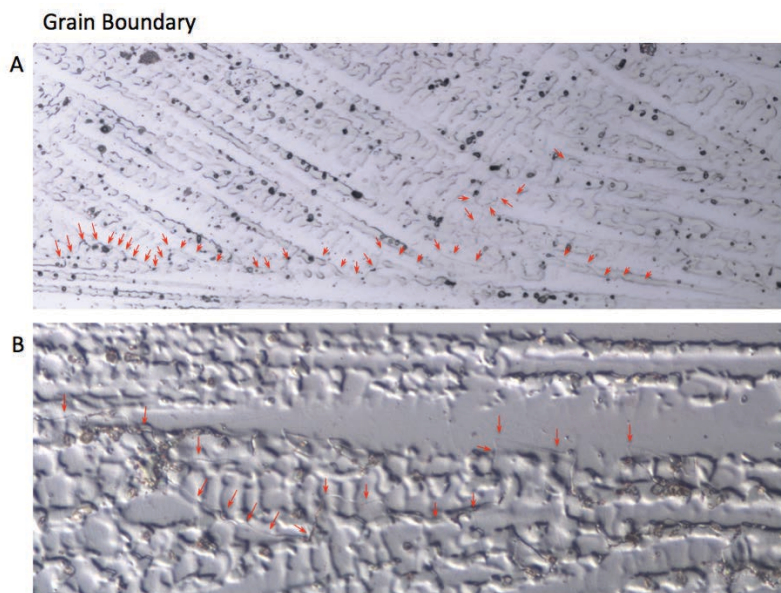
Fig 3- 94: Thin and non-tortuous grain boundary in sample G147, with several segments moved through dendrite core

2) Sample G148:

In case of sample 148, that is in position 24 on UTS ranking, has an grain boundary like a thick and tortous film, similar than sample G156's grain boundary.
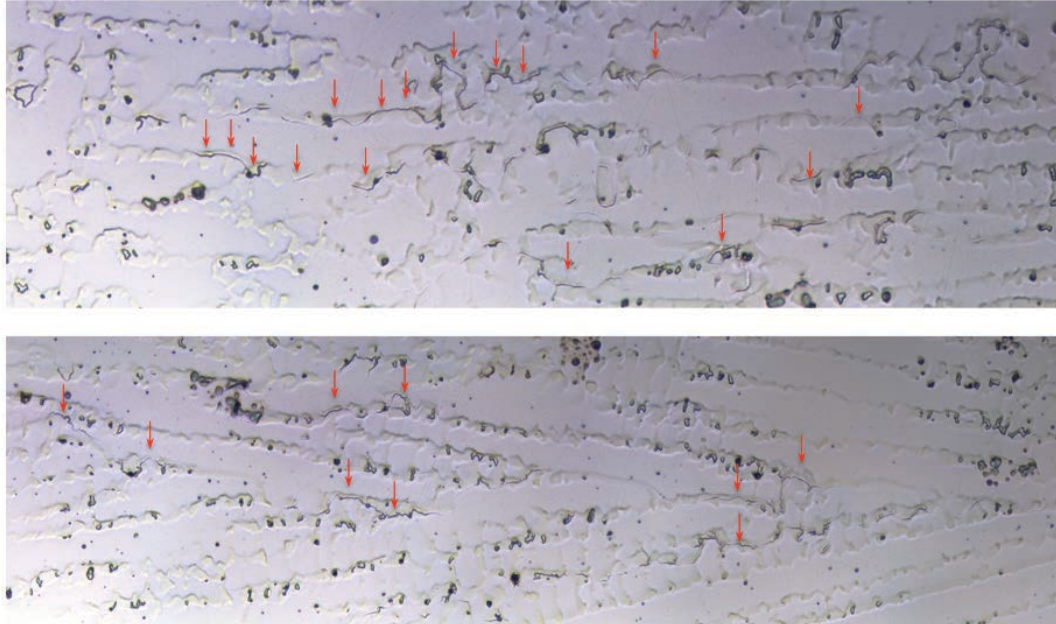
Fig 3- 95: Thick grain boundary film observed on sample G148.

c) Test P14

1) Sample G91

Sample G91 is in position 3 on UTS ranking so it is one of the best results of this trial. Its Grain Boundaries, on weld bead 2 and 5, are mainly formed by a thick and tortuous film, as shown with red arrows on figure Fig 3- 96-A and B, when it is within the interdendritic area, and formed by a thin line when it is going through dendritic core, shown with green arrows on Fig 3- 96-A and B.

Grain boundaries should always be located within the interdendritic zone, because this is the final solidification place where the growing grains are found. This is the path show by the red dotted line on figure B. But actually, grain boundary has been displaced toward dendritic core, highlighted path by green arrows.

Figures B and C show that don't move GB segments have been fixed by intermetallic particles, which have arrested the misorientation component displacement. In other words, intermetallic particles are pinning dislocation movement.

Two considerations should be taken in account to explain grain boundary displacement: 1st, Grain boundary located at final solidification place has both, a compositional component and a misorientation components. 2nd, In general, diffusion of main alloying elements, specially those segregated during solidification process, is very low, even for short times at high temperatures, it could be considered null. Then, grain boundary (GB) high lighted by green arrows only has misorientation component of GB, who has moved by creeps-like mechanism. GB is move toward a low energy location, reducing in that way residual stress of weld bead.

The explanation of the small segment of GB movement is applying John Lippold`s theory about Migrated Grain Boundaries, which one may be is not completely applied due grain boundary type considerations and Migrated Grain boundary length.
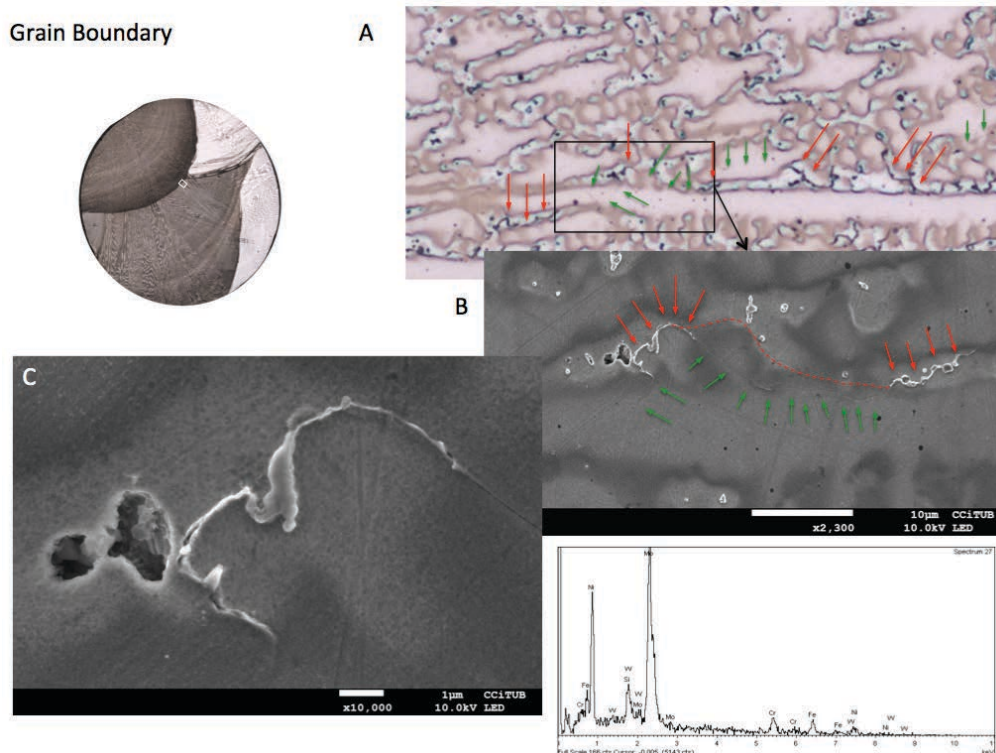
Fig 3- 96: Displaced grain boundary close to FL on sample G91

On Fig 3- 96 C it is seen that GB is decorated by several particles. These particles are

defining GB tortuosity path through the interdendritic zone. As see on EDX spectrum the biggest particle in Fig 3- 96 C corresponds with a molybdenum rich intermetallic phase.

Also it is seen a hole produced by cavitation. In those areas with high secondary dendritic arms coherency liquid feedback is limited, so when shrinkage is produced by solidification the required volume of liquid is not supplied, then last liquid undergoes a negative pressure, which can create the cavitation holes.

Other feature to be noted is that on Interdendritic GB's segment, in addition to be thicker than its segment which goes through dendritic core (DC), several cavities are observed, noted by blue arrows on Fig 3- 97C and D, which seem to be produced by shear stress acting on GB. On contrary, always have been observed that DC GB is producing a thin and straight line without any evidence of interaction between GB and DC matrix, noted by white arrows.

Orange arrows are pointing a neck produced during GB displacement around a particle. What is noted is that particle and GB are placed on opposite side than expected to fulfill with GB displacement's argumentation.
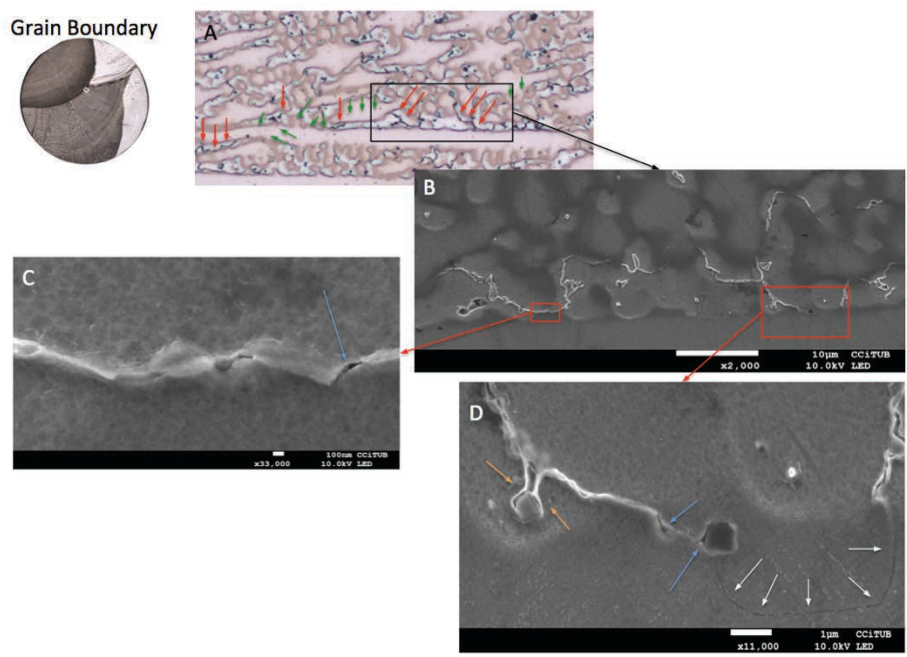
Fig 3- 97: Displaced grain boundary close to FL on sample G91,

Close to the above area, a pinned GB segment by small particles, shows several cavities which seems to be produced by uniaxial load, blue arrows, while few of them seems to be produced by shear stress, green arrows. This area is close to a triple point, which means that a complex stress system is acting on this GB segment. Fig 3- 98
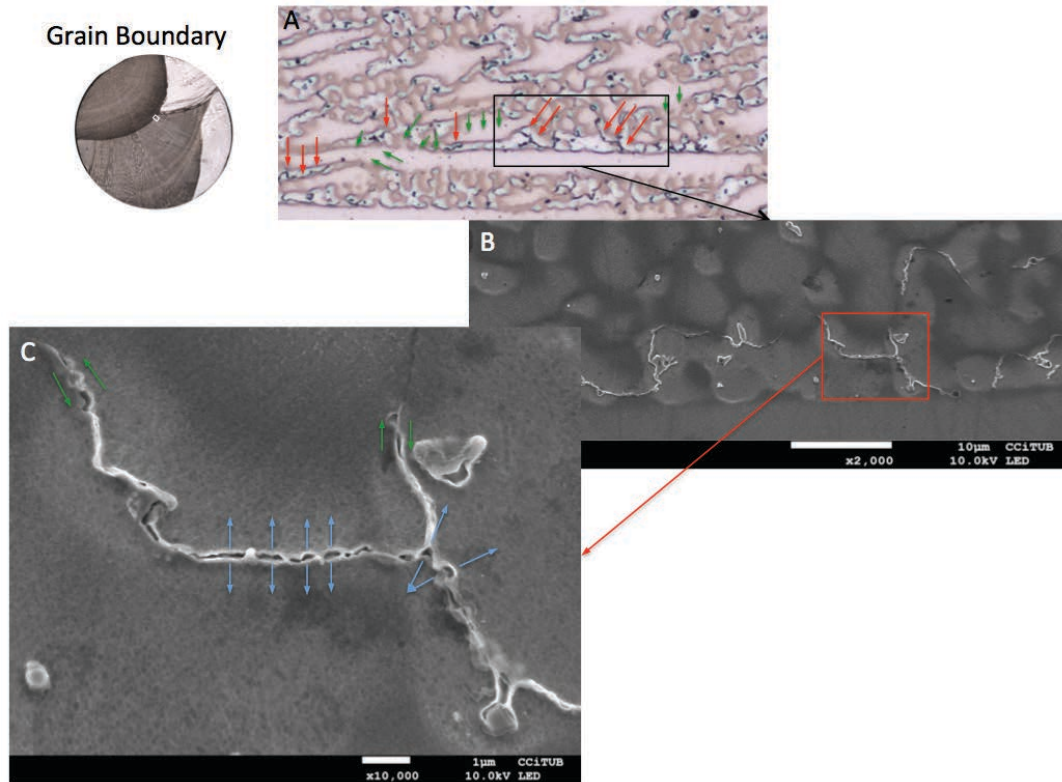
Fig 3- 98: Displaced grain boundary close to FL on sample G91

3.10.4 Secondary Phase particles.

In the interdendritic zone different particles have been observed, with shapes and sizes that seem to depend on different factors.

a) Test P31

1) Sample G156:

G156 is one of tensile samples with higher strength, it is placed on position 8 in UTs ranking. Chemical compositions of their weld bead are pretty close, with FS1 and FS4 having the higher dilution, Fig 3- 99.

In Fig 3- 100, the borderline between FS2 and FS3 is shown. Here is seen how grain orientation goes through fusion line, producing grains even longer than weld bead width. This is harmful for cracking resistance; especially in case of DDC cracking were cracks developed easily along sub grain boundaries.

Fig 3- 99: Sample G156 Micro sample

Fig 3- 100: Large grains crossing FL between weld bead FS2 and FS5, sample G156

Along the interdendritic zone are observed the secondary phases that have precipitated during the solidification, Fig 3- 101. According to the theory these secondary phases must be rich molybdenum and tungsten, which are the elements that have positive segregation during solidification. Also in dendritic core several

rounded particles are observed.
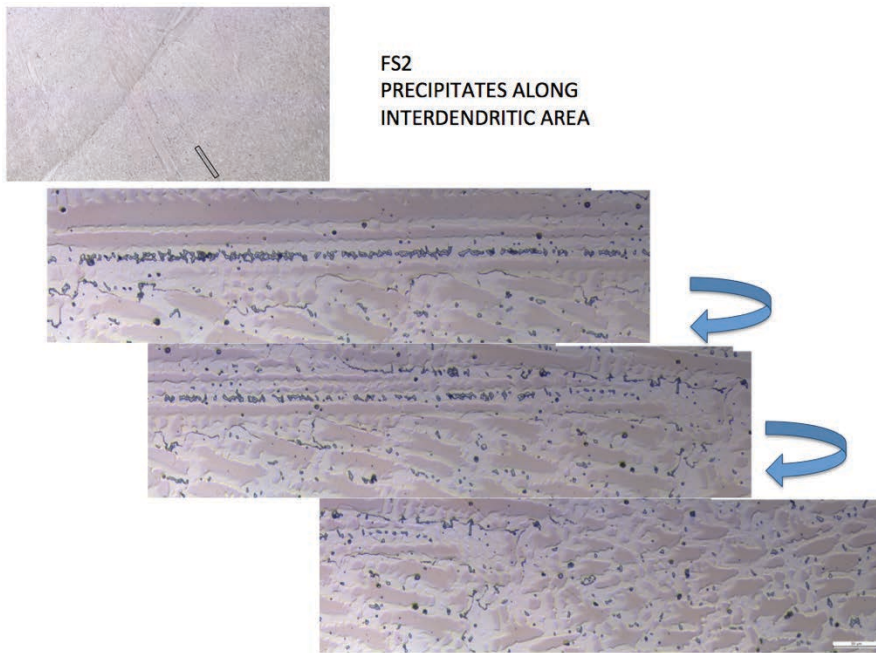
Fig 3- 101: Long line of precipitates place along grain boundary, FS2, Sample G156

Precipitates in weld bead FS5 has same shape and almost same distribution than those observed on weld bead FS2, this in consistent with their closer chemical composition, Fig 3- 102 and Fig 3- 103.
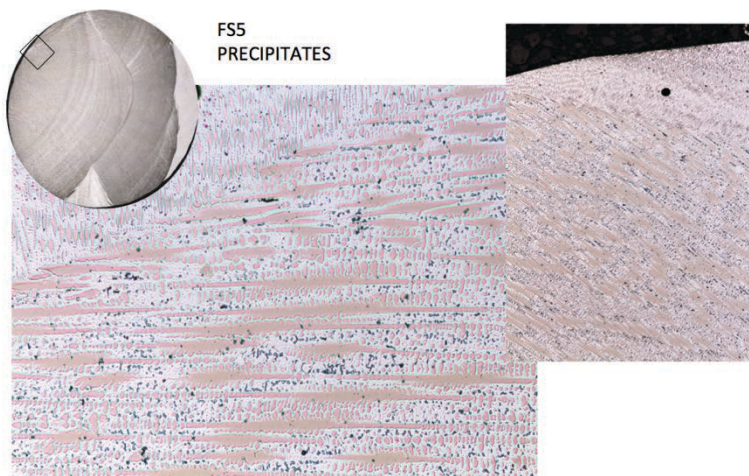
Fig 3- 102:High density of precipitates observed close to FL between FS5 and FS6, G156.
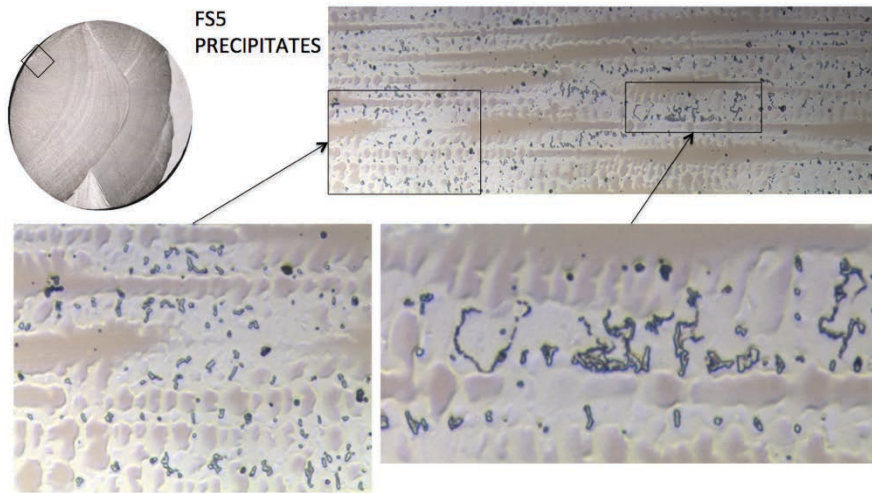
Fig 3- 103: Higher magnification of precipitates place close to FL between FS5 and FS6.

Precipitates observed on weld bead FS1 are very different than those seen on those weld beads having higher concentrations of key alloying elements. The difference is not only on their shape, but also in their sizes, amount and distribution, see Fig 3- 104. In dendritic core also rounded particles are observed.
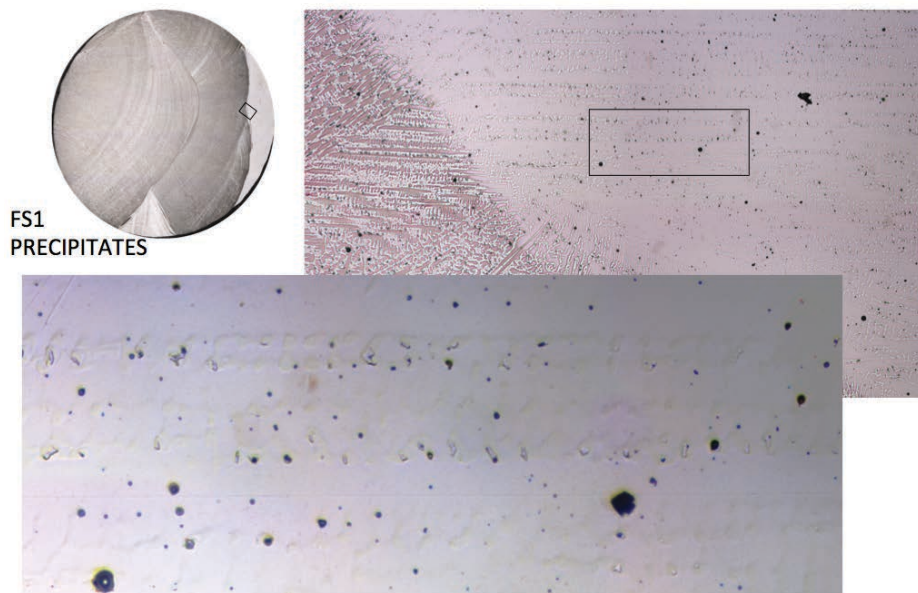
Fig 3- 104: Low density of precipitates on FS1, G156

Precipitates observed on FS1 and FS4 are almost the same shape, size and distribution, only amount of precipitates are higher on FS4, Fig 3- 104 and Fig 3- 105.
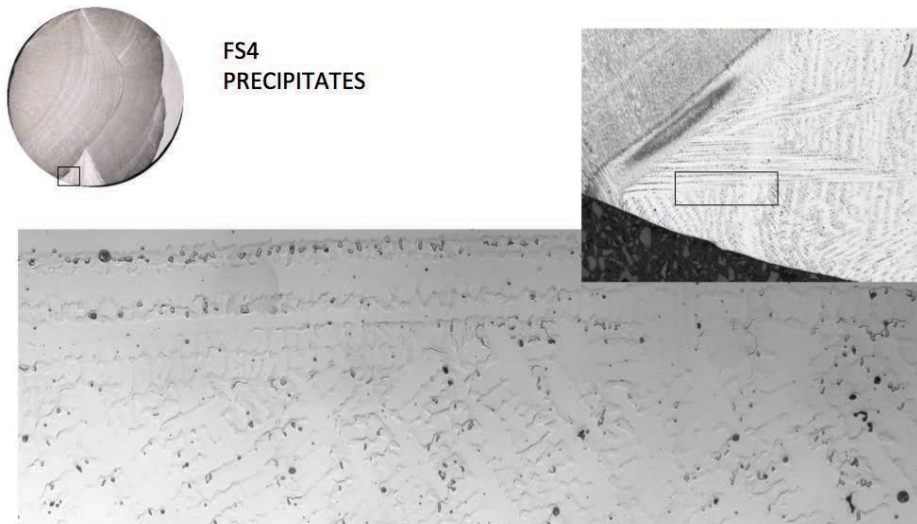
Fig 3- 105: Low density of precipitates on FS4, G156
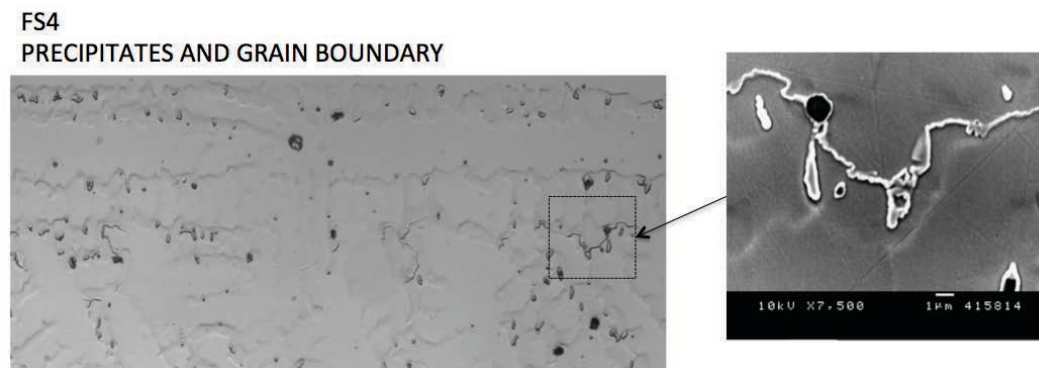
Fig 3- 106: Precipitates on FS4, G156

By EDX analysis, see Fig 3- 107, have been determined that those rounded particles present in dendritic core and interdendritic zone, are aluminum oxides. Also, had been confirmed that interdendritic precipitates are rich in molybdenum and tungsten. In upper-right side of the image, it seen a precipitate formed by an aluminum oxide particle and by molybdenum rich particles, which could mean that aluminum oxide particles act like nuclei-sites of molybdenum rich particles.
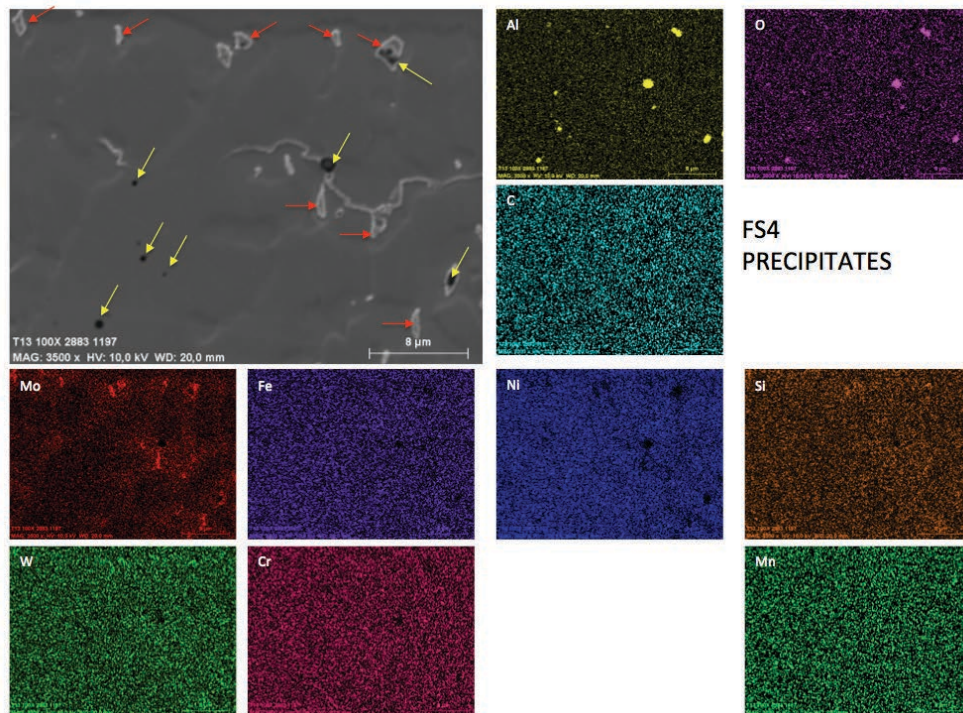
Fig 3- 107: EDX mapping on FS4. Mo-rich and Al_xO_x precipitates identification.

No so far away from above area, but closer to fusion line between FS4 and FS5 are the following area which show similar precipitates and also a small cavity along interdendritic zone. This small cavity has 3 types of particles, some aluminum oxide, other are molybdenum rich particle and also is observed some carbide Fig 3- 109.
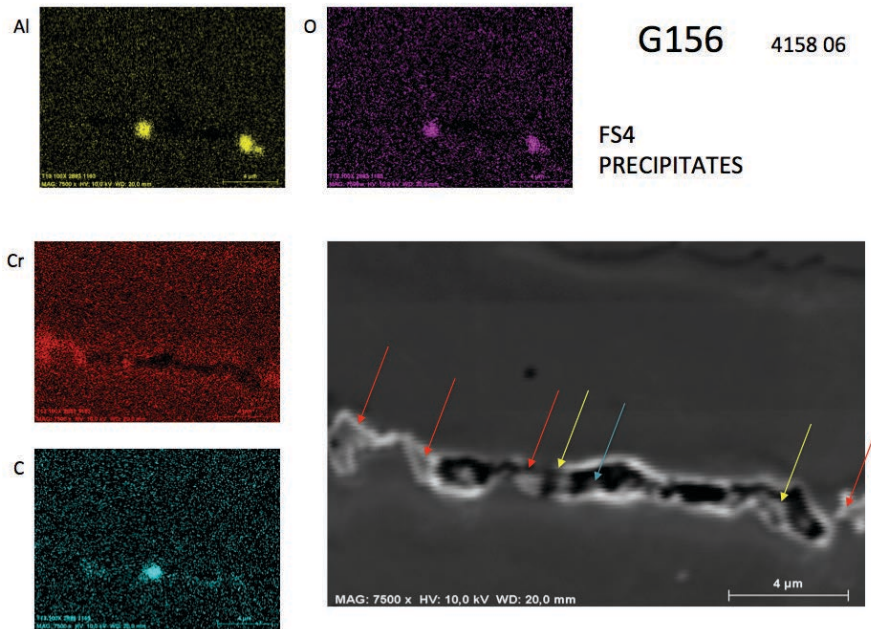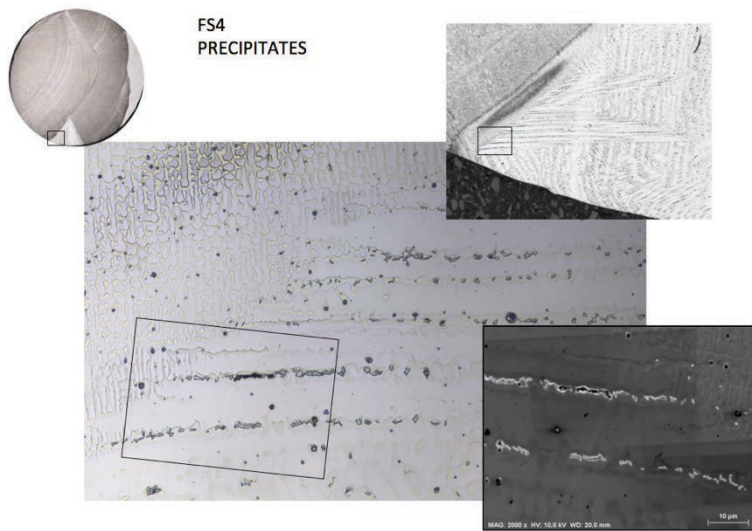
Fig 3- 109

Fig 3- 108: Precipitates on FS4, G156

This small cavity has 3 types of particles, some aluminum oxide, other are molybdenum rich particle and also is observed some carbide Fig 3- 109.
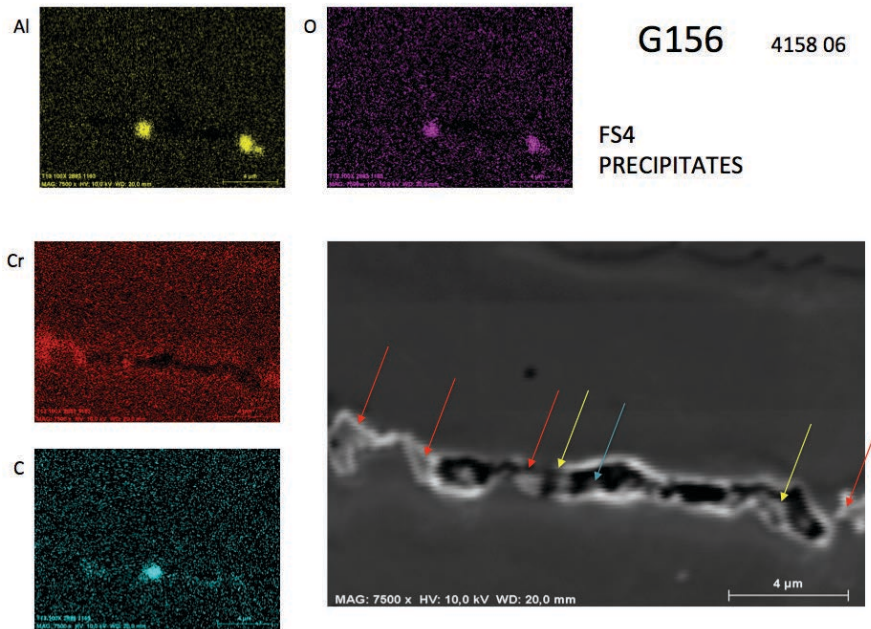
Fig 3- 109: EDX mapping on FS4. Mo-rich, Al_xO_x and Carbide precipitates identification

EDX analysis performed on aluminium rich particles show also the presence of oxygen, calcium and silicon Fig 3- 110. These particles are coming from flux. But observed amount of aluminium rich particles seems to be higher than expected, when used Calcium-Silicate flux only has an alumina level close to 3%.
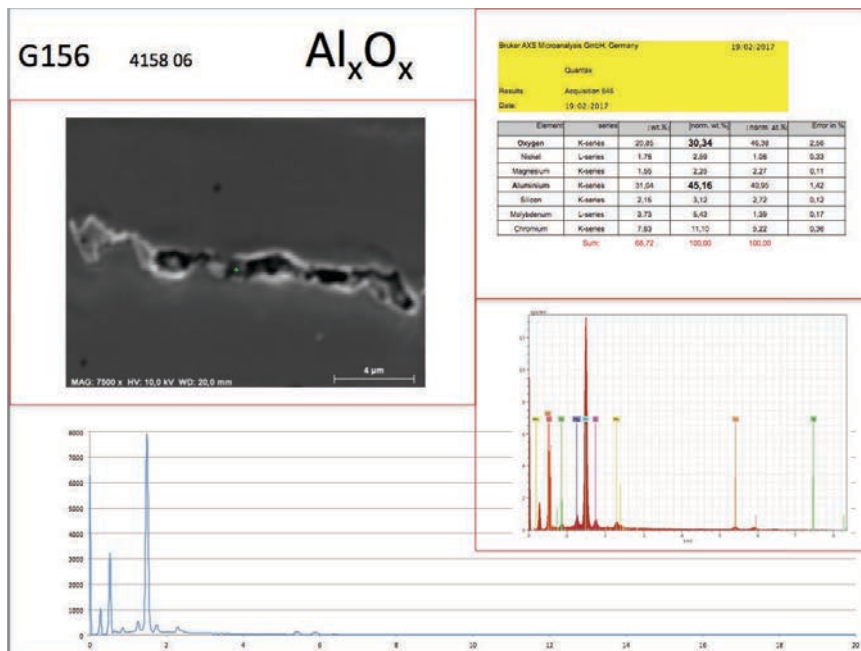
Fig 3- 110: Qualitative and Quantitative compositional analysis of Al-rich particles. FS4, Sample G156.

133

EDX analysis done on molybdenum rich particles, Fig 3- 110, show the presence of molybdenum, tungsten, Chromium, nickel and iron with a stoichiometric relationship close to A7B6 of the Mu or P intermetallic compounds.
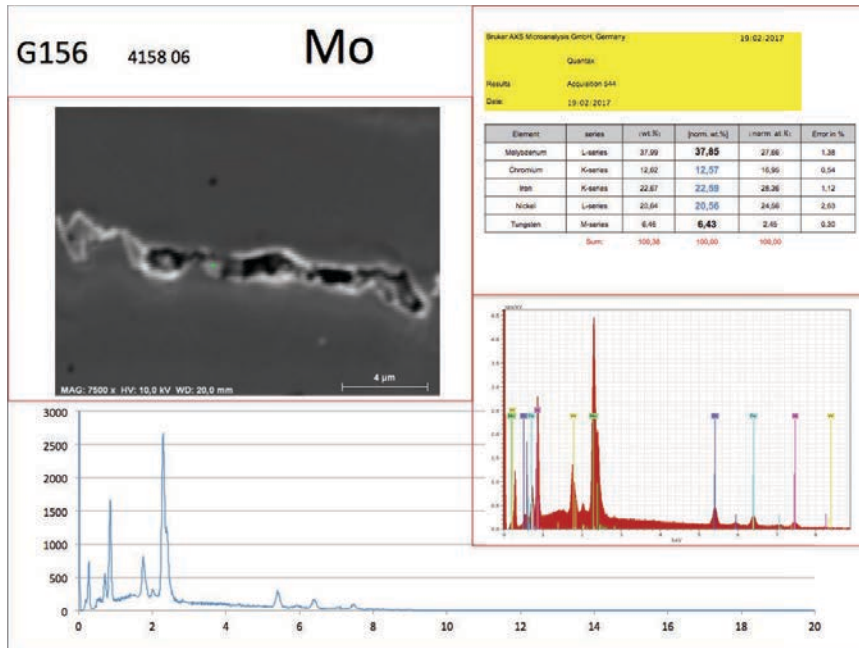
Fig 3- 111: Qualitative and Quantitative compositional analysis of Mo-rich particles. FS4, Sample G156.

Other of the molybdenum rich particles on same picture is showing a stoichiometric relationship close to A7B6 of Mu or P phases, too.
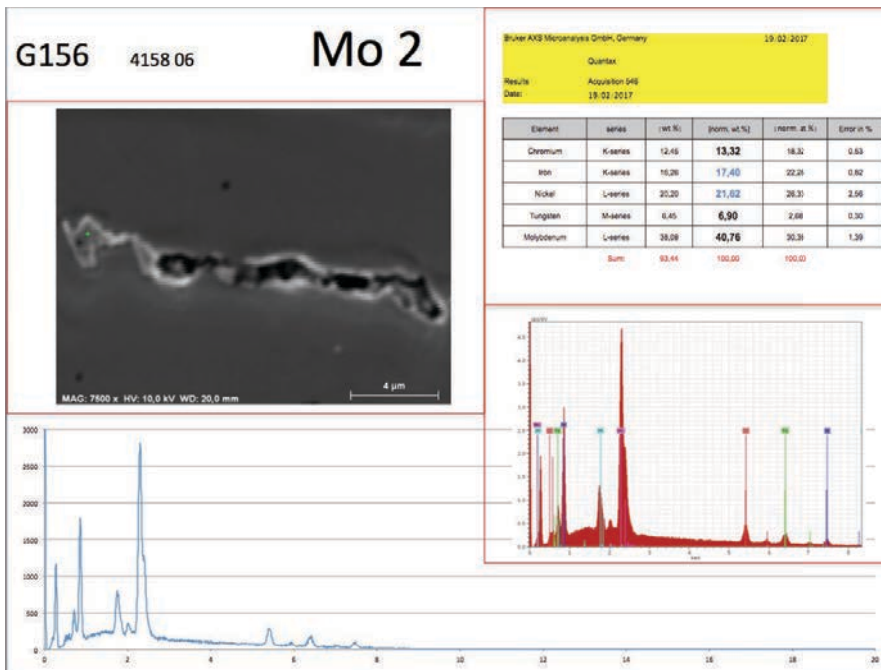
Fig 3- 112: Qualitative and Quantitative compositional analysis of Mo-rich particles. FS4, Sample G156.
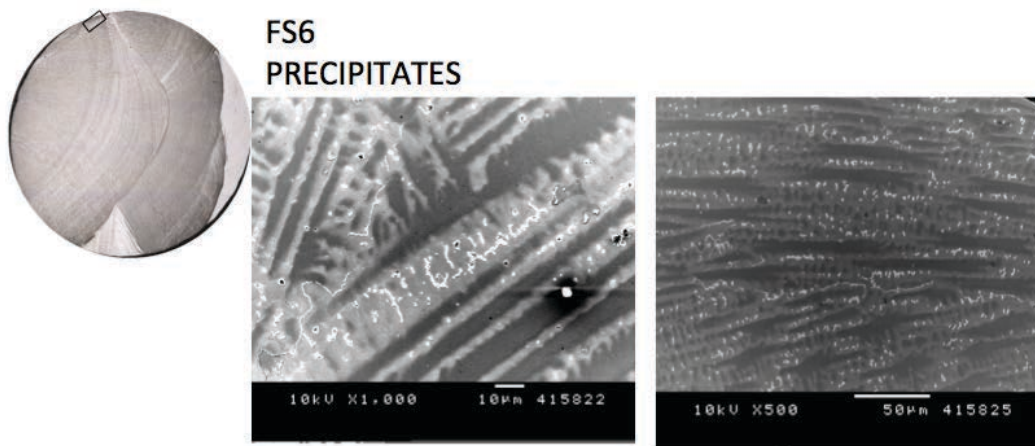
Fig 3- 113: SEM image of high density of precipitates on FS6, G156.

On FS6 weld bead there are also big amount of precipitates along interdendritic region, as saw in FS2 and FS5 weld beads, having all these 3 weld beads the lower iron content, what is the same, the lower Nickel equivalent level, Fig 3- 113.

By EDX analysis was detected the presence of Aluminates, Molybdenum rich particles and few carbides, Fig 3- 114. Again, is noted that there are several precipitates showing aluminates and molybdenum rich particles together.

135

FS6
PRECIPITATES
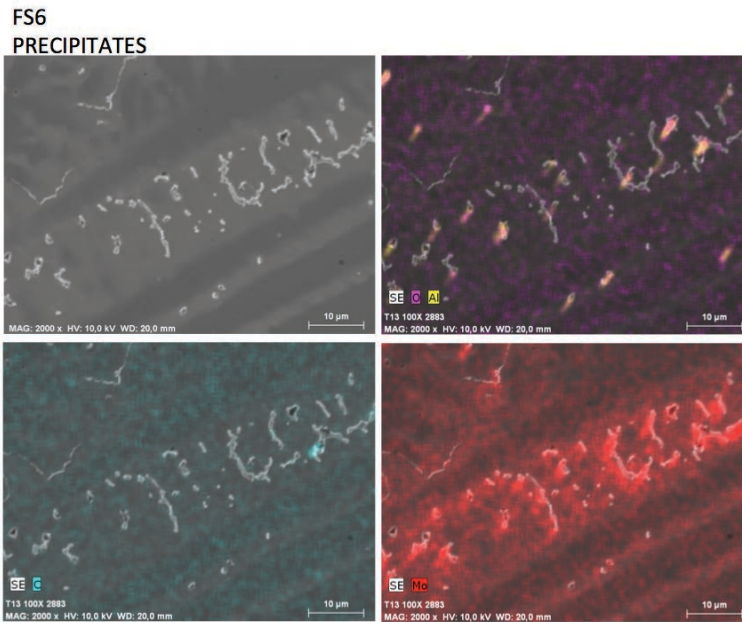
Fig 3- 114: EDX mapping on FS6, Sample G156, Identification of Mo-rich, Al-rich and Carbide particles.

At higher magnification molybdenum rich precipitate shown a shape that could produce by peritectic-like reaction, Fig 3- 115. EDX mapping performed on this precipitate shown 2 particles of aluminium oxide are observed within the precipitate, suggesting that molybdenum-rich precipitate has been nucleated and grown from them. EDX mapping also show presence of silicon and maybe some trace of zirconium and tantalum, Fig 3- 115.
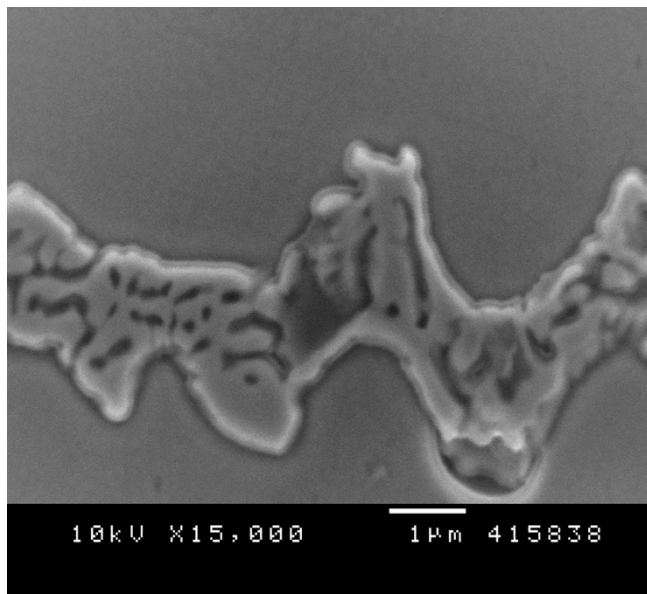
Fig 3- 115: Mo-rich precipitate type locate at FS2, FS5 and FS6
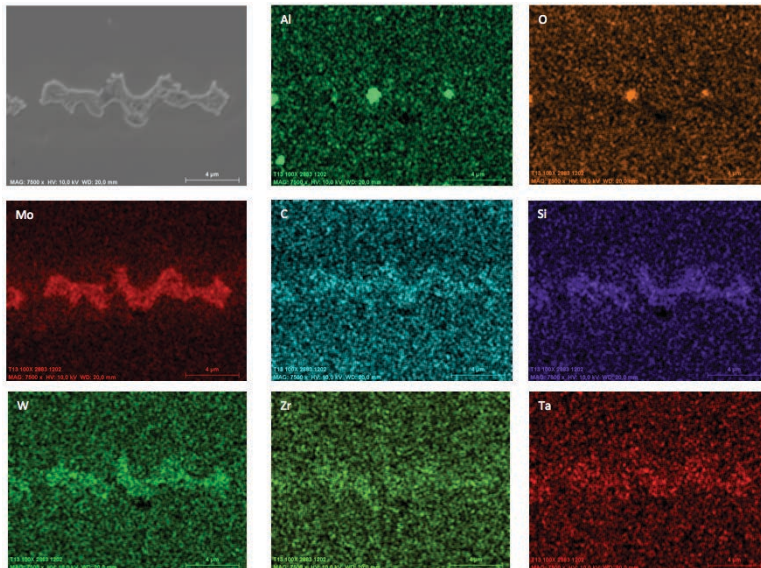
Fig 3- 116: EDX Mapping of above precipitate

The spectrum at the centre of the precipitate confirms the presence of the silicon, Fig 3- 117, as shown on EDX mapping. The stequiometric relationship between main components still is close to A7B6, but compared with previous spectrum there are no Tungsten.
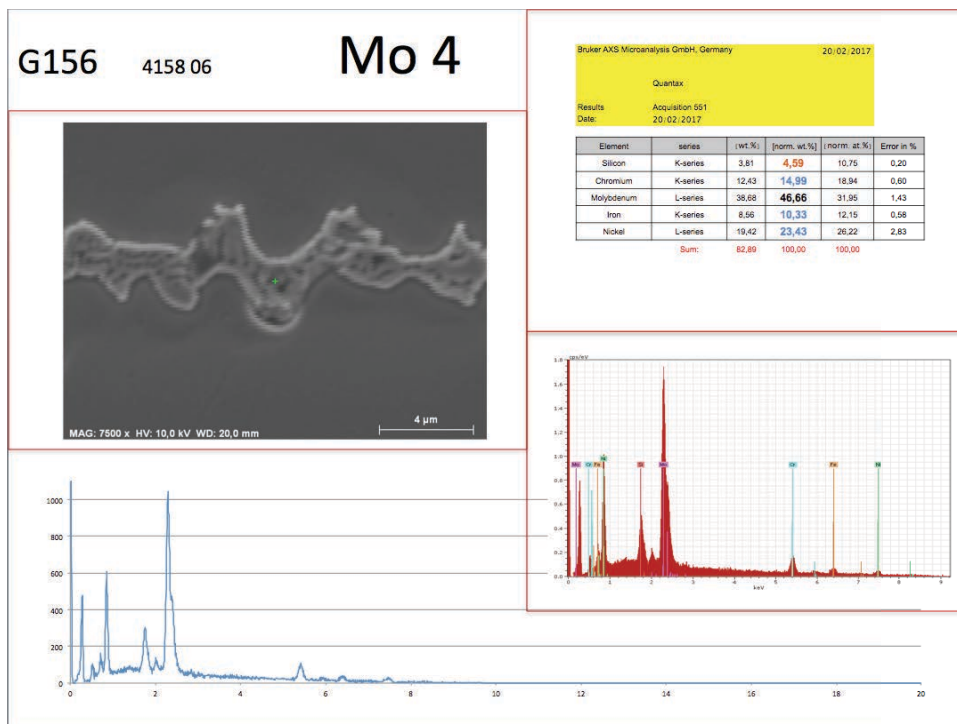
Fig 3- 117: Qualitative and Quantitative compositional analysis of Mo-rich particles. FS2, FS5 and FS6, Sample G156.

EDX analysis performed by a Field Emission Scanning Electron Microscope at 10kV, on

a thinner molybdenum rich precipitate, located in FS2 close to fusion line with FS5, shown the presence of silicon too, which confirm that this precipitate incorporate silicon on its composition.
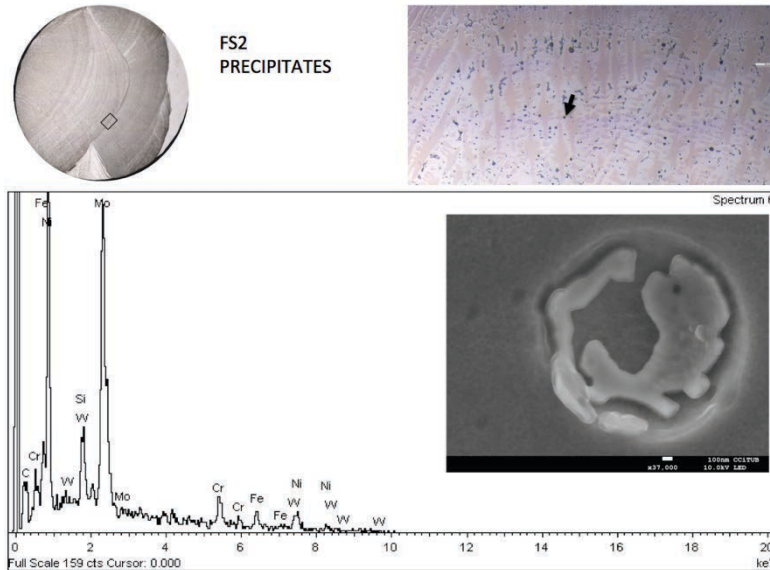
Fig 3- 118: Qualitative compositional analysis of Mo-rich particles. FS2, Sample G156.

b) Test P14.

1) Sample G91

In case of sample G91, Silicon is not detected as chemical component of the first analysed molybdenum rich particle, or silicon signal were cover by Tungsten signal, which is more or less located on same place. At left side of this Mo particle a dark area was observed, EDX spectrum show that this particles has carbon and molybdenum as main components, Fig 3- 119.
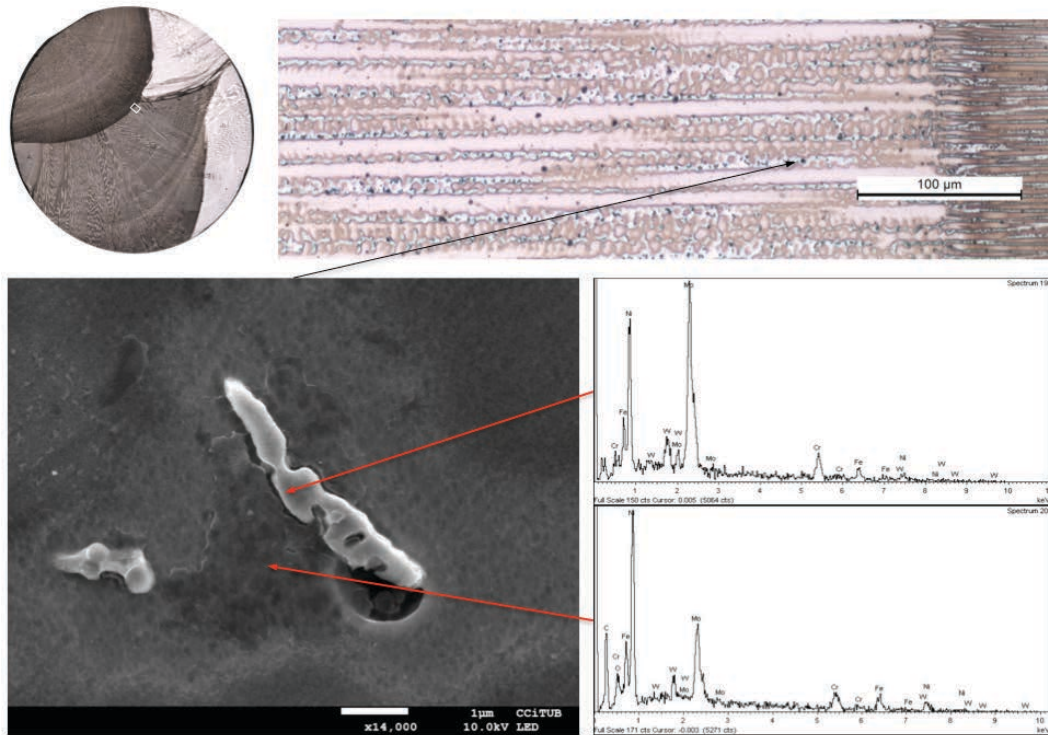
Fig 3- 119: Qualitative compositional analysis of Mo-rich particle and concentrated-carbide area particles. FS2, Sample G91.

Close to the above particle, were a found a cluster of four precipitates, Three of them were showing a simple arrange 2 components, one of them dark and the other bright, while the fourth one is showing 6 dark particles joined by bright component, Fig 3-120. All dark particles, in this picture, are aluminates, checked by EDX, while bright one corresponds with molybdenum rich precipitates. Bright area of complex particle is showing, in addition to Mo, W, Fe, Ni, what are main components of Mu/P intermetallic phase, the Si that been observed also in previous spectra like part of the intermetallic phase.
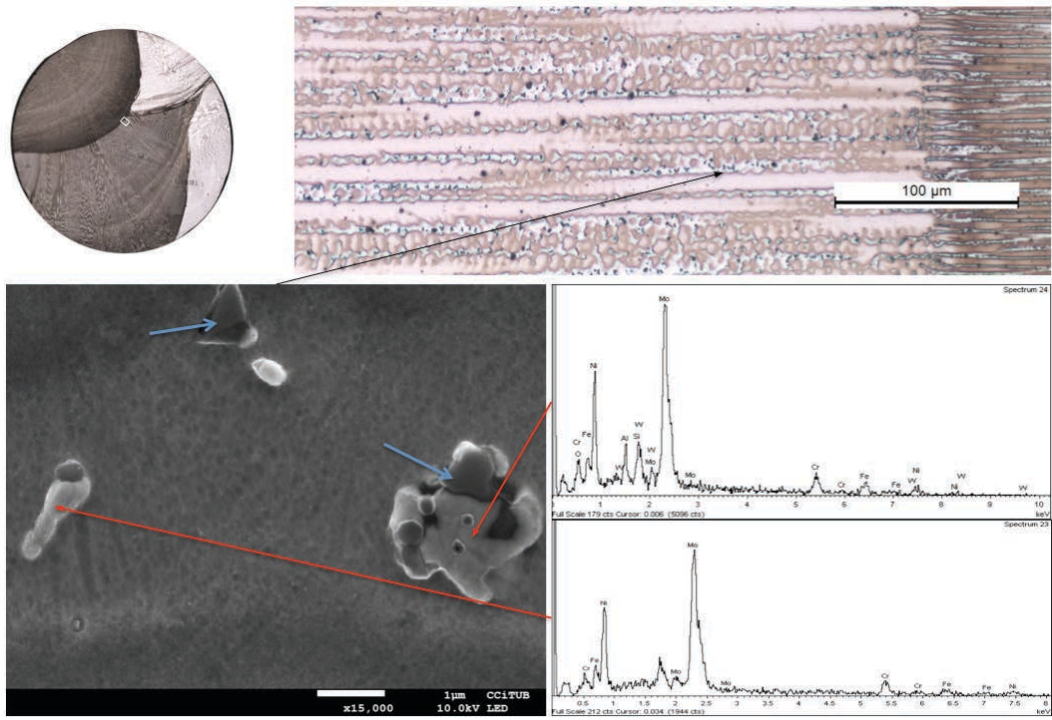
Fig 3- 120: Qualitative compositional analysis of Mo-rich and Al_xO_x particles. FS2, Sample G91.

4. Conclusions

4.1 Regarding DOE variables effect on Weld Metal Strength

1) Fluxes play a small role on deposited weld strength. However, they have a strong effect on weldability and welding performance that is translated as weld metal soundness.

2) Deposited weld metal strength is higher when welds have been done by DCEP (Direct Current-Electrode Positive) than weld metal strength of welds done by AC. This effect is stronger by using thicker wires.

3) Deposited weld metal strength is higher when welds have been done using thinner wires. The improvement effect of wire diameter is more effective on welds carried out by AC.

4) The voltage has an indirect effect on weld metal strength. The samples welded in high voltage set up are weaker than those welded with the low

5) Statistical Analysis of variance performed on obtained results show that the observed variations of the results are not statistically significant to guarantee that these differences had been produced by applied variations on tested variables. To enhance the comprehension of DOE variables effect on weld metal strength is suggested that a new set of samples been welded increasing variables ranges and with better control of hidden variables.

6) AC produces wider currents ranges (D=80 amp) than ranges of welding currents produced by DC (D=32 amp). What means that the difference between average welding current of the samples welded using AC is high, meanwhile the averages current of the samples welded by DC were closer.

4.2 Regarding Compositional Effect on Weld metal Strength

7) The compositional differences between the adjacent weld beads, which are forming the cylindrical section of the tensile specimens, were larger than initially expected. Although in most of the tensile specimens the differences of

the Nickel content were between 19% and 26%, the minimum measured difference was 6%, and the maximum reached 53%.

8) Actual Chemical composition of tensile specimen has substantial effect on its measured strength

9) The relationship between hardness and chemical composition is no so clear, at least from the statistical point of view. Although that some of the alloying mixtures are showing a hardness differences produced by thermal cycles, while other doesn't show any effect.

10) Due to the convective agitation effect, some weld beads show a high-alloyed layer at the bottom, which seems to be harmful to mechanical strength.

4.3   Regarding Fracture Surface Analysis.

11) Tensile tested samples have a texturized rupture surface produced by intergranular fracture mode, showing ductile grains decohesion by micro voids coalescence.

12) The superficial cracks opened along the cylindrical section of the tensile specimens during testing, "hook cracks" are an indication of the "sensitization" of weld metals, produced any hot or warm cracking mechanism,

13) By flux F1, the weld metal slag inclusions have an average size between 0,35 to 0,50 microns. Neither inclusion's average size nor its sizes distribution of seems to be directly determined by any of the DOE variables.

4.4   Regarding Microstructure.

14) The solidification macrostructure is mainly formed by large grains, some of them are even longer than weld bead width, this could be harmful to mechanical strength and for crack resistance.

15) Grain boundaries displacement through dendrite core has been observed. This movement seems to be produced as a stress relief mechanism.

16) Precipitates in Interdendritic area fix grain boundary displacement.

17) Evidence of residual stress has been observed on grain boundary, by the formation of uniaxial and shear microcavities.

18) There are many aluminates distributed along both interdendritic areas and within dendrites core.

19) Some of the Molybdenum-rich particles seen to be nucleated from aluminates particles. Per the references, the Mo-rich precipitates used to be nucleated from M6C carbides due to its compositional and structural similarity.

20) Some of the molybdenum-rich precipitates show Silicon as a component. That is difference than Mo-rich precipitates composition found in the references.

21) The carbides detected has been lower than expected.

22) The iron picks up due dilution reduce the number of precipitates on interdendritic zones.

23) The presence molybdenum-rich precipitates seem to improve mechanical strength.

24) Molybdenum, Tungsten, Silicon, Zirconium, and Manganese show positive segregation pattern. Meanwhile Aluminum and Iron show negative segregation.

5. Bibliography

5.1 Weldability, Welding Metallurgy and Welding Consumables:

[1-1] Manikandan Manoharan, Arivazhagan Natarajan and Nageswara Rao Muktinutalapati. **Welding Metallurgy of Corrosion-Resistant Superalloy C-276**, p. 101-110.

[1-2] D. R. Hull, R. V. Miner and C. A. Barrett. **The Effects of Seven Alloying Elements on the Microstructure and Stress-Rupture Behavior of Nickel-Base Superalloys**. Lewis Research Center. Cleveland, Ohio. October 1984.

[1-3] Dr. Norman Stephenson. **Versatility of highly-alloyed Ni-Cr-Mo welding consumables. Welding and Metal Fabrication**. Volume 58, Numbers 7 and 8, August/September and October 1990.

[1-4] Richard E. Avery and David Parsons. **Welding stainless and 9% nickel steel cryogenic vessels**. Welding Journal. November 1995, p. 45-50.

[1-5] L. Karlsson, S. Rigdal, E-L Bergquist and N. Thalberg. **Comparison of Ni-base Consumables for Submerged Arc Welding of 9% Nickel Steel**. ESAB AB, P. O. Box 8004, SE-402 77 Göteborg, Sweden.

[1-6] M. J. Cieslak. **The Welding and Solidification Metallurgy of Alloy 625. Chemical composition and solidification microstructure are correlated to hot cracking susceptibility**. Welding Research Supplement, p. 49S-56S.

[1-7] Ir. Tony Lefevre. **CTOD fracture toughness testing AT-165 ºC of a submerged arc welded joint in a 28 mm thick 9% Nickel Steel plate**. Project: Hammerfest LNG Plant. Laboratorium Soete, Universiteit Gent. May 6, 2003, p. 1-17.

[1-8] Ir. Tony Lefevre. **CTOD fracture toughness testing AT-165 ºC of a shielded metal arc welded joint in a 31 mm thick 9% Nickel Steel plate**. Project: Hammerfest LNG Plant. Laboratorium Soete, Universiteit Gent. July 6, 2003, p. 1-17.

[1-9] E. **Bauné. Electrodes enrobées freezal ENI9 pour le soudage des aciers cryogeniques à 9% Nickel. Resultats de characterisation mécanique sur joint soude en position PF Verticale montante (3G1) sur tôles 9% Nicke**l chez client CMP Dunkerque. Air Liquide Welding. 15 mai 2003, p. 1-5.

[1-10] Michael G. Castelli, Sverdrup Technology, Inc, Robert V. Miner. Nacional Aeronautics and Space Administration and David N. Robinson, University of Akron. **Thermomechanical Deformation Behavior of a Dynamic Strain Aging Alloy, Hastelloy X**. NASA Technical Memorandum 105316. April 1992, p. 1-25.

 [1-11] **Welding Metallurgy and Weldability of Nickel base alloys**, J N DuPont, J C Lippold, Samueld D. Kiser,   Copyright © 2009 by John Wiley & Sons, Inc. All rights reserved. Published by John Wiley & Sons, Inc., Hoboken, New Jersey. Lippold, John C.; Samuel D. Kiser; John N. DuPont. Welding Metallurgy and Weldability of Nickel-Base Alloys (Posición en Kindle111-113). Wiley. Kindle Edition .

[1-12] **Welding Metallurgy of Stainless Steels**, Erin Folkhard, Spirnger-Verlag Wien New York, 1988.

[1-13] **ASM Specialty Handbook**, **Nickel, cobalt and their alloys**, ASM International, Material Park OH, 2000.

5.2   Cracking:

[2-1] V. R. Davé, M. J. Cola, M. Kumar, A. J. Schwartz, and G. N. A. Hussen. **Grain Boundary Character in Alloy 690 and Ductility-Dip Cracking Susceptibility**. Welding Research. January 2004, p. 1S-5S.

[2-2] M. G. Collins and J. C. Lippold. **An Investigation of Ductility Dip Cracking in Nickel-Based Filler Materials-Part I**. Welding Research. October 2003, p. 288S-295S.

[2-3] M. G. Collins, A. J. Ramirez, and J. C. Lippold. **An Investigation of Ductility Dip Cracking in Nickel-Based Weld Metals-Part II**.. Welding Research. December 2003, p. 348S-354S.

[2-4] M. G. Collins, A. J.Ramirez, and J. C. Lippold. **An Investigation of Ductility Dip Cracking in Nickel-Based Weld Metals-Part III**. February 2004, p. 39S-49S.

[2-5] V. Shankar, T. P. S. Gill, S. L. Mannan and S. Sundaresan. **Solidification cracking in austenitic stainless steel welds**. Sadhana Vol 28, Parts 3 & 4, June/August 2003, pp. 359-382.

[2-6] R. Vallant, H. Cerjak. **The influence of different Nb/C ratio in Ni-base weld metals type 70/20 and 70/15 on the hot cracking susceptibility**. Institute for Materials Science, Welding and Forming, Graz University of Technology. Materials Center Leoben. Austria. IIW Document Nro. II-1535-04.

[2-7] Jae-Il Jang, Baik-Woo Lee, Jang-Bog Ju, Dongil Kwon and Woo-Sik Kim. **Crack-Initiation Toughness and Crack-Arrest Toughness in Advanced 9 Pct Ni Steel Welds Containing Local Brittle Zones**. Metallurgical and Materials Transactions A. Volume 33A, August 2002, p. 2615.

[2-8] F. M. L. Arantes, R. E. Trevisan. **Experimental and theoretical evaluation of solidification cracking in weld metal**. Journal of Achievements in Materials and Manufacturing Engineering. Volume 20 Issues 1-2. January-February 2007, p. 407-410.

[2-9] L. Karlsson, E-L Bergquist, S. Rigdal and N. Thalberg. **Evaluating Hot Cracking Susceptibility of Ni-base SAW Consumables for Welding of 9% Ni Steel**. ESAB AB. P.O. Box 8004, SE-402 77 Göteborg, Sweden, p. 1-19.

[2-11] John C. Lippold. **Recent Developments in Weldability Testing for Advanced Materials.** Welding Engineering Program. The Ohio State University. Columbus, OH USA.

[2-16] J. C. Lippold, N. E. Nissley, A. J. Ramirez and C. R. M. Alfonso. **Evaluation of Ductility-Dip Cracking in High-Chromium, Ni-base Filler Metals using the Strain-to-Fracture Test**. EPRI Conference June 2008.

[2-12] **Hot Cracking in Welds**, Th. Böllinghaus, H. Herold, Sringer Berling Heidelberg, New york 2005.

[2-13] **Hot Cracking in Welds IV**, Th. Böllinghaus, J Lippold, H. Herold, Sringer Berling Heidelberg, New york, First Edition 2016.

5.3   Thermodynamics:

[3-1] M. Pessah, P. Caron and T. Khan. **Effect of µ phase on the mechanical properties of a Nickel-Base single crystal Superalloy**. Office National d'Études et de Recherches Aérospatiales (ONERA). BP 72-92322 Châtillon Cedex-France. Superalloys 1992, p. 567.

[3-2] Rob Wallach. Materials Science & Metallurgy Pt IB. **Metal and Alloys: Course A. Lecture 8**. 2003-2004, p. 37-42.

[3-3] J.-C. Zhao, M. Larsen, V. Ravikumar. **Phase precipitation and time-temperature-transformation diagram of Hastelloy X**. Materials Science and Engineering A293 (2000), p. 112-119.

[3-4] K. Zhao, Y. H. Ma, L. H. Lou and Z. Q. Hu. **µ Phase in a Nickel Base Directionally Solidified Alloy**. Superalloys Division, Institute of Metal Research, Graduate School of the Chinese Academy of Sciences, Shenyang 110016, P. R. China. Materials Transactions, Vol. 46, Nº. 1 (2005) pp. 54 to 58.

[3-5] M. Raghavan, B. J. Berkowitz and J. C. Scanlon. **Electron Microscopic Analysis of Heterogeneous Precipitates in Hastelloy C-276**. Metallurgical Transactions A, Volume 13A, June 1982, p. 979-984.

[3-6] R. W. Kirchner and F. G. Hodge. **New Ni-Cr-Mo alloy demonstrates high-temperature structural stability with resultant increases in corrosion-resistance and mechanical properties**, p. 1042.

[3-7] P. E. A. Turchi, L. Kaufman and Zi-Kui Liu. **Modeling of Ni-Cr-Mo based alloys: Part I-phase stability. Computer Coupling of Phase Diagrams and Thermochemistry** 30 (2006), p. 70-87.

[3-8] M. J. Perricone, J. N. Dupont and M. J. Cieslak. **Solidification of Hastelloy Alloys: an Alternative Interpretation**. Metallurgical and Materials Transactions A. Volume 34A, May 2003, p.1127-1132.

[3-9] M. J. Cieslak, T. J. Headley and A. D. Romig, Jr. **The Welding Metallurgy of Hastelloy Alloys C-4, C-22 and C-276**. Metallurgical Transactions A. Volume 17A, November 1986, p. 2035-2047.

[3-10] N. Yukawa, M. Morinaga, H. Ezaki and Y. Murata. **Alloy Design of Superalloys by the d-Electrons Concept**. Toyohashi University of Technology, p. 935-944.

[3-11] P. E. A. Turchi, L. Kaufman and Zi-Kui Liu. **Modeling of Ni-Cr-Mo based alloys: Part II-Kinetics. Computer Coupling of Phase Diagrams and Thermochemistry** 31 (2007), p. 237-248.

 [3-12] M. J. Cieslak, G. A. Knorovsky, T. J. Headley and A. D. Romig, Jr. **The Use of New Phacomp in Understanding the Solidification Microstructure of Nickel Base Alloy Weld Metal**. Metallurgical Transactions A. Volume 17A, December 1986, p. 2107-2116.

[3-13] Gouenou Girardin and David Delafosse. **Measurement of the saturated dislocation pinning force in hydrogenated nickel and nickel base alloys**. Scripta Materialia 51 (2004), p. 1177-1181.

5.4   Process:

5.4.1   Fluxes

[4-1-1] C. S. Chai and T. W. Eagar. **Slag-Metal Equilibrium During Submerged Arc Welding**. Metallurgical Transactions B. Volume 12B, September 1981, p. 539-547.

[4-1-2] P. Kanjilal, T. K. Pal and S. K. Majumdar. **Prediction of Element Transfer in Submerged Arc Welding**. Welding Research. May 2007, Vol. 86, p. 135S-146S.

[4-1-3] C. S. Chai and T. W. Eagar. **The Effect of SAW Parameters on Weld Metal Chemistry**. Welding Research. March 1980, p. 93S-97S.

5.4.2   Saw process:

[4-2-1] Juntai. Choi, Joosung Lee and Daesoon-Kim. **Study on the strength of Ni-alloyed weld metals deposited by Squarewave AC SA power source**. Safety and Reliability of Welded Components in Energy and Processing Industry, p. 633-638.

[4-2-2] T O´Donnell. **Technical Report Nº 305080091 from Application Engineering**. David C. Lincoln Technology Center. The Lincoln Electric Company. February 15, 2005. Welding 9% Nickel Plate for SAW LNG Applications, p. 1-22.

5.4.3   Mechanical Properties:

[4-3-1] W. G. Welland. **Producing Strong Welds in 9% Nickel Steel**.. Welding Research. September 1978, p. 263S-271S.

5.4.4   Fractography:

[4-4-1] Fukuhisa Matsuda, Hiroji Nakagawa, Seishiro Ogata and Seiji Katayama. **Fractographic Investigation on Solidification Crack in the Varestraint Test of Fully Austenitic Stainless Steel**. Vol. 7, Nº 1 1978, p. 59-70.

[4-4-2] ASM Metal Handbook vol 12, **Fractography**, ASM International® The MaterialsInformation Society, Second printing, May 1992.

[4-4-3] W.T. Becker, University of Tennessee, Emeritus; S. Lampman, "**Fracture Appearance and Mechanisms of Deformation and Fracture",** ASM International, page 84

5.5   Welding LNG Tanks, Welding for Cryogenic Application. New materials consumables:

[5-1] Stefan Eich y Josef Heinemann (UTP Schweissmaterial GmbH) y A. Canadell y J. M. Miguel (Böhler-Thyssen España). **Soldadura de tanques de acero al 9 por 100 de Níquel**. Tecnología. Oilgas. Mayo 2002, p. 76,78,79.

[5-2] Jan Hilkes, Fred Neessen (Lincoln Smitweld BV) y Silvia Caballero (Lincoln KD). **Soldadura de Acero al 9%Ni para Aplicaciones GNL**. CEIS. Seminario sobre Soldabilidad de Materiales para usos Criogénicos, p. 1-20.

[5-3] Ph Bourges, M. Malingraux (Industeel), Y. Gainand (SAIPEM) y J. P. Lyonnet. **Fabrication and Welding of thick plates in 9% Nickel Cryogenic Steel**. CEIS. Seminario sobre Soldabilidad de Materiales para usos Criogénicos, p. 1-11.

[5-4] Dr. José María Miguel (Böhler-Thyssen España). **Soldadura de Tanques de Acero al 9% Níquel**. CEIS. Seminario sobre Soldabilidad de Materiales para usos Criogénicos, p. 1-6.

[5-5] Manabu Hoshino, Naoki Saitoh, Hirohide Muraoka and Osamu Saeki. **Development of Super-9%Ni Steel Plates with Superior Low-Temperature Toughness for LNG Storage Tanks**. Nippon Steel Technical Report Nº 90. July 2004, p. 20-24.

[5-6] K. Hickmann, A. Kern, U. Schriever and J. Stumpfe. **Production and Properties of High-Strength Nickel-Alloy Steel Plates for Low Temperature Applications**. ThyssenKrupp Stahl AG, Division Metallurgy/Heavy Plate, Profit Center Heavy Plate, Germany.

[5-7] Samuel D. Kiser. **Nickel-Alloy Consumable Selection for Severe Service Conditions**. Welding Journal. November 1990, p. 30-35

[5-8] G. Gregorio, R. Delporte, R. Dumezere de Soudometal Bruselas. **Soldadura de aceros 3.5, 5 y 9% Ni para aplicaciones criogénicas. Soldadura y Tecnologías de Unión**. Julio-Agosto 1990/Nº 4, p. 70-88.

[5-9] **Welding Manual of 9%Ni Steel**. Nippon Steel Corporation. February, 1975.

[5-10] Avelino Vázquez González. **La soldadura de tanques criogénicos de GNL**. Soldadura y Tecnologías de Unión 74. Marzo/Abril2002, p. 12-17.

[5-11] **Use of Nickel in the construction of LNG storage tanks. Technology LNG storage tank construction**. Petromin January/February 2005, p. 38-43.

[5-12] Douglas P. Fairchild. Patent 6114656. **Welding methods for producing ultra-high strength weldments with weld metals having excellent cryogenic temperature fracture toughness**. September 5, 2000.

[5-13] Dr. Chris Farrar. **Conferencia Sobre consumibles de Soldadura para temperaturas de Criogenia y Soldadura de Aceros 9% de Níquel**. Metrode Products Limited. Barcelona, 28 de Mayo de 1987, p. 1-29.

[5-14] F. Koshiga, J. Tanaka, I. Watanabe and T. Takamura. **Matching Ferritic Consumable Welding of 9% Nickel Steel to Enhance Safety and Economy**. Welding Research. April 1984, p. 105S-115S.

[5-15] Fredrik Hägg (AVESTA POLARIT). **How to Achieve Good Impact Properties at Cryogenic Temperatures**. CEIS. Seminario sobre Soldabilidad de Materiales para usos Criogénicos, p. 1-7.

[5-16] Tim O´Donnell and Brian Boehringer. **Technical Report Nº 709140001 from Application Engineering**. David C. Lincoln Technology Center. The Lincoln Electric Company. November 12, 2007, p. 1-12.

[5-17] Dr. Norman Stephenson. **Versatility of highly-alloyed Ni-Cr-Mo welding consumables. Welding and Metal Fabrication**. Volume 58, Numbers 7 and 8. August/September and October 1990.

[5-18] L. Karlsson, S. Rigdal, L.-E. Stridh, N. Thalberg. **Efficient Welding of 9% Nickel Steel for LNG Applications**. Stainless Steel World 2005.

[5-19] **Traducción Parcial de la Conferencia Pronunciada por el Dr. Farrar** de Metrode en Técnica del Electrodo, Barcelona. Mayo 1987. 3ª Parte.

[5-20] R. H. Tharby, BSc, AIM, AWeldl, D. J. Heath, MWeldl and J. W. Flannery, BS, MS (USA). **Welding 9% nickel steel a review of the current practices**. Conference on Welding Low Temperature Containment Plant. The Welding Institute. November 1973.

[5-21] E. F. Nippes and J. P. Balaguer. **A Study of the Weld Heat-Affected Zone Toughness of 9% Nickel Steel**. Welding Research. September 1986, p. 237S-243S.

[5-22] Richard E. Avery and David Parsons. **Welding Stainless and 9% Nickel Steel Cryogenic Vessels**. Welding Journal. November 1995, p. 45-50.

[5-23] Jan Hilkes, Fred Neessen (Lincoln Smitweld BV) y Silvia Caballero (Lincoln KD). **Soldadura de Acero al 9%Ni para Aplicaciones GNL**. Seminario sobre Soldabilidad de Materiales para usos Criogénicos, CESOL y Feria Internacional De Bilbao, España, 25 de Septiembre de 2003.

5.6   Metallography And Microstructure

[6-1] **ASM Metal Handbook vol 9**, **Metallography And Micostructure**, ASM International® The MaterialsInformation Society, Second printing, May 1992.

6. Resumen,

Hasta mediados del siglo XX, el gas era considerado como un residuo de la explotación petrolera con importantes barreras tecnológicas y económicas para su procesado y comercialización por lo que gran parte de este era quemado en los países de producción.

Fig R 1:Quemadores de Gas

Desde finales del siglo XX, el aumento de la demanda de energía sumado con los altos niveles de contaminación producido por la quema de petróleo y carbón hicieron que se desarrollen las tecnologías y normas para el transporte seguro y rentable de los gases derivados del petróleo.

Desde entonces, El gas natural ha tenido una penetración muy importante en la cadena de consumo debido a su alto poder energético y a la baja cantidad, comparada con el petróleo y carbón, de residuos, sólidos y gaseosos, que han hecho que este se perciba como un combustible limpio.
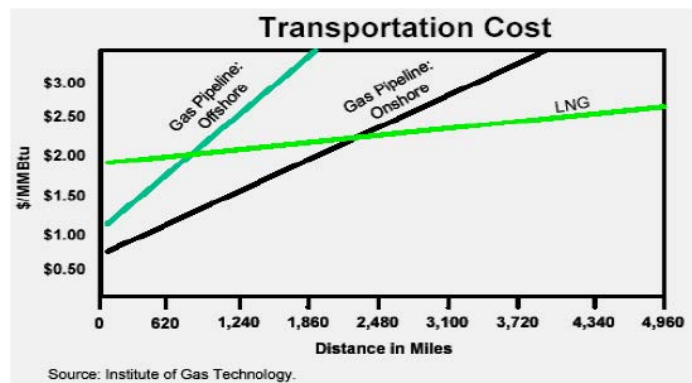
Fig R 2: Costo por MMBtu en función de la distancia entre fuente y consumo

El transporte de este producto se realiza en estado líquido, por medio de 2 tecnologías, presurización o por enfriamiento, LPG y LNG. La primera requiere de plantas de presurizado y gasoductos. Las distancias económicamente rentables para la conducción por gasoducto rondan la docena de miles de kilómetros, requiriendo de plantas de re presurización a lo largo del gasoducto.
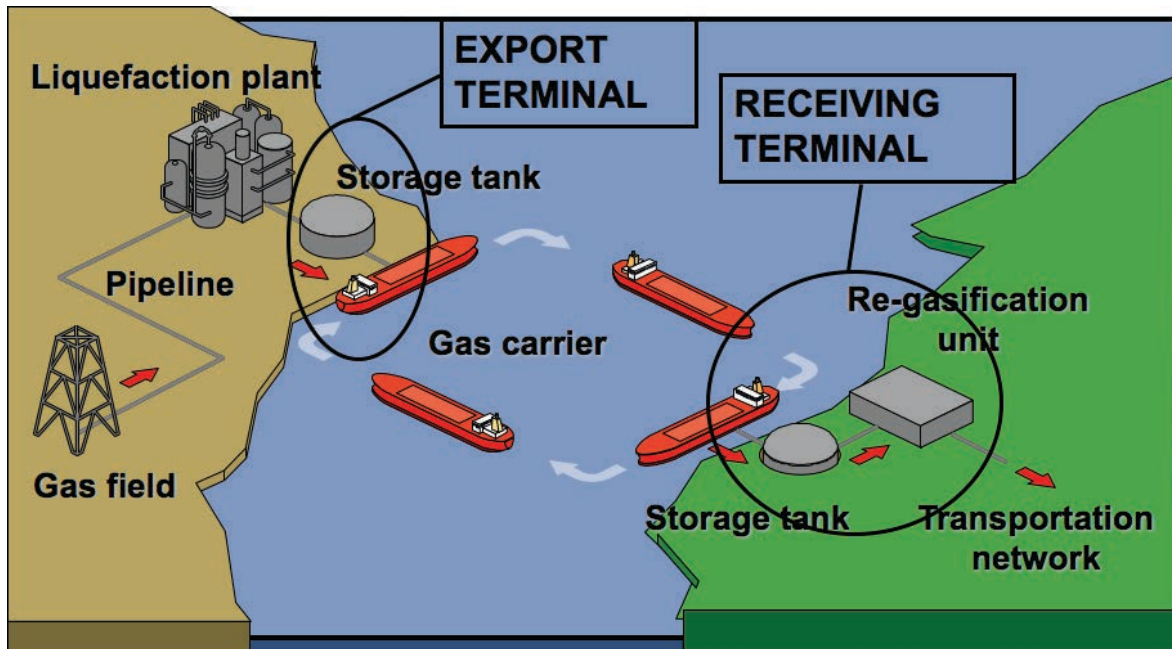
Cuando la distancia entre los productores y los consumidores que muy grande la licuación por enfriamiento a presión atmosférica es la opción más económica y segura.

En este caso en, el gas obtenido del pozo se conduce hasta la planta de licuefacción donde se realiza la separación de los distintos componentes sólidos, líquidos y gaseosos, por procesos de filtración y licuación diferencial. El Gas natural producto de este proceso se almacena temporalmente en un tanque de LNG mientras en cargado en el barco que lo transportará a destino. Una vez en destino el barco descarga a un tanque de LNG, de donde se suministra a la planta de regasificación. De esta el gas es canalizado a alta presión por los gasoductos de distribución o a las plantas de generación eléctrica.

El Gas Natural, con más de un 80% de metano tiene una temperatura de licuefacción alrededor de los -165ºC. Temperatura a la cual el gas reduce su volumen por un factor de 600/1.

Esta temperatura de operación hace inviable el uso de materiales ferríticos, debido a que estos presentan un modo de fractura frágil por debajo de una temperatura crítica, llamada de transición. Para la construcción de grandes contenedores el material más usado en es Acero A-553-T1 que tiene un contenido nominal de 9% de níquel y cuya estructura cristalina está formada por una matriz de martensita con algo de austenita

revenida. Esta microestructura se consigue a través del doble tratamiento térmico; de temple y revenido.

Para soldar este acero, para esta aplicación, no se pueden usar materiales de aportes similares al 9%Ni en vista de la imposibilidad de realizar los tratamientos térmicos necesarios para conseguir la homogeneidad de propiedades. Por otro lado, los consumibles de soldadura austeníticos presentan un comportamiento dúctil con una alta energía absorbida incluso a -196ºC y dentro de estos las aleaciones base níquel de la familia NiCrMo presentan una alta resistencia mecánica, y un coeficiente de expansión térmica cercano a del acero 9%Ni.

Composition		Range	
		Low	High
Methane	C1	83.0%	99.8%
Ethane	C2	0.0%	14.0%
Propane	C3	0.0%	4.0%
Butane	C4	0.0%	2.5%
Nitrogen	N	0.0%	1.3%

Table R 1: Composición típica del Gas Natural

Dentro de esta familia de aleaciones base níquel se ha usado la aleación Hastalloy C-276, la cual incrementa su resistencia mecánica por solución sólida, siendo los principales aleantes el cromo y molibdeno ambos alrededor de 15%, y con un 2,5% de tungsteno y un 5% de hierro. Aun que ésta es una aleación que en esencia es monofásica Gamma, el último liquido suele transformarse en carburos o fases TCP como la pase Mu y P. Estas tres fases tienen una composición muy cercana por lo que su identificación a través del EDX no es posible.

Actualmente, la mayoría de los tanques que se están construyendo tienen una capacidad de almacenamiento entre los 150.000 y 200.000, por lo que el espesor de chapa de la 1 era virola de entre 27 a 50mm, lo que implica que las soldaduras son multi pasada, necesitándose entre 16 y 30 pasadas para rellenar las juntas de esta primera virola. Normalmente las juntas verticales se sueldan con procesos manuales o semi-automáticos mientras que las horizontales se sueldan con proceso automático de arco sumergido.

Según las normas de diseño de tanques atmosféricos para almacenamiento criogénico, el espesor de las chapas está determinado por los Esfuerzos Máximos Admisibles que se calculan a partir de la resistencia mecánica del elemento estructural más débil, el metal base o la junta de soldadura. En el caso de la soldadura, la resistencia mecánica de ésta se determina a partir del ensayo de tracción con probeta cilíndricas obtenidas del metal depositado, a partir del cupón de homologación del procedimiento de soldadura.

Durante la homologación de los procedimientos manuales o semi automáticos los resultados obtenidos en los ensayos de tracción longitudinal y transversal son equivalentes. En el caso de la soldadura automática de las juntas horizontales, los resultados obtenidos de las tracciones transversales siempre han sido muy superiores a los resultados de las tracciones cilíndricas, determinando éste último resultado el espesor de las chapas del tanque, con un impacto económico de varios cientos de miles de euro por tanque.

Además de los bajos valores que se obtienen de las tracciones cilíndricas del metal de soldadura de las juntas horizontales con respecto a las tracciones transversales, con mucha frecuencia se observa que una importante diferencia en la resistencia presentada los diferentes ensayos de tracción de una misma probeta soldada, siendo estas diferencias mucho mayores que la diferencia observada entre dos condiciones experimentales. Situación que dificulta la correcta interpretación de los resultados de los diferentes ensayos o pruebas realizadas.

Como se mostrará en el capítulo 1.4 antes de este ensayo se realizaron otros 6 ensayos y unas cuantas homologaciones de procedimientos, en las cuales se usaron chapas de 12, 21, 26,5 y 27mm de espesor, con hilos de 2,4mm y 1,6mm siempre de la clasificación AWS A5.14 ER-NiCrMo-4, correspondiente a la aleación Hastalloy C-276, con diferentes fluxes, niveles de rigidización, diámetro de probeta cilíndrica etc.

Este trabajo de doctorado se he realizado sobre el séptimo ensayo realizado en verano de 2008 en las instalaciones de Lincoln Electric Cleveland, en que se probaron 4 fluxes, 2 diámetros de hilo, corriente alterna y continua y dos niveles de voltaje,

desarrollándose un diseño experimental 2^3 con cada flux. Como se realizaron todas las pruebas correspondientes al DOE, se soldaron 8 probetas por flux, y en total 32 probetas.

El material base usado en este experimento fueron chapas de acero A553 T1, con 9%Ni y templadas y revenidas con un espesor de 21mm. El diseño de junta de estas probetas es en "X" asimétrica y desbalanceada con un talón de 1mm y una separación de 2mm. Siguiendo el diseño de junta real de las chapas de producción. Con el fin de evitar que el baño de fusión se descuelgue se colocó un respaldo de flux.

Los ensayos realizados a cada probeta han sido los siguientes:

Tracciones Cilíndricas de metal de soldadura: 2 probetas ensayadas en 2008, 2 probetas ensayadas en Barcelona en 2016, en total se dispone de 124 resultados

Charpy V Notch a -196ºC

Macro

Análisis Químico General, realizado sobre las caras laterales de las macros.

Análisis Químico en las probetas de tracción.

Ensayos de microdureza Vickers y Knoob.

Las tablas con los resultados de estos ensayos están en el apéndice.

El análisis estadístico de los resultados muestra que los fluxes tienen un pequeño efecto en las propiedades mecánicas, estando todos los resultados dentro de los requisitos de diseño. Solo se observa una diferencia importante en el caso de las soldaduras realizadas con el flux F4 con el cual todos los valores UTS han estado muy por debajo de los valores esperados.

El diámetro del hilo ha mostrado un efecto similar al de las pruebas realizadas en Barcelona en 2005, y es que las soldaduras realizadas con hilo de menor diámetro presentan una resistencia mecánica superior que cuando se suelda con hilos de mayor

diámetro. Es posible que el aumento de la tasa de aporte de material junto con las menores corriente de soldadura sean la explicación de este efecto.

Con respecto al tipo de corriente, la resistencia mecánica de las soldaduras realizadas corriente alterna es ligeramente inferior que cuando se suelda con corriente continua. Es posible que efecto se produzca debido a la mayor estabilidad de arco y menores amperajes de las soladuras con DC.

El voltaje también tiene un pequeño efecto sobre la resistencia del metal de soldadura, presentando una resistencia mecánica menor aquellas soldaduras realizadas con el esquema de bajo voltaje.

Ahora, cuando se realizó el análisis estadístico de las variaciones observo que la diferencia entre las medias de los resultados no es estadísticamente significativa como para poder garantizar con una probabilidad razonable de que las variaciones de resistencia mecánica hayan sido provocadas por las variaciones realizadas sobre las variables analizadas. Hay dos lecturas de este resultado: 1ero, se deberían soldar algunos cupones adicionales ampliando los rangos de estudio de las variables analizadas. 2do, se debe analizar el experimento con el fin de determinar las variables ocultas o parámetros no controlados que estén afectando los resultados. Que será la línea de investigación que se desarrollará a continuación, y con el fin de determinar qué variables no controladas afectan a los resultados.

Dispersión de Resultados:

Como ya se comentó anteriormente y como se verá en detalle en el desarrollo del libro la resistencia mecánica de las tracciones realizadas a cada probeta presentaron una dispersión importante. Con el fin de poder visualizar con facilidad la resistencia mecánica de cada probeta con respecto al grupo total de 124 muestras ensayadas se ha creado el llamado $UTS_{ranking}$ que define la posición que ocupa el valor UTS de una probeta con respecto al grupo.

En la Table R 3 se muestra como los resultados de las tracciones realizadas a la probeta P02 están localizados en las posiciones 29, 32, 56 y 58, lo que representa que la máxima distancia entre el menor y el mayor valor del set es de 29 posiciones, este salto de 29 posiciones representa un 23% de las 124 posiciones. Este grupo contiene otras muestras que tienen sus resultados con una distancia de 23 al 25%, lo que implica que sus resultados están el dentro de un rango correspondiente a un cuarto de la muestra. Se debe toma en cuenta que los resultados mostrados en la Table R 2, corresponde a los resultados

Test	UTSranking			
P02	58	56	32	29
P05	43	30	27	38
P09	117	112	94	90
P10	83	102	108	79
P12	95	116	109	100
P13	36	60	31	55
P19	66	73	41	64
P28	35	52	26	46
P29	106	107		

Table R 2: UTS ranking de valores Cercanos

que presentaron la menor variación de resultados.

El caso extremo de dispersión lo tiene la probeta P31, que tiene a una de sus muestras ubicada en la posición 8 del ranking mientras que la peor está localizada en la posición 122 y las dos centrales están en las posiciones 82 y 87. Esta dispersión cubre el 91% del rango, lo cual en términos absolutos representa 715MPa de UTS para la probeta de mayor resistencia, alrededor de 650MPa para las resistencias intermedias y 626MPa para la mas débil. Aunque este sea el caso extremo no se puede considerar como aislado ya que otras 5 probetas presentan variaciones superiores a 80 posiciones, que representa una variación superior al 65% de la muestra.

La primera sospecha cae sobre la zona donde se ha extraído la probeta cilíndrica, ya que al ser soldaduras multipasada se sospecha que existe una

Test	UTSranking			
P01	11	19	1	28
P03a	49	53	2	50
P04	114	7	47	89
P08	93	104	5	16
P14	85	57	3	54
P15	70	33	20	51
P26	111	98	24	81
P27	97	4	45	
P31	82	8	87	122

Table R 3: UTS ranking de valores Lejanos

diferencia en la composición química en los cordones de soldadura en función de su ubicación. Como ya se mencionó antes, la aleación usada como metal de aportación

mejora su resistencia mecánica por solución sólida, por lo que las variaciones en su composición deberían afectar a su resistencia

La determinación de la composición química de cada probeta de tracción se realizó con la técnica de fluorescencia de rayos X XRF. Con el fin de corregir posibles errores de conteo o medición se realizaron varias mediciones sobre cada probeta, determinando con estos valores la composición química promedio de la sección cilíndrica de la probeta de tracción. Esta repetición de mediciones se realizó siguiendo un arreglo matricial de 3X3, o sea 9 mediciones por cada probeta. Cuando se estaba calculando los promedios y las desviaciones estándares de las mediciones realizadas se observó que varias de las mediciones realizadas presentaban variaciones importantes.

Cuando se analizaron estadísticamente los resultados de los ensayos mecánicos con la composición química especifica de las probetas de tracción se obtuvieron coeficientes de correlación superiores a 0,8 evidenciando estadísticamente la fuerte dependencia de la resistencia mecánica con la composición química.

Además de la composición química, se realizaron análisis por difracción de rayos X con el fin de determinar si existía alguna modificación estructural importante que causara la dispersión de resultados. También se aplicó el análisis fractográfico y metalográfico para determinar las características diferenciadoras entre las probetas de mayor y menor resistencia mecánica.

Conclusiones

Respecto al efecto de las variables del DOE sobre la resistencia del metal de soldadura

1) Los Fluxes juegan un pequeño rol en la resistencia del metal de soldadura. Sin embargo, tienen un fuerte efecto sobre la soldabilidad y el rendimiento de soldadura que se traduce calidad y limpieza del metal de soldadura.

2) La resistencia del metal de soldadura es más alta cuando las soldaduras han sido hechas por el DCEP (Corriente Directa-Electrodo Positivo) que la resistencia del metal

de soldadura de las soldaduras hechas por AC. Este efecto es más fuerte cuando se suelda con hilos gruesos.

3) La resistencia del metal de la soldadura es más alta cuando las soldaduras se han hecho usando alambres más finos. El efecto de mejora de Resistencia mecánica por diámetro del alambre es incrementado cuando se suelda con corriente alterna.

4) El voltaje tiene un efecto indirecto en la resistencia del metal de la soldadura. Las muestras soldadas con voltajes mas altos son más débiles que las soldadas con el bajos voltajes

5) Análisis estadístico de varianza realizado sobre los resultados obtenidos muestran que las variaciones observadas de los resultados no son estadísticamente significativas para garantizar que estas diferencias se hayan producidas por variaciones aplicadas a las variables ensayadas. Para mejorar la comprensión de las variables del DOE se sugiere el efecto sobre la resistencia del metal de soldadura que se ha soldado un nuevo conjunto de muestras aumentando las gamas de variables y con un mejor control de las variables ocultas.

6) La CA produce rangos de corrientes más amplias (D = 80 amperios) que los rangos de corrientes de soldadura producidos por DC (D = 32 amp). Lo que significa que la diferencia entre la corriente de soldadura media de las muestras soldadas usando AC es alta, mientras que la corriente media de las muestras soldadas por CC fue más estrecha.

Respecto al Efecto de Composición sobre la Resistencia del Metal de Soldadura

7) Las diferencias de composición entre los cordones de soldadura adyacentes, que forman la sección cilíndrica de los especímenes de tracción, eran mayores de lo inicialmente esperado. Aunque en la mayoría de los especímenes de tracción las diferencias de contenido de níquel estaban entre el 19% y el 26%, la diferencia mínima medida fue del 6% y el máximo alcanzó el 53%.

8) La composición química real del espécimen de tracción tiene un efecto sustancial sobre su resistencia medida

9) La relación entre dureza y composición química no es tan clara, al menos desde el punto de vista estadístico. Aunque algunas de las composiciones han mostrando diferencias de dureza producidas por ciclos térmicos, mientras que otras no muestran ningún efecto.

10) Debido al efecto de agitación convectiva, algunos cordones de soldadura muestran una banda de alta aleación en el fondo, lo que parece perjudicial para la resistencia mecánica.

En relación con el análisis de superficies de fractura.

11) Las muestras sometidas a prueba de tracción presentan una superficie de rotura texturizada producida por el modo de fractura intergranular, mostrando la decohesión ductil de los granos mediante la coalescencia de micro-huecos.

12) Las grietas superficiales abiertas a lo largo de la sección cilíndrica de los especímenes de tracción durante la prueba, las "grietas de gancho" son una indicación de la "sensibilización" de los metales de soldadura, produjeron cualquier mecanismo de fisuración en caliente o por solidificación.

13) Por el flujo F1, las inclusiones de escoria de metal de soldadura tienen un tamaño medio entre 0,35 y 0,50 micras. Ni el tamaño medio de la inclusión ni su distribución de tamaños parecen estar directamente determinados por ninguna de las variables del DOE.

En cuanto a la microestructura.

14) La macroestructura de solidificación está formada principalmente por granos grandes, algunos de ellos son incluso más largos que el ancho del cordón de soldadura, esto podría ser dañino para la resistencia mecánica y para la resistencia a la fisuración.

15) Se ha observado el desplazamiento de los límites de grano a través del núcleo dendrítico. Este movimiento parece ser producido como un mecanismo de alivio del estrés.

16) Los precipitados en el área interdendrítica fijan el desplazamiento del límite del grano.

17) Se ha observado evidencia de estrés residual en el límite del grano, mediante la formación de microcavidades uniaxiales y de corte.

18) Hay muchos aluminatos distribuidos a lo largo de ambas áreas interdendríticas y dentro del núcleo de las dendritas.

19) Algunas de las partículas ricas en molibdeno parecen haberse desarrollado a partir de aluminatos. Según las referencias, los precipitados ricos en Mo suelen nuclearse a partir de carburos M6C debido a su similitud estructural y de composición.

20) Algunos de los precipitados ricos en molibdeno muestran silicio como un componente. Segúnlas referencias encontradas, esta fase está formada por Fe, Cr, Mo, Ni y W.

21) Los carburos detectados han sido más bajos de lo esperado.

22) El increment de hierro debido a la dilución con el metal base reduce el número de precipitados en las zonas interdendríticas.

23) La presencia de precipitados ricos en molibdeno parece mejorar la resistencia mecánica.

24) El molibdeno, el tungsteno, el silicio, el circonio y el manganeso muestran un patrón de segregación positivo. Mientras tanto, el aluminio y el hierro muestran una segregación negativa.

7. Appendix

7.1.1 Weld metal Strength; Results.

Test performed in LECO, 2,0mm wire

cajon	SAMPLE	TEST	DIAM	FLUX CODE	Yield	UTS	Elong	Testing Lab
C64	10125-01A	P17	2,0 mm	F1	412 MPa	662 MPa	46,0 %	LECO
C65	10125-02A	P17	2,0 mm	F1	419 MPa	646 MPa	36,0 %	LECO
C66	10126-01A	P18	2,0 mm	F1	397 MPa	652 MPa	34,0 %	LECO
C67	10126-02A	P18	2,0 mm	F1	397 MPa	654 MPa	40,0 %	LECO
C68	10127-01A	P19	2,0 mm	F1	441 MPa	666 MPa	40,0 %	LECO
C69	10127-02A	P19	2,0 mm	F1	439 MPa	662 MPa	38,0 %	LECO
C70	10128-01A	P20	2,0 mm	F2	407 MPa	560 MPa	14,0 %	LECO
C71	10128-02A	P20	2,0 mm	F2	427 MPa	650 MPa	34,0 %	LECO
C72	10219-01A	P21	2,0 mm	F1	434 MPa	678 MPa	39,0 %	LECO
C73	10219-02A	P21	2,0 mm	F1	461 MPa	680 MPa	40,0 %	LECO
C74	10220-01A	P22	2,0 mm	F4	410 MPa	611 MPa	25,0 %	LECO
C75	10220-02A	P22	2,0 mm	F4	412 MPa	628 MPa	37,0 %	LECO
C76	10221-01A	P23	2,0 mm	F4	416 MPa	647 MPa	39,0 %	LECO
C77	10221-02A	P23	2,0 mm	F4	421 MPa	639 MPa	36,0 %	LECO
C78	10222-01A	P24	2,0 mm	F4	428 MPa	664 MPa	40,0 %	LECO
C79	10222-02A	P24	2,0 mm	F4	420 MPa	663 MPa	48,0 %	LECO
G7	10355-01A	P25	2,0 mm	F4	426 MPa	670 MPa	42,0 %	LECO
G8	10355-02A	P25	2,0 mm	F4	434 MPa	659 MPa	42,0 %	LECO
G10	10356-02A	P26	2,0 mm	F2	433 MPa	643 MPa	32,0 %	LECO
G9	10356-01A	P26	2,0 mm	F2	432 MPa	658 MPa	36,0 %	LECO
G11	10357-01A	P27	2,0 mm	F2	434 MPa	650 MPa	30,0 %	LECO
G12	10358-01A	P28	2,0 mm	F2	451 MPa	683 MPa	38,0 %	LECO
G13	10358-02A	P28	2,0 mm	F2	456 MPa	675 MPa	41,0 %	LECO
G14	10359-01A	P29	2,0 mm	F3	398 MPa	645 MPa	40,0 %	LECO
G15	10359-02A	P29	2,0 mm	F3	401 MPa	645 MPa	40,0 %	LECO
G16	10436-01A	P30	2,0 mm	F3	422 MPa	648 MPa	27,0 %	LECO
G17	10436-02A	P30	2,0 mm	F3	429 MPa	661 MPa	36,0 %	LECO
G18	10437-01A	P31	2,0 mm	F3	419 MPa	654 MPa	39,0 %	LECO
G19	10437-02A	P31	2,0 mm	F3	408 MPa	626 MPa	38,0 %	LECO
G20	10438-01A	P32	2,0 mm	F3	445 MPa	697 MPa	39,0 %	LECO
G21	10438-02A	P32	2,0 mm	F3	442 MPa	681 MPa	39,0 %	LECO

App 3- 1: Drawer Num, Sample ID, Test ID, Yield Point 0,1%, UTS, Elongation, of samples welded with wire of 2,0 mm, and test performed at LECO.

Test performed in LECO, 1,6mm wire

cajon	SAMPLE	TEST	DIAM	FLUX CODE	Yield	UTS	Elong	Testing Lab
C32	09136-01A	P01	1,6 mm	F1	446 MPa	705 MPa	36,0 %	LECO
C33	09136-02A	P01	1,6 mm	F1	442 MPa	694 MPa	35,0 %	LECO
C34	09137-01A	P02	1,6 mm	F1	445 MPa	671 MPa	31,0 %	LECO
C35	09137-02A	P02	1,6 mm	F1	439 MPa	672 MPa	37,0 %	LECO
C36	09421-01A	P03a	1,6 mm	F1	447 MPa	676 MPa	41,0 %	LECO
C37	09421-02A	P03a	1,6 mm	F1	448 MPa	674 MPa	41,0 %	LECO
C38	09138-01A	P04	1,6 mm	F1	416 MPa	641 MPa	39,0 %	LECO
P04-no	09138-02A	P04	1,6 mm	F1	425 MPa	652 MPa	38,0 %	LECO
C40	09139-01A	P05	1,6 mm	F3	445 MPa	678 MPa	38,0 %	LECO
C41	09139-02A	P05	1,6 mm	F3	443 MPa	685 MPa	37,0 %	LECO
C42	09140-01A	P06	1,6 mm	F3	439 MPa	671 MPa	43,0 %	LECO
C43	09140-02A	P06	1,6 mm	F3	453 MPa	664 MPa	43,0 %	LECO
C44	09142-01A	P07	1,6 mm	F3	445 MPa	680 MPa	39,0 %	LECO
C45	09142-02A	P07	1,6 mm	F3	439 MPa	680 MPa	41,0 %	LECO
C46	09143-01A	P08	1,6 mm	F3	420 MPa	651 MPa	41,0 %	LECO
C47	09143-02A	P08	1,6 mm	F3	425 MPa	645 MPa	40,0 %	LECO
C48	09417-02A	P09	1,6 mm	F4	422 MPa	636 MPa	39,0 %	LECO
C49	09417-01A	P09	1,6 mm	F4	427 MPa	642 MPa	39,0 %	LECO
C50	09418-01A	P10	1,6 mm	F4	425 MPa	654 MPa	39,0 %	LECO
C51	09418-02A	P10	1,6 mm	F4	425 MPa	646 MPa	36,0 %	LECO
C52	09420-01A	P11	1,6 mm	F4	420 MPa	642 MPa	35,0 %	LECO
C53	09420-02A	P11	1,6 mm	F4	421 MPa	631 MPa	37,0 %	LECO
C54	09721-01A	P12	1,6 mm	F4	443 MPa	650 MPa	32,0 %	LECO
C55	09721-02A	P12	1,6 mm	F4	432 MPa	638 MPa	30,0 %	LECO
C56	09722-01A	P13	1,6 mm	F2	425 MPa	682 MPa	46,0 %	LECO
C57	09722-02A	P13	1,6 mm	F2	427 MPa	671 MPa	45,0 %	LECO
C58	09725-01A	P14	1,6 mm	F2	430 MPa	654 MPa	40,0 %	LECO
C59	09725-02A	P14	1,6 mm	F2	435 MPa	672 MPa	39,0 %	LECO
C60	09727-01A	P15	1,6 mm	F2	437 MPa	663 MPa	40,0 %	LECO
C61	09727-02A	P15	1,6 mm	F2	434 MPa	684 MPa	41,0 %	LECO
C62	10124-01A	P16	1,6 mm	F2	432 MPa	660 MPa	37,0 %	LECO
C63	10124-02A	P16	1,6 mm	F2	450 MPa	661 MPa	38,0 %	LECO

App 3- 2: Drawer Num, Sample ID, Test ID, Yield Point 0,1%, UTS and Elongation, of samples welded with wire of 1,6 mm, and test performed at LECO.

Test Perfomed in BOSE, 2,0mm wire

cajon	SAMPLE	TEST	DIAM	FLUX CODE	Yield	UTS	Elong	Testing Lab
G129	ZOU 17.1	P17	2,0 mm	F1	412 MPa	628 MPa	41,8 %	BOSE
G130	ZOU 17.2	P17	2,0 mm	F1	451 MPa	658 MPa	37,0 %	BOSE
G131	ZOU 18.1	P18	2,0 mm	F1	487 MPa	684 MPa	35,0 %	BOSE
G132	ZOU 18.2	P18	2,0 mm	F1	452 MPa	671 MPa	34,8 %	BOSE
G133	ZOU 19.1	P19	2,0 mm	F1	480 MPa	680 MPa	35,2 %	BOSE
G134	ZOU 19.2	P19	2,0 mm	F1	474 MPa	669 MPa	35,8 %	BOSE
G135	ZOU 20.1	P20	2,0 mm	F2	452 MPa	693 MPa	36,7 %	BOSE
G136	ZOU 20.2	P20	2,0 mm	F2	465 MPa	664 MPa	38,7 %	BOSE
G137	ZOU 21.1	P21	2,0 mm	F1	487 MPa	677 MPa	37,3 %	BOSE
G138	ZOU 21.2	P21	2,0 mm	F1	473 MPa	698 MPa	34,7 %	BOSE
G139	ZOU 22.1	P22	2,0 mm	F4	433 MPa	645 MPa	35,5 %	BOSE
G140	ZOU 22.2	P22	2,0 mm	F4	437 MPa	653 MPa	35,0 %	BOSE
G141	ZOU 23.1	P23	2,0 mm	F4	425 MPa	643 MPa	37,6 %	BOSE
G142	ZOU 23.2	P23	2,0 mm	F4	446 MPa	652 MPa	35,8 %	BOSE
G143	ZOU 24.1	P24	2,0 mm	F4				BOSE
G144	ZOU 24.2	P24	2,0 mm	F4	464 MPa	692 MPa	35,0 %	BOSE
G145	ZOU 25.1	P25	2,0 mm	F4	473 MPa	697 MPa	34,8 %	BOSE
G146	ZOU 25.2	P25	2,0 mm	F4	445 MPa	670 MPa	40,4 %	BOSE
G147	ZOU 26.1	P26	2,0 mm	F2	467 MPa	648 MPa	25,3 %	BOSE
G148	ZOU 26.2	P26	2,0 mm	F2	464 MPa	692 MPa	32,1 %	BOSE
G149	ZOU 27.1	P27	2,0 mm	F2	479 MPa	722 MPa	43,2 %	BOSE
G150	ZOU 27.2	P27	2,0 mm	F2	457 MPa	678 MPa	38,6 %	BOSE
G151	ZOU 28.1	P28	2,0 mm	F2	465 MPa	689 MPa	36,9 %	BOSE
G152	ZOU 28.2	P28	2,0 mm	F2	457 MPa	678 MPa	38,6 %	BOSE
G153	ZOU 30.1	P30	2,0 mm	F3	461 MPa	659 MPa	28,8 %	BOSE
G154	ZOU 30.2	P30	2,0 mm	F3	462 MPa	668 MPa	41,2 %	BOSE
G155	ZOU 31.1	P31	2,0 mm	F3	452 MPa	657 MPa	40,2 %	BOSE
G156	ZOU 31.2	P31	2,0 mm	F3	481 MPa	715 MPa	33,2 %	BOSE
G157	ZOU 32.1	P32	2,0 mm	F3	466 MPa	690 MPa	39,6 %	BOSE
G158	ZOU 32.2	P32	2,0 mm	F3	473 MPa	706 MPa	40,9 %	BOSE

App 3- 3: Drawer Num, Sample ID, Test ID, Yield Point 0,1%, UTS and Elongation, of samples welded with wire of 2,0 mm, and test performed at BOSE.

Test performed in BOSE, 1,6mm wire

cajon	SAMPLE	TEST	DIAM	FLUX CODE	Yield	UTS	Elong	Testing Lab
G65	ZOU 01.1	P01	1,6 mm	F1	525 MPa	731 MPa	40,5 %	BOSE
G66	ZOU 01.2	P01	1,6 mm	F1	475 MPa	686 MPa	33,9 %	BOSE
G67	ZOU 02.1	P02	1,6 mm	F1	467 MPa	684 MPa	34,7 %	BOSE
G68	ZOU 02.2	P02	1,6 mm	F1	460 MPa	686 MPa	40,7 %	BOSE
G69	ZOU 3a.1	P03a	1,6 mm	F1	503 MPa	725 MPa	41,0 %	BOSE
G70	ZOU 3a.2	P03a	1,6 mm	F1	466 MPa	675 MPa	42,0 %	BOSE
G71	ZOU 04.1	P04	1,6 mm	F1	504 MPa	715 MPa	40,8 %	BOSE
G72	ZOU 04.2	P04	1,6 mm	F1	444 MPa	677 MPa	44,6 %	BOSE
G73	ZOU 05.1	P05	1,6 mm	F3	447 MPa	688 MPa	42,3 %	BOSE
G74	ZOU 05.2	P05	1,6 mm	F3	470 MPa	680 MPa	39,9 %	BOSE
G75	ZOU 06.1	P06	1,6 mm	F3	473 MPa	700 MPa	37,2 %	BOSE
G76	ZOU 06.2	P06	1,6 mm	F3	455 MPa	698 MPa	41,9 %	BOSE
G77	ZOU 07.1	P07	1,6 mm	F3	493 MPa	701 MPa	38,1 %	BOSE
G78	ZOU 07.2	P07	1,6 mm	F3	481 MPa	706 MPa	39,1 %	BOSE
G79	ZOU 08.1	P08	1,6 mm	F3	476 MPa	721 MPa	40,3 %	BOSE
G80	ZOU 08.2	P08	1,6 mm	F3	472 MPa	697 MPa	38,2 %	BOSE
G81	ZOU 09.1	P09	1,6 mm	F4	461 MPa	651 MPa	40,1 %	BOSE
G82	ZOU 09.2	P09	1,6 mm	F4	471 MPa	652 MPa	40,8 %	BOSE
G83	ZOU 10.1	P10	1,6 mm	F4	443 MPa	643 MPa	33,2 %	BOSE
G84	ZOU 10.2	P10	1,6 mm	F4	463 MPa	658 MPa	36,2 %	BOSE
G85	ZOU 11.1	P11	1,6 mm	F4	425 MPa	654 MPa	41,0 %	BOSE
G86	ZOU 11.2	P11	1,6 mm	F4	455 MPa	636 MPa	34,0 %	BOSE
G87	ZOU 12.1	P12	1,6 mm	F4	457 MPa	643 MPa	33,7 %	BOSE
G88	ZOU 12.2	P12	1,6 mm	F4	454 MPa	647 MPa	38,3 %	BOSE
G89	ZOU 13.1	P13	1,6 mm	F2	470 MPa	685 MPa	43,5 %	BOSE
G90	ZOU 13.2	P13	1,6 mm	F2	452 MPa	673 MPa	41,6 %	BOSE
G91	ZOU 14.1	P14	1,6 mm	F2	481 MPa	724 MPa	39,4 %	BOSE
G92	ZOU 14.2	P14	1,6 mm	F2	455 MPa	674 MPa	39,6 %	BOSE
G93	ZOU 15.1	P15	1,6 mm	F2	462 MPa	694 MPa	39,8 %	BOSE
G94	ZOU 15.2	P15	1,6 mm	F2	447 MPa	675 MPa	38,8 %	BOSE
G95	ZOU 16.1	P16	1,6 mm	F2	486 MPa	717 MPa	42,8 %	BOSE
G96	ZOU 16.2	P16	1,6 mm	F2	483 MPa	692 MPa	36,0 %	BOSE

App 3- 4: Drawer Num, Sample ID, Test ID, Yield Point 0,1%, UTS and Elongation, of samples welded with wire of 1,6 mm, and test performed at BOSE.

7.1.2   Weld metal Toughness; Results.

Charpy V Notch @ -196°C			
	CVN 1	CVN 2	CVN 3	Avg
P01	76 J	75 J	75 J	75,3 J
P02	94 J	91 J	89 J	91,3 J
P03a	79 J	73 J	81 J	77,7 J
P04	79 J	80 J	79 J	79,3 J
P05	85 J	84 J	84 J	84,3 J
P06	80 J	83 J	83 J	82,0 J
P07	92 J	89 J	89 J	90,0 J
P08	89 J	89 J	91 J	89,7 J
P09	85 J	85 J	84 J	84,7 J
P10	88 J	84 J	87 J	86,3 J
P11	92 J	83 J	75 J	83,3 J
P12	80 J	75 J	69 J	74,7 J
P13	98 J	99 J	91 J	96,0 J
P14	95 J	91 J	95 J	93,7 J
P15	95 J	92 J	89 J	92,0 J
P16	83 J	85 J	83 J	83,7 J
P17	81 J	72 J	75 J	76,0 J
P18	76 J	72 J	79 J	75,7 J
P19	71 J	69 J	72 J	70,7 J
P20	87 J	85 J	85 J	85,7 J
P21	66 J	71 J	65 J	67,3 J
P22	91 J	83 J	91 J	88,3 J
P23	83 J	73 J	76 J	77,3 J
P24	80 J	77 J	75 J	77,3 J
P25	72 J	76 J	79 J	75,7 J
P26	79 J	83 J	76 J	79,3 J
P27	81 J	88 J	73 J	80,7 J
P28	73 J	77 J	72 J	74,0 J
P29	83 J	80 J	79 J	80,7 J
P30	79 J	81 J	73 J	77,7 J
P31	69 J	66 J	65 J	66,7 J
P32	68 J	69 J	69 J	68,7 J

App 3- 5: Charpy V Notch results per Test, Single and Average Values.

7.1.3 Weld Metal General Chemical Composition; Results.

Report number	%P	%S	%O	%N	%C	%Mg	%Cu	%B	%Pb	%Ce	%Ca	%Ti	%Al	%Si	%Mn	%Zr	%V	%Nb	%Ta	%Co	%W	%Fe	%Mo	%Cr	%Ni	LOCATION	FLUX CODE	DIAM	TEST	ID
09136	0,003	0,004	0,048	0,014	0,008	0,003	0,000	0,003	0,000	0,010	0,003	0,010	0,080	0,200	0,380	0,001	0,020	0,016	0,000	0,02	2,30	25,43	12,28	12,16	47,05	ID	F1	1,6	P01	09136-01A
09136		0,004	0,048	0,014	0,006				0,000	0,010	0,003	0,010	0,080	0,200	0,370	0,001	0,020	0,015	0,000	0,02	2,45	22,61	12,79	12,63	48,76	OD	F1	1,6	P01	09136-02A
09137	0,004	0,006	0,045	0,011	0,011	0,003	0,000	0,003	0,000	0,010	0,003	0,010	0,080	0,210	0,370	0,001	0,020	0,015	0,010	0,02	2,67	18,86	13,27	13,35	51,07	ID	F1	1,6	P02	09137-01A
09137	0,004	0,007	0,045	0,011	0,011	0,003	0,000	0,003	0,000	0,010	0,002	0,010	0,090	0,220	0,390	0,001	0,020	0,016	0,000	0,02	2,27	26,06	12,10	12,17	46,59	OD	F1	1,6	P02	09137-02A
09421	0,004	0,004	0,058	0,009	0,010	0,003	0,000	0,003	0,000	0,010	0,003	0,010	0,090	0,230	0,380	0,001	0,020	0,015	0,010	0,02	2,59	19,81	13,32	13,47	50,00	ID	F1	1,6	P03a	09421-01A
09421	0,004	0,004	0,058	0,009	0,009	0,003	0,000	0,003	0,000	0,010	0,002	0,010	0,080	0,220	0,370	0,001	0,020	0,015	0,000	0,02	2,18	27,02	12,02	11,67	46,34	OD	F1	1,6	P03a	09421-02A
09138	0,003	0,004	0,061	0,008	0,010	0,002	0,000	0,003	0,000	0,010	0,002	0,010	0,080	0,230	0,360	0,001	0,020	0,014	0,010	0,02	2,63	18,71	13,55	13,35	50,98	ID	F1	1,6	P04	09138-01A
09138	0,004	0,004	0,061	0,008	0,007	0,003	0,000	0,003																		OD	F1	1,6	P04	
09139	0,005	0,008	0,067	0,027	0,018	0,003	0,000	0,003	0,000	0,010	0,002	0,010	0,060	0,310	0,380	0,001	0,020	0,016	0,000	0,02	2,34	24,69	12,24	11,97	47,91	ID	F3	1,6	P05	09139-01A
09139	0,005	0,007	0,067	0,027	0,009	0,003	0,000	0,003	0,000	0,010	0,002	0,010	0,050	0,330	0,370	0,001	0,020	0,016	0,000	0,02	2,40	23,61	12,47	12,16	48,50	OD	F3	1,6	P05	09139-02A
09140	0,005	0,004	0,062	0,013	0,012	0,003	0,000	0,003	0,000	0,010	0,002	0,010	0,060	0,310	0,380	0,001	0,020	0,015	0,000	0,02	2,41	23,43	12,52	12,36	48,44	ID	F3	1,6	P06	09140-01A
09140	0,005	0,004	0,062	0,013	0,006	0,000	0,000	0,003	0,000	0,010	0,002	0,010	0,050	0,330	0,370	0,001	0,020	0,015	0,000	0,02	2,42	23,11	12,61	12,39	48,62	OD	F3	1,6	P06	09140-02A
09142	0,005	0,010	0,047	0,023	0,010	0,004	0,000	0,002	0,000	0,010	0,009	0,010	0,060	0,280	0,380	0,001	0,020	0,016	0,000	0,02	2,52	21,96	12,70	12,72	49,26	ID	F3	1,6	P07	09142-01A
09142	0,005	0,007	0,047	0,023	0,008	0,003	0,000	0,002	0,000	0,010	0,003	0,010	0,060	0,280	0,370	0,001	0,020	0,016	0,000	0,02	2,33	25,10	12,11	12,03	47,61	OD	F3	1,6	P07	09142-02A
09143	0,005	0,007	0,049	0,021	0,008	0,004	0,000	0,003	0,000	0,010	0,003	0,010	0,060	0,300	0,370	0,001	0,020	0,015	0,000	0,02	2,10	29,16	11,65	11,05	45,22	ID	F3	1,6	P08	09143-01A
09143	0,005	0,007	0,049	0,021	0,014	0,004	0,000	0,001	0,000	0,010	0,004	0,010	0,060	0,300	0,360	0,001	0,020	0,015	0,000	0,02	2,45	22,50	12,70	12,43	49,09	OD	F3	1,6	P08	09143-02A
09417	0,004	0,003	0,030	0,008	0,013	0,002	0,000	0,001	0,000	0,010	0,003	0,010	0,120	0,170	1,780	0,001	0,020	0,017	0,000	0,02	2,25	22,93	12,40	12,89	47,36	ID	F4	1,6	P09	09417-01A
09417	0,004	0,003	0,300	0,008	0,010	0,003	0,000	0,002	0,010	0,010	0,005	0,010	0,120	0,170	1,870	0,001	0,020	0,016	0,010	0,02	2,34	20,29	12,93	13,32	48,83	OD	F4	1,6	P09	09417-02A
09418	0,005	0,004	0,029	0,010	0,009	0,003	0,000	0,002	0,000	0,010	0,002	0,010	0,120	0,150	1,560	0,001	0,020	0,017	0,000	0,02	2,36	21,53	12,56	13,17	48,42	ID	F4	1,6	P10	09418-01A
09418	0,005	0,004	0,029	0,010	0,011	0,002	0,000	0,002	0,000	0,010	0,002	0,010	0,120	0,150	1,390	0,001	0,020	0,017	0,000	0,02	2,17	25,09	11,94	12,29	46,74	OD	F4	1,6	P10	09418-02A
09420	0,004	0,004	0,044	0,008	0,010	0,002	0,000	0,002	0,000	0,010	0,002	0,010	0,130	0,170	1,570	0,001	0,020	0,017	0,010	0,02	2,32	22,26	12,59	13,09	47,77	ID	F4	1,6	P11	09420-01A
09420		0,004	0,044	0,008	0,015																					OD	F4	1,6	P11	09420-02A
09721	0,003	0,003	0,049	0,008	0,011	0,002	0,000	0,002	0,000	0,010	0,002	0,010	0,130	0,160	1,350	0,001	0,020	0,018	0,010	0,02	2,46	19,88	12,96	13,79	49,15	ID	F4	1,6	P12	09721-01A
09721	0,004	0,004	0,049	0,008	0,010	0,002	0,000	0,002	0,010	0,010	0,003	0,010	0,060	0,160	1,360	0,001	0,020	0,019	0,000	0,02	2,39	21,43	12,62	13,45	48,34	OD	F4	1,6	P12	09721-02A
09772	0,003	0,004	0,044	0,031	0,015	0,003	0,000	0,002	0,030	0,010	0,014	0,010	0,080	0,270	0,380	0,001	0,020	0,016	0,000	0,13	2,38	23,80	12,74	12,85	47,42	ID	F2	1,6	P13	09722-01A
09772	0,006	0,004	0,044	0,031	0,019	0,006	0,030	0,003	0,010	0,010	0,002	0,010	0,080	0,280	0,380	0,001	0,020	0,020	0,000	0,15	2,32	22,00	13,18	12,84	48,63	OD	F2	1,6	P13	09722-02A
09725	0,006	0,004	0,041	0,026	0,012	0,006	0,040	0,003	0,010	0,010	0,003	0,010	0,090	0,280	0,370	0,001	0,020	0,019	0,010	0,16	2,25	22,30	13,66	12,75	48,03	ID	F2	1,6	P14	09725-01A
09725	0,006	0,004	0,041	0,026	0,008	0,007	0,040	0,003	0,000	0,010	0,002	0,010	0,070	0,270	0,380	0,001	0,020	0,020	0,000	0,15	2,43	19,26	14,12	13,48	49,66	OD	F2	1,6	P14	09725-02A
09727	0,007	0,004	0,047	0,016	0,010	0,006	0,040	0,003	0,000	0,010	0,002	0,010	0,070	0,300	0,390	0,001	0,020	0,022	0,000	0,16	2,13	26,21	12,46	11,60	46,54	ID	F2	1,6	P15	09727-01A
09727	0,007	0,004	0,047	0,016	0,011	0,005	0,030	0,003	0,000	0,010	0,002	0,010	0,080	0,300	0,390	0,002	0,020	0,023	0,000	0,16	2,22	24,40	12,71	11,93	47,67	OD	F2	1,6	P15	09727-02A
10124	0,006	0,004	0,056	0,015	0,011	0,005	0,040	0,003	0,000	0,010	0,002	0,010	0,090	0,340	0,380	0,002	0,020	0,021	0,000	0,17	2,50	20,90	14,07	13,09	48,35	ID	F2	1,6	P16	10124-01A
10124	0,007	0,004	0,056	0,015	0,011	0,006	0,040	0,003	0,000	0,010	0,002	0,010	0,090	0,380	0,390	0,003	0,020	0,022	0,010	0,17	2,70	17,42	14,52	13,82	50,42	OD	F2	1,6	P16	10124-02A

App 3- 6: Test ID, Diameter of the Wire, Flux Code, side of measurement and General Chemical Composition, of samples welded with wire of 1,6 mm.

ID	TEST	DIAM	FLUX CODE	LOCATION	%Ni	%Cr	%Mo	%Fe	%W	%Co	%Ta	%Nb	%V	%Zr	%Mn	%Si	%Al	%Ti	%Ca	%Ce	%Pb	%B	%Cu	%Mg	%C	%N	%O	%S	%P	Report number
10125-01A	P17	2	F1	ID	47,36	13,21	13,84	21,80	2,73	0,09	0,000	0,017	0,130	0,001	0,370	0,280	0,120	0,010	0,003	0,000	0,000	0,003	0,000	0,004	0,009	0,013	0,045	0,004	0,004	10125
10125-02A	P17	2	F1	OD	42,63	11,50	12,44	30,14	2,25	0,08	0,000	0,016	0,110	0,001	0,390	0,260	0,120	0,010	0,003	0,000	0,000	0,003	0,000	0,004	0,013	0,013	0,045	0,004	0,004	10125
10126-01A	P18	2	F1	ID	46,33	11,73	13,04	25,45	2,44	0,08	0,000	0,016	0,120	0,001	0,370	0,260	0,120	0,010	0,019	0,000	0,000	0,003	0,000	0,005	0,010	0,013	0,044	0,004	0,005	10126
10126-02A	P18	2	F1	OD	48,12	12,55	13,44	22,20	2,65	0,08	0,000	0,017	0,130	0,001	0,380	0,260	0,120	0,010	0,003	0,000	0,000	0,003	0,000	0,004	0,008	0,013	0,044	0,004	0,005	10126
10127-01A	P19	2	F1	ID	47,15	12,91	13,91	22,28	2,66	0,08	0,000	0,016	0,130	0,001	0,370	0,300	0,120	0,010	0,003	0,000	0,000	0,003	0,000	0,004	0,011	0,010	0,055	0,004	0,004	10127
10127-02A	P19	2	F1	OD	47,05	13,05	13,92	22,20	2,71	0,09	0,000	0,016	0,130	0,001	0,370	0,300	0,120	0,010	0,002	0,000	0,000	0,003	0,000	0,004	0,011	0,010	0,055	0,004	0,004	10127
10128-01A	P20	2	F2	ID	41,69	11,17	12,15	31,73	2,22	0,07	0,000	0,016	0,100	0,001	0,380	0,330	0,080	0,010	0,002	0,000	0,000	0,002	0,000	0,004	0,017	0,032	0,037	0,005	0,004	10218
10128-02A	P20	2	F2	OD	45,32	12,48	13,15	25,42	2,57	0,08	0,000	0,016	0,120	0,001	0,380	0,340	0,090	0,010	0,002	0,000	0,000	0,002	0,000	0,005	0,017	0,032	0,037	0,005	0,005	10218
10219-01A	P21	2	F1	ID	47,89	13,49	13,93	20,78	2,83	0,09	0,000	0,016	0,140	0,001	0,380	0,280	0,140	0,010	0,002	0,000	0,000	0,003	0,000	0,004	0,010	0,011	0,045	0,006	0,004	10219
10219-02A	P21	2	F1	OD	47,56	13,82	14,09	20,58	2,87	0,09	0,000	0,017	0,140	0,001	0,380	0,300	0,090	0,010	0,002	0,000	0,000	0,003	0,000	0,004	0,010	0,011	0,045	0,005	0,004	10219
10220-01A	P22	2	F4	ID	43,13	12,21	12,60	27,48	2,25	0,08	0,000	0,018	0,120	0,001	1,750	0,230	0,090	0,010	0,004	0,000	0,000	0,001	0,000	0,003	0,008	0,013	0,029	0,004	0,004	10220
10220-02A	P22	2	F4	OD	44,01	12,68	12,97	25,70	2,36	0,08	0,000	0,017	0,120	0,001	1,690	0,220	0,100	0,010	0,003	0,000	0,000	0,001	0,000	0,004	0,009	0,013	0,029	0,004	0,004	10220
10221-01A	P23	2	F4	ID	42,36	11,73	12,29	29,54	2,19	0,07	0,000	0,017	0,110	0,001	1,340	0,200	0,090	0,010	0,003	0,000	0,000	0,002	0,000	0,004	0,013	0,012	0,031	0,004	0,004	10221
10221-02A	P23	2	F4	OD	42,65	11,93	12,49	28,77	2,22	0,08	0,000	0,016	0,120	0,001	1,410	0,200	0,090	0,010	0,002	0,000	0,000	0,002	0,000	0,003	0,012	0,012	0,031	0,004	0,004	10221
10222-01A	P24	2	F4	ID	45,66	12,93	12,93	22,99	2,46	0,08	0,000	0,016	0,130	0,001	1,730	0,230	0,090	0,010	0,002	0,000	0,000	0,002	0,000	0,003	0,012	0,011	0,036	0,005	0,004	10222
10222-02A	P24	2	F4	OD	47,01	13,51	13,95	20,69	2,62	0,08	0,000	0,016	0,013	0,001	1,600	0,220	0,100	0,010	0,002	0,000	0,000	0,002	0,000	0,004	0,019	0,011	0,036	0,004	0,005	10222
10355-01A	P25	2	F4	ID																					0,010	0,009	0,030	0,004		10355
10355-02A	P25	2	F4	OD	44,82	12,07	12,23	26,46	2,35	0,08	0,000	0,190	0,120	0,001	1,500	0,200	0,100	0,010	0,006	0,000	0,000	0,002	0,000	0,004	0,013	0,064	0,037	0,004	0,005	10355
10356-01A	P26	2	F2	ID	44,21	11,74	12,42	28,17	2,41	0,08	0,000	0,017	0,110	0,001	0,390	0,320	0,090	0,010	0,002	0,000	0,000	0,002	0,000	0,005	0,016	0,037	0,042	0,008	0,004	10356
10356-02A	P26	2	F2	OD	45,85	12,55	13,05	24,87	2,60	0,08	0,000	0,017	0,120	0,001	0,390	0,330	0,100	0,010	0,003	0,000	0,000	0,003	0,000	0,005	0,016	0,037	0,042	0,008	0,004	10356
10357	P27	2	F2	ID	45,82	12,30	12,93	25,26	2,59	0,08	0,000	0,017	0,120	0,001	0,390	0,370	0,090	0,010	0,002	0,000	0,000	0,003	0,000	0,017	0,013	0,094	0,048	0,008	0,005	10357
10357	P27	2	F2	OD	49,41	13,92	14,11	18,34	3,04	0,09	0,000	0,018	0,140	0,002	0,390	0,400	0,100	0,010	0,002	0,010	0,000	0,003	0,000	0,005	0,009	0,094	0,048	0,008	0,005	10357
10358-01A	P28	2	F2	ID	47,71	13,10	13,41	21,82	2,81	0,09	0,000	0,018	0,130	0,001	0,390	0,400	0,090	0,010	0,002	0,000	0,000	0,003	0,000	0,004	0,011	0,095	0,051	0,008	0,005	10358
10358-02A	P28	2	F2	OD	48,72	13,75	13,89	19,55	2,93	0,09	0,000	0,017	0,014	0,001	0,400	0,380	0,100	0,010	0,002	0,000	0,000	0,003	0,000	0,005	0,009	0,016	0,058	0,008	0,005	10358
10359-01A	P29	2	F3	ID	42,36	10,93	11,94	31,49	2,24	0,07	0,000	0,017	0,100	0,001	0,370	0,360	0,080	0,010	0,002	0,000	0,000	0,002	0,000	0,004	0,020	0,105	0,050	0,008	0,005	10359
10359-02A	P29	2	F3	OD	38,89	8,91	10,14	41,34	1,72	0,06	0,000	0,016	0,080	0,001	0,400	0,320	0,070	0,010	0,002	0,010	0,000	0,002	0,000	0,004	0,017	0,105	0,050	0,009	0,004	10359
10436-01A	P30	2	F3	ID	41,97	10,71	11,26	32,76	2,22	0,07	0,000	0,018	0,100	0,001	0,390	0,350	0,090	0,010	0,009	0,000	0,000	0,002	0,000	0,006	0,013	0,026	0,051	0,006	0,006	10436
10436-02A	P30	2	F3	OD	42,02	11,13	11,56	31,93	2,27	0,08	0,000	0,018	0,110	0,001	0,400	0,350	0,090	0,010	0,003	0,000	0,000	0,002	0,000	0,005	0,014	0,026	0,051	0,005	0,005	10436
10437-01A	P31	2	F3	ID	46,20	11,54	13,32	25,56	2,32	0,08	0,000	0,015	0,110	0,001	0,360	0,370	0,090	0,010	0,002	0,000	0,000	0,003	0,000	0,005	0,012	0,012	0,049	0,005	0,005	10437
10437-02A	P31	2	F3	OD	50,52	13,30	14,70	17,64	2,72	0,09	0,010	0,013	0,130	0,001	0,370	0,390	0,100	0,010	0,002	0,000	0,000	0,003	0,000	0,005	0,009	0,012	0,073	0,005	0,006	10437
10438-01A	P32	2	F3	ID	47,32	13,05	13,64	22,11	2,74	0,08	0,000	0,016	0,120	0,001	0,380	0,400	0,100	0,010	0,002	0,000	0,000	0,003	0,000	0,005	0,010	0,012	0,073	0,005	0,005	10438
10438-02A	P32	2	F3	OD	49,14	13,71	14,20	18,82	2,95	0,09	0,000	0,016	0,130	0,001	0,380	0,400	0,110	0,010	0,002	0,000	0,000	0,003	0,000	0,006	0,010	0,012	0,073	0,006	0,006	10438

App 3- 7: Test ID, Diameter of the Wire, Flux Code, side of measurement and General Chemical Composition, of samples welded with wire of 2,0 mm.
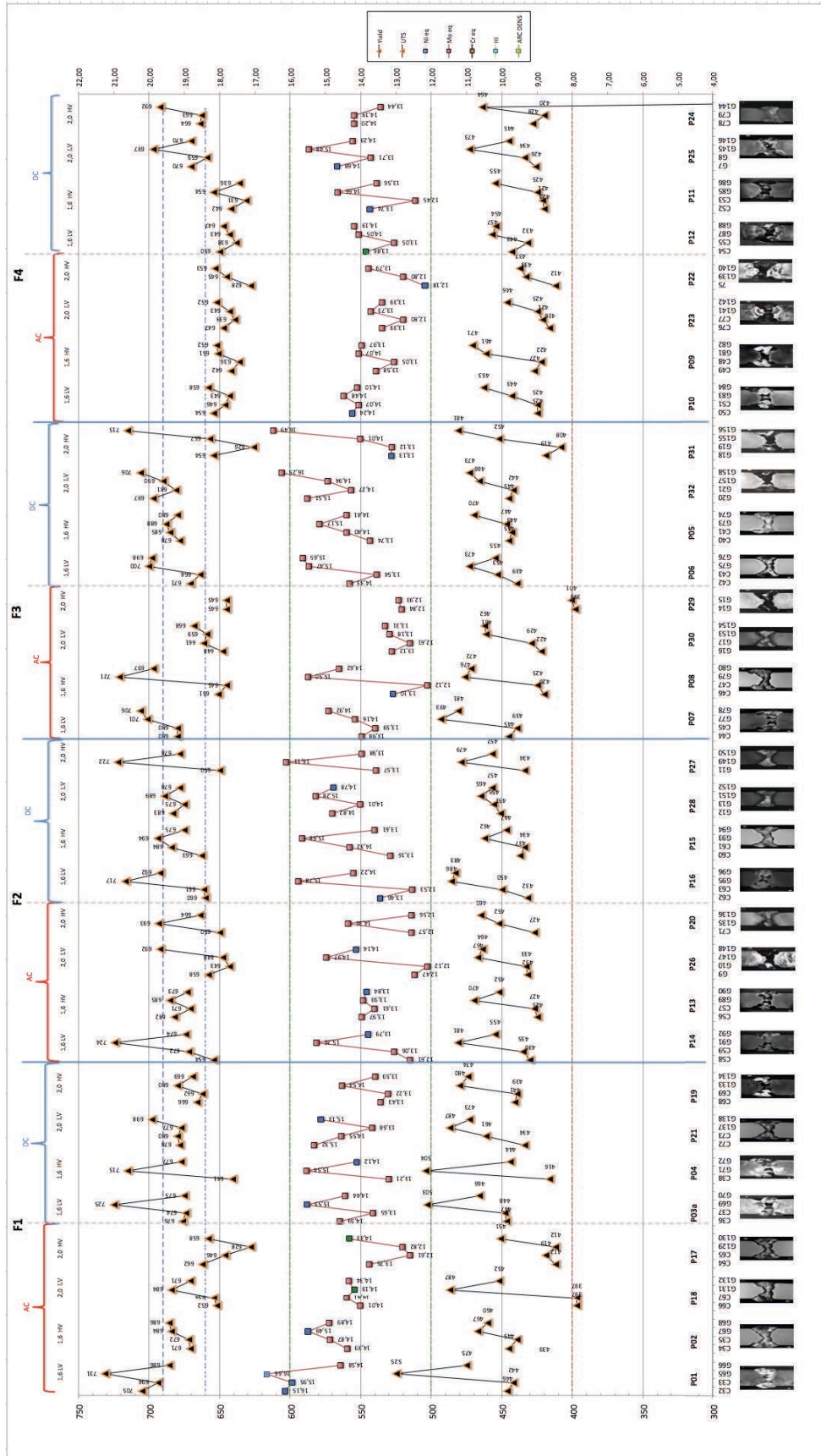
App 3- 8: Yield strength, UTS and Mo$_{eq}$ graph, grouped by: DOE Variables, Test ID. The drawer number identifies unitary samples.

7.1.4   XRF typical report

HELMUT FISCHER GmbH + Co. KG
Industriestrasse 21
71069 Sindelfingen

Fischerscope®   XRAY XDAL
Product: **P01 09136-02A**   **Dir.: pablo Ozaeta**   **Block: 1**
Application: 56 / NiCrMoFeW Co
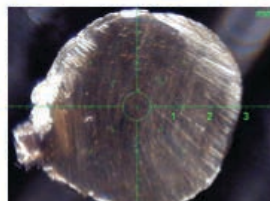
Calibración: sin patrones

n	Ni[%]	Cr[%]	Mo[%]	Fe[%]	W [%]	Co[%]	mq[ ]
1	54.0	15.3	13.8	14.1	2.74	-0.021	0.658
2	51.8	14.6	13.3	17.5	2.75	0.001	0.627
3	50.2	14.1	12.9	20.1	2.72	-0.003	0.633
4	48.9	13.7	12.5	22.5	2.59	-0.054	0.632
5	51.7	14.7	13.3	17.7	2.67	-0.000	0.645
6	50.5	14.0	12.9	19.9	2.69	-0.004	0.649
7	51.3	14.7	13.1	18.1	2.74	0.003	0.653
8	52.6	15.1	13.7	15.8	2.78	-0.000	0.641
9	52.4	14.9	13.6	16.5	2.73	-0.194	0.645

Mean	51.48 %	14.57 %	13.22 %	18.04 %	2.713 %
Standard deviation	1.506 %	0.545 %	0.444 %	2.510 %	0.057 %
C.O.V. (%)	2.93	3.74	3.36	13.91	2.09
Range	5.15 %	1.62 %	1.37 %	8.32 %	0.193 %
Number of readings	9	9	9	9	9
Min. reading	48.9 %	13.7 %	12.5 %	14.1 %	2.59 %
Max. reading	54.0 %	15.3 %	13.8 %	22.5 %	2.78 %
Measuring time	60 sec				

Operator:
Date: 28/01/2016 Time: 17:07:37
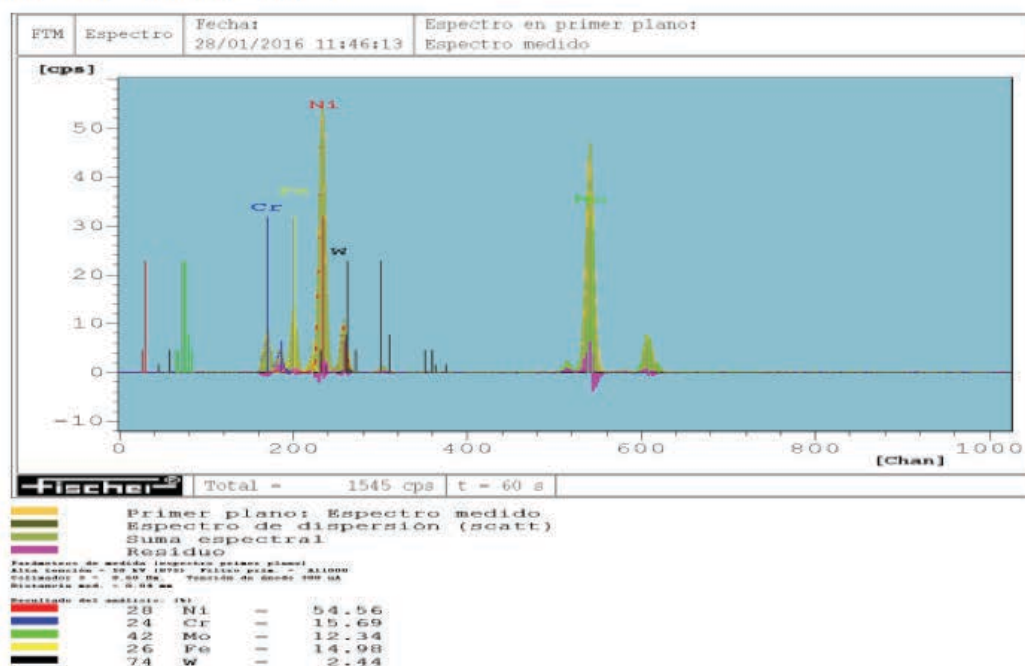
App 3- 9: XRF Report of one the checked samples.

Boxplot of Heat Input
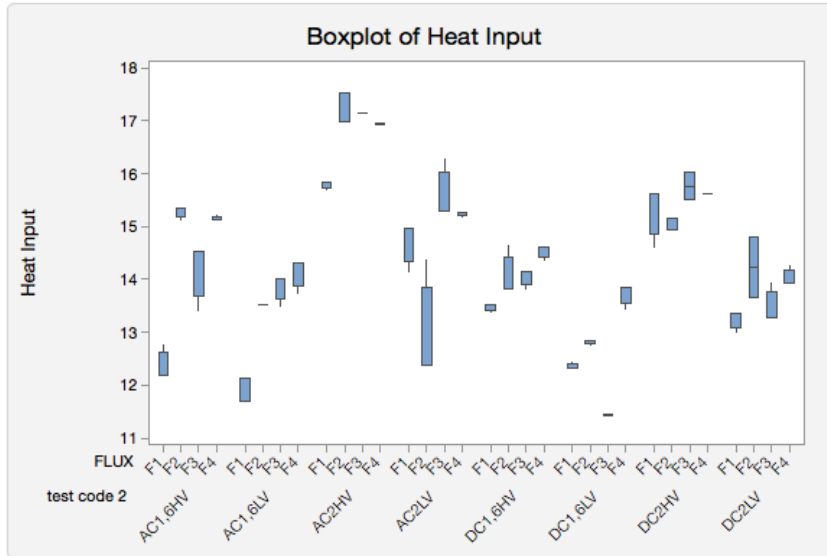
Summary Statistics

test code 2	FLUX	N	Minimum	Q1	Median	Q3	Maximum	95% Median CI
AC1,6HV	F1	4	12,1900	12,1900	12,1900	12,6250	12,7700	(12,1900; 12,7700)
	F2	4	15,1400	15,1950	15,3600	15,3600	15,3600	(15,1400; 15,3600)
	F3	4	13,4100	13,6900	14,5300	14,5300	14,5300	(13,4100; 14,5300)
	F4	4	15,1200	15,1200	15,1200	15,1875	15,2100	(15,1200; 15,2100)
AC1,6LV	F1	3	11,7000	11,7000	12,1300	12,1300	12,1300	(11,7000; 12,1300)
	F2	3	13,51	13,51	13,51	13,51	13,51	(13,51; 13,51)
	F3	4	13,5000	13,6275	14,0100	14,0100	14,0100	(13,5000; 14,0100)
	F4	4	13,7300	13,8725	14,3000	14,3000	14,3000	(13,7300; 14,3000)
AC2HV	F1	4	15,6900	15,7300	15,8500	15,8500	15,8500	(15,6900; 15,8500)
	F2	3	16,9700	16,9700	17,5200	17,5200	17,5200	(16,9700; 17,5200)
	F3	2	17,14	17,14	17,14	17,14	17,14	(17,14; 17,14)
	F4	4	16,9200	16,9300	16,9600	16,9600	16,9600	(16,9200; 16,9600)
AC2LV	F1	4	14,1500	14,3525	14,9600	14,9600	14,9600	(14,1500; 14,9600)
	F2	4	12,3700	12,3700	12,3700	13,8625	14,3600	(12,3700; 14,3600)
	F3	4	15,3000	15,3000	15,3000	16,0275	16,2700	(15,3000; 16,2700)
	F4	4	15,1900	15,2100	15,2700	15,2700	15,2700	(15,1900; 15,2700)
DC1,6HV	F1	4	13,3800	13,4150	13,5200	13,5200	13,5200	(13,3800; 13,5200)
	F2	4	13,8300	13,8300	13,8300	14,4300	14,6300	(13,8300; 14,6300)
	F3	4	13,8200	13,9025	14,1500	14,1500	14,1500	(13,8200; 14,1500)
	F4	4	14,3600	14,4250	14,6200	14,6200	14,6200	(14,3600; 14,6200)
DC1,6LV	F1	4	12,3100	12,3100	12,3100	12,4000	12,4300	(12,3100; 12,4300)
	F2	4	12,7700	12,7850	12,8300	12,8300	12,8300	(12,7700; 12,8300)
	F3	4	11,4300	11,4300	11,4300	11,4375	11,4400	(11,4300; 11,4400)
	F4	4	13,4500	13,5500	13,8500	13,8500	13,8500	(13,4500; 13,8500)
DC2HV	F1	4	14,6100	14,8600	15,6100	15,6100	15,6100	(14,6100; 15,6100)
	F2	3	14,9500	14,9500	15,1700	15,1700	15,1700	(14,9500; 15,1700)
	F3	4	15,5100	15,5100	15,7700	16,0300	16,0300	(15,5100; 16,0300)
	F4	3	15,61	15,61	15,61	15,61	15,61	(15,61; 15,61)
DC2LV	F1	4	13,0000	13,0875	13,3500	13,3500	13,3500	(13,0000; 13,3500)
	F2	4	13,6500	13,6500	14,2250	14,8000	14,8000	(13,6500; 14,8000)
	F3	4	13,2900	13,2900	13,2900	13,7775	13,9400	(13,2900; 13,9400)
	F4	4	13,9400	13,9400	13,9400	14,1800	14,2600	(13,9400; 14,2600)

App 3- 10: Heat Input vs. DOE variables.

174

Boxplot of Heat on wire
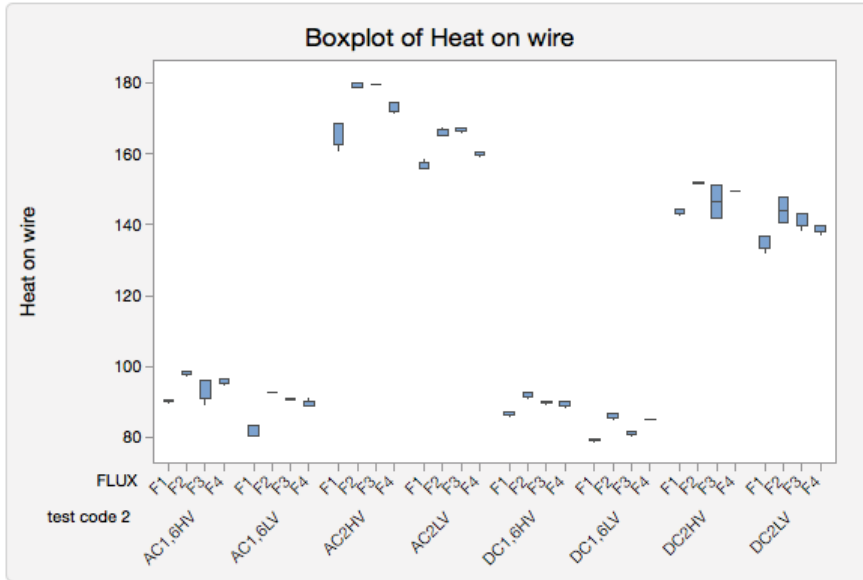
Summary Statistics

test code 2	FLUX	N	Minimum	Q1	Median	Q3	Maximum	95% Median CI
AC1,6HV	F1	4	89,9000	90,1200	90,7800	90,7800	90,7800	(89,9000; 90,7800)
	F2	4	97,5400	97,7725	98,4700	98,4700	98,4700	(97,5400; 98,4700)
	F3	4	89,400	91,118	96,270	96,270	96,270	(89,400; 96,270)
	F4	4	94,7800	95,1600	96,3000	96,3000	96,3000	(94,7800; 96,3000)
AC1,6LV	F1	3	80,2900	80,2900	80,2900	83,2300	83,2300	(80,2900; 83,2300)
	F2	3	92,78	92,78	92,78	92,78	92,78	(92,78; 92,78)
	F3	4	90,5500	90,5500	90,5500	91,0300	91,1900	(90,5500; 91,1900)
	F4	4	88,8900	88,8900	88,8900	90,3450	90,8300	(88,8900; 90,8300)
AC2HV	F1	4	160,800	162,735	168,540	168,540	168,540	(160,800; 168,540)
	F2	3	178,860	178,860	180,110	180,110	180,110	(178,860; 180,110)
	F3	2	179,7	179,7	179,7	179,7	179,7	(179,7; 179,7)
	F4	4	171,290	172,033	174,260	174,260	174,260	(171,290; 174,260)
AC2LV	F1	4	155,720	155,720	155,720	157,693	158,350	(155,720; 158,350)
	F2	4	165,290	165,290	165,290	166,918	167,460	(165,290; 167,460)
	F3	4	166,140	166,408	167,210	167,210	167,210	(166,140; 167,210)
	F4	4	159,250	159,535	160,390	160,390	160,390	(159,250; 160,390)
DC1,6HV	F1	4	86,0000	86,3275	87,3100	87,3100	87,3100	(86,0000; 87,3100)
	F2	4	90,9400	91,3350	92,5200	92,5200	92,5200	(90,9400; 92,5200)
	F3	4	89,4600	89,6625	90,2700	90,2700	90,2700	(89,4600; 90,2700)
	F4	4	88,3200	88,7975	90,2300	90,2300	90,2300	(88,3200; 90,2300)
DC1,6LV	F1	4	78,8500	79,0500	79,6500	79,6500	79,6500	(78,8500; 79,6500)
	F2	4	85,1400	85,5700	86,8600	86,8600	86,8600	(85,1400; 86,8600)
	F3	4	80,6100	80,8700	81,6500	81,6500	81,6500	(80,6100; 81,6500)
	F4	4	84,9500	84,9500	84,9500	85,1300	85,1900	(84,9500; 85,1900)
DC2HV	F1	4	142,580	143,038	144,410	144,410	144,410	(142,580; 144,410)
	F2	3	151,490	151,490	152,010	152,010	152,010	(151,490; 152,010)
	F3	4	141,870	141,870	146,435	151,000	151,000	(141,870; 151,000)
	F4	3	149,35	149,35	149,35	149,35	149,35	(149,35; 149,35)
DC2LV	F1	4	132,080	133,243	136,730	136,730	136,730	(132,080; 136,730)
	F2	4	140,450	140,450	144,045	147,640	147,640	(140,450; 147,640)
	F3	4	138,420	139,643	143,310	143,310	143,310	(138,420; 143,310)
	F4	4	137,210	137,853	139,780	139,780	139,780	(137,210; 139,780)

App 3- 11: Heat on Wire vs. DOE variables.

175

Boxplot of Dep Rate
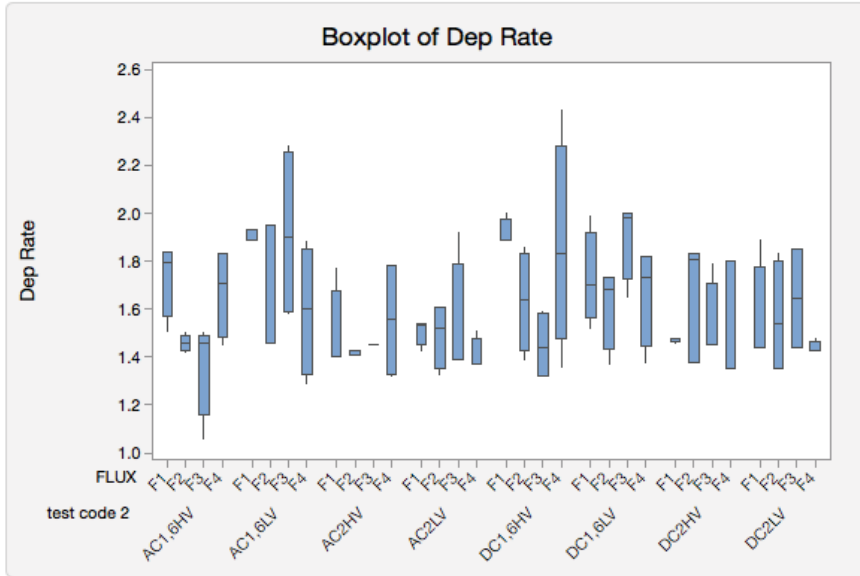
Summary Statistics

test code 2	FLUX	N	Minimum	Q1	Median	Q3	Maximum	95% Median CI
AC1,6HV	F1	4	1,51000	1,57000	1,79500	1,84000	1,84000	(1,51000; 1,84000)
	F2	4	1,42000	1,43000	1,46000	1,49000	1,50000	(1,42000; 1,50000)
	F3	4	1,0600	1,1600	1,4600	1,4900	1,5000	(1,0600; 1,5000)
	F4	4	1,45000	1,48250	1,70500	1,83000	1,83000	(1,45000; 1,83000)
AC1,6LV	F1	3	1,89000	1,89000	1,89000	1,93000	1,93000	(1,89000; 1,93000)
	F2	3	1,4600	1,4600	1,9500	1,9500	1,9500	(1,4600; 1,9500)
	F3	4	1,5800	1,5900	1,9000	2,2550	2,2800	(1,5800; 2,2800)
	F4	4	1,2900	1,3250	1,6000	1,8525	1,8800	(1,2900; 1,8800)
AC2HV	F1	4	1,40000	1,40000	1,40000	1,67750	1,77000	(1,40000; 1,77000)
	F2	3	1,41000	1,41000	1,41000	1,43000	1,43000	(1,41000; 1,43000)
	F3	2	1,45	1,45	1,45	1,45	1,45	(1,45; 1,45)
	F4	4	1,3200	1,3250	1,5600	1,7800	1,7800	(1,3200; 1,7800)
AC2LV	F1	4	1,43000	1,45500	1,53500	1,54000	1,54000	(1,43000; 1,54000)
	F2	4	1,33000	1,35500	1,52000	1,61000	1,61000	(1,33000; 1,61000)
	F3	4	1,3900	1,3900	1,3900	1,7875	1,9200	(1,3900; 1,9200)
	F4	4	1,37000	1,37000	1,37000	1,47500	1,51000	(1,37000; 1,51000)
DC1,6HV	F1	4	1,89000	1,89000	1,89000	1,97250	2,00000	(1,89000; 2,00000)
	F2	4	1,3900	1,4275	1,6400	1,8300	1,8600	(1,3900; 1,8600)
	F3	4	1,32000	1,32000	1,44000	1,58250	1,59000	(1,32000; 1,59000)
	F4	4	1,3600	1,4775	1,8300	2,2800	2,4300	(1,3600; 2,4300)
DC1,6LV	F1	4	1,52000	1,56500	1,70000	1,91750	1,99000	(1,52000; 1,99000)
	F2	4	1,37000	1,43500	1,68000	1,73000	1,73000	(1,37000; 1,73000)
	F3	4	1,65000	1,72750	1,98000	2,00000	2,00000	(1,65000; 2,00000)
	F4	4	1,3800	1,4475	1,7350	1,8200	1,8200	(1,3800; 1,8200)
DC2HV	F1	4	1,46000	1,46250	1,47500	1,48000	1,48000	(1,46000; 1,48000)
	F2	3	1,3800	1,3800	1,8100	1,8300	1,8300	(1,3800; 1,8300)
	F3	4	1,45000	1,45000	1,45500	1,70750	1,79000	(1,45000; 1,79000)
	F4	3	1,3500	1,3500	1,3500	1,8000	1,8000	(1,3500; 1,8000)
DC2LV	F1	4	1,4400	1,4400	1,4400	1,7775	1,8900	(1,4400; 1,8900)
	F2	4	1,3500	1,3525	1,5400	1,8025	1,8300	(1,3500; 1,8300)
	F3	4	1,4400	1,4400	1,6450	1,8500	1,8500	(1,4400; 1,8500)
	F4	4	1,43000	1,43000	1,43000	1,46750	1,48000	(1,43000; 1,48000)

App 3- 12: Deposition Rate vs. DOE variables.

Boxplot of Z [ohm]
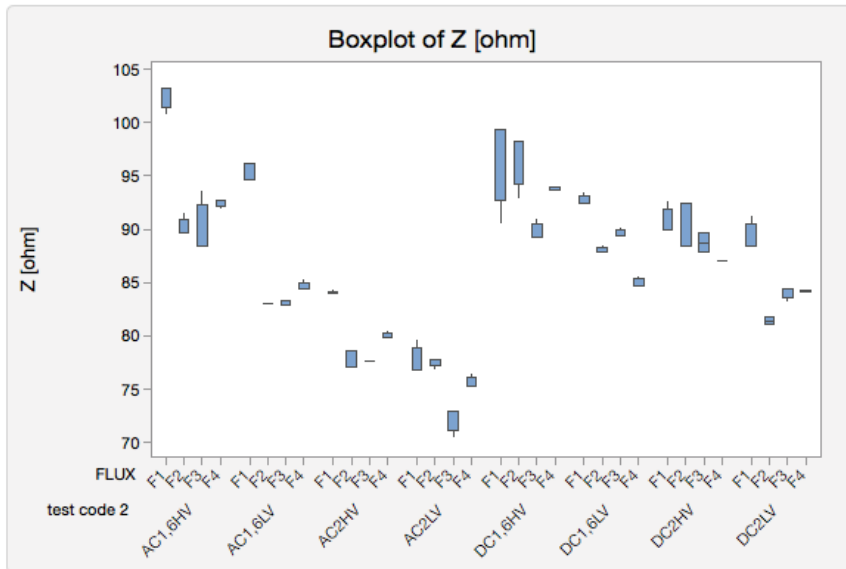
Summary Statistics

test code 2	FLUX	N	Minimum	Q1	Median	Q3	Maximum	95% Median CI
AC1,6HV	F1	4	100,880	101,460	103,200	103,200	103,200	(100,880; 103,200)
	F2	4	89,6000	89,6000	89,6000	90,9725	91,4300	(89,6000; 91,4300)
	F3	4	88,370	88,370	88,370	92,270	93,570	(88,370; 93,570)
	F4	4	92,0000	92,1850	92,7400	92,7400	92,7400	(92,0000; 92,7400)
AC1,6LV	F1	3	94,5700	94,5700	94,5700	96,1500	96,1500	(94,5700; 96,1500)
	F2	3	83	83	83	83	83	(83; 83)
	F3	4	82,9600	82,9600	82,9600	83,2375	83,3300	(82,9600; 83,3300)
	F4	4	84,4500	84,4500	84,4500	85,0125	85,2000	(84,4500; 85,2000)
AC2HV	F1	4	84,0100	84,0100	84,0100	84,1975	84,2600	(84,0100; 84,2600)
	F2	3	77,0600	77,0600	77,0600	78,6700	78,6700	(77,0600; 78,6700)
	F3	2	77,66	77,66	77,66	77,66	77,66	(77,66; 77,66)
	F4	4	79,9200	79,9200	79,9200	80,3175	80,4500	(79,9200; 80,4500)
AC2LV	F1	4	76,8400	76,8400	76,8400	78,8500	79,5200	(76,8400; 79,5200)
	F2	4	76,9400	77,1575	77,8100	77,8100	77,8100	(76,9400; 77,8100)
	F3	4	70,6100	71,1925	72,9400	72,9400	72,9400	(70,6100; 72,9400)
	F4	4	75,3400	75,3400	75,3400	76,1200	76,3800	(75,3400; 76,3800)
DC1,6HV	F1	4	90,600	92,770	99,280	99,280	99,280	(90,600; 99,280)
	F2	4	92,930	94,260	98,250	98,250	98,250	(92,930; 98,250)
	F3	4	89,3100	89,3100	89,3100	90,5250	90,9300	(89,3100; 90,9300)
	F4	4	93,6300	93,7250	94,0100	94,0100	94,0100	(93,6300; 94,0100)
DC1,6LV	F1	4	92,4100	92,4100	92,4100	93,1000	93,3300	(92,4100; 93,3300)
	F2	4	87,8300	87,8300	87,8300	88,2650	88,4100	(87,8300; 88,4100)
	F3	4	89,4500	89,4500	89,4500	89,8925	90,0400	(89,4500; 90,0400)
	F4	4	84,7100	84,7100	84,7100	85,3400	85,5500	(84,7100; 85,5500)
DC2HV	F1	4	89,9500	89,9500	89,9500	91,9375	92,6000	(89,9500; 92,6000)
	F2	3	88,420	88,420	88,420	92,450	92,450	(88,420; 92,450)
	F3	4	87,8900	87,8900	88,7650	89,6400	89,6400	(87,8900; 89,6400)
	F4	3	87,01	87,01	87,01	87,01	87,01	(87,01; 87,01)
DC2LV	F1	4	88,3800	88,3800	88,3800	90,4650	91,1600	(88,3800; 91,1600)
	F2	4	81,0400	81,0400	81,3950	81,7500	81,7500	(81,0400; 81,7500)
	F3	4	83,2600	83,5575	84,4500	84,4500	84,4500	(83,2600; 84,4500)
	F4	4	84,1300	84,1750	84,3100	84,3100	84,3100	(84,1300; 84,3100)

App 3- 13: Electrical Impedance vs. DOE variables.

Boxplot of [mohm/mm2]
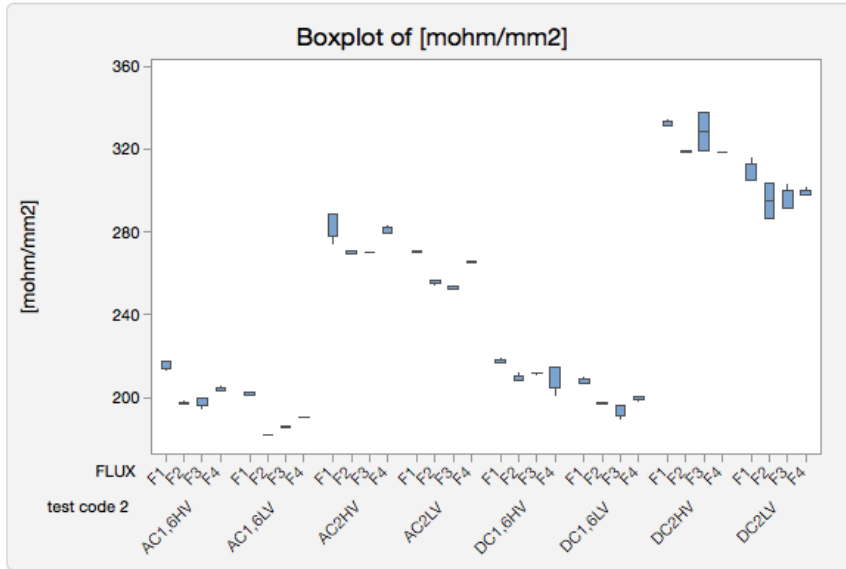
Summary Statistics

test code 2	FLUX	N	Minimum	Q1	Median	Q3	Maximum	95% Median CI
AC1,6HV	F1	4	213,060	214,223	217,710	217,710	217,710	(213,060; 217,710)
	F2	4	196,970	196,970	196,970	197,885	198,190	(196,970; 198,190)
	F3	4	194,870	196,073	199,680	199,680	199,680	(194,870; 199,680)
	F4	4	203,400	203,400	203,400	204,713	205,150	(203,400; 205,150)
AC1,6LV	F1	3	200,920	200,920	202,530	202,530	202,530	(200,920; 202,530)
	F2	3	181,97	181,97	181,97	181,97	181,97	(181,97; 181,97)
	F3	4	185,420	185,635	186,280	186,280	186,280	(185,420; 186,280)
	F4	4	190,460	190,493	190,590	190,590	190,590	(190,460; 190,590)
AC2HV	F1	4	274,700	278,140	288,460	288,460	288,460	(274,700; 288,460)
	F2	3	269,740	269,740	269,740	270,940	270,940	(269,740; 270,940)
	F3	2	269,94	269,94	269,94	269,94	269,94	(269,94; 269,94)
	F4	4	279,490	279,490	279,490	282,055	282,910	(279,490; 282,910)
AC2LV	F1	4	269,820	269,993	270,510	270,510	270,510	(269,820; 270,510)
	F2	4	254,650	255,190	256,810	256,810	256,810	(254,650; 256,810)
	F3	4	252,670	252,670	252,670	253,495	253,770	(252,670; 253,770)
	F4	4	264,850	265,048	265,640	265,640	265,640	(264,850; 265,640)
DC1,6HV	F1	4	216,560	216,560	216,560	218,330	218,920	(216,560; 218,920)
	F2	4	208,080	208,080	208,080	210,638	211,490	(208,080; 211,490)
	F3	4	211,380	211,523	211,950	211,950	211,950	(211,380; 211,950)
	F4	4	200,940	204,433	214,910	214,910	214,910	(200,940; 214,910)
DC1,6LV	F1	4	206,990	206,990	206,990	208,903	209,540	(206,990; 209,540)
	F2	4	196,520	196,520	196,520	197,405	197,700	(196,520; 197,700)
	F3	4	189,560	191,263	196,370	196,370	196,370	(189,560; 196,370)
	F4	4	198,380	198,800	200,060	200,060	200,060	(198,380; 200,060)
DC2HV	F1	4	331,610	331,610	331,610	333,748	334,460	(331,610; 334,460)
	F2	3	318,530	318,530	318,530	319,380	319,380	(318,530; 319,380)
	F3	4	319,140	319,140	328,295	337,450	337,450	(319,140; 337,450)
	F4	3	318,79	318,79	318,79	318,79	318,79	(318,79; 318,79)
DC2LV	F1	4	305,300	305,300	305,300	312,950	315,500	(305,300; 315,500)
	F2	4	286,830	286,830	295,175	303,520	303,520	(286,830; 303,520)
	F3	4	291,310	291,310	291,310	300,085	303,010	(291,310; 303,010)
	F4	4	297,610	297,610	297,610	300,288	301,180	(297,610; 301,180)

App 3- 14: Electrical Stick-out times electrical resistivity vs. DOE variables.

Best Subsets Regression: UTS versus Amp; Volt; WFS; Heat Input; Heat on wire; Arc Density; Dep Rate; [mohm/mm2]; Z [ohm]

Model Summary

Number of Predictors	R-sq	R-sq(adj)	R-sq(pred)	Mallows' Cp	S	Amp	Volt	WFS	Heat Input	Heat on wire	Arc Density	Dep Rate	[mohm/mm2]	Z [ohm]
1	18,7	17,8	15,2	11,0	19,20	X								
1	15,4	14,4	11,6	15,0	19,59					X				
1	15,3	14,3	11,5	15,1	19,60				X					
1	8,5	7,4	4,2	23,2	20,37			X						
1	7,4	6,3	3,6	24,5	20,49									X
2	23,5	21,8	18,4	7,3	18,73	X	X							
2	23,2	21,5	18,2	7,6	18,76			X		X				
2	21,9	20,1	16,9	9,2	18,93	X						X		
2	21,8	20,0	16,4	9,3	18,94					X	X			
2	21,5	19,7	15,7	9,7	18,97	X			X					
3	29,7	27,2	23,1	1,9	18,06	X	X					X		
3	29,1	26,7	22,5	2,6	18,13			X		X		X		
3	27,3	24,7	19,8	4,8	18,37	X			X			X		
3	27,2	24,7	20,4	4,8	18,37					X	X	X		
3	25,5	22,9	18,1	6,9	18,59		X			X		X		
4	31,7	28,5	22,9	1,5	17,90		X	X				X	X	
4	31,4	28,1	22,6	1,9	17,95		X			X		X	X	
4	31,1	27,8	22,5	2,3	17,99	X	X				X	X		
4	31,0	27,7	22,2	2,4	18,00	X	X			X		X		
4	30,9	27,6	22,2	2,5	18,01	X	X	X				X		
5	32,2	28,2	21,4	2,9	17,95		X	X				X	X	X
5	32,1	28,0	21,3	3,1	17,96	X	X					X	X	X
5	31,9	27,9	21,2	3,2	17,98	X	X	X				X	X	
5	31,9	27,8	21,6	3,3	17,99		X	X	X			X	X	
5	31,9	27,8	20,9	3,3	17,99		X				X	X	X	X
6	32,7	27,8	20,1	4,3	17,99		X	X	X			X	X	X
6	32,5	27,6	19,9	4,6	18,02	X	X		X			X	X	X
6	32,3	27,4	19,9	4,8	18,04	X	X	X	X			X	X	
6	32,3	27,4	19,5	4,8	18,04		X		X		X	X	X	X
6	32,2	27,3	18,8	4,9	18,05		X	X			X	X	X	X
7	32,8	27,1	17,2	6,2	18,08		X	X	X		X	X	X	X
7	32,8	27,0	18,5	6,2	18,08		X	X	X	X	X	X	X	
7	32,7	27,0	18,6	6,3	18,10	X	X	X	X		X	X	X	
7	32,6	26,9	16,9	6,4	18,11	X	X		X		X	X	X	X
7	32,5	26,8	17,8	6,5	18,12	X	X		X	X	X	X	X	
8	32,9	26,3	15,5	8,1	18,18		X	X	X	X	X	X	X	X
8	32,8	26,2	16,6	8,2	18,19	X	X	X	X	X	X	X	X	
8	32,8	26,2	15,6	8,2	18,19	X	X	X	X		X	X	X	X
8	32,7	26,1	15,0	8,3	18,21	X	X		X	X	X	X	X	X
8	32,4	25,7	15,2	8,6	18,25	X	X	X	X	X		X	X	X
9	33,0	25,4	13,8	10,0	18,29	X	X	X	X	X	X	X	X	X

App 3- 15: Best subset regression for UTS against welding Parameters and

Best Subsets Regression: UTS versus %Ni XRF; %Cr XRF; %Mo XRF; %Fe XRF; %W XRF

Model Summary

Number of Predictors	R-sq	R-sq(adj)	R-sq(pred)	Mallows' Cp	S	%Ni XRF	%Cr XRF	%Mo XRF	%Fe XRF	%W XRF
1	67,3	66,9	65,7	6,5	12,16				X	
1	66,7	66,4	65,3	8,1	12,27			X		
1	66,1	65,7	64,4	10,0	12,39	X				
1	63,0	62,5	61,1	18,6	12,94		X			
1	53,7	53,2	51,6	44,5	14,47					X
2	69,0	68,3	66,9	3,6	11,90	X		X		
2	68,9	68,2	66,7	4,1	11,93		X		X	
2	68,5	67,8	66,4	5,1	12,00			X	X	
2	67,5	66,7	65,4	8,0	12,20				X	X
2	67,4	66,6	65,0	8,4	12,22	X			X	
3	70,3	69,3	67,6	2,0	11,72		X	X	X	
3	70,3	69,3	67,6	2,1	11,72	X	X	X		
3	70,2	69,2	67,5	2,3	11,74	X	X		X	
3	70,1	69,1	67,4	2,6	11,76	X		X	X	
3	69,4	68,3	66,8	4,6	11,90	X		X		X
4	70,3	68,9	67,2	4,0	11,79	X	X		X	X
4	70,3	68,9	67,2	4,0	11,79		X	X	X	X
4	70,3	68,9	67,2	4,0	11,79	X	X	X	X	
4	70,3	68,9	67,2	4,1	11,79	X	X	X		X
4	70,2	68,8	67,1	4,3	11,81	X		X	X	X
5	70,3	68,6	66,6	6,0	11,86	X	X	X	X	X

App 3- 16: Best subset regression for UTS against Actual Tensile samples Chemical composition

Best Subsets Regression: UTS versus Amp; Volt; WFS; Heat Input; Heat on wire; Arc Density; Dep Rate; [mohm/mm2]; %Nieq XRF; %Creq XRF; %Moeq XRF

Model Summary

Number of Predictors	R-sq	R-sq(adj)	R-sq(pred)	Mallows' Cp	S	Amp	Volt	WFS	Heat Input	Heat on wire	Arc Density	Dep Rate	[mohm/mm2]	%Nieq XRF	%Creq XRF	%Moeq XRF
1	66,1	65,7	64,6	17,3	12,38											X
1	65,9	65,5	64,3	18,1	12,42									X		
1	63,0	62,5	61,1	26,9	12,94										X	
1	20,4	19,4	16,9	155,6	18,98	X										
1	16,8	15,8	13,0	166,5	19,40						X					
2	70,0	69,3	68,1	7,5	11,71						X					X
2	69,6	68,9	67,5	8,9	11,80							X				X
2	69,4	68,7	67,3	9,4	11,83			X								X
2	69,0	68,3	66,7	10,6	11,90						X					X
2	67,8	67,0	65,6	14,3	12,14						X			X		
3	70,8	69,8	68,2	7,1	11,62						X	X				X
3	70,6	69,6	68,1	7,7	11,66						X			X		X
3	70,6	69,6	68,0	7,7	11,66						X				X	X
3	70,5	69,4	67,9	8,2	11,69						X			X	X	
3	70,4	69,4	67,6	8,4	11,70							X	X			X
4	71,8	70,5	68,4	6,1	11,49		X				X			X		X
4	71,5	70,2	67,3	7,1	11,55	X					X			X		X
4	71,5	70,1	67,9	7,2	11,56		X				X	X				X
4	71,2	69,8	67,1	8,0	11,61	X					X	X				X
4	71,2	69,8	67,9	8,1	11,62						X	X		X		X
5	73,5	71,9	69,4	3,1	11,21		X				X	X	X			X
5	72,4	70,8	67,7	6,3	11,43	X					X	X	X			X
5	72,4	70,7	67,9	6,4	11,44	X	X	X					X			X
5	72,3	70,7	68,4	6,6	11,45		X					X	X	X		X
5	72,3	70,6	68,3	6,7	11,46		X					X	X		X	X
6	73,8	71,9	68,6	4,1	11,21	X	X	X				X	X			X
6	73,7	71,8	69,0	4,5	11,24		X				X	X	X	X		X
6	73,7	71,7	69,0	4,6	11,24		X				X	X	X		X	X
6	73,6	71,6	68,3	4,9	11,26	X	X				X	X	X			X
6	73,6	71,6	68,3	4,9	11,27		X			X	X	X	X			X
7	74,2	71,9	68,4	5,1	11,21	X	X	X			X	X	X			X
7	74,0	71,8	68,2	5,5	11,24	X	X	X				X	X	X		X
7	74,0	71,8	68,2	5,5	11,24	X	X	X				X	X		X	X
7	73,9	71,7	68,1	5,8	11,26	X	X	X				X	X	X	X	
7	73,9	71,7	68,0	5,8	11,26	X	X	X		X		X	X			X
8	74,3	71,7	67,9	6,7	11,25	X	X	X			X	X	X	X		X
8	74,3	71,7	67,9	6,7	11,25	X	X	X			X	X	X		X	X
8	74,3	71,7	67,5	6,8	11,25	X	X	X	X		X	X	X			X
8	74,2	71,6	67,5	7,1	11,28	X	X	X		X	X	X	X			X
8	74,1	71,5	67,7	7,2	11,28	X	X	X			X	X	X	X	X	
9	74,5	71,5	67,1	8,2	11,28	X	X	X	X		X	X	X	X		X
9	74,4	71,5	67,1	8,2	11,28	X	X	X	X		X	X	X		X	X
9	74,3	71,4	67,4	8,6	11,31	X	X	X			X	X	X	X	X	X
9	74,3	71,4	67,0	8,6	11,31	X	X	X		X	X	X	X	X		X
9	74,3	71,4	66,9	8,7	11,32	X	X	X	X		X	X	X	X	X	
10	74,5	71,2	66,3	10,1	11,34	X	X	X	X	X	X	X	X	X		X
10	74,5	71,2	66,5	10,1	11,35	X	X	X	X		X	X	X	X	X	X
10	74,5	71,2	66,2	10,1	11,35	X	X	X	X	X	X	X	X		X	X
10	74,3	71,0	66,5	10,6	11,38	X	X	X		X	X	X	X	X	X	X
10	74,3	71,0	66,0	10,6	11,38	X	X	X	X	X	X	X	X	X	X	
11	74,5	70,9	65,7	12,0	11,41	X	X	X	X	X	X	X	X	X	X	X

App 3- 17: Best subset regression for UTS against Welding parameters and Chemical Composition